ISSN 2712-8172

MAGAZINE OF CIVIL ENGINEERING

Magazine of Civil Engineering

ISSN 2712-8172

Online peer-reviewed open-access scientific journal in the field of Civil and Construction Engineering

Founder and Publisher: Peter the Great St. Petersburg Polytechnic University

This journal is registered by the Federal Service for Supervision of Communications, Information Technology, and Mass Media (ROSKOMNADZOR) in 2020. Certificate El No. FS77-77906 issued February 19, 2020.

Periodicity: 8 issues per year

Publication in the journal is open and free for all authors and readers.

Indexing: Scopus, Web of Sceince (ESCI, RSCI), DOAJ, Compendex, Google Academia, Index Copernicus, ProQuest, Ulrich's Serials Analysis System, CNKI

Corresponding address: 29 Polytechnicheskaya st., Saint Petersburg, 195251, Russia

Chief science editor:
D.Sc., Galina L. Kozinetc

Deputy chief science editors:
D.Sc., Sergey V. Korniyenko

Executive editor: Ekaterina A. Linnik

Translator, editor: Irina Ye. Lebedeva

Proofreader: Philipp Chrysanthes S. Bastian

DT publishing specialist:
Anastasiya A. Kononova

Contacts:
E-mail: mce@spbstu.ru
Web: http://www.engstroy.spbstu.ru

Date of issue: 26.12.2025

Contents

Magazine of Civil Engineering

ISSN 2712-8172

journal homepage: http://engstroy.spbstu.ru/

Research article

UDC 693.547

DOI: 10.34910/MCE.140.1

Modulus of elasticity of concrete at an early age

G.V. Nesvetaev , ***A. Chepurnenko*** , ***B.M. Yazyev*** , ***Yu.I. Koryanova***✉

[1] *Don State Technical University, Rostov-on-Don, Russian Federation*

✉ *koryanova.yi@mail.ru*

Keywords: E-modulus of concrete, compressive strength, degree of maturity of concrete, massive monolithic reinforced structure

Abstract. Introduction. The assessment of the risk of early crack formation during hardening of massive monolithic reinforced concrete structures due to temperature gradients predetermines the relevance of studies aimed at increasing the reliability of methods for calculating temperature fields and stresses. When developing technological regulations for concreting, modeling methods are used to assess the risk of early crack formation, the implementation of which requires equations for changing the strength and deformation properties of concrete over time. Highly mobile and self-compacting concrete mixtures with modifiers, which are widely used in concreting the above structures, predetermine the relevance of clarifying known and identifying new patterns of change in the properties of concrete in the early period of hardening, in particular, obtaining equations for changing the E-modulus from prescription factors and temperature conditions. Purpose of the study: obtaining equations for changes in the early and subsequent periods of hardening of the E-modulus of concrete from highly mobile and self-compacting concrete mixtures depending on the prescription factors and temperature conditions during hardening. Methods. Analysis of known approaches to assessing changes in the E-modulus of concrete over time. Modeling using a three-component structural model "matrix – contact zone – aggregate." Experimental studies of the E-modulus depending on the compressive strength limit in the early and subsequent hardening periods of concrete from highly mobile and self-compacting concrete mixtures. Results: Equations are proposed that describe the change in time of the E-modulus of concretes from highly mobile and self-compacting concrete mixtures depending on the compressive strength limit, taking into account the maturity index. The possibility of using the equation EN 1992-1-1 for the change in E-modulus from compressive strength limit for the specified concretes is shown.

Funding: The study was supported by the grant of the Russian Science Foundation No. 25-19-00164, https://rscf.ru/project/25-19-00164/

Citation: Nesvetaev, G.V., Chepurnenko, A., Yazyev, B.M., Koryanova, Yu.I. Modulus of elasticity of concrete at an early age. Magazine of Civil Engineering. 2025. 18(8). Article no. 14001. DOI: 10.34910/MCE.140.1

1. Introduction

When concreting massive monolithic structures, one of the important tasks is to prevent the risk of early crack formation due to temperature gradients in the early period of hardening caused by heat dissipation from the concrete. When concreting foundation slabs, Russian standard SP 70.13330.2012 allows, in the case of using self-compacting concrete mixtures, laying "simultaneously over the entire site of the structure" without the installation of working joints. Such practice takes place within the concreting section and when erecting massive foundation slabs with a volume of hundreds and even thousands of cubic meters when using self-compacting concrete mixtures of grades S4, S5 in a relatively short period of time [1]. As a result, significant temperature gradients are formed in the hardening concrete mass [2, 3]. The review presented in [4] shows that, based on the results of field observations in the period 2016-2022,

in structures with a top modulus of 1.4...2.4 made of concrete classes B25...B45, there were temperature differences between the center and the top of more than 20 °C at an initial temperature of the concrete mix of 8...29 °C and an ambient temperature of 4...30 °C. The time to reach the maximum difference ranged from 24 to 62 hours. The modeling data presented there [5–8] showed temperature differences of up to 30 °C and more, with a time to reach the maximum of 24...75 hours.

Russian standard SP 435.1325800.2018 prescribes "measures to reduce the influence of temperature and humidity fields and stresses associated with heat dissipation during concrete hardening" during the construction of massive monolithic structures, in connection with which the assessment of temperature fields and stresses to prevent early crack formation is an urgent task [8, 9], the solution of which, when developing technological regulations for concreting, is implemented by methods of modeling temperature fields and stresses [7, 10], including using numerical methods [5–7, 11]. As shown, for example, in [11], the most dangerous period is 1 ... 5 days, due to significant temperature changes. In [12], the effect of temperature conditions of hardening, different from normal, on the E-modulus of concrete is considered, and in [13], detailed studies of the effect of loading rate on the deformation diagram and the E-modulus of concrete under sulfate aggression are carried out. It is obvious that the study of the patterns of change in the E-modulus of concrete depending not only on the prescription factors but also on the temperature conditions during hardening, especially in the early period, and operation, and loading parameters, is a pressing task.

When studying crack formation processes in the early period of hardening of massive structures, methods of fracture mechanics are used, taking into account changes in heat dissipation and deformation properties of concrete over time [14].

Positive experience in constructing massive structures using prescription regulation of temperature fields [1] confirms the relevance of theoretical and experimental studies of the stress-strain state of structures in the early period of concrete hardening. When modeling, certain assumptions are often made regarding the kinetics of strength and E-modulus [11]. The authors [11] come to the conclusion that "the minimum thickness of a slab structure made of concrete classes B20...B50, above which it can be considered massive concrete, is about 0.6 m." A similar opinion is contained in [15].

Most software packages, including ANSYS, Abaqus, Lira-SAPR, SCAD, and a number of others, do not allow by default to specify the change in the E-modulus of concrete over time [16]. This problem is partially solved by developing and implementing user subroutines in FORTRAN and Python [17, 18], which requires a highly qualified programmer, as well as a deep understanding of the principles of operation of software packages. In the Midas Civil software package, the E-modulus of concrete can only be specified explicitly as a function of time [19], which predetermines the relevance of studies of dependencies $E_\tau = f\left(E_{28}\right)$. A thorough analysis of various equations describing the dependence of the E-modulus of concrete, including with mineral admixtures, on the ultimate strength is presented in [20].

In this regard, the purpose of this work is: obtaining equations for changes in the early and subsequent periods of hardening of the E-modulus of concrete from highly mobile and self-compacting concrete mixtures depending on the prescription factors and temperature conditions during hardening.

2. Methods

The assessment of the level of thermal stress state in the early period of hardening of concrete of a massive structure involves determining the magnitude of tensile stresses over time at each step of the calculations:

$$\Delta\sigma\left(z\right)=\frac{E\left(z,t\right)}{1-\upsilon}\cdot\left(\Delta\varepsilon-\alpha\cdot\Delta T\left(z\right)-\Delta\varepsilon_{cr}\left(z\right)\right), \quad (1)$$

where $\Delta\varepsilon$ is the average increment of total deformation over the slab thickness; $\Delta T\left(z\right)$ is the difference between the temperature at the point at the current and previous time step; $\Delta\varepsilon_{cr}\left(z\right)$ is the increment of creep deformation; υ is the Poisson's ratio of concrete; α is the coefficient of linear thermal expansion of concrete; $E\left(z,t\right)$ is the E-modulus of concrete over time. The multiplier $\left(1-\upsilon\right)$ in the denominator in Eq. (1) takes into account the work of concrete under biaxial tension (compression) $\left(\sigma_x=\sigma_y=\sigma\right)$ [10].

In special cases, equations of the form [4, 21] are used:

$$\sigma_T = \frac{k_r \cdot E \cdot \alpha \cdot \Delta T}{(1+\varphi)} \quad (2)$$

or [12]:

$$\sigma_{IIT} = \frac{\alpha_T \cdot E}{1-\upsilon} \cdot \left(T_{cp} - T_{II}\right), \quad (3)$$

where σ_T, σ_{IIT} – tensile stress from temperature gradients, MPa; k_r takes into account the degree of restriction on the upper top of the slab (0.83 [16]); E – E-modulus of concrete, MPa; $\Delta T\left(T_{cp} - T_{II}\right)$ – temperature difference between the center and the upper top of the slab at any time t, ºC; φ – creep coefficient of concrete.

In any case, to determine the magnitude of tensile stresses, data on the kinetics of elasticity of hardening concrete are needed, taking into account the effect of changing temperature. Numerous dependences of the E-modulus of concrete on the compressive strength limit are known [20, 23]. In general, some of them can be presented as:

$$E_0 = k \cdot \frac{a \cdot (b \cdot R + c)}{d + e \cdot R}. \quad (4)$$

The coefficients of some Eqs. (4) are given in Table 1.

Table 1. Coefficients of Eqs. (4).

Year	Author	Curve No. (Fig. 1)	Coefficients					
			k	***a***	***b***	***c***	***d***	***e***
1919	Uoker	6 [27]	53500	1	1	0	20	1
1937	Roš	5 [26]	55000	1	1	0	15	1
1988	Chistyakov	3 [27]	54000	1	1	0	20	1
1996	Karpenko	2 [28]	52000	1	1	0	18	1
1996	Nesvetaev	7	56700	1	1	0	22.5	1

Another group of equations has the general form:

$$E_0 = k \cdot \frac{a}{b + \frac{c}{d + R}}. \quad (5)$$

The coefficients of some Eqs. (5) are given in Table 2.

Table 2. Coefficients of Eqs. (5).

Year	Author	Curve No. (Fig. 1)	Coefficients				
			k	***a***	***b***	***c***	***d***
1990	Kvirikadze	9	1000	60	1	29	3.8
1996	Nesvetaev	1	$456 \cdot E_a/67 + 544$	$0.05R + 57$			

E_a [GPa] – E-modulus of coarse aggregate.

According to EN 1992-1-1 and ACI 318-08, IS:456 (India), CSA (Canada), the relationship between the E-modulus and the compressive strength of concrete $\left(f_{cm}, f_c\right)$ is given by the equations:

$$\text{EN}: \; E_{cm} = 22000 \cdot \left(\frac{f_{cm}}{10}\right)^{0.3}; \quad (6)$$

$$\text{ACI}: \; E_c = k \cdot \sqrt{f}. \quad (7)$$

In Eq. (7), k = 4700 (ACI), 5000 (IS), 4500 (CSA), the value f is taken to be f_c (ACI, CSA) f_{ck} (IS).

All the above-considered dependencies are proposed for concretes at the design age; the possibility of their application for describing the dependence of the E-modulus on the compressive strength limit at an early age requires confirmation. In any case, the question of the patterns of change in the E-modulus of concrete over time is relevant.

3. Research Methodology

Modeling. There are two options for taking into account the change in the E-modulus of concrete over time. In the first option, the dependence of the E-modulus on time is determined as:

$$E_t = \beta \cdot E_{28}, \tag{8}$$

for example, according to equations similar to [29–31]:

$$E_t = E_{28} \cdot \left(\frac{t}{2.3 + 0.92 \cdot t} \right)^{0.4} = \beta_t \cdot E_{28}, \tag{9}$$

according to EN 1992-1-1:

$$E_{cm}(t) = \left(\frac{f_{cm}(t)}{f_{cm}} \right)^{0.3} \cdot E_{cm} \quad \text{or} \quad E_t = \left(\frac{R_t}{R_{28}} \right)^{0.3} \cdot E_{28}. \tag{10}$$

In the first case, the values of the coefficient β depend only on time, in connection with which, for concretes with different kinetics of compressive strength, it may be necessary to clarify the coefficients in Eq. (9). Eq. (10) is free of this drawback, but its applicability for temperature conditions other than normal may require correction of the numerical values of the coefficients.

In the second variant, the dependence of the E-modulus of concrete is determined at any moment of the given time as a function of the compressive strength limit.

The E-modulus of concrete depends on the E-modulus of the coarse aggregate E_{CA}, the solution component (matrix) and the E-modulus of the contact zone (transition zone) E_{tz}. Obviously E_{CA}, unlike E_m and E_{tz}, does not change over time, while it can change in a wide range of 40 ... 120 GPa. The use of structural models for the analysis of the E-modulus of concrete as a two-component system "matrix – aggregate" has been used for at least more than half a century [22]. In [23], various two-component models are analyzed and their applicability for determining the E-modulus of concrete under compression and tension is shown, and it is shown that at the age of 1 ... 3 days, there is a sharp increase in the E-modulus. In [24], a four-component model "coarse aggregate – contact zone – matrix – structural defects" is analyzed. The influence of porosity parameters on the E-modulus is considered in [25, 31].

In our studies, we used a three-component model of "matrix – contact zone – aggregate." The E-modulus of concrete during modeling was determined depending on the concentration V_m, V_a, V_{tz} and elastic properties E_m, E_{CA}, E_{tz} of the matrix, coarse aggregate and the contact zone between them, the influence of which on the result at a loading level of up to 0.4 is small, according to the equation:

$$E_H = \frac{2}{\dfrac{1}{E_a \cdot V_a + E_m \cdot V_m + E_{tz} \cdot V_{tz}} + \dfrac{V_a}{E_a} + \dfrac{V_m}{E_m} + \dfrac{V_{tz}}{E_{tz}}}. \tag{11}$$

By modeling the change in the E-modulus of the matrix over time, for example, using Eq. (10), it is possible to obtain the dependence of the E-modulus of concrete on time using Eq. (11). Modeling the dependence of the E-modulus on time using Eq. (11) is implemented using the following algorithm:

– according to the equation:

$$R_\tau = R_{28} \cdot \exp\left(s \cdot \left(1 - \sqrt{\frac{28}{\tau_m - \tau_i}} \right) \right), \quad (12)$$

at values of s 0.2, 0.25, 0.38, respectively, for fast (R), normal (M), and slow-hardening concrete (S), the values R_τ at τ_i 0.125 are determined. The values of τ_m, days, at a concrete curing temperature different from normal (increased when cured in massifs) are determined by the concrete degree of maturity M_b [10]:

$$\tau_m = \frac{M_b}{480}; \quad (13)$$

- the values of the coefficient β_{EN} in the equation $E_\tau = \beta_{EN} \cdot E_{28}$ are determined by equation (10);
- the values of the coefficient β_τ are determined by Eq. (9);
- for concrete of class, for example, B30 (C25/30), the value of the ultimate strength of the matrix at the design age is 40 MPa, the E-modulus E_m of the matrix is 28000 MPa, the values of the matrix at the age from 1 to 28 days are determined by Eq. (12);
- the value of the E-modulus E_m of the matrix at the age from 1 to 28 days is determined by Eq. (10);
- according to Eq. (11), the values of the E-modulus of concrete $E_{H,\tau}$ with the specified matrix were determined with the E-modulus of coarse aggregate E_{CA} = 40 (120) GPa and a volume concentration of coarse aggregate of 0.4, a volume concentration of the matrix of 0.6 (the volume concentration of the contact zone, due to the smallness of its effect on the deformation modulus at a loading level of up to 0.4, was taken to be equal to 0) at an age from 1 to 28 days;
- based on the obtained values $E_{H,\tau}$, the values were determined $\beta_H = {E_{H,\tau}}/{E_{H,28}}$.

Experimental studies

Experimental studies of changes in the E-modulus of concrete were performed using three Portland cements of class C42.5, one of which was admixtures-free (CEM I), two with different mineral admixture (CEM II). Concrete mixtures contained superplasticizing admixture PCE (L) or NF (C), or did not contain admixtures. Concrete curing conditions were normal, indoors in the laboratory, in the massif at a peak temperature of 39...42 °C. The compressive strength of concrete was determined at the age of 1, 2, 3, 28 days. For samples hardened in the massif, the reduced age was determined τ_m by the concrete degree of maturity M_b. The E-modulus of concrete was determined through the dynamic E-modulus. More than 65 years ago, it was shown that determining the dynamic E-modulus gives practically equal results regardless of the use of longitudinal or transverse vibrations, and the dimensions of the samples do not affect the result [32, 33]. Determination of the dynamic E-modulus allows obtaining results both at an early age and under various impacts on concrete on the same samples, which increases the reliability of the results [34]. Research in the field of improving the methodology for determining the dynamic E-modulus of concrete on various samples confirms the effectiveness of the method [35]. In this regard, in the work to determine the E-modulus of concrete on samples of 100×100×100 mm aged from 1 to 28 days, a method based on the use of longitudinal vibrations was used.

A total of 65 pairs of values "$E - R$" were obtained with a range of compressive strength of 9.3...69.2 MPa and E-modulus of 21.41...37.75 GPa.

4. Results and Discussion

Fig. 1 shows the dependence of the E-modulus of concrete on the compressive strength limit according to the equations in Tables 1 and 2.

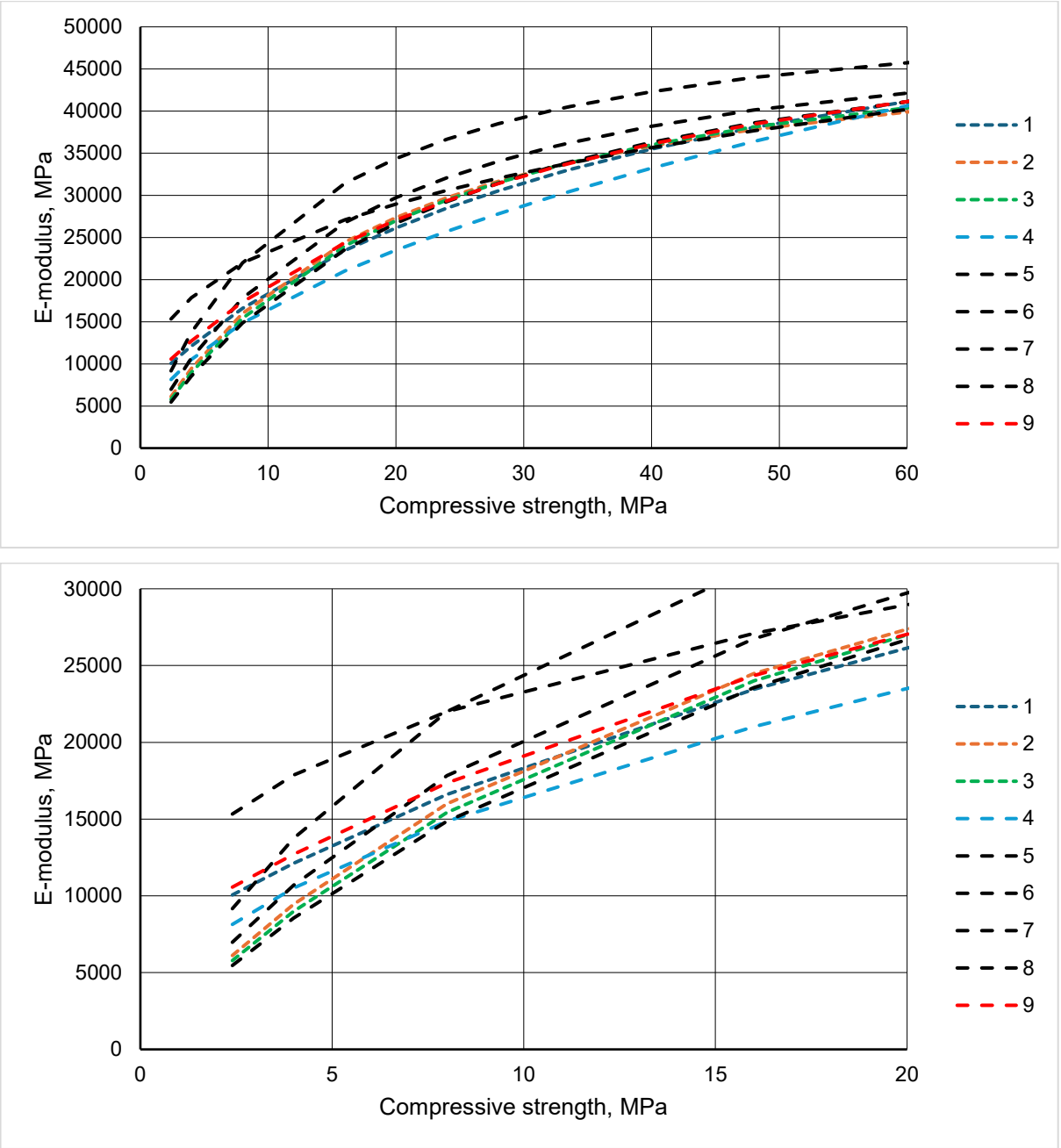

Figure 1. Dependence of the E-modulus of concrete on the compressive strength: 1–3, 5–7, 9 are indicated in Tables 1 and 2; 4 – according to Eq. (7); 8 – according to Eq. (6).

It is obvious that all dependencies in Table 1, except for Curve No. 5, provide relatively close values; at a strength value of more than 15 MPa, the difference does not exceed 5 %. At lower strength values, the difference increases and at a strength of 3 MPa, it reaches 2.5 times along Curves Nos. 2 and 8. Dependence EN 1992-1-1 (Curve No. 8) shows maximum values of the E-modulus at low values of the compressive strength, which can be considered as the early period of concrete hardening. As shown below, this is due to the influence of a constant value of the E-modulus of coarse aggregate over time.

Fig. 2 shows the calculated values of the coefficient β in Eq. (8).

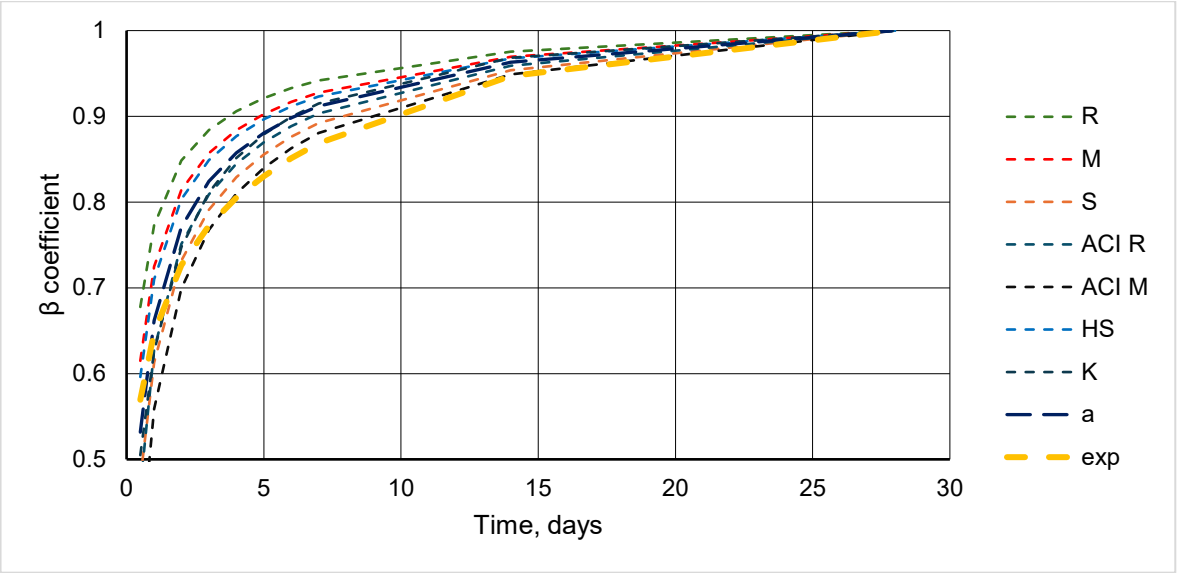

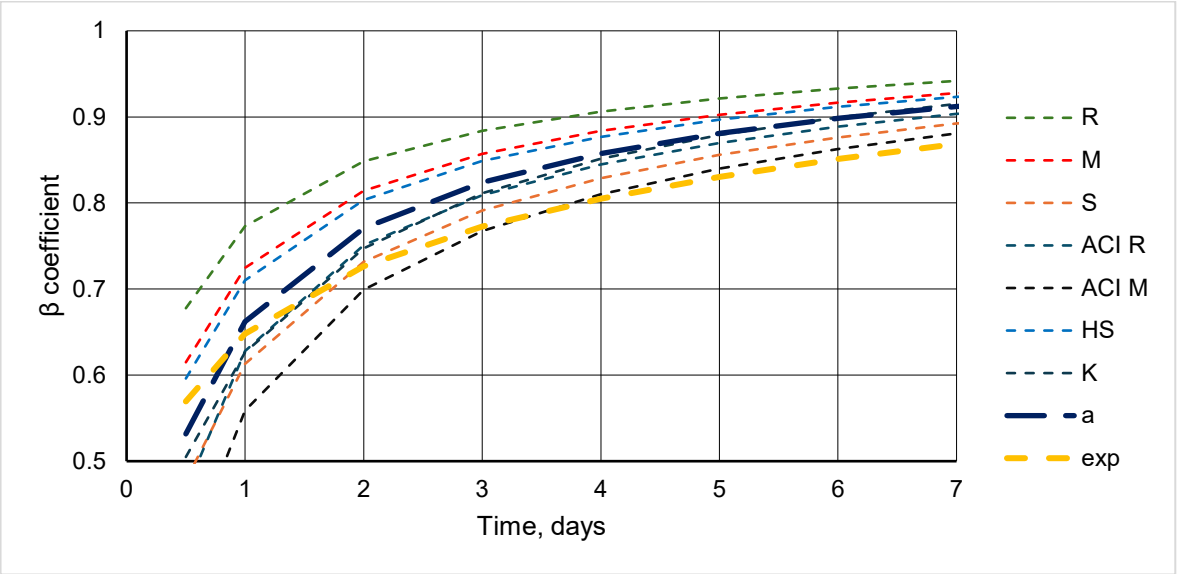

Figure 2. Dependence of the coefficient β on time.

Curves R, M, S – respectively, when determining the strength according to Eq. (12) for rapidly, normally and slowly hardening concrete β according to Eq. (10); Curves ACI R, M – respectively, when determining the strength according to Eq. (12) for rapidly and normally hardening concrete, the E-modulus according to Eq. (6), Curve K – β according to Eq. (9); Curve HS – when determining the modulus of the matrix according to Eq. (10), the E-modulus of concrete according to Eq. (11) with the E-modulus of coarse aggregate of 40 GPa; Curve a – is the average of all calculated values β; Curve exp – are the authors' experimental data.

At the age of one day, the difference in the calculated values β is 38 %, at the age of two days – 21 %, at the age of three days – 15 %. The dependence of the average calculated value of the coefficient β on time is described by the equation:

$$\beta = \exp\left(0.095 \cdot \left(1 - \sqrt{\frac{28}{\tau}}\right)\right). \quad (14)$$

The coefficients closest to the average value β are those according to Eq. (9) [29], as well as for quickly hardening concrete according to the ACI equation – Eq. (7).

The experimental values of the coefficient according to the authors' data β, obtained during tests of concrete with a fairly low E-modulus of coarse aggregate (siliceous sandstone with a E-modulus of 41.8...43.6 GPa) in principle fit into the overall picture.

Fig. 3 shows the dependence of the E-modulus on the compressive strength limit according to the authors' experimental data and some calculated dependencies. The calculated strength at the daily age of the studied concretes ranged from 5.1 MPa for slowly hardening concrete with a design strength from 27.1 to 29.3 MPa for quickly hardening concrete with a design strength of 69.2 MPa. The actual strength at the daily age ranged from 9.3 MPa with a design strength from 27.1 to 16.4 MPa with a design strength of 34.5 MPa (some samples were tested at the age of 2 days instead of 1 day). The E-modulus at the daily age ranged from 21140 to 24220 MPa, at the design age from 30515 to 37750 MPa.

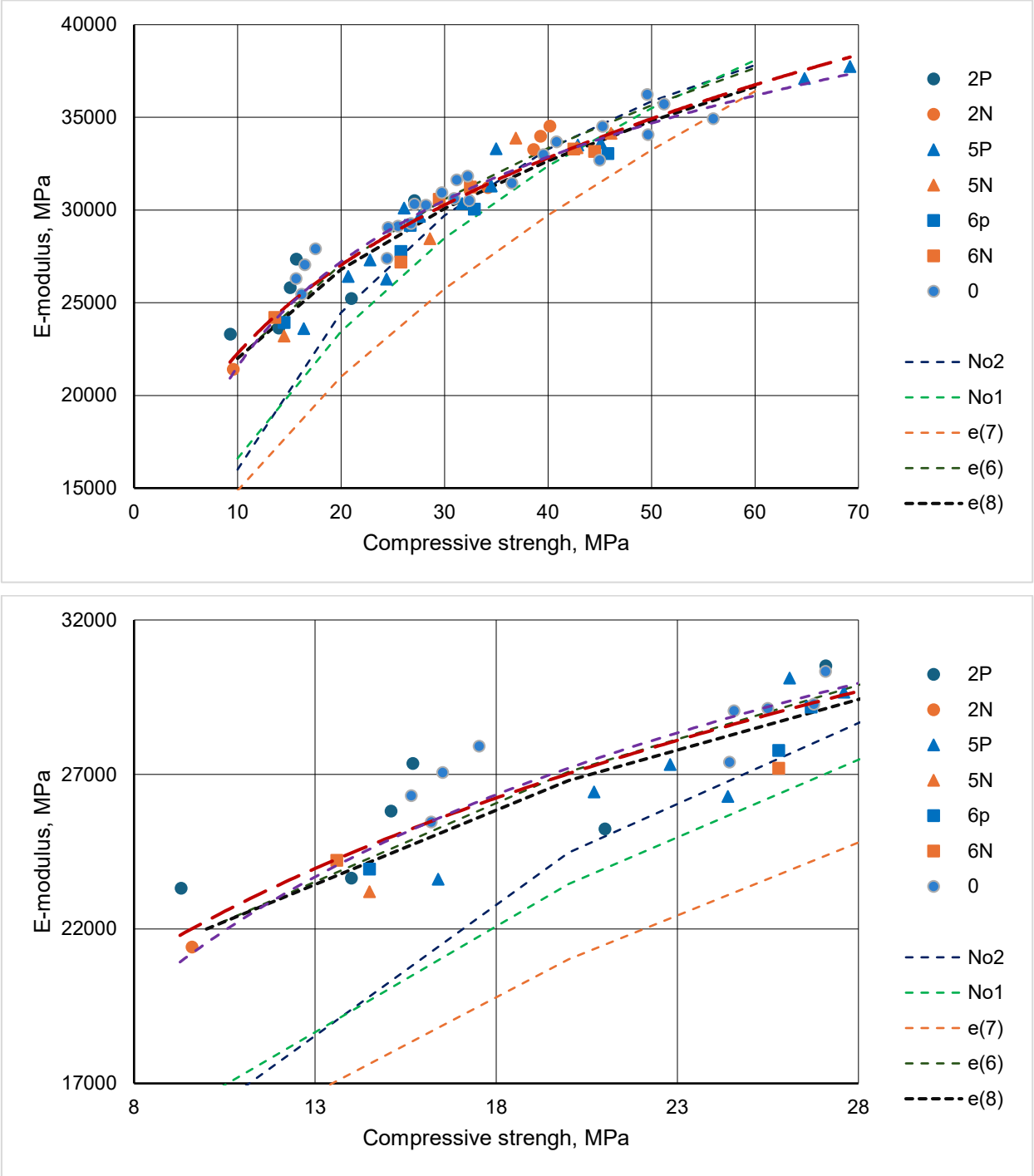

Figure 3. Dependence of the E-modulus on the compressive strength: 2, 5, 6 – cements; P – PCE superplasticizer; N – NF superplasticizer; 0 – without admixtures; Curves 1, 2 – curves in Fig. 1; e(6), e(7), e(8) – according to Eqs. (6), (7), (8).

It is obvious that Eq. (7) and Curves Nos. 1, 2 in Fig. 1, obtained for concrete of the design age, are not suitable for describing the dependence of the E-modulus of hardening concrete at an early age.

The dependence of the E-modulus of the concretes studied by the authors on the compressive strength limit is described by the equation:

$$E = 11685 \cdot R^{0.28}, \quad (15)$$

with an approximation reliability index of R^2 = 0,923, which indicates good convergence and the possibility of using the equation for practical purposes.

Eq. (15), reduced to the form EN 1992-1-1, has the form:

$$E_t = 22265 \cdot \left(\frac{R_t}{10} \right)^{0.28}, \quad (16)$$

the difference in values when calculating according to Eqs. (6) and (16) is less than 1 % in the range of compressive strength limits of 10…70 MPa.

Theoretical prerequisites for constructing a calculation method

The first option is the dependence of the E-modulus on the time of hardening of concrete at an early age is determined by Eq. (14) with the duration of the induction period in most cases being 0.15–0.25 days.

The second option is the dependence of the E-modulus on the time of hardening of concrete at an early age is determined by Eq. (16), while the strength value R_τ is determined at the given age τ_m depending on the degree of maturity of the concrete M_b.

5. Conclusions

1. Some dependencies have been analyzed $E_\tau = f\left(E_{28}\right)$, it has been shown that the closest to the average value for all analyzed dependencies is provided by Eq. (9).
2. The dependence of the change in time of the E-modulus has been obtained taking into account the degree of maturity of hardening concrete with superplasticizing admixtures.
3. When calculating the time-varying values of the E-modulus of concrete based on the value of the compressive strength limit $E_\tau = f\left(R_\tau\right)$ it is advisable to use the dependence EN 1992-1-1.

References

1. Kaprielov, S.S., Sheinfeld, A.V., Kiseleva, Yu.A., Prigozhenko, O.V., Kardumyan, G.S., Urgapov, V.I Erection of Unique Structures Made of Modified Concrete and Used for Construction of the Complex "Federation" MMDTS "Moscow-City". Industrial and Civil Engineering. 2006. 8. Pp. 20–22.
2. Kuriakose, B., Rao, B.N., Dodagoudar, G.R. Early-age Temperature Distribution in a Massive Concrete Foundation. Procedia Technology. 2016. 25. Pp. 107–114. DOI: 10.1016/j.protcy.2016.08.087
3. Makeeva, A.V., Semenov, K.V., Makeev, A.A., Amelina, A.V. Crack resistance of massive concrete structures during the building period taking into account temperature effects. Bulletin of BSTU named after V.G. Shukhov. 2019. 8. Pp. 30–39. DOI: 10.34031/article_5d49408e0e0b61.97206550
4. Nesvetaev, G.V., Chepurnenko, A.S., Koryanova, Y.I., Sukhin, D.P. Evaluation of some methods for calculating thermal stresses during concreting of massive reinforced concrete foundation slabs. Engineering Journal of Don. 2022. 7(91). URL: http://www.ivdon.ru/en/magazine/archive/n7y2022/7817 (date of application: 22.01.26).
5. Fairbairn, E.M.R., Silvoso, M.M., Toledo Filho, R.D., Alves, J.L.D., Ebecken, N.F.F. Optimization of mass concrete construction using genetic algorithms. Computers & Structures. 2004. 82(2–3). Pp. 281–299. DOI: 10.1016/j.compstruc.2003.08.008
6. Agakhanov, E.K., Kurachev, R.M., Chepurnenko, A.S., Kulinich, I.I. Non-linear heat conduction problem for radiation-heat shield of nuclear reactor]. Engineering Journal of Don. 2015. 4. URL: ivdon.ru/ru/magazine/archive/n4y2015/3421 (date of application: 22.10012026).
7. Aniskina, N.A., Nguyen Trong Chuc, Bryansky, I.A., Dam Huu Hung. Determination of the Temperature Field and Thermal Stress State of the Massive of Stacked Concrete by Finite Element Method. Vestnik MGSU. 2018. 13(11). Pp. 1407–1418. DOI: 10.22227/1997-0935.2018.11.1407-1418
8. Semenov, K., Kukolev, M., Zaichenko, N., Popkov, S., Makeeva, A., Amelina, A., Amelin, P. Unsteady Temperature Fields in the Calculation of Crack Resistance of Massive Foundation Slab During the Building Period. Proceedings of EECE 2019. Springer. Cham, 2020. Pp. 455–467. DOI: 10.1007/978-3-030-42351-3_40
9. Bofang, Z. Thermal Stresses and Temperature Control of Mass Concrete. Elsevier/Butterworth-Heinemann. Amsterdam, Boston, 2014. 500 p.

10. Nesvetaev, G.V., Koryanova, Y.I., Chepurnenko, A.S., Sukhin, D.P. On the issue of modeling temperature stresses during concreting of massive reinforced concrete slabs. Engineering Journal of Don. 2022. 6. URL: ivdon.ru/ru/magazine/archive/n6y2022/7691 (date of application: 23.01.26).
11. Bolgov, A.N., Nevskii, A.V., Ivanov, S.I., Sokurov, A.Z. Numerical Modeling of Thermal Stresses in Concrete of Massive Structures during the Hardening Period. Industrial and Civil Engineering. 2022. 4. Pp. 6–13. DOI: 10.33622/0869-7019.2022.04.06-13
12. Klausen, A.E., Kanstad, T., Bjøntegaard, Ø., Sellevold, E.J. The effect of realistic curing temperature on the strength and E-modulus of concrete. Materials and Structures. 2018. 51. Article no. 168. DOI: 10.1617/s11527-018-1299-4
13. Liu, R., Mao, X., Li, B., Li, Y., Zhang, L. Experimental study on dynamic mechanical properties of concrete under sulfate attack. Frontiers in Materials. 2025. 12. Article no. 1560181. DOI: 10.3389/fmats.2025.1560181
14. Wang, Y.-S., Mo, L.-H., Xie, S.-X., Wang, C.-Y., Yu, X.-B. Early-age cracking in mass concrete: Modeling and case study of an extra-large exhibition pool. Journal of Building Engineering. 2023. 80. Article no. 108118. DOI: 10.1016/j.jobe.2023.108118
15. Abelev, M.Yu., Krasnovskiy, B.M. Technologies of Installation of Slab Foundations of 17-Storey Panel Buildings. Industrial and Civil Engineering. 2021. 4. Pp. 40–46. DOI: 10.33622/0869-7019.2021.04.40-46
16. Turina, V.S., Chepurnenko, A.S., Akopyan, V.F. Methodology for determining true temperature stresses during the construction of massive monolithic reinforced concrete structures. Construction Materials and Products. 2024. 7(3). Article no. 5. DOI: 10.58224/2618-7183-2024-7-3-5
17. Lin, Y., Chen, H.L. Thermal analysis and adiabatic calorimetry for early-age concrete members: Part 2. Evaluation of thermally induced stresses. Journal of Thermal Analysis and Calorimetry. 2016. 124. Pp. 227–239. DOI: 10.1007/s10973-015-5131-x
18. Mardmomen, S., Chen, H.L. Prediction of the early age thermal behavior of mass concrete containing SCMs using ANSYS. Journal of Thermal Analysis and Calorimetry. 2023. 148(15). Pp. 7899–7917. DOI: 10.1007/s10973-023-12243-9
19. Nikolenko, S.D., Sazonova, S.A., Zvyagintseva, A.V. Calculation of Crack Formation During the Thermal Stress State of Concrete Masses and Development of Measures to Improve the Operational Properties of Concrete. IOP Conference Series: Materials Science and Engineering. 2021. 1079(3). Article no. 032028. DOI: 10.1088/1757-899X/1079/3/032028
20. Qin, X., Xu, Z., Liu, M., Zhang, Y., Wang, Y., Yang, Z., Ling, X. Mechanical Properties and Elastic Modulus Prediction of Mixed Coal Gangue Concrete. Materials. 2025. 18(6). Article no. 1240. DOI: 10.3390/ma18061240
21. Kumar Mehta, P., Monteiro, P.J.M. Concrete: Microstructure, Properties and Materials. McGraw-Hill. USA, 2001. 239 p.
22. Popovics, S. Structural Model Approach to Two-Phase Composite Materials: State of the Art. American Ceramic Society Bulletin. 1969. 48(11). Pp. 1060–1064.
23. Yoshitake, I., Rajabipour, F., Mimura, Y., Scanlon, A. A Prediction Method of Tensile Young's Modulus of Concrete at Early Age. Advances in Civil Engineering. 2012. Article no. 391214. DOI: 10.1155/2012/391214
24. Li, X., Du, C., Li, C., Xu, Y., Gong, W. Effects of Initial Defects on Effective Elastic Modulus of Concrete with Mesostructure. Journal of Wuhan University of Technology – Materials Science. 2024. 39(6). Pp. 1484–1495. DOI: 10.1007/s11595-024-3018-z
25. Chen, H., Xu, F. Quantitative Characterization Model of Macroscopic Mechanical Properties of Recycled Concrete Based on Porosity and Pore Sizes. Advances in Materials Science Engineering. 2024. Article no. 5261052. DOI: 10.1155/2024/5261052
26. Roš, M. Versuche und Erfahrungen an ausgeführten Eisenbetonbauwerken in der Schweitz 1924–1937: Bericht Nr. 99. Eidgenössiche Materialprüfungs u. Versuchsanstalt Zürich. Zürich, 1937. 405 S.
27. Mordovskiy, S.S. Initial Modulus of Elasticity of Concrete and Ways to Determine IT. Traditsii i innovatsii v stroitelstve i arkhitekture. stroitelstvo i stroitelnyye tekhnologii [Traditions and innovations in construction and architecture. Construction and construction technologies]. Samara: Samara State Technical University, 2022. Pp. 37–45.
28. Karpenko, N.I. Obshchiye modeli mekhaniki zhelezobetona [General models of reinforced concrete mechanics]. Moscow: Strojizdat, 1996. 412 p.
29. Karpenko, N.I., Travush, V.I., Kaprielov, S.S., Mishina, A.V., Andrianov, A.A., Bezgodov, I.M. The Research of Physical, Mechanical and Rheological Properties of High Strength Steel Fiber Reinforced Concrete. Academia. Architecture and Construction. 2013. 1. Pp. 106–113.
30. Singh, B.P., Yazdani, N., Ramirez, G. Effect of a Time Dependent Concrete Modulus of Elasticityon Prestress Losses in Bridge Girders. International Journal of Concrete Structures and Materials. 2013. 7(3). Pp.183–191. DOI: 10.1007/s40069-013-0037-0
31. Xu, F., Pan, H. Research on Quantitative Characterization Model of Compressive Strength or Elastic Modulus of Recycled Concrete Based on Pore Grading. Materials. 2025. 18(3). Article no. 3. DOI: 10.3390/ma18010003
32. Batchelder, G.M., Lewis, D.W. Comparison of Dynamic Methods of Testing Concretes Subjected to Freezing and Thawing. Proceedings, ASTM. 1953. 53. Pp. 1053–1068.
33. Woods, K.B., McLaughlin, J.F. Application of Pulse Velocity Tests to Several Laboratory Studies of Materials. Highway Research Board Bulletin. 1959. 206. Pp. 14–27.
34. Chen, D., Zou, J., Zhao, L., Xu, S., Xiang, T., Liu, C. Degradation of Dynamic Elastic Modulus of Concrete under Periodic Temperature-Humidity Action. Materials. 2020. 13(3). Article no. 611. DOI: 10.3390/ma13030611
35. Kim, M.S., Son, J.J., Chung, C.W., Lee, C.J. Factors Influencing Measurement of Dynamic Elastic Modulus from Disk-Shaped Concrete. Specimen International Journal of Concrete Structures and Materials. 2024. 18. Article no. 68. DOI: 10.1186/s40069-024-00710-y

Information about the authors:

***Grigory Nesvetaev**, Doctor of Technical Sciences*
ORCID: https://orcid.org/0000-0003-4153-1046
E-mail: nesgrin@yandex.ru

Anton Chepurnenko, *Doctor of Technical Sciences*
ORCID: https://orcid.org/0000-0002-9133-8546
E-mail: anton_chepurnenk@mail.ru

Batyr Yazyev, *Doctor of Technical Sciences*
ORCID: https://orcid.org/0000-0002-5205-1446
E-mail: ps62@yandex.ru

Yulia Koryanova, *PhD in Technical Sciences*
ORCID: https://orcid.org/0000-0002-2341-9811
E-mail: koryanova.yi@mail.ru

Received 03.06.2025. Approved after reviewing 28.11.2025. Accepted 28.11.2025.

Magazine of Civil Engineering

ISSN 2712-8172

journal homepage: http://engstroy.spbstu.ru/

Research article

UDC 624.044.2

DOI: 10.34910/MCE.140.2

High-strength concrete behavior in post-limit conditions

P.D. Arleninov[1,2] ✉

[1] *JSC Research Center of Construction, Research Institute of Concrete and Reinforced Concrete (NIIZHB) named A.A. Gvozdev, Moscow, Russian Federation*

[2] *National Research Moscow State University of Civil Engineering, Moscow, Russian Federation*

✉ *arleninoff@gmail.com*

Keywords: elastic modulus, limit state, descending branch, high-strength concrete, microcracks

Abstract. The objects of study were specimens of various shapes and aspect ratios made of high-strength modified concrete B90–B100 with a modified elastic modulus of 55,000 MPa. This modulus significantly exceeds the normative values specified in the building code SP 63.13330 when the concrete is loaded beyond its ultimate state. The need for this study stems from insufficient research on the deformation characteristics of high-strength concretes in extreme states (after reaching the ultimate load – with or without subsequent unloading), as well as the inapplicability of classical microcracking theories (Berg, Winter) to describe their behavior, which requires the development of new evaluation methods. Since high-strength concretes fail brittly, the research methods included two approaches to loading specimens – loading by stresses (standard method) and additionally by deformations up to the peak failure load with subsequent unloading and holding (from 1 hour to 8 days); the elastic modulus was determined according to GOST 24452 before and after loading, while microcrack development was monitored using ultrasonic testing methods (through-transmission and surface sounding). Based on the research results, it was established that during short-term holding (1 hour), the elastic modulus increased by 40–71 % (reaching 73,602–101,192 MPa) – this is explained by crack closure during specimen compression and the inertia of the stress relaxation process, while strength decreased by 20 %. After holding ≥1 day, the elastic modulus (49,684–57,683 MPa) and strength approached the initial values (±6 %), despite visible damage to specimens after initial peak load attainment. At the same time, the ultrasonic wave travel time and Poisson's ratio (0.21–0.26) remained practically unchanged up to 90 % of the failure load, which does not correspond to classical microcracking development models. The main conclusions of the work: high-strength concretes retain nearly linear deformation behavior even after reaching the ultimate state. These results cast doubt on existing theoretical models describing crack formation processes and emphasize the importance of accounting for stress relaxation in structural assessments, as well as the necessity for comprehensive research on high-strength concretes.

Citation: Arleninov, P.D. High-strength concrete behavior in post-limit conditions. Magazine of Civil Engineering. 2025. 18(8). Article no. 14002. DOI: 10.34910/MCE.140.2

1. Introduction

This study investigated the behavior of modern high-strength heavy concrete under extreme conditions. The objects of research were prism specimens in accordance with GOST 24452-2023 currently in force in the territory of the Russian Federation with an aspect ratio of 1:4, and cylinder specimens with an aspect ratio of 1:2.

High-strength concretes are currently widely used in both civil and industrial construction, including in reinforced concrete [1, 3] and steel-reinforced concrete structures [4–5]. While the strength characteristics of high-strength concretes themselves and the influence of various factors on them have been studied to some extent, albeit insufficiently well, their deformation characteristics are significantly less

studied, as noted by many authors [6–8]; as for research on the extreme states of high-strength concrete behavior, such studies either do not exist at all or are isolated [9].

In which building structure operation scenarios is it necessary to know how concrete behaves in an extreme state? Several definitions of the extreme state of concrete behavior have been proposed by various authors [10–12]. First, let us define what we call an extreme state for this study. We will consider as extreme a state where a specimen is uniformly loaded to the maximum load it can withstand under a given loading method (the maximum load may differ under different loading methods), but is not brought to failure – unloading is performed, after which we study how such high stress levels in the specimen affected its main strength and deformation characteristics.

The relevance of the work lies in the fact that in certain scenarios, it is necessary to know the elastic modulus characteristics of non-uniform concrete already having internal structural defects – microcracks; and these are not necessarily structures operating at stress levels close to ultimate. In certain cases, microcracks can appear in a structural element during the concrete hardening stage – these can be shrinkage processes in reinforced concrete and especially steel-reinforced concrete structures, as well as thermal deformations during the hardening of concrete in massive structures accompanied by significant heat release and consequently the presence of a temperature gradient across the element's cross-section.

The use of a theoretical framework based on the fundamental research of Berg et al. [13], both in its original form (c 1) and based on modified theories [14–16], does not yield reliable results – Formulas (2), (3) respectively. Study [17] only processes previously obtained experimental data [18–20] without proposing its own expression for predicting microcracking processes.

release and consequently the presence of a temperature gradient across the element's cross-section.

The use of a theoretical framework based on the fundamental research of Berg et al. [13], both in its original form (c 1) and based on modified theories [14–16], does not yield reliable results – Formulas (2), (3) respectively. Study [17] only processes previously obtained experimental data [18–20] without proposing its own expression for predicting microcracking processes.

$$\frac{R^0_{crc}}{R_b} = 0.35 \cdot \lg R_b - 0.5, \quad \frac{R^v_{crc}}{R_b} = 0.35 \cdot \lg R_b - 0.175; \tag{1}$$

$$\frac{R^0_{crc}}{R_b} = 0.33 \cdot K_{crc} \ln R_b - 0.15, \quad \frac{R^v_{crc}}{R_b} = 0.35 \cdot \lg R_b + 0.1; \tag{2}$$

$$R^0_{crc} = \left(1 - e^{-0.052 \cdot R_b^{0.642}}\right) \cdot R_b, \quad R^v_{crc} = 4.652 \cdot R_b^{0.642} \cdot R^0_{crc}, \tag{3}$$

where R^0_{T}, R^v_{T} are the parametric points of the conditional lower and upper levels of cracking relative to the prismatic strength R_b; K_{crc} – empirical coefficient equal to 1 for heavy concrete.

In this regard, the A.A. Gvozdev Research Institute of Concrete and Reinforced Concrete (NIIZhB) set the goal of conducting extensive experimental-theoretical studies aimed at developing a standardized methodology for experimentally determining crack formation limits in high-strength concretes, as well as options for physical modeling of microcracks with assessment of their influence on the strength and deformation characteristics of concrete specimens. In other words, sometimes it is necessary to understand how a structure or structural element will behave after being subjected to loads exceeding design resistance for some time and having potentially sustained damage in the form of microstructural failures.

As for normal-strength concretes, according to the classical theory of Berg (which, incidentally, does not contradict research by American specialists from Cornell University under the guidance of Professor Winter [18–20] conducted in the 1960–1970s – most subsequent theoretical studies are based on these experiments), microcracks in concrete begin to develop approximately after reaching 0.4–0.5 of the failure load (which to some extent corresponds to the level of design concrete resistance), and closer to stress levels of 0.7–0.8 of the failure load, the intensity of microdamages increases significantly. The different levels of microcrack formation according to Berg and Winter can be graphically represented in Figs. 1 and 2.

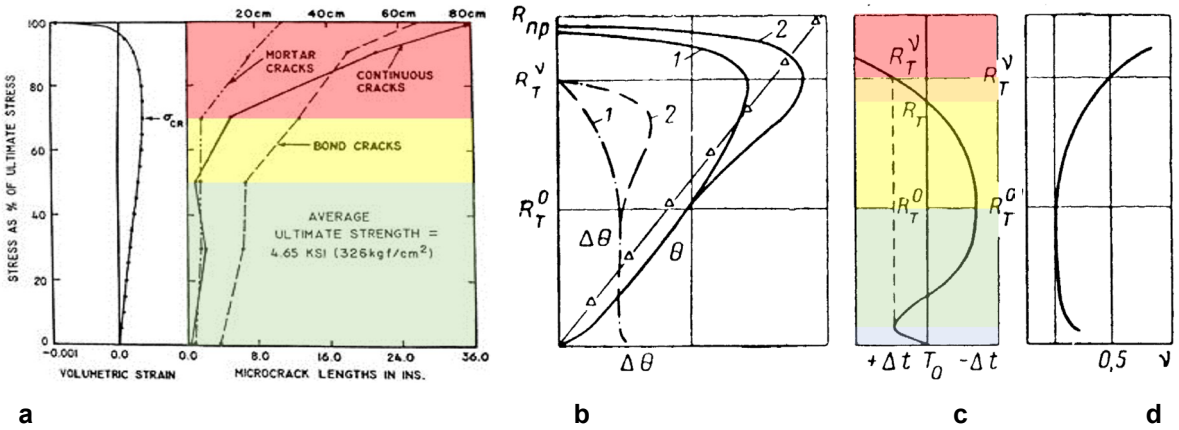

Figure 1. a) The dependence of the total length of microcracks on the stress level (Winter); b, c, d) the dependence of volumetric deformations, ultrasound transmission time, and Poisson's ratio on the stress level, respectively (Berg): grey – decompression of the least stable structures; green – compaction of the material; yellow – development of micro–fractures; orange – Intensive development of micro-fractures; red – a sharp increase in the length of microcracks.

The research presented in this article is a part of the extensive work described above. The impact of micro-fractures of the concrete structure on the modulus of elasticity at stress levels close to the destructive load was evaluated.

2. Materials and Methods

2.1. Materials Employed

Experimental studies were conducted on high-strength self-sealing heavy concrete B90-B100 on standard materials used in the Russian Federation (Portland cement, sand, crushed stone, active mineral additives, complex additives). The initial modulus of elasticity of concrete was 55,000 MPa. This particular composition with a modified modulus of elasticity was chosen relative to the one given in SP 63.13330 (43,000 MPa), since concretes of classes higher than B80 are usually used in high-rise construction and there an increase in the modulus of elasticity is almost always critical and the use of concretes of such classes with a conventional modulus of elasticity is not entirely rational [21, 22]. Sika additives were used directly in this composition, but concrete with the same characteristics can also be obtained with analog additives.

2.2. Test Methodology

From the prepared mixtures, specimens were molded: cubes with dimensions 100×100×100 mm, 150×150×150 mm for determining cube compressive strength according to GOST 10180 and GOST 31914; prisms 100×100×400 mm, prisms 150×150×600 mm, and cylinders Ø150×600 mm. Fig. 2 shows the types of tested specimens (the research discussed in this article was conducted only on the specified specimens, but in a larger comprehensive study, specimens with greater variability of geometric dimensions were tested – in addition to the above-mentioned prisms and cylinders, studies were performed on cylinders of all diameters 70, 100, and 150 mm, as well as on specimens with various cross-section to height ratios from 1:2 to 1:4). The measurement base included tensometry, dial indicators, portable deformometer, ultrasonic devices of surface and through action. Mechanical and digital dial indicators were used when determining the modulus of elasticity in accordance with GOST 24452, at 70 % of the destructive load they were removed and measurements were performed using tensometry and removable deformometers based on the Demec principle.

Figure 2. Description of the test mode for determining the modulus of elasticity after operation in an extreme state in the axes stress level – test time.

Testing was conducted on 5 reference specimens (of each standard size), on which the modulus of elasticity and destructive load (R1) were determined in accordance with GOST 24452, 5 specimens that were loaded with deformations and used to obtain the descending branch and determine the peak load value sustained by the specimen (R2) – typically this load is somewhat less than that obtained in standard testing according to GOST 24452, and 4 specimens of various standard sizes, which were first loaded with deformations up to the peak value of destructive load, then unloaded, held for a certain time, and subsequently tested for modulus of elasticity and then to failure (R3). The obtained results were compared with the values of modulus of elasticity obtained on these same specimens at the beginning of the experiment. The general testing scheme is shown in Fig. 3.

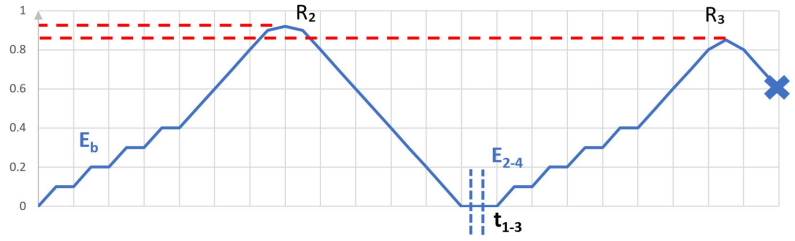

Figure 3. Description of the test mode for determining the modulus of elasticity after operation in an extreme state in the axes stress level – test time.

Loading by deformations was performed because high-strength concretes behave elastically almost up to failure, which occurs instantaneously and is accompanied by a sharp crack – essentially an explosion. Determining the peak load without specimen failure and consequently obtaining the descending branch in the $\sigma - \varepsilon$ graph is a rather complex task, and solving it by trivial methods is far from always possible [23, 24].

The determination of the microcrack initiation level in concrete was carried out according to the classical method of Professor Berg (Fig. 1b, c, d). For this purpose, at each loading stage, the specimens in the press were subjected to ultrasonic testing using ultrasonic testing devices. Both surface and through sounding were performed (see Fig. 4a) using UK-1401 and Pulsar 1.0 devices, respectively. During through sounding, a wet contact was used, so to ensure experimental purity, the device was rigidly fixed to the specimen, not removed, and measurements were taken in one section at the center of the specimen.

For surface sounding, 12 control points were marked on the lateral surface for conducting 6 measurements (using the UK-1401 device) – 3 vertically and 3 diagonally at angles from 45 to 70° to the horizontal. Fig. 4b shows a specimen brought to peak destructive load (immediately unloaded after reaching it) for subsequent elastic modulus testing. As can be seen from the figure, the specimen retained its shape but sustained several damages (chips and cracks) visible to the naked eye. On different specimens, these damages varied in appearance but were mostly concentrated at the edges, although some specimens exhibited vertically oriented cracks extending almost the full height of the specimen.

Fig. 3 indicates various holding intervals for the specimens to allow stress relaxation to occur. According to the results presented in the following section, the significant influence of stress relaxation is evident. The destructive load R3 also differs from loads R1 and R2, as shown below.

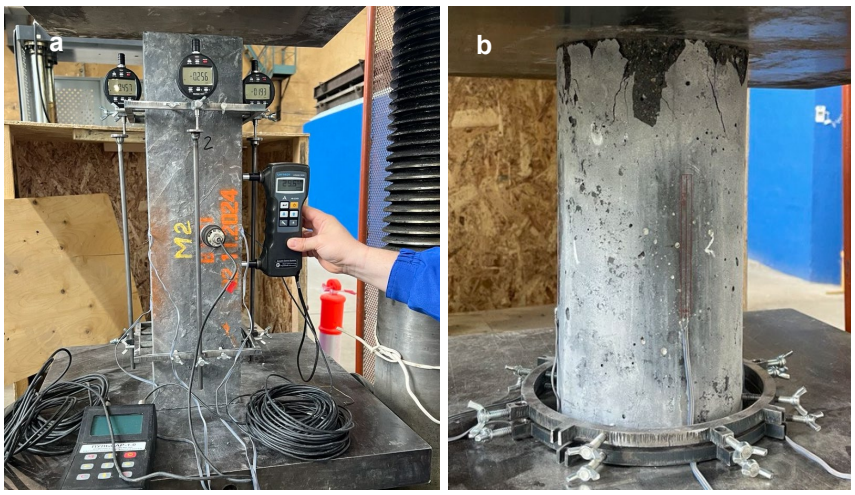

Figure 4. a) A cylinder sample brought to a destructive load during testing, but not destroyed; b) Ultrasonic sounding systems for the sample.

3. Results and Discussion

During the testing, ultrasonic monitoring could be conducted right up to specimen failure (up to 0.98–0.99 of the destructive load). However, through-transmission testing using the specified equipment yielded no results – the ultrasonic wave transit time remained virtually unchanged until specimen failure, possibly due to the orientation of microcracks in the specimen.

The pattern of changes in the ultrasonic transit time graph during measurements from one side up to stress levels of 0.6 of the destructive load closely resembles classical research (referring only to the qualitative behavior of the curve). Beyond the 0.6 stress level, the curve does not change direction, and up to loads approaching 0.9 of the destructive load, the ultrasonic wave transit time remains unchanged (see Fig. 5b).

Even at stress levels from 0.9 up to failure, there was no sharp decrease in ultrasonic transit time that would indicate a rapid increase in micro-failure volume. All this suggests qualitatively different behavior of high-strength concrete under loads entering the nonlinear region.

In Fig. 5a, using one of the specimens as an example, the development of volumetric deformations under load is shown – here the differences from classical theories are even more pronounced, as the curve never reached a plateau. The Poisson's ratio was recorded to vary from 0.21 to 0.26 (the graph of Poisson's ratio variation versus stress level is shown in Fig. 5c).

As previously mentioned, attempts to use formulas from both Berg's classical theory [13] and modified versions [14–15] for predicting microcrack development processes in concrete failed to yield positive results. Below are the results of determining microcrack formation boundaries using Formulas (1) and (2); other tested expressions showed even greater discrepancies with experimental results.

According to Formula (1): $\frac{R_{crc}^{0}}{R_b} = 0.537;\ \frac{R_{crc}^{v}}{R_b} = 0.862.$

According to Formula (2): $\frac{R_{crc}^{0}}{R_b} = 0.857;\ \frac{R_{crc}^{v}}{R_b} = 1.107.$

Berg's formula, as can be seen, gives too low values for the parametric points R_{crc}^{0} and R_{crc}^{v}, although the proposed theory's description indicates its applicability to high-strength concretes with strength classes up to 100 MPa. Formula (2) shows a lower microcrack formation boundary much closer to the experimental results, but when determining the upper boundary, a mathematical error occurs (value greater than 1).

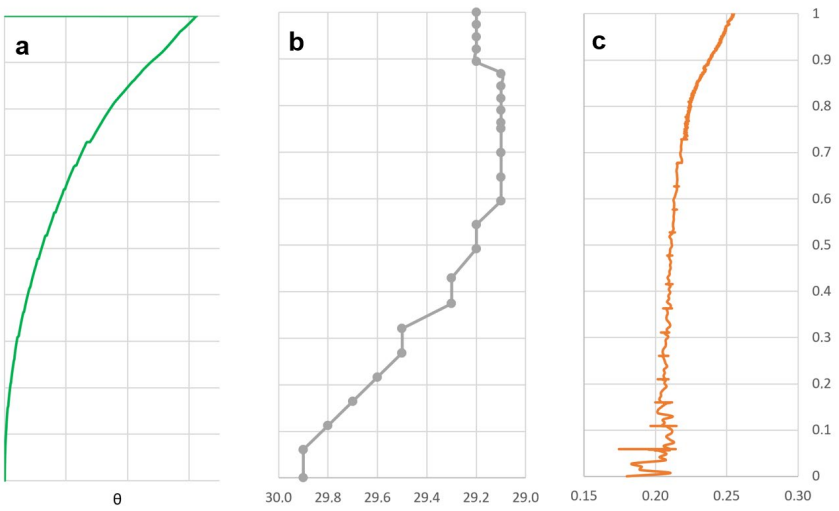

Figure 5. a) The dependence of volumetric deformations on the stress level; b) the dependence of the transit time on the stress level; c) the dependence of the Poisson's ratio on the stress level.

According to the test results, the following values of the modulus of elasticity were recorded after the concrete reached its ultimate load and various holding periods after unloading before reloading, compared with the initial modulus of elasticity determined directly on the same specimen.

E_b = 53,000 MPa – average initial modulus of elasticity for the group of specimens.

E_{b1} = 59,141 MPa, E_1 = 1.71 Eb (101,192 MPa) – modulus of elasticity determined almost immediately after reaching the failure load followed by unloading (stress relaxation holding period was about 1 hour). Specimen: cylinder Ø150×300 mm.

E_{b2} = 52,335 MPa, E_2 = 1.41 Eb (73,602 MPa) – modulus of elasticity determined almost immediately after reaching the failure load followed by unloading (stress relaxation holding period was about 1 hour). Specimen: cylinder Ø150×300 mm.

E_{b3} = 54,314 MPa, E_3 = 1.06 Eb (57,683 MPa) – modulus of elasticity determined on an unloaded specimen after a free-state holding period of 8 days. Specimen: cylinder Ø150×300 mm.

E_{b4} = 57,778 MPa, E_4 = 1.00 Eb (57,967 MPa) – modulus of elasticity determined on an unloaded specimen after a free-state holding period of 3 days. Specimen: prism 150×150×600 mm.

E_{b5} = 52,042 MPa, E_5 = 1.00 Eb (51,994 MPa) – modulus of elasticity determined on an unloaded specimen after a free-state holding period of 1 day. Specimen: prism 150×150×600 mm.

Analysis of these results shows that with short holding periods after reaching the failure load, despite accumulated damage, the concrete's modulus of elasticity significantly increased by 1.4 to 1.7 times. This may be related to the deformation mechanics of high-strength concrete under extreme loads – nearly linear deformation until failure, minimal accumulation of internal defects (microcracks) and their closure at even higher stress levels, and certain inertia in the relaxation process of internal stresses after removing compressive load. These results are new and previously unpublished.

With holding periods of one day or more, significant relaxation of internal stresses occurs in the specimen, and the obtained modulus of elasticity values become close to the initial modulus (±6 %). Such results are also extremely unusual since the already failed specimen retained its basic initial deformation characteristics.

A crucial aspect in this case is the duration of the holding period sufficient for the residual post-unloading stresses to relax. Its exact value depends on many factors, primarily the concrete mix composition; thus, it may differ for each concrete type. In this experiment, several scenarios of post-loading holding periods were considered, and one day can be taken as an averaged, sufficient period for the relaxation of all internal stresses.

If we compare the already destructive loads, in particular R1, R2, R3, the generally expected results were recorded in qualitative perception, but the quantitative figures are somewhat unusual:

R1 = 88.2–99.5 MPa is the average destructive load during testing according to GOST 24452, depending on the type of sample;

R21 = 92.3 MPa, R31 = 72.7 MPa – cylinder Ø150×300 mm; exposure time is 1 hour;

R22 = 92.5 MPa, R32 = 80.6 MPa – cylinder Ø150×300 mm; exposure time is 1 hour;

R23 = 96.4 MPa, R33 = 94.7 MPa – cylinder Ø150×300 mm; exposure for 8 days;

R24 = 85.3 MPa, R34 = 83.3 MPa – prism 150×150×600 mm; exposure for 1 day;

R25 = 89.0 MPa, R35 = 87.0 MPa – prism 150×150×600 mm; exposure for 3 days.

Analyzing these results, it can be seen that all tested samples show a decrease in load R2 relative to load R1 by 6 %, and load R3 relative to load R2 by 20 % for short exposures of an hour, and only 2 % for exposures of more than a day. To summarize, with short exposures, there was a significant increase in the modulus of elasticity but at the same time a significant decrease in the strength of concrete. At exposures of more than a day, all data stabilized, approaching the initial results. These results are of great interest and confirm one of the most important roles of the stress relaxation process in concrete. Research needs to be continued on different types under different test scenarios.

4. Conclusions

A series of experimental studies were conducted to determine the main deformation characteristics of high-strength concretes after their operation in the post-peak state, where creating such conditions for concrete itself represents a separate complex engineering task that was incidentally solved during this work. The research was performed on concrete specimens with compressive strength class B90-B100 and modified modulus of elasticity of 55,000 MPa. Based on the results of this work, several important conclusions can be drawn. Firstly, it allows for an assessment of the applicability of established approaches used to describe the deformation process of concretes.

- Classical theories for determining the level of microcrack formation and their derivatives describing the behavior of high-strength concretes are not fully applicable to high-strength concretes (more detailed studies on microcrack appearance in high-strength concretes will be presented in a separate article).
- Secondly, new results were obtained for the investigated mix composition, which can, however, be extrapolated to other modern modified high-strength concretes:
- High-strength concretes can demonstrate nearly linear behavior not only up to high stress levels close to failure but also after reaching their failure load (exceeding the limit state).
- No significant reduction was observed in the modulus of elasticity measured on unloaded specimens after they reached their limit state.
- The duration of concrete specimen holding after reaching their ultimate failure load significantly affects the modulus of elasticity determined on unloaded specimens. Moreover, with short holding times, a sharp increase in the modulus of elasticity was recorded.
- These results are of great interest and confirm one of the most important roles of the stress relaxation process in concrete. Research needs to be continued on different types under different test scenarios.

References

1. Kaprielov, S.S., Sheinfeld, A.V., Al-Omais, D., Zaitsev, A.S. High-Strength Concretes in Constructions of Foundations of the High-Rise Complex “OKO” in MIBC “MOSCOW-CITY.” Industrial and Civil Construction. 2017. 3. Pp. 53–57.
2. Kaprielov, S.S., Sheinfeld, A.V., Kardumyan, G.S., Chilin, I.A. About selection of compositions of high-quality concretes with organic-mineral modifiers. Construction Materials. 2017. 12. Pp. 58–63.
3. Polskoy, P.P., Mailyan, D., Beskopylny, A.N., Meskhi, B., Shilov, A.V., Umarov, A. Strength of Compressed Reinforced Concrete Elements Reinforced with CFRP at Different Load Application Eccentricity. Polymers. 2023. 15. Pp. 26. DOI: 10.3390/polym15010026
4. Lu, T., Jin, H., Guan, K. Experimental Research on Axial Compression Performance of High-Performance-Fiber-Reinforced-Cement-Composite-Prefabricated Monolithic Composite Columns. Buildings. 2023. 13. Pp. 1748–1763. DOI: 10.3390/buildings13071748
5. Ince, E.G., Özkal, F.M. Optimization of Structural Steel Used in Concrete-Encased Steel Composite Columns via Topology Optimization. Applied Sciences. 2024. 14(3). Article no. 1170. DOI: 10.3390/app14031170
6. Bezgodov, I., Kaprielov, S., Sheynfeld, A. Relationship between Strength and Deformation Characteristics of High-Strength Self-Compacting Concrete. International Journal for Computational Civil and Structural Engineering. 2022. 18(2). Pp. 175–183. DOI: 10.22337/2587-9618-2022-18-2-175-183
7. Domarova, E.V. Influence of Creep on the Stress-Strain State of Reinforced Concrete Multistory Buildings. Construction and Reconstruction. 2022. 3(101). Pp. 14–22. DOI: 10.33979/2073-7416-2022-101-3-14-22
8. Bezgodov, I.M., Kapustin, D.E., Efishov, L.I. Physical-Mechanical and Rheological Characteristics of High-Strength Concrete and Granite. Industrial and Civil Construction. 2024. 8. Pp. 48–56. DOI: 10.33622/0869-7019.2024.08.48-56
9. Kolchunov, V.I., Ilyushchenko, T.A. Kriterii osobogo predelnogo sostoyaniya ramnykh sistem iz vysokoprochnogo zhelezobetona [Criteria for special limit states of frame systems made of high-strength reinforced concrete]. Bezopasnost stroitelnogo fonda

Rossii. problemy i resheniya [Safety of Russia's Building Stock. Problems and Solutions: Proceedings of International Academic Readings]. Kursk: Universitetskaya kniga, 2023. Pp. 64–72.

10. Bondarenko, V.M., Kljueva, N.V., Kolchunov, V.I., Androsova, N.B. Some Results of Analysis and Scientific Research on Structural Safety and Survivability Theory. Construction and Reconstruction. 2012. 4(42). Pp. 3–16.
11. Kolchunov, V., Fedorov, S. Serviceability Limit State Parameters for High Strength Concrete Structures. International Journal for Computational Civil and Structural Engineering. 2024. 20(3). Pp. 145–158. DOI: 10.22337/2587-9618-2024-20-3-145-158
12. Wang, T., Zhang, L., Zhao, H., Chen, Q. Progressive collapse resistance of reinforced-concrete frames with specially shaped columns under loss of a corner column. Magazine of Concrete Research. 2016. 68(9). Pp. 435–449. DOI: 10.1680/jmacr.15.00108
13. Berg, O.Ya., Shcherbakov, E.N., Pisanko, G.N. Vysokoprochnyy beton [High-strength concrete]. Moscow: Stroyizdat, 1971. 209 p.
14. Istomin, A.D., Belikov, N.A. Dependence of the Borders of the Microcreeping in Concrete from Strengs and Strain Condition. Bulletin of MGSU. 2011. 2-1. Pp. 159–162.
15. Semenyuk, S.D., Moskalkova, Yu.G. Methods for determining the limits of the microcrack formation. Construction of Unique Buildings and Structures. 2018. 7(70). Pp. 22–30.
16. Zinoviev, V.N. Opredeleniye mikrotreshchinoobrazovaniya betona pri szhatii tenzometricheskim metodom [Determination of concrete microcracking under compression by strain gauge method]. Izvestiya KGTU. 2010. 17. Pp. 118–122. (rus)
17. Tyukalov, Yu.Ya. Rectangular flat finite element for modeling the process of crack formation. Magazine of Civil Engineering. 2025. 18(3). Article no. 13502. DOI: 10.34910/MCE.135.2
18. Hsu, T.T.C., Slate, F.O., Sturman, G.M., Winter, G. Microcracking of Plain Concrete and the Shape of Stress-Strain Curve. JACI. 1963. 60(2). Pp. 209–223. DOI: 10.14359/7852
19. Slate, F.O., Olsefski, S. X-Rays for Study of Internal Structure and Microcracking of Concrete. 1963. JACI Proceedings. 60(5). Pp. 575–587.
20. Shah, S.P., Chandra, S. Critical Stress, Volume Change, and Microcracking of Concrete. JACI Proceedings. 1968. 65(9). Pp. 770–778.
21. Kaprielov, S.S., Sheinfeld, A.V., Selyutin, N.M. Control of Heavy Concrete Characteristics Affecting Structural Stiffness. International Journal for Computational Civil and Structural Engineering. 2022. 18(1). Pp. 24–39. DOI: 10.22337/2587-9618-2022-18-1-24-39
22. Kolchunov, V., Fedorov, S. Serviceability Limit State Parameters for High Strength Concrete Structures. International Journal for Computational Civil and Structural Engineering. 2024. 20(3). Pp. 145–158. DOI: 10.22337/2587-9618-2024-20-3-145-158
23. Bezgodov, I.M. Methodological Features of the Study of Complete Diagrams of Deformation and Stress Relaxation in Concrete. Concrete Technologies. 2020. 11–12(172–173). Pp. 39–44.
24. Eryshev, V.A., Karpenko, N.I., Zhemchuyev, A.O. Integral Parameters of Concrete Diagrams for Calculations of Strength of Reinforced Concrete Elements Using the Deformation Model. International Journal for Computational Civil and Structural Engineering. 2020. 16(1). Pp. 25–37. DOI: 10.22337/2587-9618-2020-16-1-25-37

Information about the authors:

***Petr Arleninov**, PhD in Technical Sciences*
E-mail: arleninoff@gmail.com

Received 07.08.2025. Approved after reviewing 16.11.2025. Accepted 17.11.2025.

Magazine of Civil Engineering

ISSN 2712-8172

journal homepage: http://engstroy.spbstu.ru/

Research article

UDC 691.3

DOI: 10.34910/MCE.140.3

Durability of ultra-high-performance concrete with silica fume and rice husk ash

E.O. Ferreira , ***A.T. Maia*** , ***W. Mazer*** ✉

Federal Technological University of Parana, Parana, Brazil

✉ *wmazer@utfpr.edu.br*

Keywords: ultra-high performance concrete, durability, silica fume, rice husk ash, high temperature.

Abstract. This study analyzed the behavior of Ultra-high performance concrete (UHPC) with two different pozzolans: silica fume and rice husk ash. The use of UHPC as a structural repair material has become common, making it necessary to evaluate its behavior in these situations. The study was conducted by determining compressive strength, assessing permeability and porosity, and assessing its behavior against sulfate attack and exposure to high temperatures. The compressive strength of the concretes was greater than 130 MPa. Regarding porosity and permeability, the concrete composed of silica fume exhibits approximately 20 % lower water absorption than those molded with rice husk ash. Analyzing sulfate attack, the concrete composed of rice husk ash exhibited approximately 50 % lower sulfate penetration than the silica fume composites. The performance of the materials, when subjected to temperatures of 200 and 300 °C, showed reductions in mechanical strength of approximately 26 and 36 %, respectively. At a temperature of 400 °C, the spalling phenomenon occurred. Therefore, there is potential for the use of such a composite due to its high mechanical strength and good performance in relevant characteristics, related to low permeability and high durability.

Acknowledgments. The authors would like to thank CAPES – Coordination for the Improvement of Higher Education Personnel and the Graduate Program in Engineering from the Federal Technology University of Paraná who collectively financed this project.

We thank the Multi-User Center for Materials Characterization – CMCM of UTFPR-CT for carrying out the SEM and DES tests.

Citation: Ferreira, E.O.F., Maia, A.T.M., Mazer, W.M. Durability of ultra-high-performance concrete with silica fume and rice husk ash. Magazine of Civil Engineering. 2025. 18(8). Article no. 14003. DOI: 10.34910/MCE.140.3

1. Introduction

Ultra high-performance concrete (UHPC) is a concrete that has high cement content, aggregates of reduced dimensions, high mechanical strength, and low permeability, has been gaining prominence, with the increased use of mineral admixtures such as silica fume (SF) and rice husk ash (RHA). SF is a product from the production process of the ferrosilicon and iron metallic industries and RHA is considered a residue from the controlled burning of rice husks during the processing of this cereal. Both additions, due to the high silica content in their composition, become materials with high pozzolanic activity, improving the microstructure and mechanical resistance of UHPC [1].

Several studies have been carried out to disseminate the use of UHPC as a structural recovery material in reinforced concrete buildings that present damage that could compromise the safety of the building and users, increasing its durability and restoring its useful life [2–4].

With the interest in spreading the use of UHPC as a material for the rehabilitation of structures, understanding its behavior in terms of durability becomes relevant because it presents itself as a material of very low permeability, preventing the entry of aggressive agents and improving mechanical resistance [2].

The alternative application of UHPC as a recovery material has been studied because it presents better performance against aggressive environmental actions, as shown by the works of Chen et al. [5], Bajaber and Hakeem [6], and Li et al. [7] and high velocity impact [8]. Also, according to Tayeh et al. [2], UHPC require less working time to carry out their application when they exhibit self-compacting behavior, increase the durability and life expectancy of repaired structures, and require fewer preventive actions.

Its mechanical characteristics for UHPC, and its resistance values obtained within the interval of 28 and 90 days are likely to measure the growth gain for this material [9]. Due to its low permeability, UHPC in situations prone to attack by sulfates has a lower deterioration rate than conventional concretes [6, 10–12].

Due to its dense microstructure, when UHPC is subjected to high temperatures, it exhibits explosive behavior. However, this type of sudden shattering phenomenon is controlled with the use of mineral additions and fiber incorporation in cementitious composites [13, 14].

Given the various variations in the availability of pozzolanic materials, this work aims to contribute to the study of UHPCs composed of pozzolans available in Brazil to encourage research and application of this type of product.

2. Materials and Methods

2.1. Materials

The concretes were made with Portland cement CP V – ARI. The cement was characterized and had a specific mass of 3.07 g/cm^3 and a specific surface area of 379.0 m^2/kg.

The RHA used has a specific mass of 2.16 g/cm^3 and a specific surface area of 345.8 m^2/kg obtained by the BETTERSIZE/S3 PLUS laser particle analyzer with an analysis range of 0.01 to 3500 μm by wet method using distilled water.

The quartz powder (QP) used in this research, according to the manufacturer, has a specific mass of 2500 kg/m^3.

For the granulometry of SF, the results of D(10), D(50), and D(90) are 4.92, 14.0, and 32.72 μm, respectively. With this, it was identified that the average diameter of the material is greater than that addressed in the literature – in the order of 0.2 μm – this occurs for other authors such as Romano et al. [15] and Fraga et al. [16], where, according to them, in situations where the SF presents particle agglomeration, the diameters are not congruent with those specified by the manufacturer, as the grains of the material agglomerate resulting in a grain of greater diameter, and do not undergo full use and reactive potential in the mixtures, affecting the formation of C-S-H gel through the consumption of free calcium hydroxide in the mixtures.

The particle size composition of this research is shown in Fig. 1.

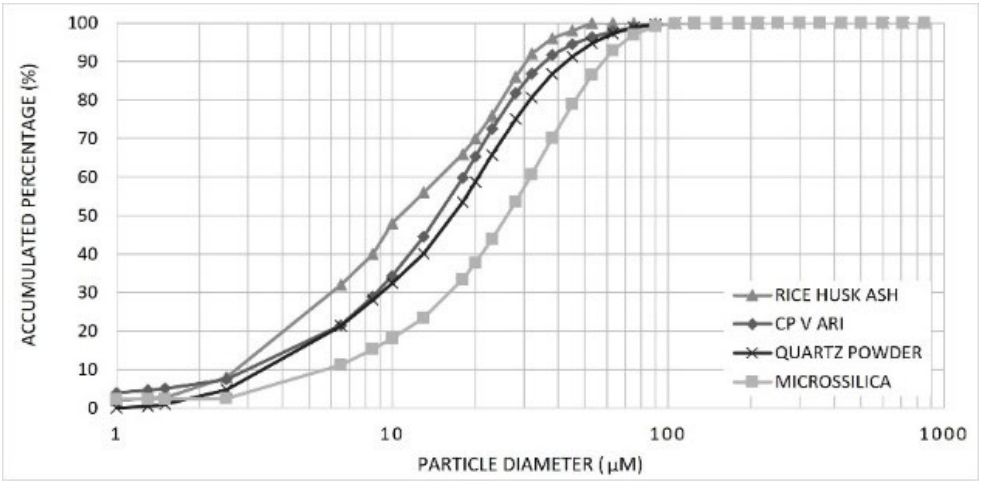

Figure 1. Granulometry of powdery materials.

According to X-ray diffractometry, cementitious and pozzolanic materials demonstrate different structures, as shown in Fig. 2 and Table 1. The test detected that for QP, there is a crystalline structure since it is possible to identify an intense peak. As for the materials CP-V ARI cement, SF and RHA, these have graphs with low intensities, this representation indicates that the products have an amorphous structure.

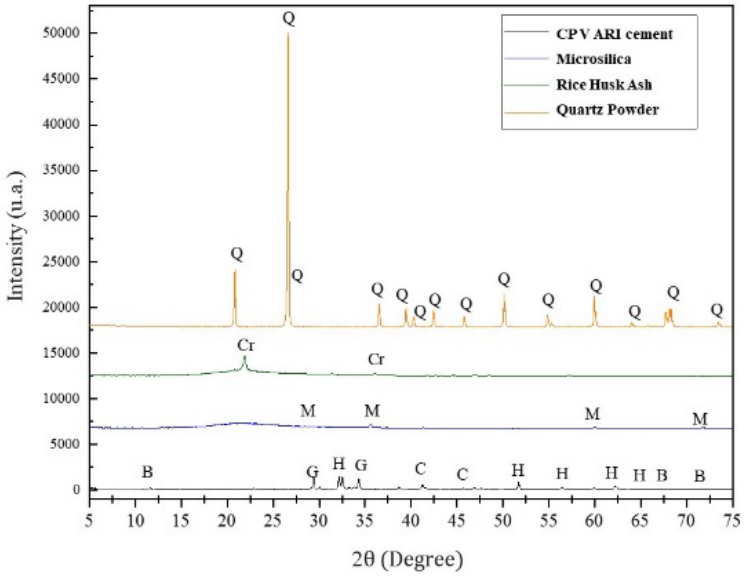

Figure 2. X-ray diffraction (XRD) results for CP V ARI cement, SF, RHA, and QP.

Table 1. XRD results for cement, QP, SF, and RHA.

Mineral	Chemical formula	Acronym	Cement	QP	SF	RHA
Quartz	SiO_2	Q/M	–	100	100	–
Cristobalite	SiO_2	Cr	–	–	–	100
Calcite	$CaCO_3$	C	20	–	–	–
C_3S	Ca_3SiO_5	H	67	–	–	–
Brownmillerita	Ca_2FeAlO_5	B	7	–	–	–
Gypsum	$CaSO_4.2H_2O$	G	6	–	–	–

The packaging of two grains of sand with different granulometries was prepared, where they were dosed according to the packaging based on the Equation Andreasen and Andersen modified adopting q = = 0.37, and the granulometric curve obtained shown in Fig. 3.

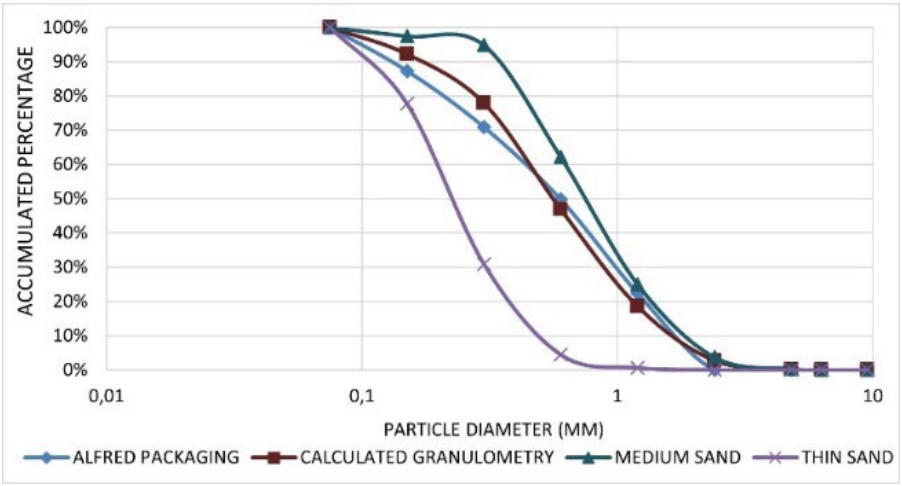

Figure 3. Particle packing according to the modified Andreasen and Andersen model.

A superplasticizer based on polycarboxylate ether with a specific mass of 1.120 g/cm^3 was used 4 % of the mass of the cement. The mix design is showed in Table 2.

Table 2. Concrete mix design.

Material	Cement	Fine sand	Medium sand	QP	SF	RHA	Water	Superplasticizer
Mix 1 (kg/m^3)	855	204	578	239	195	–	197	42
Mix 2 (kg/m^3)	861	204	578	230	–	189	197	42

2.2. Methods

2.2.1. Compression tests

The UHPCs were tested according to NBR 5739 – Concrete – Compression tests of cylindrical specimens [17] to determine the resistance to compression, using six samples submitted to the axial compression test in a press with a capacity of 200 kN with a test speed of 0.45 MPa/s, performing tests at ages of 28 and 90 days.

2.2.2. Water absorption capacity

To analyze the water absorption capacity and determine the void ratio, the methodology described by NBR 9778 – Hardened mortar and concrete – Determination of water absorption, void ratio, and specific mass [18] was adopted. in which, for each mixture with different pozzolanic materials, six samples were manufactured and submitted to the test at the age of 90 days.

The test started with the drying of the specimens in an oven at 105 °C for 24 hours. Subsequently, successive weighings were carried out until the difference in mass between two weighings was less than 1 %. After that, the dry mass (ms) of each sample was determined and then submerged in water for 72 hours. After this time, the specimens were submerged in another container where the temperature was raised to boiling point for 5 hours and after cooling down completely, the submerged mass was determined using the hydrostatic balance (mi). At the end of the test, the saturated mass was also measured in the dry surface condition $(msat)$.

At the end, the water absorption (A) was determined using Equation 1:

$$A = \frac{msat - ms}{ms} * 100. \tag{1}$$

We obtained the void ratio (VR) according to Equation 2:

$$VR = \frac{msat - ms}{msat - mi} * 100. \tag{2}$$

The specific mass was determined by Equation 3:

$$pr = \frac{ms}{ms - mi} * 100. \tag{3}$$

2.2.3. Absorption of water by capillarity

Initially, the samples were dried in an oven at 105 °C until constant mass, and the dry mass of the samples (ms) was determined. Then, the sides of the specimens were sealed with epoxy paint, and the samples were placed on a rack in a container of water until the water level covered a height of 5 mm from the samples. According to the procedures of NBR 9779 [19], the samples were weighed after 3, 6, 24, 48, and 72 h, at which point the saturated mass $(msast)$ was determined. After the last weighing, the specimens were broken diametrically to measure the capillary rise in each sample.

The final result of water absorption is calculated according to Equation 4, where S means the cross-sectional area of the sample in contact with water, and a visual analysis of the water percolation profile inside the concrete is carried out as required by NBR 9779 [19]:

$$C = \frac{msast - ms}{S}. \tag{4}$$

2.2.4. Attacks of sulfates – magnesium

The methodology for determining the attack of sulfates in concrete is based on measuring the expansion of prismatic specimens subjected to an environment saturated with sulfates over a period at high temperatures, however, this technique requires approximately two years to obtain results [20].

The concrete portions of each specimen were dried in an oven for 8 hours at 100 °C and after removing from the oven and reaching room temperature, each sample was ground in a pan mill until the particles reached a diameter less than 150 μm, which are used to determine the amount of sulfates in each sample.

The sulfate content of the samples is determined according to Equation 5, described by NBR16937-6 – Aggressive waters – Durability of concrete – Part 6: Determination of sulfate soluble in water [21]:

$$SO_4^{-2} = \frac{\text{Mcalcined} \times 0.4116}{\text{Mcollected}} \times 100, \quad (5)$$

where 0.4116 = is the conversion factor of barium sulfate to sulfate ion $\left(SO_4^{-2}\right)$.

2.2.5. Influence of temperature increase on axial compressive strength

NBR 14432 – Fire resistance requirements for building construction elements – Procedure [22] describes the required fire resistance time of a maximum of 120 minutes, therefore, for this test, 18 specimens were prepared, of which divided into three groups for three different temperatures. The test specimens underwent submerged curing and at the age of 28 days they were removed from the water and kept in a chamber for 10 days so that the moisture content was reduced until reaching hygroscopic equilibrium with the environment [23].

To carry out the tests at temperatures of 200, 300, and 400 °C, the concretes of each analysis group were subjected to heating at a rate of 10 °C/min in a muffle furnace until the temperature established for each set analyzed, which were then maintained for 120 continuous minutes under the action of high temperature, and, after heating, the samples were naturally cooled inside the muffle until they reached room temperature.

Representing the standard fire curve, Fig. 4 shows that during the heating period, there is a continuous rise and temperature uniformity (T) within 120 minutes, between t_1 and t_2, as determined by NBR 14432 [22].

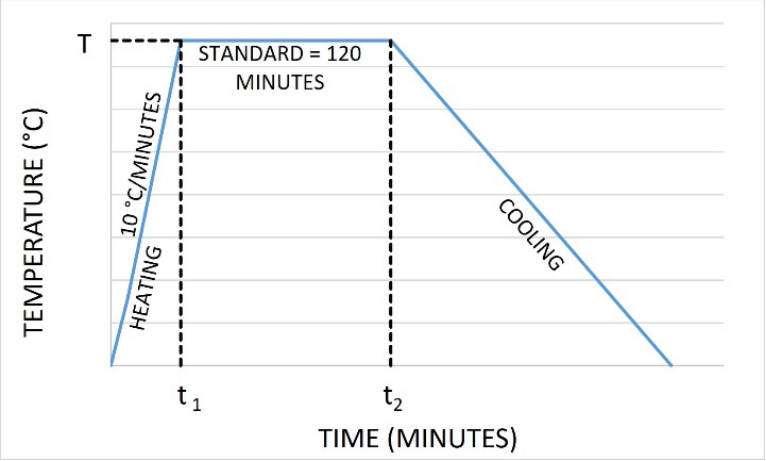

Figure 4. Heating scheme for the temperature influence test.

To characterize the effect of high temperatures on UHPC, axial compression tests were carried out to identify the influence on the mechanical properties of the material [24–26].

2.2.6. X-Ray diffraction test

X-ray diffraction is a test where it is possible to characterize the crystalline structure of materials using Shimadzu's XRD 7000 equipment. The equipment software detects the intensity at the peak position, the interplanar distance, and the peak width.

3. Results and Dicussion

3.1. Compression Tests

The axial compression results were obtained according to the methodology determined by NBR 5739 [17] and the method of statistical refinement of Peirce's treatment was used to determine the final values of resistance to compression, presented in Fig. 5.

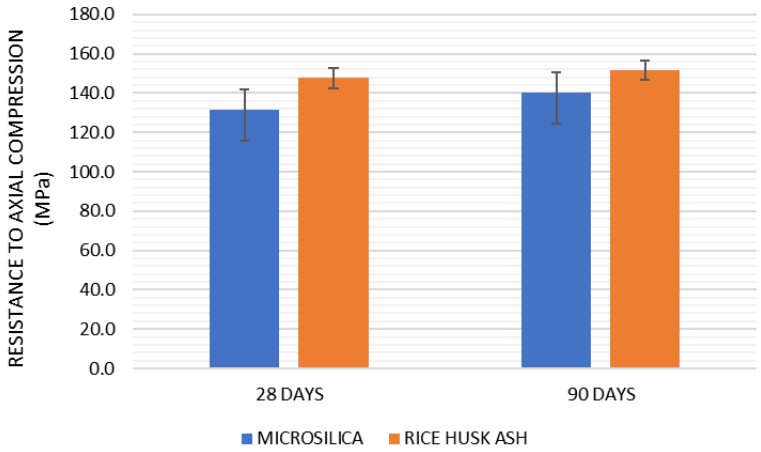

Figure 5. Comparison between strengths at different test ages.

With the results obtained, it is possible to identify that for concretes composed of RHA, the resistance to axial compression was about 8 % higher than in comparison to concretes with SF. Given the results, between the ages of 28 to 90 days, the strength gain for SF concretes was 8 % and approximately 3 % for concretes with RHA. The results shown in Fig. 5 show that after 90 days, there was a strength gain of around 7 and 3 % for concrete cast with SF and with RHA, respectively, as also shown in Table 3.

Table 3. Axial compression results for UHPC.

Specimen	SF	RHA	SF	RHA
Age	**28 days**		**90 days**	
Average (MPa)	131.39	147.62	140.41	151.73
Standard deviation (MPa)	10.39	5.05	15.85	3.66
Coefficient of variation (%)	7.91	3.42	11.29	2.41

Based on the methodology for the statistical analysis of UHPC using the analysis of variance for different sample sizes, at the 95 % confidence interval, it is possible to observe the compressive strength of the concretes composed of SF at 28 days is equal to the results obtained at 90 days and equal to the compressive strength of the samples with RHA at 28 days.

The compressive strength with SF at 28 days is equal to 90 days and is also equal to the compressive strength with RHA at 28 days. In both concrete, even with the variation of its pozzolanic addition, it was not possible to observe a significant difference in the compressive strength gain between the ages of 28 and 90 days, in addition to that, there was no difference between the strengths with different mineral additions for a same age. The values obtained are higher than the values observed by Bulgakov et al. [27] and by Lesovik et al. [28], who used SF.

3.2. Water Absorption Capacity and Void Index

For the test described by NBR 9778 [18], each group composed of six specimens was submitted to the water absorption test at the age of 90 days. The results of absorption by immersion and the voids index are shown in Table 4.

Table 4. Results of the absorption test by immersion of the voids index.

Specimen	SF		RHA	
Test	**Absorption**	**Voids index**	**Absorption**	**Voids index**
Average (%)	2.02	4.53	1.98	4.39
Standard deviation (%)	0.13	0.33	0.19	0.41
Coefficient of variation (%)	6.39	7.39	9.58	9.28

Through statistical analysis, for concretes molded with SF, the average water absorption was 2.02 %, and for concretes with RHA, it was 1.98 %, as shown in Table 3, indicating that both results equal a 95 % confidence index. As for the voids index, with the average result obtained for SF of 4.53 % and for concretes consisting of RHA of 4.39 %, both are statistically equal to a confidence index of 95 % according to the analysis of variance.

According to Dinakar et al. [29] and Medeiros-Junior et al. [30], concretes with levels of water absorption by immersion after 72 hours below 3 % are considered good in the aspect of low infiltration capacity, thus being able to state that for concretes molded we have a low absorption rate, with values slightly lower than those observed by [27].

3.3. Absorption of Water by Capillarity

The test described by NBR 9779 [18] was performed on six concrete samples for each pozzolan analyzed to determine the average values of capillary absorption at the age of 90 days. The results are shown in Table 5.

Table 5. Results of the capillary absorption test.

Specimen	SF	RHA
Average (%)	0.065	0.082
Standard deviation (%)	0.005	0.003

Graphically, Fig. 6 shows the correlation between absorption over test times.

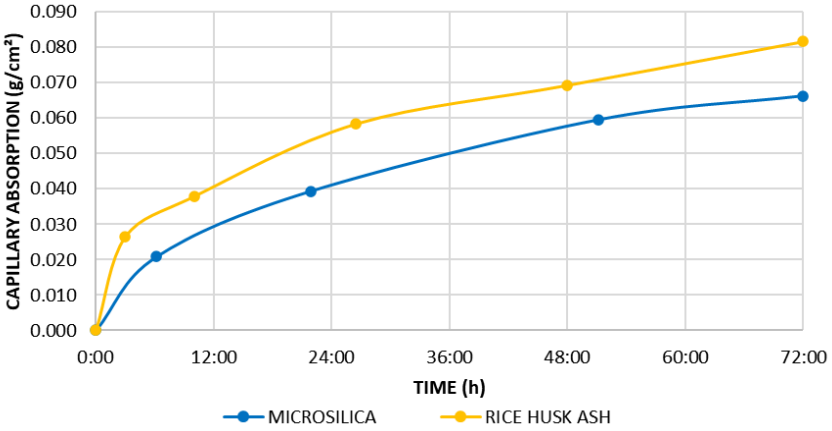

Figure 6. Absorption by capillarity as determined by NBR 9779 [18].

It is possible to identify in Fig. 6 that the water content absorbed by capillarity increased as the test time elapsed in both mixtures. Note that there is a tendency for absorption to stabilize due to the maximum absorption rate of the material.

It is possible to identify that concretes made with RHA tend to have an absorption rate of approximately 20 % more than those molded with SF, demonstrating that this pozzolan has a more porous matrix that allows greater water flow through the composite, such effect is corroborated with the analysis of variance at a confidence index of 95 %, which demonstrates a statistical difference in the permeability content for concretes with different pozzolanic additions.

This analysis had already been described previously since the criterion that the pores are connected and have different dimensions for each type of material, influencing the effective capacity to resist the penetration of water in the cementitious matrix.

3.4. Attacks of Sulfates – Magnesium

To measure the attack content of sulfates in UHPC made with SF, after the test, the results are presented in Table 6.

Table 6. Results obtained for the sulfate content test.

Specimen	SF	RHA
Average (%)	1.417	0.942
Standard deviation (%)	0.297	0.088

Table 6 presents the result of the average value of sulfate attack content for concretes with SF being 1.417 % and for concretes with RHA of 0.942 %. Due to the lack of parameters for this material, Mazer et al. [20] indicate that for concrete, contents above the 0.46 % limit already indicate the existence of significant penetration of sulfates in the structure, whereas Sun et al. [31], in solutions with 50 g/l, the sulfate content was 0.329 % due to the normalization of the concentration due to the rapid formation of gypsum and ettringite in the pores, which prevented a greater penetration of ions inside the concrete. With this, it is possible to state that in concrete composed of SF, there is a propensity of approximately 50 % of this type of material to suffer from the penetration of sulfates in its structure.

To correlate the results of the penetration of sulfates with the permeability of the materials, Fig. 7 demonstrates that for concrete made with SF, the tendency for penetration of sulfate ions is lower than for composite concrete by RHA.

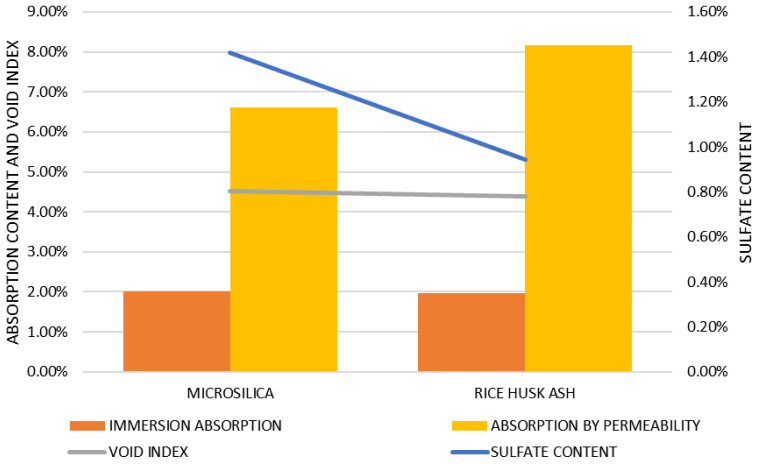

Figure 7. Correlation between sulfate absorption and penetration levels.

According to Sun et. al. [31] and Zou et al. [32] at a higher solution concentration, more sulfate ions penetrate the concrete for the same immersion time, with this, the correlation between the absorption rate of the material and the lowest. The value of penetration of sulfate ions into concrete is because in the initial stage of the attack, the expansive products fill the pores of the materials and prevent the transport of sulfate ions.

Regarding the mechanical resistance of the specimens submitted to the sulfate attack test, Table 7 presents the results obtained in the axial compression test of the specimens after 90 days of testing.

Table 7. Compression results of UHPC after sulfate attack.

Specimen	SF	RHA
Average (MPa)	85.55	85.34
Standard deviation (MPa)	12.19	15.32
Coefficient of variation (%)	14.25	17.96

According to the results of Table 7, it is possible to identify the influence of sulfate attack on the concrete structure in terms of mechanical strength since, compared to the results obtained in Table 1, there was a decrease in the resistance to axial compression of 60 % for the UHPC molded with SF and of 56 % for the specimens constituted of RHA.

Such results corroborate the difference in the sulfate content penetrated in the samples since the ratio between the sulfate penetration content and the axial compression strength for concretes with SF is 0.016 and for concretes with RHA is 0.011, indicating a greater propensity to occur with the first pozzolan analyzed, statistically confirmed by the analysis of variance with 95 % confidence where for concretes with RHA they have less penetration of sulfates.

Using the analysis of variance criterion to determine the resistance to sulfate attack, the compressive strengths of concrete submitted to the sulfate attack test, regardless of the type of addition used, present statistically equal values with 95 % confidence, that there is a reduction in resistance about the reference concretes of the same age since they are statistically different. This factor can be explained by the reactions that occur in the cementitious matrix of UHPC molded with RHA, in which the sulfates reacted in the most superficial pores, preventing the progression of the action into the material.

3.5. Influence of Temperature Increase on Axial Compressive Strength

The first group of samples was subjected to heating at a temperature of 200 °C and after cooling, they were subjected to the axial compression test to determine the mechanical resistance of the UHPC, as shown in Table 8.

Table 8. Compression results of the heating test up to 200 °C.

Specimen	SF	RHA
Average (MPa)	89.83	109.44
Standard deviation (MPa)	29.72	8.13
Coefficient of variation (%)	33.10	7.43

For the samples subjected to 300 °C, the specimens with SF did not show visible signs of degradation or chipping, however, two samples of the concrete molded with RHA suffered from the spalling phenomenon. Its compressive strength results are shown in Table 9.

Table 9. Compression results of the heating test up to 300°C.

Specimen	SF	RHA
Average (MPa)	79.95	105.17
Standard deviation (MPa)	14.21	13.37
Coefficient of variation (%)	17.77	8.99

The samples subjected to heating up to 400 °C had the spalling phenomenon evident and already described by Abid et al. [13], it was not possible to perform the mechanical resistance test on the specimens.

According to Tables 8 and 9, the compressive strength of UHPC composed of SF elevated at 200 and 300 °C are statistically different from the reference compressive strength, indicating a loss of strength of 31.6 and 39.2 %, respectively, but the resistances at 200 and 300 °C are equal.

The compressive strength, heated to 200 and 300 °C, with RHA, are statistically different from the reference compressive strength, indicating a loss of strength of 25.9 and 28.7 %, respectively, but the strengths at 200 and 300 °C are equal.

Changing the type of addition shows a difference in the compressive strength between them for the same temperature, that is, concretes with SF show a greater loss of strength than in comparison with UHPC that use RHA. Two RHA samples exhibited spalling at a temperature of 300 °C, likely because they have a higher capillary absorption coefficient than the SF samples, indicating finer pores, which resulted in a greater capillary height. Additionally, the RHA samples also have a lower void ratio, hindering water escape from their interior. The combination of these effects may have caused spalling in both samples. However, the remaining intact samples showed less strength loss compared to the reference samples, when compared to the strength loss of the SF samples.

3.6. X-Ray Diffraction Test

The results of changes in the microstructures of concretes made of SF pozzolan are shown in Fig. 8.

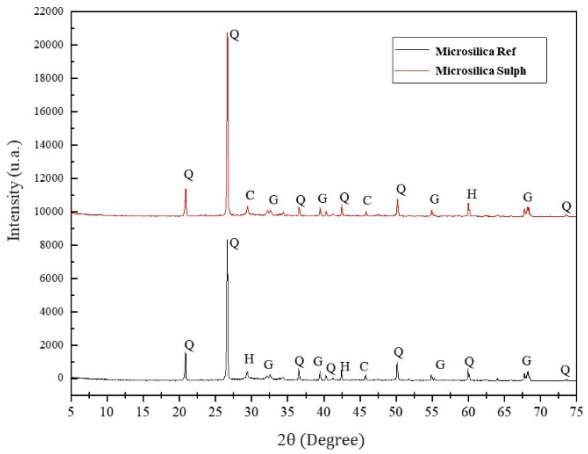

Figure 8. XRD results for reference concrete with SF compared to concrete subjected to sulfate attack.

As seen in Fig. 8, the peaks for the UHPC with reference SF (SF Ref) in comparison with the SF concrete subjected to sulfate attack (SF Sulph) are similar, and their mineralogical percentages are shown in Table 10.

Table 10. XRD result for reference concretes with SF compared to concretes subjected to sulfate attack.

Mineral	Chemical formula	Acronym	SF Ref	SF Sulph
Quartz	SiO_2	Q	56	53
Tobermorite	$Ca_5Si_6O_{16}(OH)_2.4H_2O$	T	30	38
Portlandite	$Ca(OH)_2$	P	0	0
Ettringite	$3CaO.Al_2O_3.3CaSO_4.32H_2O$	E	11	1
Gypsum	$CaSO_4.2H_2O$	G	3	8

According to Table 10, the presence of sulfate ions resulted in an increase in the gypsum content of concrete subjected to this type of exposure, as described by Zou et al. [32]. Despite the samples being subjected to Mg sulfate attack, the exposure time, the low void content and the low water/binder ratio did not allow the material to decompose to a chemically identifiable degree.

Fig. 9 together with Table 11 shows the results of the XRD test for the concretes using SF Ref and when molded with the same pozzolan but submitted to 200, 300, and 400 °C, being represented by SF 200°C, SF 300 °C, and SF 400 °C, respectively.

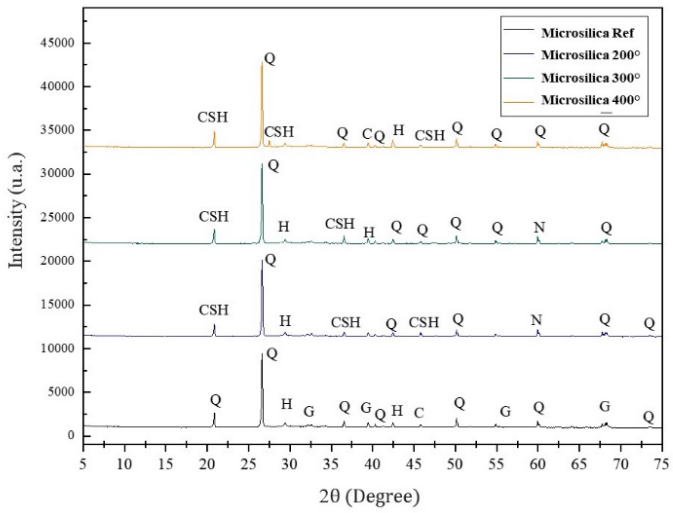

Figure 9. XRD results for reference concrete with SF compared to concretes subjected to different temperature rises.

Table 11. XRD results for reference concretes with SF compared to concretes subjected to different temperature rises.

Mineral	Chemical formula	Acronym	SF Ref	SF 200°	SF 300°	SF 400°
Quartz	SiO_2	Q	56	57	64	61
Tobermorite	$Ca_5Si_6O_{16}(OH)_2.4H_2O$	T	30	23	16	14
Portlandite	$Ca(OH)_2$	P	0	0	1	1
Ettringite	$3CaO.Al_2O_3.3CaSO_4.32H_2O$	E	11	18	16	23
Gypsum	$CaSO_4.2H_2O$	G	3	2	2	1

Concretes subjected to different temperature gradients show some changes in the final chemical composition about the reference, and for samples subjected to temperatures above 200 °C, it is possible to identify that there is a reduction in the Van Der Walls forces and the C-S-H of material. From 200 °C, the water chemically linked to the C-S-H (tobermorite) is lost, which can be identified by the increase in the free SiO_2 content in the structure, the decrease in the tobermorite content and the decomposition of the gypsum. With this, the mechanical strength of the material was compromised as shown in the results of resistance to axial compression previously.

For concrete made of RHA, the results of the XRD test are presented in Fig. 10 and the mineralogical percentages are described in Table 12, where it is possible to identify that the peaks of greater intensities coincide both between the reference concrete (RHA Ref) for this pozzolan as well as for concrete subjected to sulfate attack (RHA Sulph).

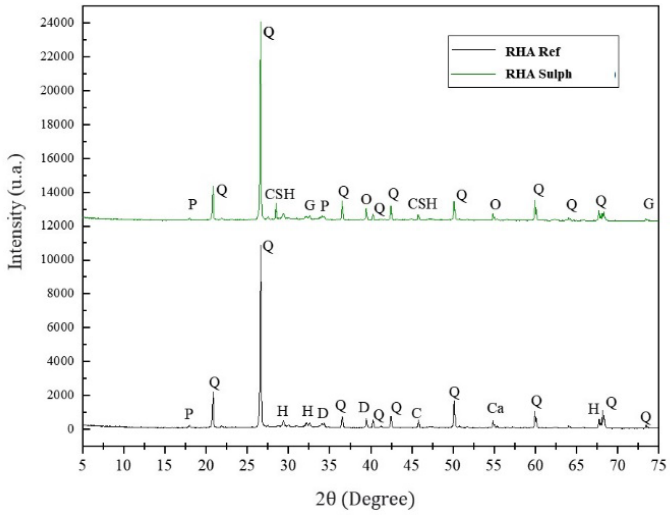

Figure 10. XRD results for the reference concretes with RHA compared to the concrete subjected to sulfate attack.

Table 12. XRD test results for concretes with RHA after sulfate test.

Mineral	Chemical formula	Acronym	RHA Ref	RHA Sulph
Quartz	SiO_2	Q	46	50
Tobermorite	$Ca_5Si_6O_{16}(OH)_2.4H_2O$	T	32	31
Portlandite	$Ca(OH)_2$	P	1	1
Ettringite	$3CaO.Al_2O_3.3CaSO_4.32H_2O$	E	15	13
Gypsum	$CaSO_4.2H_2O$	G	6	5

Table 12 presents the minerals formed based on Fig. 10, where the highest mineral percentage is silica in both analyzed samples. For the RHA Sulph and RHA Ref samples, the low rate of change in the ettringite content may be a consequence of hydration reactions due to the heat treatment to which the samples were subjected, preventing chemical changes in the UHPC compounds.

Concrete molded with RHA pozzolan (RHA Ref) together with concrete of the same pozzolan subjected to 200, 300, and 400 °C have the values shown in Fig. 11 as XRD test results and in Table 13, with the samples RHA 200 °C, RHA 300 °C, and RHA 400 °C abbreviations referring to each temperature to which the samples were submitted.

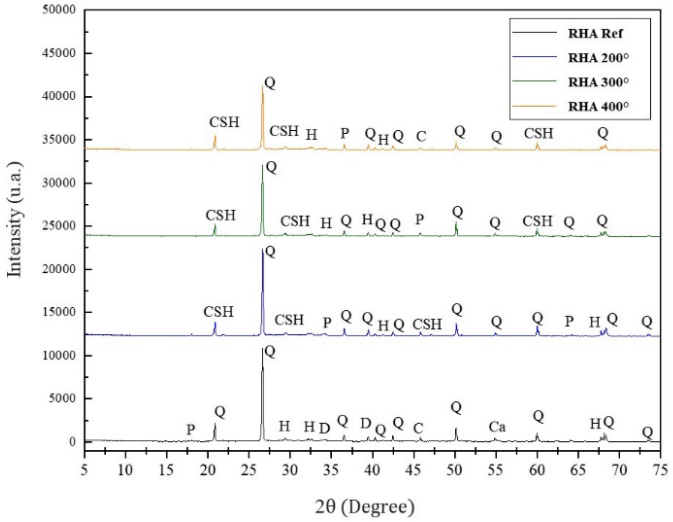

Figure 11. XRD results for reference concretes with RHA compared to concretes submitted to different temperature rises.

Table 13. XRD results for the reference concrete with RHA compared to concretes subjected to different temperature rises.

Mineral	Chemical formula	Acronym	RHA Ref	RHA 200°	RHA 300°	RHA 400°
Quartz	SiO_2	Q	46	56	66	55
Tobermorite	$Ca_5Si_6O_{16}(OH)_2.4H_2O$	T	32	35	18	18
Portlandite	$Ca(OH)_2$	P	1	1	0	0
Ettringite	$3CaO.Al_2O_3.3CaSO_4.32H_2O$	E	15	7	14	12
Gypsum	$CaSO_4.2H_2O$	G	6	2	2	15

According to Table 13, the hydrated calcium silicate (tobermorite) decomposed right after the temperature of 200 °C due to the loss of water from the structure, generating the release of silica oxide due to the dehydration of the CH [33]. The degradation of portlandite is observed in concretes shortly after exposure above 300 °C, as well as the degradation of gypsum after its exposure to temperatures greater than 200 °C.

Both the analyses for concrete molded with SF and for those composed of RHA show the decomposition of hydrated calcium silicate, which is the main compound responsible for the mechanical strength of concrete in general, in addition to the formation of other oxides that do not contribute to the gain on the load capacity of UHPC.

4. Conclusions

This work aimed to analyze the behavior of UHPC using two types of pozzolanic materials – SF and RHA.

For the mechanical performance, both had similar resistance capacities even after the analysis of age progression, being the difference in axial resistance between the materials being about 10 % greater for the concretes composed of RHA. This result for the sample group and due to the curing methodology applied to the specimens presents equal performance between the materials.

Analyzing permeability, this factor becomes important to determine the performance of products against the durability of UHPC. It was identified that even with the variation of the results between the concretes molded with SF and with RHA in the capillary permeability test, this factor depends on the structure of the pores of the materials, because the different concretes present water absorption levels and indices of analogous voids. As a repair material, the choice of a matrix composed of SF would be the most indicated since the propensity for fluid penetration due to permeability is lower than that of concrete made of RHA.

To analyze the behavior of the material in aggressive environments, after subjecting the concrete to sulfate attack, it was possible to observe a significant difference in the behavior when the samples were molded with SF and when they were made of RHA since the first pozzolan allowed a greater penetration of ions than compared to RHA, about 50 % higher. This may be due to the pore structure of this type of cementitious matrix, which, according to the results obtained by the XRD analysis, influenced the chemical composition of the material because of the more significant attack in concrete composed of SF. If thinking of an application as a repair material for structural recovery, concrete composed of RHA would be more indicated because of the lower propensity to suffer from this phenomenon in aggressive environments.

From the point of view of the mechanical behavior of concretes in situations where they undergo a significant temperature rise, for both analyzed compositions, the performance of concretes is presented the same. According to the analysis of variance adopted, the mechanical resistances of the different cementitious matrices are equivalent, and the microscopic evaluation using XRD demonstrates the chemical decomposition of the agents responsible for the mechanical resistance of the materials for both pozzolans.

Taking the analysis carried out in this work, the replacement of SF by RHA does not interfere with the mechanical performance of UHPC. Therefore, with the results obtained in this work, the application of any of the two pozzolans to produce concrete should be determined based on the aggressiveness class or the environment in which the material is expected to be used.

References

1. Sieg, A.P.A. et al. Concreto de pós-reativos – estudo das adições minerais: Cinza de casca de arroz, metacaulim e sílica ativa. Anais do 54° Congresso Brasileiro do Concreto. Maceió, 2012. Pp. 1–15.

2. Tayeh, B.A., Abu Bakar, B.H., Megat Johari, M.A., Voo, Y.L. Utilization of Ultra-high Performance Fibre Concrete (UHPFC) for Rehabilitation – A Review. Procedia Engineering. 2013. 54. Pp. 525–538. DOI: 10.1016/j.proeng.2013.03.048
3. Yoo, D., Yoon, Y. A Review on Structural Behavior, Design, and Application of Ultra-High-Performance Fiber-Reinforced Concrete. International Journal of Concrete Structures and Materials. 10(2). Pp. 125–142, 2016. DOI: 10.1007/s40069-016-0143-x
4. Yalçınkaya, Ç., Çopuroğlu, O. Hydration heat, strength and microstructure characteristics of UHPC containing blast furnace slag. Journal of Building Engineering. 2021. 34. Article no. 101915. DOI: 10.1016/j.jobe.2020.101915
5. Chen, Y., Yu, R., Wang, X., Chen, J., Shuiet, Zh. Evaluation and optimization of Ultra-High Performance Concrete (UHPC) subjected to harsh ocean environment: Towards an application of Layered Double Hydroxides (LDHs). Construction and Building Materials. 2018. 177. Pp. 51–62. DOI: 10.1016/j.conbuildmat.2018.03.210
6. Bajaber, M., Hakeem, I. UHPC evolution, development, and utilization in construction: a review. Journal of Materials Research and Technology. 2021. 10. Pp. 1058–1074. DOI: 10.1016/j.jmrt.2020.12.051
7. LI, J., Wu, Z., Shi, C., Yuan, Q., Zhang, Z. Durability of ultra-high performance concrete – A review. Construction and Building Materials. 2020. 255. Article no. 119296. DOI: 10.1016/j.conbuildmat.2020.119296
8. Mai, V.C., Luu, X.B., Nguyen, V.T. Ultra high-performance fiber reinforced concrete panel subjected to high velocity impact. Magazine of Civil Engineering. 2021. 107(7). Article no. 10703. DOI: 10.34910/MCE.107.3
9. Reddy, G.G.K., Ramadoss, P. Influence of alccofine incorporation on the mechanical behavior of ultra-high performance concrete (UHPC). Materials Today: Proceedings. 2020. 33(1). Pp. 789–79. DOI: 10.1016/j.matpr.2020.06.180
10. Abbas, S., Nehdi, M.L., Saleem, M.A. Ultra-High Performance Concrete: Mechanical Performance, Durability, Sustainability and Implementation Challenges. International Journal of Concrete Structures and Materials. 2016. 10. Pp. 271–295. DOI: 10.1007/s40069-016-0157-4
11. Wang, D., Shi, C., Wu, Z., Xiao, J., Huang, Zh., Fang, Zh. A review on ultra-high-performance concrete: Part II. Hydration, microstructure and properties. Construction and Building Materials. 2015. 96. Pp. 368–377. DOI: 10.1016/j.conbuildmat.2015.08.095
12. Lessly, S.H., Lakshmana Kumar, S., Raj Jawahar, R., Prabhu, L. Durability properties of modified ultra-high performance concrete with varying cement content and curing regime. Materials Today: Proceedings. 2021. 45(7). Pp. 6426–6432. DOI: 10.1016/j.matpr.2020.11.271
13. Abid, M., Hou, X., Zheng, W., Hussain, R.R. High temperature and residual properties of reactive powder concrete – A review. Construction and Building Materials. 2017. 147. Pp. 339–351. DOI: 10.1016/j.conbuildmat.2017.04.083
14. Rawat, S., Lee, C.K., Zhang, Y.X. Performance of fiber-reinforced cementitious composites at elevated temperatures: A review. Construction and Building Materials. 2021. 292. Article no. 123382. DOI: 10.1016/j.conbuildmat.2021.123382
15. Romano, R.C.O., Schreurs, H., John, V.M., Pileggi, R.G. Influência da técnica de dispersão nas propriedades de silica ativa. Cerâmica. 2008. 54(332). Pp. 456–461. DOI: 10.1590/S0366-69132008000400011
16. Fraga, Y.S.B., Rêgo, J., Capuzzo, V.M.S., da Silva Andrade, D. Efeito da ultrasonicação da sílica ativa e da nanossílica colloidal em pastas de cimento. Matéria (Rio de Janeiro). 2020. 25(4). DOI: 10.1590/s1517-707620200004.1147
17. ABNT. NBR 5739: Concreto – ensaio se compressão de corpos-de-prova cilíndricos. Associação brasileira de normas técnicas. Rio de Janeiro, 2007. 4 p.
18. ABNT. NBR 9778: Argamassa e concreto endurecidos – determinação da absorção de água, índices de vazios e massa específica. Associação brasileira de normas técnicas. Rio de Janeiro, 2005. 4 p.
19. ABNT. NBR 9779: Argamassa e concreto endurecidos – determinação da absorção de água por capilaridades. Associação brasileira de normas técnicas. Rio de Janeiro, 2012. 3 p.
20. Mazer, W., Macioski, G.; Soto, N. Determinação de ions sulfato em estruturas de concreto. Blucher Chemical Engineering Proceedings. 2015. 1(2). Pp. 13574–13580.
21. ABNT. NBR 16937-6: Águas agressivas – durabilidade do concreto. parte 6: Determinação de sulfato solúvel em água. Associação brasileira de normas técnicas. Rio de Janeiro, 2021. 6 p.
22. ABNT. NBR 14432: Exigências de Resistencia ao fogo de elementos construtivos de edificações – procedimento. Associação brasileira de normas técnicas. Rio de Janeiro, 2001. 14 p.
23. Ganasini, D. Concretos de Alto Desempenho reforçado com microfibras de polipropileno e submetidos a elevadas temperaturas. 135 p. Dissertação (Mestrado) — Centro de Ciências Tecnológicas, Programa de Pós-Graduação em Engenharia Civil. Universidade do Estado de Santa Catarina., Joinville, 2019.
24. Lee, N. et al. Microstructural investigation of calcium aluminate cement-based ultra-high performance concrete (uhpc) exposed to high temperatures. Cement and Concrete Research. v. 102. p. 109–118. 2017. ISSN 0008-8846.
25. Ju, Y. et al. Experimental investigation of the effect of silica fume on the thermal spalling of reactive powder concrete. Construction and Building Materials. v. 155. Pp. 571–583. 2017. ISSN 0950-0618.
26. Zhang, D., Tan, K.H. Effect of various polymer fibers on spalling mitigation of ultra-high performance concrete at high temperature. Cement and Concrete Composites. v. 114. Pp. 103815. 2020. ISSN 0958-9465.
27. Bulgakov, B.I., Nguyen, V.Q.D., Aleksandrova, A.V., Larsen, O.A., Galtseva, N.A. High-performance concrete produced with locally available materials. Magazine of Civil Engineering. 2023. 117(1). Article No. 11702. DOI: 10.34910/MCE.117.2
28. Lesovik, V.S., Popov, D.Y., Fediuk, R.S., Sabri, M.M., Vavrenyuk, S.V., Liseitsev, Y.L. Shrinkage of ultra-high performance concrete with superabsorbent polymers. Magazine of Civil Engineering. 2023. 121(5). Article No. 12108. DOI: 10.34910/MCE.121.8
29. Dinakar, P., Sahoo, P.K., Sriram, G. Effect of metakaolin content on the properties of high strength concrete. International Journal of Concrete Structures and Materials. v. 7. p. 215–223. 2013. ISSN 1976-0485.
30. De Medeiros-Junior, R.A., Munhoz, G. da S., de Medeiros, M.H.F. Correlations between water absorption, electrical resistivity and compressive strength of concrete with different contents of pozzolan. Revista ALCONPAT. 2019. 9(2). Pp. 152–166. https://doi.org/10.21041/ra.v9i2.335.
31. Sun, D., Wu, K., Shi, H., Zhang, L., Zhang, L. Effect of interfacial transition zone on the transport of sulfate ions in concrete. Construction and Building Materials. 2018. 192. Pp. 28–37. DOI: 10.1016/j.conbuildmat.2018.10.140

32. Zheng, W., Luo, B., Wang, Y. Compressive and tensile properties of reactive powder concrete with steel fibers at elevated temperatures. Construction and Building Materials. 2013. 41. Pp. 844–851. DOI: 10.1016/j.conbuildmat.2012.12.066
33. Zou, D., Qin, Sh., Liu, T., Jivkov, A. Experimental and Numerical Study of the Effects of Solution Concentration and Temperature on Concrete under External Sulfate Attack. Cement and Concrete Research. 2021. 139. Article no. 106284. DOI: 10.1016/j.cemconres.2020.106284

Information about the authors:

Elizamary Otto Ferreira,
ORCID: https://orcid.org/0000-0002-2262-7424
E-mail: elizamaryotto@gmail.com

Alessandra Tourinho Maia,
ORCID: https://orcid.org/0000-0003-2168-4301
E-mail: alessandra.tourinho@gmail.com

Wellington Mazer, *Doctor of Science*
ORCID: https://orcid.org/0000-0002-9941-999X
E-mail: wmazer@utfpr.edu.br

Received 15.12.2023. Approved after reviewing 19.11.2025. Accepted 20.11.2025.

Magazine of Civil Engineering

ISSN 2712-8172

journal homepage: http://engstroy.spbstu.ru/

Research article

UDC 624

DOI: 10.34910/MCE.140.4

Effect of de-sanding (recycling system) process on the piles bearing capacity

H.N. Hasan ✉, ***A.A.H. Al-Saidi***

Civil Engineering Department, University of Baghdad, Baghdad, Iraq

✉ *hayder.hasan2001m@coeng.uobaghdad.edu.iq*

Keywords: bored pile, bentonite, finite element, bearing capacity, recycling system.

Abstract. The technique adopted in this study includes an innovative and unconventional method, which plays an important role in enhancing the bearing capacity of piles, called a recycling system. Full-scale models were conducted on two groups of piles: the first group was constructed without using this system, and the second group was constructed using it. All piles were tested by static load test. 3D finite element in the PLAXIS program was adopted to understand the load-carrying response of piled, several parameters were studied such as the thickness of the filter cake, type of soil, L/D ratio, and separation between the friction and end bearing. The results revealed that using the recycling system significantly increased the pile-bearing capacity, reaching 50 %. The effectiveness of the recycling system in cohesionless soils is more efficient than in cohesive soils. Pile's bearing capacity improvement ratio reaches 65 and 38 % for sandy and clayey soils, respectively. In addition, the thickness of the filter cake significantly reduces the pile-bearing capacity, which may exceed 40 % if this system is not used. Using the recycling system, the pile bearing capacity was improved by 60–64 % and 85–98 % for friction and end bearing, respectively.

Acknowledgment. Our sincere thanks and appreciation to the Palm Towers residential complex in Baghdad Governorate, Iraq, for their full funding of this research and the use of the recycling system method in implementing all the working piles in the project after the method's success.

Citation: Hasan, H.N., Al-Saidi, A.A.H. Effect of de-sanding (recycling system) process on the piles bearing capacity. Magazine of Civil Engineering. 2025. 18(8). Article no. 14004. DOI: 10.34910/MCE.140.4

1. Introduction

Bored piles are increasingly used to effectively transfer the loads of the superstructure to the sub-soil when the soil conditions at the site and certain other functional requirements cannot support the shallow foundations [1, 2]. The construction of bored piles is accompanied by the presence of drilling residues and sludge in the body of the pile; these residues and sludge significantly reduce the bearing capacity of the bored piles [3, 4]. The traditional methods of cleaning the pile from these residues and sludge are cleaning pocket [5] and airlifting [6], which are widely used methods. In this study, the cleaning pocket method, and a new method (recycling system) were used to clean the piles to determine their effect on the bearing capacity of the piles. The cleaning pocket method includes lowering a pocket with smooth ends to collect the drilling residues from the pile body after the drilling is completed.

The authors found that studies related to the recycling system are almost non-existent, as previous researchers did not deal with this process. Hence, the lack of research on this topic made the results of this study independent, and there is no possibility of comparing it with any previously published results. The recycling system (de-sanding) is a non-traditional method that relies on pumping fresh bentonite from the top of the pile and withdrawing it from the bottom of the pile by an integrated system to obtain an impurity-free pile body before starting the concrete casting process [7], as shown in Fig. 1.

The aim of this investigation was to assess the influence of the recycling system on improving the bearing capacity of bored piles. The impact of the thickness of the filter cake, soil type, L/D and the separation between the friction and end-bearing pile capacity on the behavior of the bored piles when using this technique were evaluated.

Figure 1. The recycling system used in situ.

2. Methods

The proposed site lies on area number (173/23 m 30) within Al-Muthana airport land in Baghdad. From a geological point of view, the investigated area is located on the Mesopotamian plain zone within the unstable shelf region according to the tectonic division of Iraq [8]. The field test showed that the soil profile consists mainly of the following layers: the uppermost layer (0–8.5 m) is classified as cohesive soil, and the second layer below the top layer consists of cohesionless soil. This layer consists mainly of brown to Gray-black sand/silty sand with fine gravel and/or gravel with sand. Table 1 shows the in-situ soil properties obtained using the standard penetration test (SPT).

Table 1. The soil parameters.

Geotechnical parameters	1st Layer (0–8.5 m)	2nd Layer (8.5–14 m)	3rd Layer (14–17 m)	4th Layer (17–35 m)
Cohesion (C) (kPa)	39	0	110	0
Angle of internal friction (Ø)	1.5	31.5	4.5	40
γ dry (kN/m^3)	15	15.5	16	16.5
γ sat (kN/m^3)	19.2	18.8	20.0	19.8
e_o	0.75	0.5	0.7	0.5
Soil classification	CL – CH	SC – SM	CH	SM – SW
μ*	0.4	0.3	0.4	0.3
E (kN/m^2) ×	12480	25500	21440	48500
G (kN/m^2) ×	4457.14	9807.69	7657.14	18653.85
LL	53	–	49	–
PL	28	–	26	–

* Poisson's ratio is extracted based on [9, 10].
× The elastic and shear modulus calculated by SPT N-values, based on [9, 11].

Full-scale models were conducted on two groups of piles. The first group was constructed without using the recycling system, and the second group was constructed using it. In addition to the construction of full-scale models in the field, forty-one models were modeled in the PLAXIS-3D program, which is a finite element package specifically developed for the analysis of deformation, stability, and flows in geotechnical engineering projects [12]. Construction of bored piles with bentonite liquid reduces the bearing capacity of the piles because it forms a layer called (filter cake), this layer leads to a decrease in the adhesion between the soil and the pile [13]. Therefore, the research methodology can be divided into two main parts: field study and theoretical study, as shown in Fig. 2.

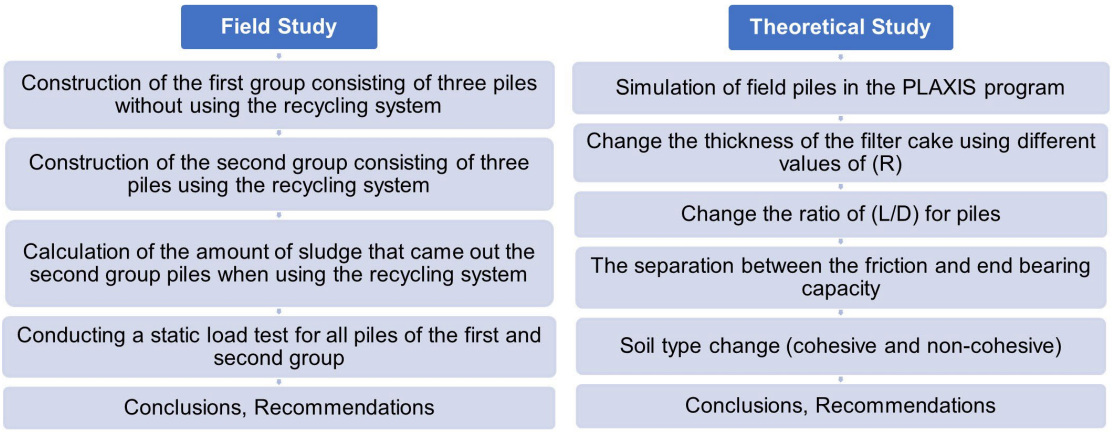

Figure 2. The flowchart of field and theoretical study.

2.1. Field Study

Many methods are used to construct bored piles. One of these methods is to use the casing to support the soil close to the surface and prevent it from collapsing [14]. Depending on the soil investigation, the casing method was used to construct the piles in this study. Six piles were identified for this study; the first group of piles was B1, B2, and B3 with a diameter of 1.2 m and the length of the piles was 25, 30, and 30 m, respectively, and were carried out for a period ranging from 5.5 to 8 h, and the piles were cleaned from the residues and drilling sludge by the cleaning pocket method [5]. The working load was 400 tons for the first pile B1 and 360 tons for the second and third piles B2 and B3. The second group of piles was selected using the recycling system B4, B5, and B6 with a diameter of 1.2 m and a working load of 360 tons. The length of the piles was 25, 30, and 30 m, respectively, which were carried out for a period ranging from 8 to 9 h. The six piles were constructed in the same zone, so the groundwater level at the time of construction was 2.8–3 m.

The control of the properties of the bentonite liquid is one of the most important factors that help to complete its tasks correctly [15], so the six piles were drilled with the same type of bentonite (sodium bentonite) and its properties were kept close during the construction. Table 2 shows the dimensions, working conditions, and properties of the bentonite used for each pile.

Table 2. The dimensions, working, and properties of the bentonite used for each pile.

Pile No.	Pile diameter (m)	Pile length (m)	Working load (ton)	Density (mg./ml)	Viscosity (sec.)	pH	Sand content (%)
				In (during boring)			
B1	1.2	25	400	1.065	48	9.5	0.6
B2	1.2	30	360	1.075	49	9.5	0.6
B3	1.2	30	360	1.065	45	10	0.6
B4	1.2	25	360	1.075	50	10	0.8
B5	1.2	30	360	1.08	50	10	1
B6	1.2	30	360	1.07	45	9.5	0.6
				Out (after use the recycling system) after boring			
B1	1.2	25	360	–	–	–	–
B2	1.2	30	360	–	–	–	–
B3	1.2	30	360	–	–	–	–
B4	1.2	25	360	1.08	40	9	2
B5	1.2	30	360	1.09	42	9.5	3.5
B6	1.2	30	360	1.08	39	9	1.5

2.1.1. Recycling system (de-sanding)

The main objective of the recycling system is to get rid of impurities and drilling residues during pile construction, thus preserving the pile from geotechnical defects. Cleaning and recirculating the bentonite slurry includes removing sludge and sand from the drilled hole using cleaning equipment and returning the cleansed slurry [16]. This method was used from the same mechanism as the bentonite cleaning system that comes out during the pouring of the pile [17], but the system was used to withdraw the bentonite that contains impurities and drilling sludge before casting the pile. After the steel cage is installed in the hole,

the tremie tube is inserted into the hole, leaving a small gap between the bottom of the hole and the tremie tube between 25 and 30 cm. The tremie tube is connected from the top with a suction pump (dewatering pump) with a capacity of 350 m^3/hr., as shown in Fig. 3, to withdraw the bentonite from the bottom of the hole. Then, the outside of the pump is connected to a de-sander with a capacity of 2500 HP, as shown in Fig. 4.

To determine the amount of sludge and sand that came out from the piles using the recycling system, three containers were manufactured with dimensions 2, 1.25, and 1 m, as shown in Fig. 5.

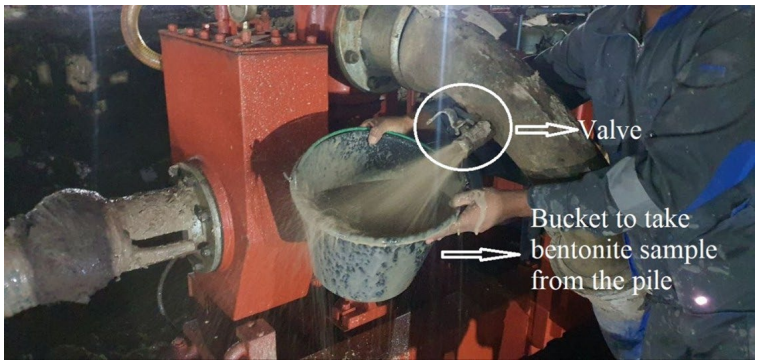

Figure 3. Bentonite sample coming out of the pile in-situ.

Figure 4. Filter sand and sludge by desander in-situ.

Figure 5. Collect sludge and sand in-container.

2.1.2. Static load test

There are several methods for determining the bearing capacity of a pile, and the static load test is one of the most important field tests [18]. The static load test was conducted after 28 days of casting the piles according to ASTM D1143 (2007) [19]. The allowable load Qa was taken as equal to two thirds of the final load, which causes a total settlement of 12 mm or a net (plastic) settlement of 6 mm [20]. The specification states that the axial pressure load to be applied to the pile shall be increased by 10 % to accommodate the increase in load required during the test [21]. The objective of the test is to determine the pile's bearing capacity during one cycle of loading and unloading [22], where the pile is loaded to two

times the design load and at a rate of eight load increments (one hour for each load) sustaining the load for at least 12 h, and then the load is lowered at a rate of four times (1 h for each unload), as shown in Fig. 6. Figs. 7–12 show the load-settlement curve for the piles after the static load test.

Figure 6. Static load test in-situ.

2.2. Theoretical Study

The PLAXIS-3D program has been used to find several parameters and knows the extent of their impact on the bearing capacity of the piles, and to determine the program's validity, six piles TR1, TR2, TR3, TR4, TR5, and TR6 were modeled in the PLAXIS program for comparison with those from the field [23]. To model the bored piles in the PLAXIS-3D program, knowledge of the soil parameters, groundwater level, pile dimensions, and the type of analysis is required [24]. The More–Coulomb model was chosen to model the soil parameters because it is closer to reality and requires fewer soil parameters [25]. To model concrete in the PLAXIS program, one must know the modulus of elasticity, Poisson's ratio, and density. Therefore, the modulus of elasticity ranges between 25 and 30 GPa, Poisson's ratio is between 0.15 and 0.25, and density is 25 kN/m^3. In this study, the density of the concrete was 25 kN/m^3, the modulus of elasticity was 30 GPa, Poisson's ratio was 0.2, and the (non-porous) property was selected [8]. Because the groundwater level when construction of the test piles was 2.8–3 m, the worst case of the groundwater level was chosen, which was 2.8 m, to model the piles.

The drainage type for the soil in the PLAXIS program is essential; therefore, the undrained type was chosen for clayey soil and the drained type for sandy soil [8]. In this study, the amount of settlement will be given and the ultimate load that the pile can bear at reaching a total settlement of 25 mm (failure). Figs. 7–12 show the results of the comparison between field tests and those resulting from the program.

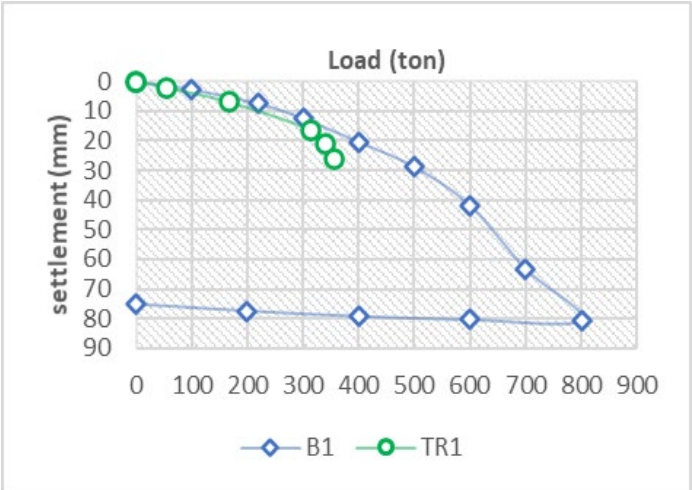

Figure 7. Load – settlement curve for B1&TR1.

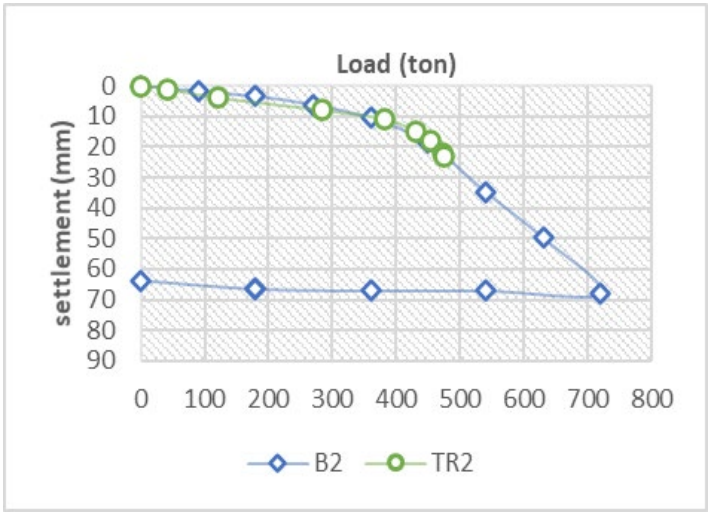

Figure 8. Load – settlement curve for B2&TR2.

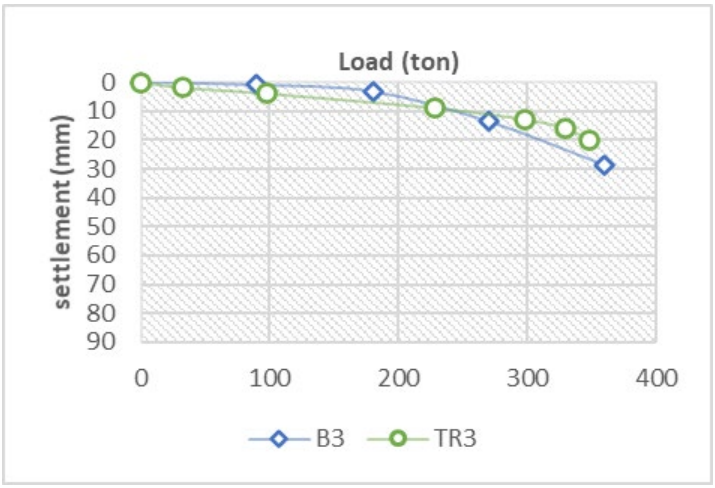

Figure 9. Load – settlement curve for B3&TR3.

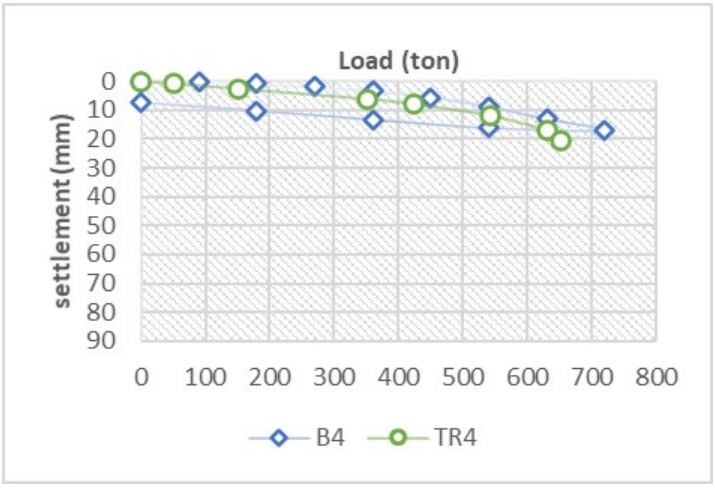

Figure 10. Load – settlement curve for B4&TR4.

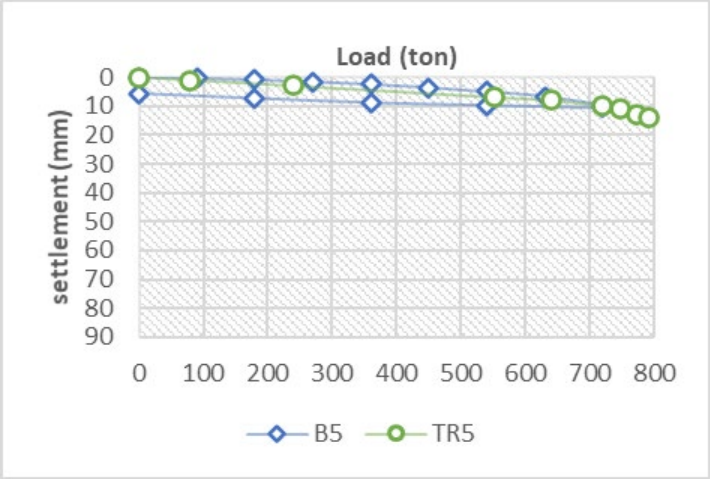

Figure 11. Load – settlement curve for B5&TR5.

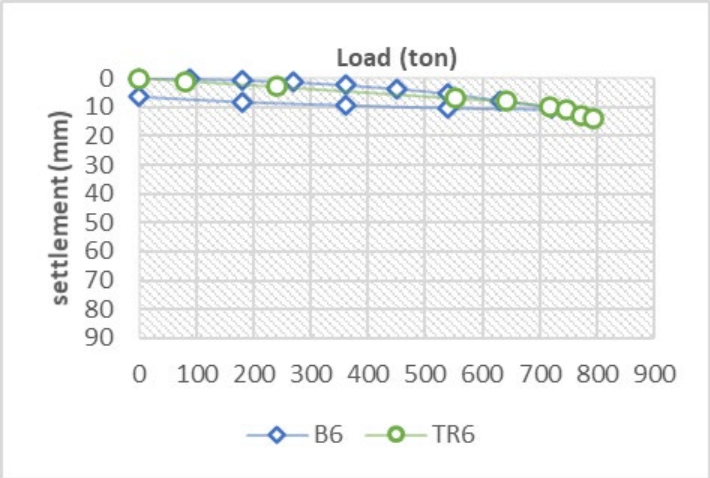

Figure 12. Load – settlement curve for B6&TR6.

2.2.1. Thickness of filter cake

Two piles were modeled with diameters equal to 1.2 m, and lengths equal to 25 and 30 m. In the normal case, the program uses an R = 1, where R is an interface coefficient (friction coefficient), which means that no parameters related to the pile or soil are reduced (full attachment between the pile and soil). Because field piles are constructed using bentonite liquid, there must be a reduction in the friction coefficient between the soil and the pile because bentonite leads to the formation of a filter cake or an insulating layer between the pile body and soil [13]. This layer of the filter cake cannot be handled by the program by giving a specific thickness such as 1, 2, 3 mm, etc., so the only way is to manipulate the R value that simulates the thickness of this layer. Therefore, different values of the interface coefficient R (1, 0.95, 0.9, 0.85, 0.8, 0.75, 0.7, 0.65, 0.6, 0.55) were used to achieve a real simulation of the piles that were constructed using the recycling system and those that were constructed without using this system. As a result of using different values of R, a new value must be extracted for each of the parameters (cohesion C, angle of internal friction Ø, Young's modulus E, and shear modulus G), the Equations (1–4) used to find the parameters above [12]:

$$C_i = R_i \times C; \tag{1}$$

$$\varnothing_i = \tanh^{-1}\left(R_i \tan \varnothing\right); \tag{2}$$

$$G_i = R_i^2 \times G; \tag{3}$$

$$E_{oed} = 2G_i \times \frac{1-\mu}{1-2\mu}. \tag{4}$$

2.2.2. Type of soil

To determine the efficiency of the recycling process on different types of soil, two types of soil were selected: clay and sand. Table 3 shows the properties of these soils, where piles of 15 m in length and 1.2 m in diameter were modeled. The symbols are as follows:

TC1 refers to the pile modeled in clay soil using the recycling system;

TC2 refers to the pile modeled in clay soil without using the recycling system;

TC3 refers to the pile modeled in sandy soil using the recycling system;

TC4 refers to the pile modeled in sandy soil without using this system.

Table 3. Soil properties used to model the piles at different soil types.

Geotechnical parameters	Clay (0–16 m)	Sand (0–16 m)
Cohesion (C) (kPa)	39	0
Angle of internal friction (Ø)	1.5	31.5
γ dry (kN/m^3)	15	15.5
γ sat (kN/m^3)	19.2	18.8
Soil classification	CL – CH	SC – SM
μ	0.4	0.3
E (kN/m^2)	12480	25500
G (kN/m^2)	4457.14	9807.69

2.2.3. L/D ratio

Because the piles constructed in the field were of different lengths 25 and 30 m, but the pile diameter of 1.2 m did not change, the length of the piles will be fixed, and the pile diameter will be changed to 1.5, 1.4, 1, and 0.8 m. To determine the effectiveness of the recycling process and its effect on the bearing capacity of the piles when the L/D ratio was changed, 16 piles were modeled in the PLAXIS program, as shown in Table 4.

Table 4. Details of piles at different value of L/D.

Pile No.	R	Length (m)	Diameter (m)	Modelling method
TD1	0.95	25	1.5	De-sanding
TD2	0.95	25	1.4	De-sanding
TD3	0.95	25	1	De-sanding
TD4	0.95	25	0.8	De-sanding
TD5	0.95	30	1.5	De-sanding
TD6	0.95	30	1.4	De-sanding
TD7	0.95	30	1	De-sanding
TD8	0.95	30	0.8	De-sanding
TD9	0.65	25	1.5	Without de-sanding
TD10	0.65	25	1.4	Without de-sanding
TD11	0.65	25	1	Without de-sanding
TD12	0.65	25	0.8	Without de-sanding
TD13	0.65	30	1.5	Without de-sanding
TD14	0.65	30	1.4	Without de-sanding
TD15	0.65	30	1	Without de-sanding
TD16	0.65	30	0.8	Without de-sanding

2.2.4. Separation between the friction and end bearing

To separate the bearing capacity in relation to the friction and end bearing for the piles that used the recycling system in their construction, two groups of piles were modeled. The first group (TF1, TF2, and TF3) was modeled using a recycling system for the interface between the pile and the soil and a non-recycling system for the interface between the base of the pile and side soil (to neglect the end bearing capacity or reduce it as much as possible because it was not cleaned well). In the second group (TF4, TF5, and TF6), these piles were modeled as tension piles, where the piles were modeled using a recycling system to determine the friction capacity of the pile, as shown in Table 5.

After modeling the previous six piles TF1–TF6, it was noted that the difference between the friction capacity when using the pile modeling method as tension piles and as the recycling system was used for the interface between the pile and the soil and the non-recycling system was used for the interface between the base of the pile and side soil was very close. Therefore, the method of tension piles was adopted to determine the friction capacity of the TF1-A, TF2-A, and TF3-A piles when the recycling system was not used in its construction, as shown in Table 5.

Table 5. The details of piles TF1–TF6 and TF1-A–TF2-A.

Pile No.	Pile length (m)	Pile diameter (m)	Modelling method
TF1	25	1.2	As (R = 0.95) for side interface and (R = 0.65) for end pile interface
TF2	30	1.2	As (R = 0.95) for side interface and (R = 0.65) for end pile interface
TF3	30	1.2	As (R = 0.95) for side interface and (R = 0.65) for end pile interface
TF4	25	1.2	As a tension pile
TF5	30	1.2	As a tension pile
TF6	30	1.2	As a tension pile
TF1-A	25	1.2	As a tension pile
TF2-A	30	1.2	As a tension pile
TF3-A	30	1.2	As a tension pile

3. Results and Discussion

After constructing the field piles and modeling them in the PLAXIS program, the following results were obtained:

1. The quantities of sludge and sand that emerged from the second group of test piles in the field B4, B5, and B6 during the recycling process were calculated using containers with dimensions of 1, 1.25, and 2 m, as shown in Table 6. Based on the sieve analysis, the sample was black poorly sand, as shown in Fig. 13. The amount of sand and sludge that came out of the second group piles B4, B5, and B6 using the recycling system is very large, where it was noted that the average quantity was approximately 0.08 m^3 for each cubic meter of the pile body. Since the quantities were 2–2.45 m^3 and based on the wet density of the poorly sand that came out from the piles was 16.12 kN/m^3, the wet weight of these quantities ranges from 3224 to 3949 kg, so there is no doubt that these quantities cause the first group of piles to fail or to obtain a low bearing capacity when it remains inside the hole before pouring.

Table 6. Quantities of sludge and sand.

Pile No.	Depth of sludge in container (m)	Vol. of sludge (m^3)	Vol. of pile (m^3)	Percentage of sludge in pile (per m^3)
B4	0.8	2	24.87*	0.08
B5	0.98	2.45	30.52*	0.080
B6	0.93	2.325	30.52*	0.076

* The size of the pile, depending on the length of the pile, is equal to 22 m (25 m – the length of the casing embedded in the soil (3 m)).

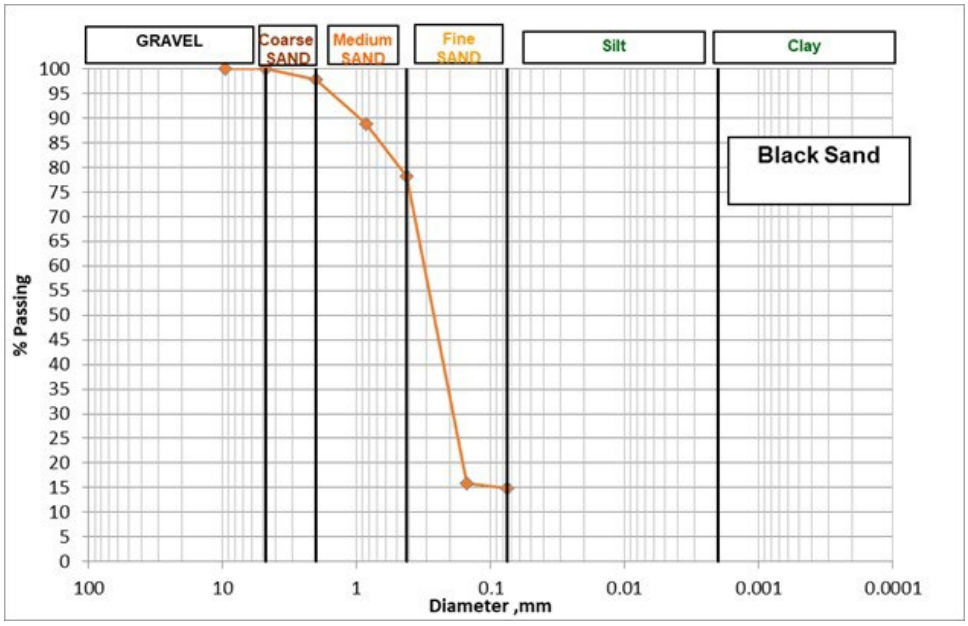

Figure 13. Sieve analysis of the sludge and sand that came out from the piles.

2. After conducting the static load test for the six field piles B1–B6, the allowable load was obtained, as shown in Table 7. After testing the first pile B1 and its failure, the working load of the second pile B2 was reduced to 360 tons in the hope of obtaining less settlement, but also failed and settlement of 12 mm was not reached when loading the fourth and fifth piles B4 and B5 when loading 200 %, so the last load was taken to find the bearing capacity of the pile. The use of the recycling system reduced the reduction in the bearing capacity of the piles to only 5 % when using an R value equal to 0.95. This means that the thickness of the filter cake layer on the sides of the pile and the thickness of the sludge layer at the base of the pile was the least possible because this system helped to get rid of large quantities of sludge and sand that were inside the pile. When the recycling system is not used, the bearing capacity of the piles reduces from 35 to 45 % when using an R value equal to 0.65–0.55. This means that the difference between using the recycling system and not using it is 30–40 % of the bearing capacity of the pile.

Table 7. Simulation of field piles in the PLAXIS program by changing R value.

Load from field (static load test)			
Pile No.		**Final load at 12 mm (ton)**	**Allowable load (ton)**
B1		290	193
B2		369	246
B3		260	173
B4		600	400
B5		720	480
B6		720	480
Load from PLAXIS			
Pile No.	**R**	**Final load at 12 mm (ton)**	**Allowable load (ton)**
TR1	0.65	263	175
TR2	0.65	392	261
TR3	0.55	282	188
TR4	0.95	561	374
TR5	0.95	759	506
TR6	0.95	759	506

3. After modeling different values of R, it was concluded that the bearing capacity of the piles at a value of R equal to 0.95 is similar to the bearing capacity of the piles when using the recycling system, and that the bearing capacity of the piles at a value of R close to 0.65 is similar to the

bearing value of the piles that were not used the recycling system during construction, as shown in Table 7. Therefore, the value of R at 0.95 will be fixed to simulate the constructed piles using the recycling system in modeling the piles that will change in type of soil, L/D ratio, and separation between the friction and end bearing. The value of the reduction in the third pile R was 45 % (R = 0.55), so this value was neglected and the value of R = 0.65 was relied on when referring to the non-use of the recycling system.

4. The bearing capacity of the piles was calculated for each ratio of L/D using the recycling system and without it, and the results showed the efficiency of the recycling process in large piles. Figs. 14–17 show the Load–Settlement curve for each group of piles. The improvement rate (the ratio of increase in pile bearing capacity) of the pile increases when L/D is lower, which means that the recycling system is more effective in large piles. Therefore, it cannot give a specific percentage of the optimum value for the improvement rate, but it can be said that the efficiency of the recycling process increases directly when the diameter and length of the bored pile increase because that increase in the diameter and length of the pile (side friction and end bearing) leads to a higher bearing capacity. In addition, increasing the diameter of the piles from 1.2 to 1.5 m and without using the recycling system does not lead to a real increase in the pile-bearing capacity.

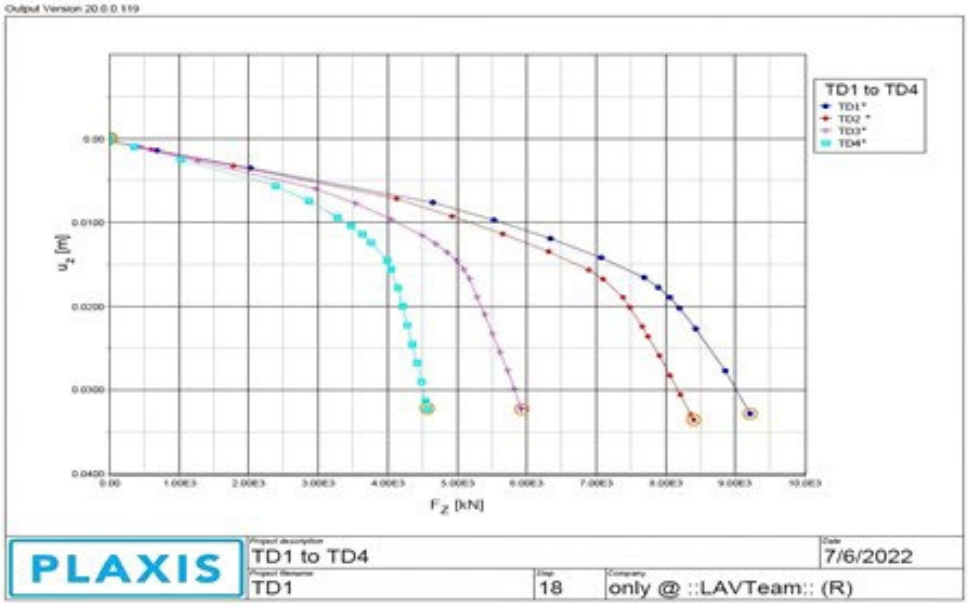

Figure 14. Load (FZ) – Settlement (UZ) curve for TD1–TD4.

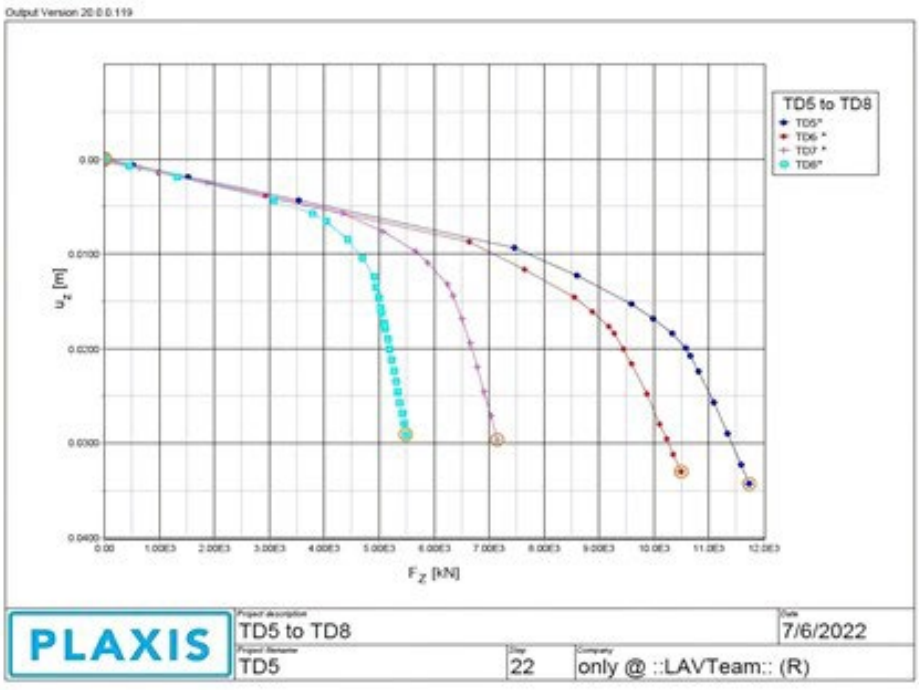

Figure 15. Load (FZ) – Settlement (UZ) curve for TD5–TD8.

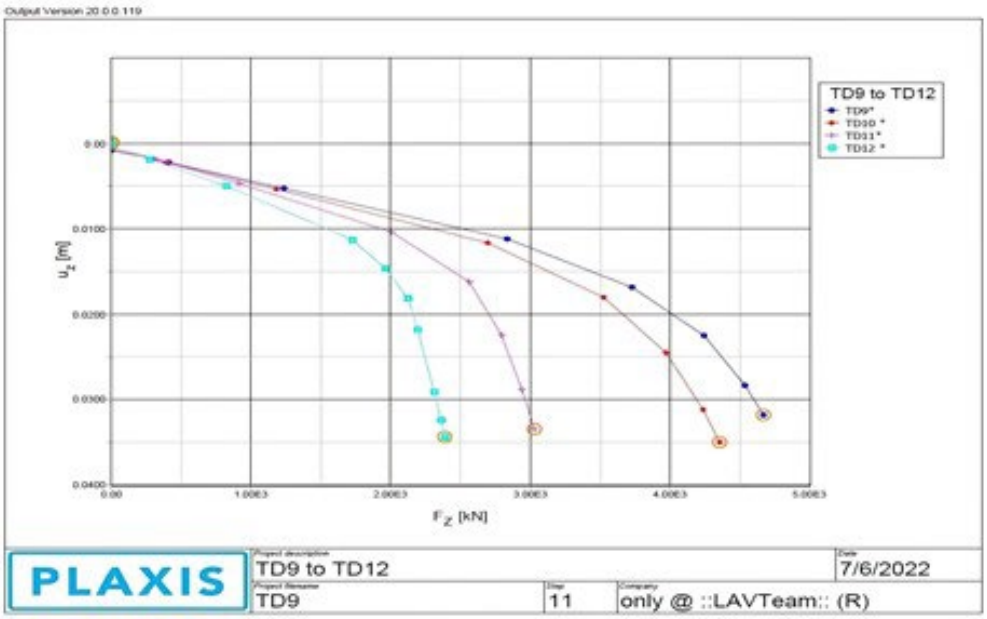

Figure 16. Load (FZ) – Settlement (UZ) curve for TD9–TD12.

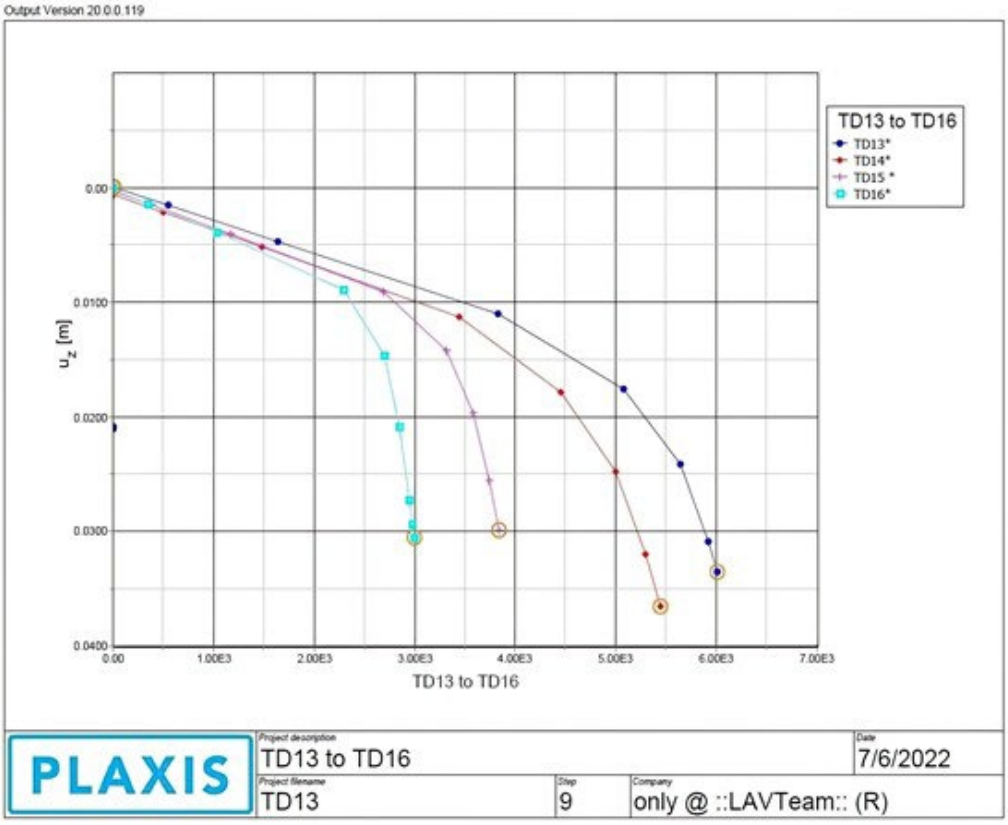

Figure 17. Load (F_Z) – Settlement (U_Z) curve for TD13–TD16.

5. After modeling the piles in clay and sandy soils, as shown in Table 8, it was observed that the use of the recycling system led to a close bearing capacity of the piles in both soils, where the allowable bearing capacity of the pile in the clay soil TC1 was 190 tons and the allowable bearing capacity of the pile in the sandy soil TC3 was 211.5 tons, which is an additional indicator of the efficiency of that process. It was also noted that the non-use of the recycling system led to a lower allowable bearing capacity for the pile in sandy soil TC4 than that of the pile TC2 in clay soil. As shown in Table 8, the difference in the improvement ratio between the piles in clay and sandy soils is 38 and 65 %, respectively, indicating that the efficiency of the recycling process in sandy soils is higher.

Table 8. Details and bearing capacity of TC1–TC4 piles.

Pile No.	R	Soil	Load from PLAXIS		
			Allowable load (ton)	Diff. (ton)	Improvement ratio %
TC1	0.95	Clay	127	49	38
TC2	0.65	Clay	78		
TC3	0.95	Sand	141	92	65
`TC4	0.65	Sand	49		

6. It was noted that the improvement in the bearing capacity of the pile with respect to friction ranged from 60 to 64 %, while the bearing capacity of the end bearing ranged from 85 to 98 %, as shown in Table 9, and the pile bearing capacity relative to the end bearing when not using the recycling system in pile with length 25 m and diameter 1.2 m was close to zero, and 15 % for the pile with length 30 m and diameter 1.2 m compared with the recycling system, which means that using the recycling system indicates that the effectiveness of this system is very active in cleaning the pile.

Table 9. Bearing capacity of piles from static load test and PLAXIS to TF1-A–TF3-A with B1–B3.

Load from field (static load test)			Friction capacity from PLAXIS			
Pile No.	Final load at 12 mm (ton)	Allowable load (ton)	Pile No.	Final load at 12 mm (ton)	Allowable friction capacity (ton)	End bearing capacity (ton)
TR1	263	175	TF1-A	260*	173	2
TR2	392	261	TF2-A	370*	247	14
TR3	282	188	TF3-A	255*	170	18

* Final load at modeling the piles as tension piles.

4. Conclusions

The most important results obtained from this study can be summarized as follows:

1. Using this system leads to a noticeable increase in the bearing capacity of the piles by about 50 % compared to not using it.
2. Using this system is very effective in obtaining a pile free of impurities and, in turn, will prevent pile failure because of not extracting all the sand and sludge while they are constructed.
3. The casting time for the piles that used the recycling system was about half an hour less than the piles that did not use it, and the amount of concrete was large, with an average of 2 m^3.
4. Using this system reduces the pile length by 15 % or more from the assumed pile length, according to design, which leads to reducing implementation costs.
5. The efficiency of the recycling system is increased, as the L/D value decreases.
6. The efficiency of the recycling system in sandy soils is higher than that of clay soils by about 27 %.
7. The pile bearing capacity was improved by 60–64 % and 85–98 % for friction and end bearing, respectively, when the recycling system was used.

References

1. Chandrasekaran, V., Garg, K.G., Prakash, C. Behaviour of Isolated Bored Enlarged Base Pile Under Sustained Vertical Loads. Soils and Foundations. 1978. 18(2). Pp. 1–15. DOI: 10.3208/sandf1972.18.2_1
2. Goudar, S., Kamatagi, A. An Experimental Evaluation of Axial Load Bearing Capacity of Belled and Straight Piles Embedded in Sand. International Journal of Engineering. 2022. 35(8). Pp. 1599–1607. DOI: 10.5829/ije.2022.35.08b.16
3. Al-Saidi, A.A., Al-Mosawe, M.j., Al-Shakarchi, Y.A.-S. Behavior of Defective Cast in Place Piles. Journal of Engineering. 2021. 27(4). Pp. 96–117. DOI: 10.31026/j.eng.2021.04.08
4. Al-Mosawe, M., Al-Shakarchi, Y., Al-Saidi, A. Influence of Defect in the Concrete Piles Using Non-Destructive Testing. Journal of Engineering. 2006. 12 (3). Pp. 1804-1816. DOI: 10.31026/j.eng.2006.03.14
5. Chong, W.L., Le, X., Rex, S. Base cleanliness of bored piles revisited–a case study. 13th Australia – New Zealand Conference on Geomechanics. Perth Convention and Exhibition Centre. Perth, 2019.
6. Lam, C., Jefferis, S.A., Suckling, T.P. Construction techniques for bored piling in sand using polymer fluids. Proceedings of the Institution of Civil Engineers: Geotechnical Engineering. 2014. 167(6). Pp. 565–573. DOI: 10.1680/geng.13.00128
7. Hasan, H.N., Al-Saidi, A.H. Evaluation of the Influence of De-sanding (Recycling System) Process on the Pile Bearing Capacity Using Full Scale Models. Journal of Engineering. 2022. 28(12). Pp. 80–92. DOI: 10.31026/j.eng.2022.12.06

8. Yahia, H.M. Soils and Soil Conditions in Sediments of the Ramadi Province (Iraq), Their Genesis, Salinity, Improvement and Use-Potential. University of Amsterdam. Amsterdam, 1971. 144 p.
9. Bowles, J.E. Foundation Analysis and Design. 5th edn. The McGraw-Hill Companies, Inc. New York, 1988. 1241 p.
10. PLAXIS. CONNECT Edition V21.01. PLAXIS 3D – Tutorial Manual. Bentley, 2021. 255 p.
11. Das, B.M., Sivakugan, N. Principles of Foundation Engineering. 9th edn. Cengage Learning, 2018. 944 p.
12. PLAXIS. CONNECT Edition V21.01. PLAXIS 3D – Reference Manual. Bentley, 2021. 576 p.
13. Federation of Piling Specialists. Federation of Piling Specialists. Bentonite Support Fluids in Civil Engineering. 2nd edn. FPS, 2006. 13 p.
14. Das, B.M., Sivakugan, N. Introduction to Geotechnical Engineering. Cengage Learning, 2015. 448 p.
15. Ibrahim, A.S., Al-bidry, M.A. Study the Effect of Particle Sizes and Concentration on the Rheological Properties of Iraqi Bentonite for Using as Drilling Fluids. Journal of Engineering. 2020. 26(3). Pp. 65–76. DOI: 10.31026/j.eng.2020.03.06
16. Department of Petroleum Engineering. PETE 203: Drilling Engineering: Laboratory Manual. King Fahd University of Petroleum & Minerals, 2003. 98 p.
17. Lam, C., Jefferis, S.A., Suckling, T.P. Treatment of bentonite fluid for excavation into Chalk. Proceedings of the Institution of Civil Engineers: Geotechnical Engineering. 2018. 171(6). Pp. 518–529. DOI: 10.1680/jgeen.18.00043
18. Shooshpasha, I., Mola-Abasia, H., Amiri, I. Evaluation of Static and Dynamic Methods for Determining the Bearing Capacity of the Driven Pipe Piles. International Journal of Engineering. 2014. 27(2). Pp. 307–314. DOI: 10.5829/idosi.ije.2014.27.02b.15
19. ASTM D1143/D1143M-2007 (R 2013). Standard Test Methods for Deep Foundations Under Static Axial Tensile Load ASTM International. West Conshohocken, PA, 2013. 15 p.
20. Murthy, V.N.S. Advanced Foundation Engineering. CBS Publishers & Distributors, 2007 795 p.
21. Astm, A.S.T.M., 2020. D1143/D1143M-20: Standard Test Methods for Deep Foundation Elements Under Static Axial Compressive Load. *West Conshohocken, PA, USA: ASTM International*.
22. Wrana, B., 2015. Pile load capacity–calculation methods. Studia Geotechnica et Mechanica, 37(4), Pp.83-93.
23. Bowers, J.T., Webb, M.C. and Beaver, J.L., 2019. Soil parameters for design with the 3D PLAXIS hardening soil model. *Transportation Research Record*, *2673*(10), pp.708-713.
24. Elkhawas, E.N.M., 2021. *ANALYSIS AND ASSESSMENT OF OFFSHORE PILES* (Doctoral dissertation, Zagazig University).
25. Brinkgreve, R.B., 2005. Selection of soil models and parameters for geotechnical engineering application. In Soil constitutive models: Evaluation, selection, and calibration (pp. 69-98).

Information about the authors:

Haider Hasan,
ORCID: https://orcid.org/0000-0002-7703-0756,
E-mail: hayder.hasan2001m@coeng.uobaghdad.edu.iq

A'amal Al-Saidi,
E-mail: dr.aamal.al-saidi@coeng.uobaghdad.edu.iq

Received 11.02.2023. Approved after reviewing 05.11.2025. Accepted 05.11.2025.

Magazine of Civil Engineering

ISSN 2712-8172

journal homepage: http://engstroy.spbstu.ru/

Research article

UDC 666.97

DOI: 10.34910/MCE.140.5

Multiphasic modeling of hydration degree for blended cement pastes by using calorimetry method

T.D. Nguyen , ***V.L. Tang*** ✉

Hanoi University of Mining and Geology (HUMG), Hanoi, Vietnam

✉ *lamvantang@gmail.com*

Keywords: Multiphasic model, hydration degree, cement paste, mineral additives.

Abstract. The evolution of the mechanical properties of concrete depends greatly on the hydration of the component binders such as cement and mineral additives. However, the prediction of the hydration degree of these binders is extremely difficult due to the complex physic-chemical mechanisms at the molecular level. In this article, the author proposes to use a multiphasic model that considers hydration development and chemical interaction between reactions while taking into account temperature and water content effects on reaction kinetics. The main goal of this study is a semi-adiabatic calorimetry test was applied to determine the input parameters by measuring the heat release during hydration. Based on the test results shown the application of three cases of blended cement paste samples is considered to show the efficiency of the model. Overall, thermogravimetric analyses and its derivative are applied to verify the delay effect of pozzolanic reactions on the hydration degree induced by portlandite content in the paste.

Citation: Nguyen, T.D., Tang, V.L. Multiphasic modeling of hydration degree for blended cement pastes by using calorimetry method. Magazine of Civil Engineering. 2025. 18(8). Article no. 14005. DOI: 10.34910/MCE.140.5

1. Introduction

Cement hydration is a process that consumes water and releases heat, accompanied by complex thermo-hydric mechanism of multiphases [1–3]. This process has important influence on the formation and evolution of the mechanical properties of cement paste at early age. However, the prediction of hydration degree and its evolution is extremely difficult due to the complex reaction mechanisms at the molecular level, especially when the paste contains some mineral additives (silica fume (SF), fly ash (FA), slag, etc.). In addition, the experiments that measure these quantities requires the modern and expensive equipment [4–6]. In order to resolve these difficulties, the numerical models are proposed to predict the evolution of hydration degree as well as the mechanical properties of cement mortar [7–18]. Several models that using separate global laws for the reactions of clinker and additions [11, 12, 14] reproduce the combined hydrations of these species but do not take account of the effect of water content on hydration. However, this effect explicitly cannot be neglected for a realistic prevision of mortar hydration in a structure. Some other authors report this essential effect and propose models coupling hydration development and water content variation in structures [17–19] as well as integration of hydration laws for mineral additions [15, 16], but this asymptotic approach cannot take account of the desiccation or rehydration effects during hydration. Wang and Lee [6, 7] proposed a shrinking-core model which considers the influences of the water/cement (W/C) ratio, cement compound compositions, and capillary water contents to simulate blended cement hydration. In this hydration model, the reaction of FA and slag is separated from that of cement hydration by considering the production/consumption of portlandite in cement paste. A similar approach to treat the reaction of slag separately from that of cement hydration is also proposed in [8]. The hydration of FA in blended cement is studied by Kinomura and Ishida [9, 10] who considering morphology and intrinsic properties of precipitated C-S-H gels due to pozzolanic reactions. An extensive modeling for continuous

hydration in pozzolanic micro-pore structures to consider the slow-down reaction is also proposed in that model.

In this article, the authors propose using an effort multiphasic model proposed by Lacarrière [1, 5] to predict the hydration degree of the blinder composed. This modeling considers hydration development and chemical interaction between reactions. It also takes into account temperature and water content effects on reaction kinetics through thermal and hydric activation. The input parameters of the model are determined based on the chemical analysis of cement and mineral additives as well as the measuring of heat hydration by using Langavant calorimeter [18, 19]. The model is tested for the pure cement and blended cement paste (with FA and SF additives). Thermogravimetric analyses (TGA) and its derivative (DTG) are also applied to verify the delay effect of pozzolanic reactions on hydration degree induced by portlandite content in the paste.

2. Methods

2.1. Hydration Degree and Multiphasic Modeling of Hydration

In the frame of hydration kinetics, the hydration of cement as well as mineral additives is a process that consumes water and releases heat, accompanied by heat and water balance mechanisms between phases. The variation of water content and temperature inside the cement mortar during hydration affect the dynamic hydration process of the component phases (hydro activity and thermal activity). Thus, the multiphasic model of hydration should be established based on the equations, which describing the development of hydration degree, water content, and temperature. A delaying parameter is also added in the case of secondary reactions such as pozzolanic ones when we consider the hydration of a binder composed. It depends on the amounts of some primary reaction products (such as portlandite for pozzolanic reactions).

According to [1, 5], the equation describing the development law of the degree of hydration is proposed as a function of the influence coefficients as follows:

$$\alpha_i = A_i \times c_i\left(\alpha_i, W\right) \times \prod_i\left(\overline{r_{mi}}\right) \times h_i\left(T\right) \times g_i, \tag{1}$$

where:

- α_i is the degree of hydration of anhydrous phase "i" (clinker or additives), which refers to the development of chemical reactions between clinker, pozzolanic or mineral additions, and water. This variable is defined as the mass of anhydrous substance, which has reacted per unit volume divided by the initial mass, or indirectly by the ratio of heat release during the hydration and the maximal heat released when mortar completely hydrated.
- A_i is a fitting parameter linked to the acceleration of the reaction kinetics due to supersaturation, which determined by experiment of Langavant calorimeter.
- $c_i\left(\alpha_i, W\right)$ is chemical activation:

$$c_i\left(\alpha_i, W\right) = \frac{V_{Andiss_i}}{V_W} = \frac{\alpha_i \times \dfrac{m_{An_i}}{\rho_{An_i}}}{V_W}, \tag{2}$$

where: V_W is initial volume of water; m_{An_i} is initial mass of anhydrous phase "i"; ρ_{An_i} is anhydrous density of phase "i"; V_{Andiss_i} is volumetric concentration in paste of dissolved anhydrous phase "i".

- $h_i\left(T\right)$ is thermal activation:

$$h_i\left(T\right) = \exp\left(\frac{E_{a_i}}{R \times T}\right), \tag{3}$$

where: E_{a_i} is the activation energy of phase "i"; R is the gas constant (8,314 J/mol.K).

- $\prod_i\left(\overline{r_{mi}}\right)$ is hydration function, which models the water accessibility to anhydrous phases:

$$\prod_i\left(\overline{r_{mi}}\right)=\exp\left(B_i\times r_{mi}^{n_i}\right), \tag{4}$$

where: B_i and n_i are fitting parameters, which determined by Langavant experiment; $\overline{r_{mi}}$ is a function (i.e., dissolution radius) of water content, porosity and solid phases in the paste:

$$\overline{r_{mi}}=\frac{C_{P\,hydr_i}\times\frac{1}{\Phi_P}}{C_{P\,anh_i}\times W_P}. \tag{5}$$

In which, W_P is the volumetric concentration of water in the paste; Φ_P is porosity of paste; $C_{P\,hydr_i}$ is the volumetric concentration of hydrate produced from grains of phase "i"; $C_{P\,anh_i}$ is anhydrous volumetric concentration in paste:

$$\Phi_P=1-\sum_i\left(C_{P\,hydr_i}+C_{P\,anh_i}\right); \tag{6}$$

$$C_{P\,hydr_i}=R_i\times\alpha_i\times\frac{m_{An_i}}{\rho_{An_i}}\times\frac{1}{V_{paste_{ini}}}; \tag{7}$$

and:

$$C_{P\,anh_i}=\left(1-\alpha_i\right)\times\frac{m_{An_i}}{V_{paste_{ini}}\times\rho_{An_i}}, \tag{8}$$

where: R_i is volume ratio between hydrates and anhydrous phase for the species "i" (cement or FA); $V_{paste_{ini}}$ is the initial paste volumetric concentration in paste.

- g_i is a factor delaying the hydration kinetics for pozzolanic constituent reactions depending on primary reactions;

g_i = C_{pCH} if i ≠ clinker (C_{pCH} is the volumetric concentration of portlandite in the paste);

g_i = 1 if i = clinker.

The schema of calculation formulas is summarized in Fig. 1. Note that input parameters in the model (except water content) are interpreted for each individual anhydrous phase "i".

The principles to determine the input parameters are introduced in Fig. 2. In this numerical model, the water content and anhydrous content are fixed for each studied sample. The parameters of clinker cement are determined through analysis of chemical composition (Bogue's composition) [22] and chemical reactions accompanying the hydration process [1]. On the other hand, the mineral additives parameters are calculated or referenced from literature (the detailed calculations are presented in [23]). Particularly, the fitting parameters of the model A_i, B_i, n were determined by the Langavant test.

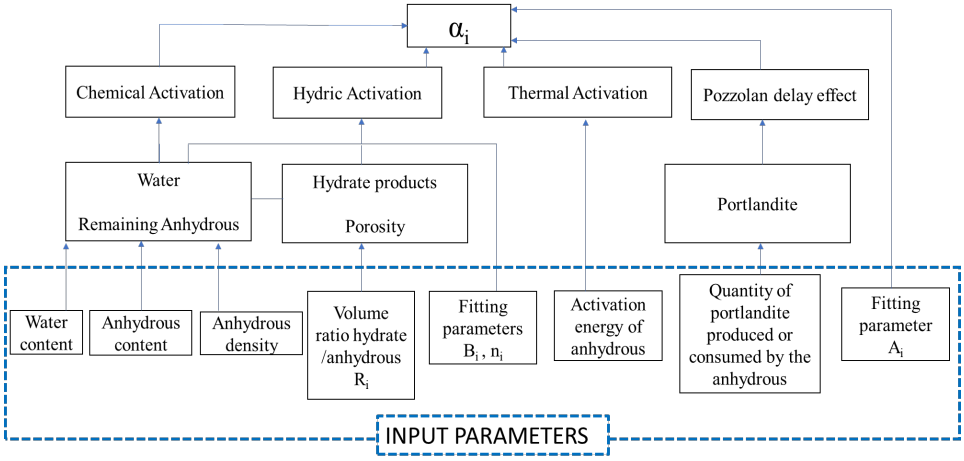

Figure 1. Schema for using input parameters of model.

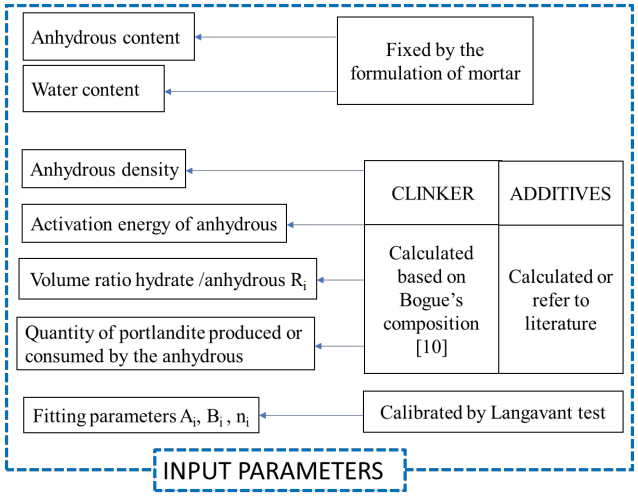

Figure 2. Determination of input parameters.

2.2. Calorimetry Method and TGA

2.2.1. Langavant Test

Langavant test for the heat of hydration of the cement method is semi-adiabatic calorimetry according to EN196-8, which consists of introducing a fresh cement specimen into an isolated Dewar flask (Fig. 3) and monitoring the temperature changes within the specimen during the first early days. After a certain time, the heat of hydration of the cement content in the sample is equal to the sum of the heat accumulated in the flask and the heat emitted to the environment during the test period. The temperature of the mortar is compared with the temperature of an inert sample placed in a reference calorimeter flask. Depending on the type of cement, in general, the heat emitted is from about 200–500 J / 1g of cement.

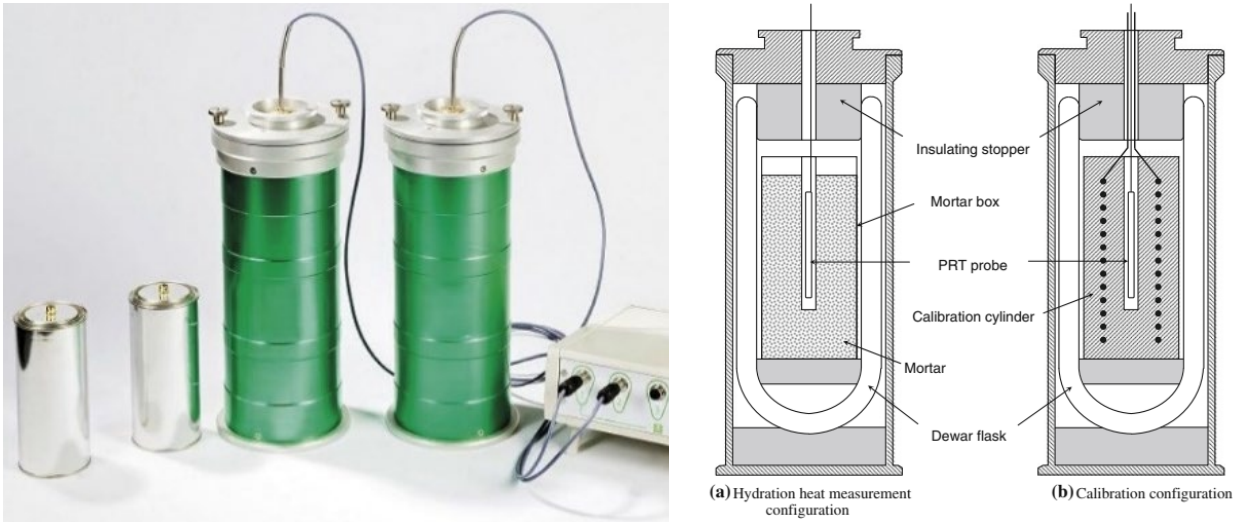

Figure 3. Schematic diagram of a Langavant calorimeter [20].

By the measuring of heat release during the hydration $Q(t)$, the degree of hydration at each time $\alpha(t)$ could be determined such as:

$$\alpha(t)=\frac{Q(t)}{Q_{\max}^{t}}, \tag{9}$$

where $Q_{\max}^{t}$ is heat release of complete hydration. The parameters A_i, B_i, n were determined by fitting the numerical curve and experimental curve of heat release and using the least squares method to calibrate.

3.1. TGA

TGA is a technique for measuring very small variations in mass under high gradient temperature which permit to quantify the portlandite content of the cement paste. During a TGA test, the decomposition of cement hydration products is manifested by the weight loss curve and endothermic peaks on the heat flux curve. The representation of the weight loss in the form of its time DTG shows the correspondence between the DTG peaks and those of heat flux.

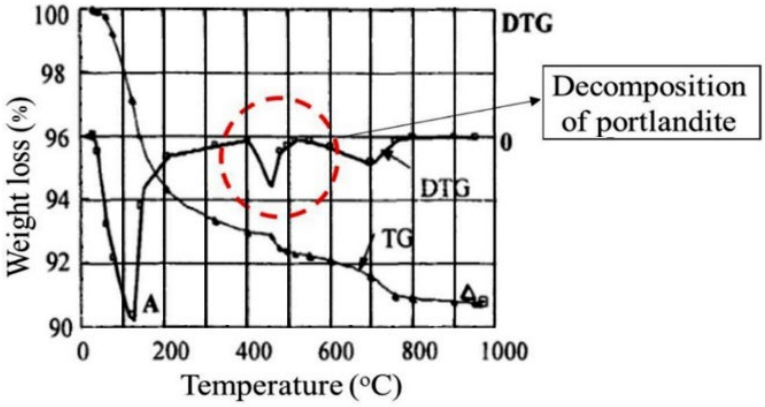

Figure 4. Weight loss of a cement paste sample during a TGA test [24].

Fig. 4 shows the typical result of a TGA test on a cement paste [24]. There are three major phases during the test and the second pic of weight loss correspond to the decomposition of portlandite, which is produced between 400 and 600 °C. This decomposition leads to an evaporation of chemically bound water and the mass content of portlandite in the mortar can be calculated from the following expression (10):

$$m_{\mathrm{Ca(OH)_2}}(t) = \frac{\left[\Delta m_{400^\circ\mathrm{C}\to 600^\circ\mathrm{C}}(t) + m_{d,400^\circ\mathrm{C}\to 600^\circ\mathrm{C}}(t)\right]}{m_{total}} \times \frac{M_{\mathrm{Ca(OH)_2}}}{M_{\mathrm{H_2O}}}, \quad (10)$$

where: $\Delta m_{400^\circ\mathrm{C}\to 600^\circ\mathrm{C}}(t)$ is the weight loss of the sample between 400 and 600 °C [kg];

$m_{d,400^\circ\mathrm{C}\to 600^\circ\mathrm{C}}(t)$ is the mass drift correction of the device between 400 and 600 °C [kg];

m_{total} : the mass total of sample [kg];

$M_{\mathrm{Ca(OH)_2}}$ and $M_{\mathrm{H_2O}}$ are consequently the molar mass of portlandite and water [kg mol^{-1}].

3. Results and Discussions

In this report, three cement paste samples were made using CEM I 52.5N cement (France Standard) with the water/binder (with or no mineral additives) ratio chosen as W/B = 0.5. The first one is pure cement paste (100 % cement), the next is mixed cement paste with FA (70 % cement and 30 % FA), and the last one is mixture of 70 % cement and 30 % SF. The chemical compositions (%) of these materials are given in Table 1.

Table 1. Chemical compositions of cement CEM I 52.5N, FA, and SF (%).

Types of materials	CaO	SiO_2	Al_2O_3	Fe_2O_3	SO_3
Cement	64.66	20.20	5.23	2.26	3.69
FA	1.00	60.76	29.72	3.49	0.09
SF	3.68	85.49	0.13	0.45	0.05

The input parameters of model are calculated or referenced from literature and showed in Table 2. Note that the quantity of heat released by the complete hydration $Q^T_{\max}$ of clinker cement could be determined directly from the Bogue's composition and the theoretical heat releases associated with each anhydrous [25] while the activation energy E_{ai} of clinker cement is identified by the formulas of Schindler [26]. On the other hand, these parameters of FA and SF are all extracted from document [15]. The others parameters of model such as Q^W_{th} (the quantity of water necessary for complete hydration of each anhydrous species), R (the volume ration hydrate/anhydrous), and Q_{CH} (the quantity of portlandite produced/consumed by clinker hydration or pozzolanic reactions) are determined by considering the chemical reactions and also the type of hydrate product when hydration occurs [1, 2]. The detailed formulas of calculation procedure can be found in [23].

Table 2. Input parameter of binder compose.

Parameters	Cement	FA	SF
Q^T_{max} (J/g)	453.9	560	845
E_{ai}/R (K)	5669	12000	11600
Q_{th}^W (g/g)	0.33	0.64	0.8
Q_{CH} (g/g)	0.27	–1.51	–1.37
R (m^3/m^3)	1.85	0.6	0.64
ρ (g/cm^3)	3.153	2.2	2.2

Table 3. Fitting parameters by calibration of model for each phase.

Parameters	Cement	FA	SF
B	3.147	30	6.08
n	0.230	0.098	0.483
A	3.80E+08	5.0E+30	1.24E+18

The three fitting parameters (A, B, n) were then calibrated using results from the Langavant tests performed on a binder composed (shown in Table 3). It should be noted that the calibration of the parameters of each anhydrous compound is done by successive calibration: first, the cement parameters are identified by a test on the pure cement and then, the parameters of the additives are based on a test on a mixture (the clinker parameters being known).

Fig. 5 showed the of evolution of heat release during the hydration at early age for three studied samples. It seems that in the first hours of the hydration, the obtain results of calibrated model are quite consistent with the results of the Langavant test, especially the case of pure cement sample. However, in the next stage, small differences between numerical model and experiment were observed and the differences were less obvious in the case of blended cement samples.

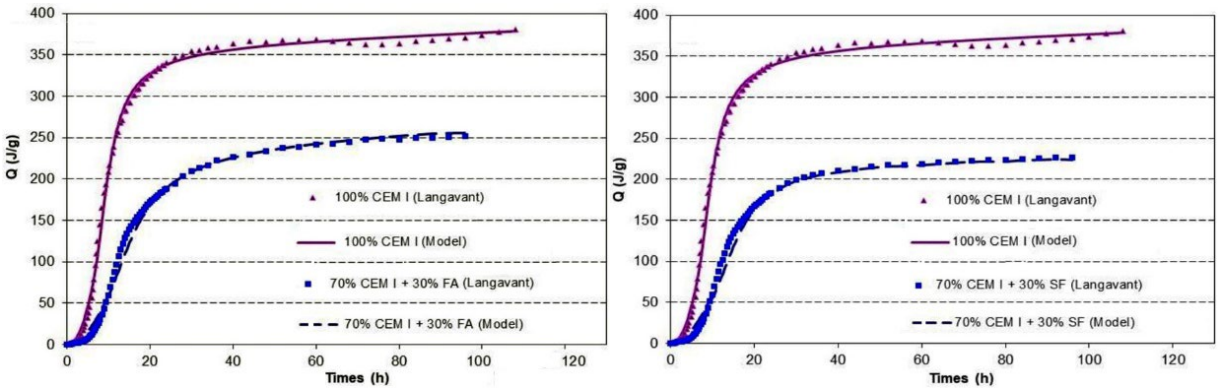

(a) 70 % cement + 30 % FA **(b) 70 % cement + 30 % SF**

Figure 5. Heat release calculation of calibrated model and Langavant at early age.

The evolution of hydration degree of FA–cement sample at early age is presented in Fig. 6. We can observe that the hydration degree of pure cement sample is greater than this one of the “cement phase” in the mixture. This can be explained cause reducing the cement concentration in the anhydrous mixture may reduce the degree of hydration. In addition, the delaying effect of mineral additive is also observed at the first hours after mixing when the hydration degree of “FA phase” equal zero. After 5–7 hours, the pozzolanic reactions will active the FA and induce the evolution of its hydration degree [19].

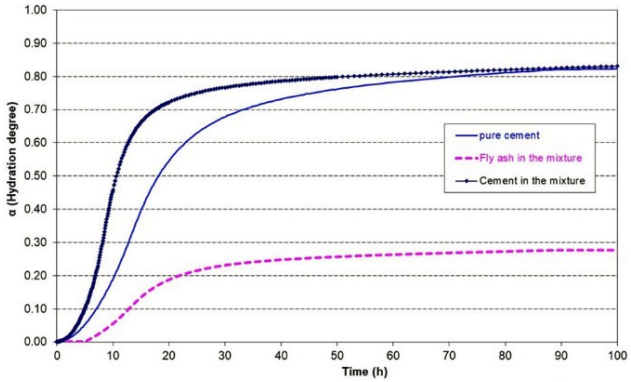

Figure 6. Evolution of Hydration degree of pure cement paste and binder composes of FA–cement paste at early age.

The evolution of hydration degree of clinker cement for long term are introduced in Fig. 7. It can be seen that the hydration degree evolved strongly in the first hours after mixing and occurs more slowly when the samples reach the age of 14 days. The hydration then progresses leisurely and become almost constant at 28 days. The maximum level of hydration reaches nearly 95 % for the case of pure cement sample.

The average hydration degree of the blended cement (α_{mix}) for long term is determined by the following equation (11):

$$\alpha_{mix} = \alpha_{cement} \times p_{cement} + \alpha_{additives} \times p_{additives}, \quad (11)$$

where: α_{cement} and $\alpha_{additives}$ are hydration degree of cement and mineral additive (i.e., FA and SF) in the mixture; p_{cement} and $p_{additives}$ are mass proportion of cement and mineral additive in the mixture. In this case, p_{cement} = 0.7 and $p_{additives}$ = 0.3.

The evolution of hydration degree for the blended cement paste are introduced in Fig. 8. The maximum level of hydration reaches 80 % for the case of FA–cement sample and only 76 % for the case of SF–cement sample. It can be observed also that the replacement of clinker (30 %) by mineral additives leads to a significant decrease of hydration degree. On the other hand, the notable difference in hydration degree evolution between the sample of FA and SF is also observed. This can be explained by the presence of a large amount of SF while maintaining the same water/binder ratio leads to internal shrinkage and decreasing of relative humidity in the paste. This phenomenon may thereby cause lack of water for hydration reactions. It should be remembered that SF is a highly absorbent mineral [27] and in the production of concrete and cement containing additives, the replacement content is usually recommended not exceed 8 %.

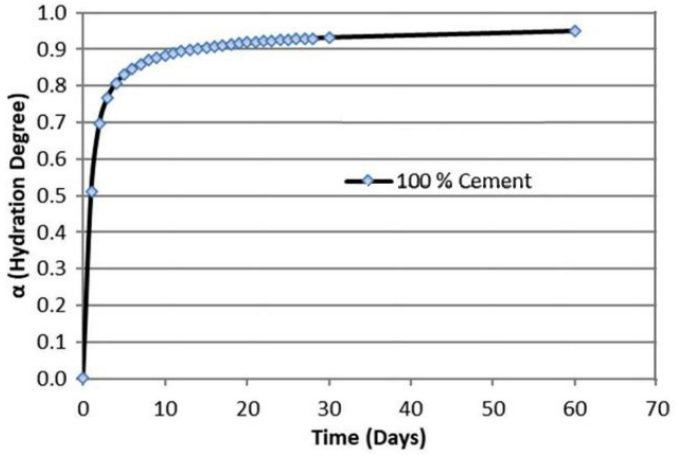

Figure 7. Evolution of hydration degree α of pure cement paste in long term.

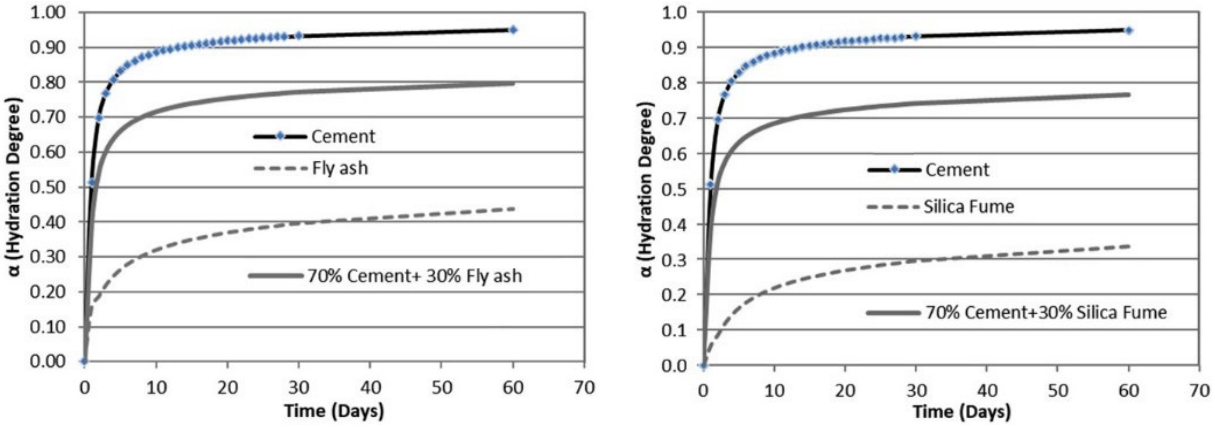

(a) 70 % cement + 30 % FA **(b) 70 % cement + 30 % SF**

Figure 8. Evolution of hydration degree *α* for blended cement paste.

The series of TGA/DTG tests on mortar were also carried out at a date of 3, 7, 28, and 60 days to estimate the effect of mineral additives on portlandite content in the paste. The evolutions of the TGA and DTG curves for each type of cement are related to the initial mass of the studied sample and presented in Figs. 9a–c. By comparing the DTG curves, we find that the mortar with 100 % cement has a large peak between 400 and 600 °C, and these peaks for mortars containing pozzolanic additions are less significant. This also prove that the portlandite produced in pure cement mortar is greater than that in mixtures paste as shown in Fig. 9d. The replacement of clinker by FA and SF reduces the clinker content and obviously the portlandite content produced in hydration process.

On the other hand, the portlandite content increases throughout the hydration process for the case of pure cement sample, but this increasing become slower after 28 days, corresponds with the completely hydration of clinker. In contrast, with mixtures containing FA and SF, the portlandite content begins to decrease after about one or two weeks and the speed of reduction becomes faster after 15 days due to the

effect of pozzolanic reactions. In addition, we can find that the portlandite content in the SF–cement sample is lower than that in the mixture contains FA. There are maybe two hypotheses to explain this phenomenon: first, the SF consume a lot of water, causing a lack of water for the hydration and obviously the quantity of portlandite produced is reduced. The secondary, pozzolanic reaction of SF is stronger than FA and it consumes more portlandite. However, when considering the hydration degree of the binder composes observed in Fig. 8, we can notice that the first hypothesis is more reasonable.

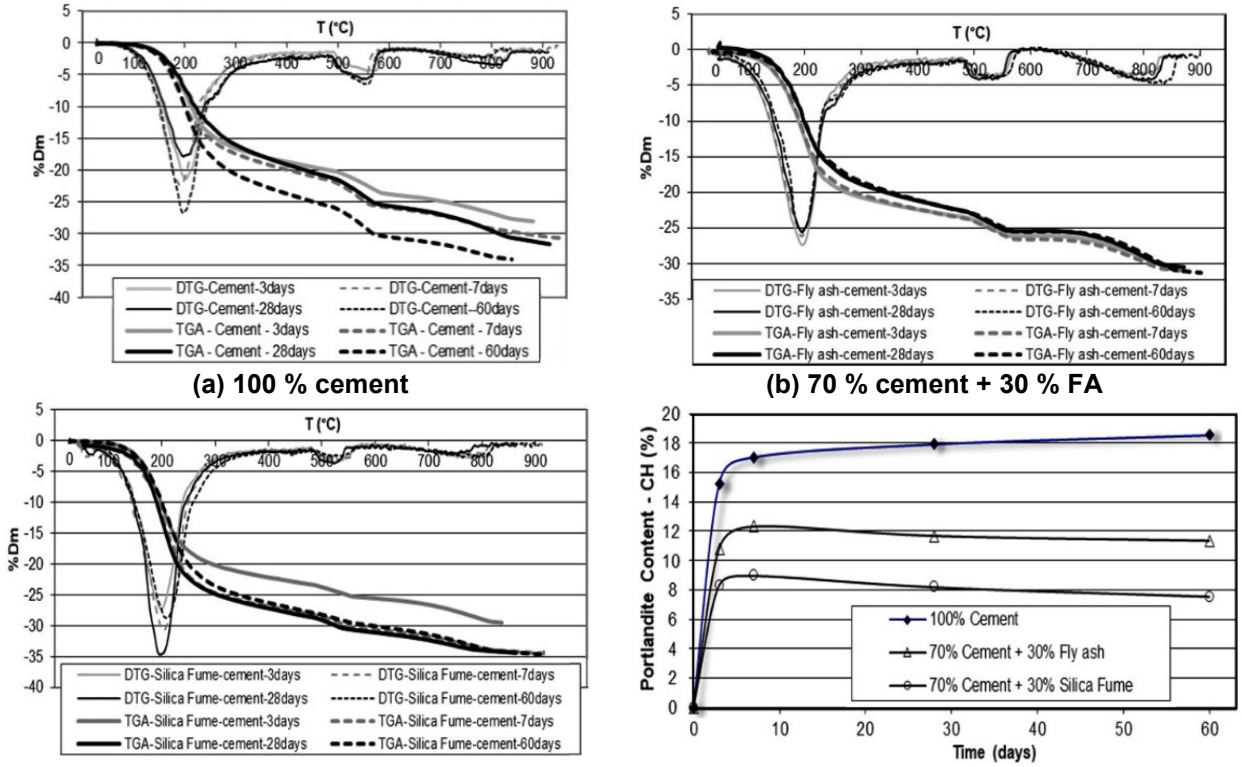

(a) 100 % cement **(b) 70 % cement + 30 % FA**

(c) 70 % cement + 30 % SF **(d) Portlandite content in the mortar**

Figure 9. TGA/DTG results and the portlandite content of the studied samples at 3, 7, 28, 60 days.

4. Conclusions

In this article, a numerical model predicting the hydration development of multicomponent cement-based materials at an early age has been applied. The hydric-thermal activation and the delaying effect of mineral additives have been taken into account in the model. The fitting parameters of the model are determined by measuring the heat released during the hydration process using Langavant test. The model is applied to calculate the hydration degree of three cement paste samples containing pure cement and blended cement with 30 % replacement of FA or SF.

With the replacement of clinker by mineral additives leads to a significant decrease of hydration degree (from 95 to 75÷80 %) even if the effect of pozzolanic reactions, which increase the hydration degree of blended cement in the long term. The obtained results of TGA/DTG tests have allowed to calculate the portlandite content in the studied samples at difference term and showed us the correspondence with the results of established model.

In addition, the hydration degree of the mixture containing SF is lower than that of FA due to the lack of water in the paste when mixing a large amount of SF. From this result, it can be shown that the replacement content of SF is usually recommended not to exceed 8 %.

Finally, the obtained results have also shown the efficacy of multiphasic model in prediction of hydration kinetics of blended cement paste, especially at the early age.

References

1. Lacarrière, L. Prévision et évaluation de la fissuration précoce des ouvrages en béton. PhD Thesis. INSA Toulouse, 2007. 250 p.
2. Buffo-Lacarrière, L., Sellier, A., Escadeillas, G., Turatsinze, A. Multiphasic finite element modeling of concrete hydration. Cement and Concrete Research. 2007. 37(2). Pp. 131–138. DOI: 10.1016/j.cemconres.2006.11.010
3. Meinhard, K., Lackner, R. Multi-phase hydration model for prediction of hydration-heat release of blended cements. Cement and Concrete Research. 2008. 38(6). Pp. 794–802. DOI: 10.1016/j.cemconres.2008.01.008
4. Lei, Z. Caractérisation de l'hydratation des liants composés. Rapport du stage. LMDC – INSA Toulouse, 2006. 45 p.

5. Lacarrière, L.B. Etude des couplages Thermo-Hydro-Chemo-Mécaniques pour la prévision du comportement des grands ouvrages en béton armé et béton précontraint. Génie civil. Université de Toulouse, 2018. 146 p.
6. Wang, X.-Y. Modeling of Hydration, Compressive Strength, and Carbonation of Portland Limestone Cement (PLC) Concrete. Materials. 2017. 10(12). Article no. 115. DOI: 10.3390/ma10020115
7. Wang, X.-Y., Lee, H.-S. Modeling the hydration of concrete incorporating fly ash or slag. Cement and Concrete Research. 2010. 40(7). Pp. 984–996. DOI: 10.1016/j.cemconres.2010.03.001
8. Merzouki, T., Bouasker, M., Khalifa, N., Mounanga, P. Contribution to the modeling of hydration and chemical shrinkage of slag-blended cement at early age. Construction and Building Materials. 2013. 44. Pp. 368–380. DOI: 10.1016/j.conbuildmat.2013.02.022
9. Kinomura, K., Ishida, T. Enhanced hydration model of fly ash in blended cement and application of extensive modeling for continuous hydration to pozzolanic micro-pore structures. Cement and Concrete Composites. 2020. 114. Article no. 103733. DOI: 10.1016/j.cemconcomp.2020.103733
10. Artamonova, O.V., Chernyshov, E.M., Slavcheva, G.S. Factors and mechanisms of nanomodification cement systems in the technological life cycle. Magazine of Civil Engineering. 2022. 1(109). Article no. 10906. DOI: 10.34910/MCE.109.6
11. Kishi, T., Maekawa, K. Thermal and mechanical modelling of young concrete based on hydration process of multi-component cement materials. Thermal Cracking in Concrete at Early Age: Proceedings of the International RILEM Symposium. CRC Press. London, 1994. 11–19.
12. Zhang, M., Ma, D., He, J., Han, Y. Sulfate corrosion resistance of foundation concrete with nano-particles. Magazine of Civil Engineering. 2023. 3(119). Article no. 11901. DOI: 10.34910/MCE.119.1
13. Roelfstra, P.E., Salet, T.A.M. Modelling of heat and moisture transport in hardening concrete. Thermal Cracking in Concrete at Early Age: Proceedings of the International RILEM Symposium. CRC Press. London, 1994. Pp. 273–281.
14. De Schutter, G. Hydration and temperature development of concrete made with blast-furnace slag cement. Cement Concrete Research. 1999. 29 (1). Pp. 143–149.
15. Waller, V. Relations entre composition des bétons, exothermie en cours de prise et résistance en compression. PhD Thesis, ENPC Paris, 1999. 297 p.
16. Inozemtcev, A.S., Korolev, E.V., Duong, T.Q. Lightweight concrete for 3D-printing with internal curing agent for Portland cement hydration. Magazine of Civil Engineering. 2022. 1(109). Article no. 10915. DOI: 10.34910/MCE.109.15
17. Bentz, D.P. Influence of water-to-cement ratio on hydration kinetics: Simple models based on spatial considerations. Cement and Concrete Research. 2006. 36(2). Pp. 238–244. DOI: 10.1016/j.cemconres.2005.04.014
18. Oh, B.H., Cha, S.W. Nonlinear Analysis of Temperature and Moisture Distributions in Early-Age Concrete Structures Based on Degree of Hydration. ACI Materials Journal. 2003. 100 (5). Pp. 361–370.
19. Yusuf, M.O. Performance of Aluminium Shaving Waste and Silica fume Blended Mortar. Magazine of Civil Engineering. 2023. 6(122). Article no. 12209. DOI: 10.34910/MCE.122.9
20. Hay, B., Hameury, J., Davee, G., Grelard, M. Assessment of Uncertainties in Calibration of Langavant Calorimeters. International Journal of Thermophysics. 2014. 35(9–10). Pp. 1757–1769. DOI: 10.1007/s10765-013-1460-9
21. Fedosov, S.V., Aleksandrova, O.V., Bulgakov, B.I., Lukyanova, N.A., Nguyen Duc Vinh, Q. Corrosion-resistant concretes for coastal underground structures. Magazine of Civil Engineering. 2024. 17(2). Article no. 12606. DOI: 10.34910/MCE.126.6
22. Bogue, R.H. La chimie du ciment Portland. Eyrolles. Paris, 1952. 586 p.
23. Nguyen, T.D. Evolution des propriétés mécaniques des bétons à base de liants composés au cours de l'hydratation. Rapport du stage. LMDC – INSA Toulouse, 2008. 85 p.
24. Khelidj, A., Loukili, A., Bastian, G. Etude expérimentale du couplage hydrochimique dans les bétons en cours de maturation: incidence sur les retraits. Matériaux et Constructons. 1998. 31. Pp. 588–594. DOI: 10.1007/BF02480608
25. Lea, F.M. The Chemistry of Cement and Concrete. Edward Arnold Ltd., London, 1970. 727 p.
26. Schindler, A.K. Effect of temperature on hydration of cementitious materials. ACI Materials Journal. 2004. 101(1). Pp. 72–81.
27. ACI Committee 234. 234R-96. Guide for the Use of Silica Fume in Concrete. 2000. 15 p.

Information about the authors:

***Trong Dung Nguyen**, Doctor of Engineering*
ORCID: https://orcid.org/0000-0002-8515-8469
E-mail: nguyentrongdung@humg.edu.vn

***Van Lam Tang**, PhD in Technical Sciences*
ORCID: https://orcid.org/0000-0002-4857-835X
E-mail: lamvantang@gmail.com

Received 14.01.2024. Approved after reviewing 28.10.2025. Accepted 30.10.2025.

Magazine of Civil Engineering

ISSN 2712-8172

journal homepage: http://engstroy.spbstu.ru/

Research article

UDC 69

DOI: 10.34910/MCE.140.6

Performance of reactive powder concrete slender columns exposed simultaneously to eccentric load and elevated temperatures

W.R. Almakinachi ✉ , ***A.I. Salahaldin***

University of Kirkuk, Kirkuk, Iraq

✉ *waelrami@uokirkuk.edu.iq*

Keywords: fire, eccentric loads, RPC, buckling of columns, uniaxial moment, slender columns

Abstract. The objective of this study is to examine the impact of elevated temperatures on the structural response of slender columns made of reactive powder concrete (RPC) subjected to eccentric axial loads. Nine RPC column specimens were exposed to a temperature at three different levels: 450 °C, 600 °C, and 750 °C, and to three eccentricities: 50 mm, 100 mm, and 150 mm. The columns underwent fire exposure while being subjected to axial loading equal to 60 % of their ultimate capacity. The outcomes of the experimental tests indicate a noticeable lateral displacement of the RPC columns at high temperatures. The results show that at a constant temperature 750 °C, the mid-height lateral buckling for various eccentricities is significantly higher comparing 50 mm with 100 mm and 150 mm by 59 % and 81 %, respectively. While this rate becomes 36 % and 35 % for 600 °C. At 750 °C, the lateral mid-height buckling is found to be significantly greater when compared to 450 °C and 600 °C by 106 % and 69 %, respectively (for 50 mm eccentricity). While the ratio becomes 48 % and 46 % (for 100 mm eccentricity), one of the main findings in the research is that a low eccentricity value 50 mm, which has a high load, gives higher buckling for each elevated temperature. The mode of failure regarding the column depended on the eccentricity value where the high eccentric loaded columns showed prolonged ductile behavior, while the least eccentric loaded columns showed a brittle type of failure.

Acknowledgment. The authors would like to thank Kirkuk Company for Precast Concrete Girders for the financial support and are grateful to the Department of Civil Engineering, University of Kirkuk for supporting the experimental research and allowing the use of laboratory and instruments.

Citation: Almakinachi, W.R., Salahaldin, A.I. Performance of reactive powder concrete slender columns exposed simultaneously to eccentric load and elevated temperatures. Magazine of Civil Engineering. 2025. 18(8). Article no. 14006. DOI: 10.34910/MCE.140.6

1. Introduction

The fire resistance of a variety of structures, especially the capacity of concrete, is greatly diminished by spalling when exposed to high temperatures [1]. Many researchers nowadays developed new construction materials that can be used in residential buildings, which can be compared to bricks that work as fire insulators autoclaved aerated concrete blocks have excellent fire resistance, making them a popular choice for use in fire-prone areas. Pure axial loaded columns are usually uncommon in practice owing to the fact that bending is nearly always present for many reasons, including the minor initial deviation of columns, the method, in which beams and slabs transfer loads, and the moments provided by continuous construction of beams through columns [2]. A study was made by Santiago et al. [3] where it was observed that the bending moment for steel beams restricted by a couple of fire-protected steel columns increases with the increase in the temperature profile. However, columns made of normal-strength concrete (NSC) provide the necessary fire resistance without the need for additional suitable insulation [4]. Abdulhaleem et

al. [5, 6] conducted a study to explore the impact of recycled aggregate concrete and the inclusion of steel fibers on the strength of self-compacting concrete (SCC). The research aimed to investigate how the use of recycled aggregates and the addition of steel fibers influenced the overall strength properties of SCC, the findings from the experimental study indicate that the inclusion of steel fibers has a beneficial impact on improving the mechanical properties of SCC, especially in terms of enhancing tensile strength. Additionally, the incorporation of 50 % recycled aggregates in the concrete mixture resulted in a notable increase of approximately 20 % in compressive strength. Concrete's fire behavior is fundamentally tied to temperature-dependent material characteristics. Because thermal diffusivity is lower in concrete than in steel, large temperature gradients are often formed inside fire-exposed concrete members. Due to the high thermal inertia, the core area may take a long time to heat up. Thus, although concrete's compressive strength is quickly lost at a critical temperature, which is not different to the corresponding temperature for steel strength loss, structural efficacy is not impaired until the mass of the material reaches the same temperature. This necessitates a thermal response study of the whole structural member [7]. Klak et al. [8] reviewed the behavior of different reinforced concrete elements when subjected to high temperatures. The study found that both the concrete and reinforcing bars are negatively impacted by fire. It was observed that the flexibility and stiffness of the structures decrease as the fire exposure increases or the stress levels rise. On the other hand, it was found that the flexibility and stiffness improve with a larger cross-section of the structural elements. However, the maximum deflection of the slab was found to decrease non-linearly during the fire test. As the temperature decreases, the bottom of the concrete slab begins to cool, leading to an increase in the yield strength of the bottom reinforcement. This causes the bottom reinforcing to contract along with the lower half of the slab. Al-Zuhairi et al. [9] conducted a study on the behavior of reinforced hybrid concrete columns consisting of two fully-bonded concretes under biaxial loading The findings indicated a noteworthy increase of 33.5 % in the ultimate load-bearing capacity of hybrid columns compared to conventional columns. Additionally, a 38 % increase in the ultimate load was observed when reducing the hybrid's ratio to 0.16. The study concluded that hybrid columns with smaller hybrid ratios can withstand higher loads and moments while exhibiting fewer axial strains.

Reactive powder concrete (RPC) was developed by Richard & Cheyrezy [10, 11], which claimed that it is a form of ultra-high-performance concrete (UHPC) with compressive strengths ranging from 200 MPa to 800 MPa, depending on the mix proportions and the curing temperature by eliminating coarse aggregates and optimizing the granular mixture, it becomes possible to achieve a homogeneous and dense cementitious matrix that demonstrates superior mechanical performance. Furthermore, the remarkable durability of RPC makes it a more practical and economical choice for tall buildings and structures with large spans, particularly those exposed to severe weather and deicing agents [12]. Achieving sustainable green development is required [13]. Typically, RPC necessitates a high concentration of cement and finely ground quartz sand, causing an increase in construction expenses and contributing significantly to the release of carbon dioxide (CO_2) into the atmosphere. By partially replacing cement with industrial by-products, such as fly ash, silica fume, slag powder, and other effective mineral additives, the peak hydration heat, construction cost, and carbon emissions of RPC can be reduced, while its microstructure, strength, impermeability, and resistance to corrosion can be improved [14, 15]. Sanjuán & Andrade. [16] conducted a study comparing the durability properties of RPC to other types of UHPC and found that RPC demonstrated exceptional durability. The research found that the air permeability coefficient of RPC was 50 times lower and the rate of steel corrosion was reduced by 25 times when compared to other types of UHPC.

Wattanapornprom et al. [17] investigated the fire resistance of RPC columns with various steel and polypropylene (PP) fiber ratios. Four columns with varying fiber ratios were tested in fires that burned for 30 min and 60 min. Following that, the behavior of RPC columns at increased temperatures was observed in terms of spalling depth, fiber failure mechanism, and residual strength. The results showed that increasing the volume percentage of steel fiber or the inclusion of PP fiber increases the column's fire resistance. Chadli et al. [18] found that the mechanical properties of RPC tend to improve when exposed to high temperatures, up to 200 °C. However, the compressive, flexural, and tensile strength decreases as the temperature rises above 200 °C. When exposed to 400 °C, a significant reduction in mechanical properties is observed compared to room temperature conditions. Additionally, the compressive strength of RPC deteriorates significantly within the temperature range of 600–800 °C. The addition of steel fibers in RPC helps to mitigate this degradation and reduces the risk of failure due to high temperatures. The results obtained by Abdulraheem & Kadhum [19] showed that it is more appropriate to evaluate the energy absorption capacity instead of using the displacement ductility index to assess the ductility of RPC columns after exposure to fire. Moreover, there was a noticeable decrease in the initial and secant stiffness of RPC columns after fire exposure, and the extent of reduction increased with the rising fire temperature from 400 °C to 600 °C. Jomaa'h et al. [20] studied the effect of the elevated temperature on RPC slender columns with various degrees in comparison with NSC slender columns, 18 total specimens were cast, 9 RPC columns and 9 NSC columns, the specimens were tested under fire exposure for 1 and 2 hours with temperatures of 450 °C, 600 °C, and 750 °C, respectively. It was found that the axial displacement and

mid-height lateral displacement due to buckling were increased with respect to the temperature rise for the previous parameters mentioned the RPC showed greater strength than NSC and the percentage of strength loss in RPC was lower than NSC. Few studies have examined the uniaxial moment and fire impact on slender RPC columns together. This experiment examined how increased temperatures affected eccentricity-loaded RPC columns. The testing range regarding the temperature levels was selected depending upon the effect of the temperature level on the RPC, it was discovered that elevated temperatures from high fire flames can be categorized into two intervals with regard to the decline in strength in RPC: specifically, 23–200 °C and 300–500 °C. Within the 23–200 °C range, RPC either sustained or experienced a rise in its initial strength. Conversely, in the 300–500 °C range, RPC exhibited a significant decrease in its original strength. Exposure to temperatures around 500 °C resulted in the spalling of RPC specimens, leading to a loss of both mechanical and physical properties, with partial or complete spalling [21]. Izzat [22, 23] conducted an investigation to assess the impact of high-temperature fire exposure on SCC short columns. The findings revealed that the ultimate load capacity of columns exposed to fire decreases as the fire flame temperature increases. At burning temperatures of 300 °C, 500 °C, and 700 °C, the average residual ultimate load capacity for gradually cooled specimens was 91 %, 81 %, and 71 %, respectively.

2. Materials and Methods

To investigate the fire effect on RPC columns subjected to eccentric loading, a large-scale setup for laboratory experiment was made by Jomaa'h et al. [20] at the Civil Engineering Department / University of Kirkuk, and it was used in this study.

2.1. Testing Device Setup

The concrete column inspection device comprises a steel frame with dimensions of 20 mm in thickness, 2.8 m in length, and 1.44 m in breadth. A temperature measurement device is used to trace temperature, and, a thermal cable (Type K) is installed inside the oven to measure the ambient temperature around samples. The furnace is shown in Fig. 1.

Figure 1. Test setup.

This oven has three fundamental layers:

1. The outside is composed of standard clay bricks.
2. Ceramic fiber blanket that can endure temperatures of 1260 °C.
3. The inside layer is composed of firebrick that can resist temperatures of 1200 °C.

A flame of high-pressure gas is used to induce fire inside the furnace. The bonding substance used to construct fire bricks is heat resisting cement, which can resist temperatures of up to 1400 °C. Fig. 2 shows a schematic top view of the oven setup. The primary purpose of the oven chamber is to steadily raise the temperature for a specified time. The burning source is composed of single methane gas burners parallel to a single-sided column model throughout its length.

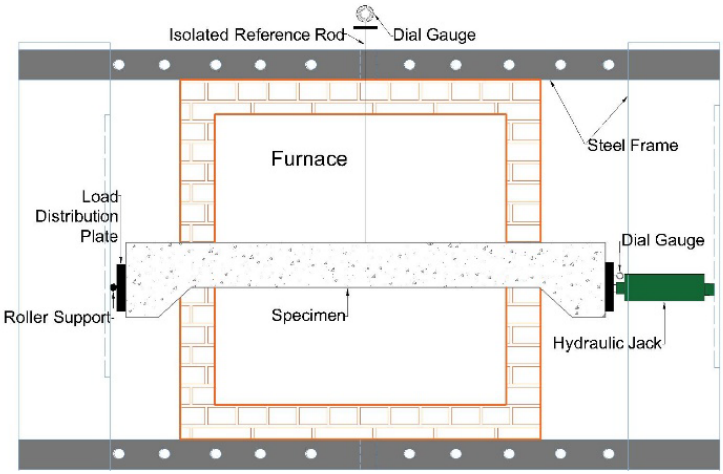

Figure 2. Top view drawing of the test device setup.

2.2. Materials

The cement used in this experiment was Ordinary Portland Cement (CEM I-R42.5), which met Iraqi Standard Specifications 5/1984 [24]. A densified micro-silica fume with a minimum silicon dioxide content of 85 %, a specific gravity of 2.3, and a specific surface of 15 m^2/g was used in this work as a mineral additive. In this investigation, river sand with a maximum particle size of 4.75 mm was also used [25]. In addition, a high-performance water-reducing agent was used to enhance the workability at low water-cement ratios. The agent's chemical constituent, polycarboxylate polymer, conforms with ASTM C494 Type E. The admixture is light-brownish in color and has a specific gravity of 1.07 (±0.005) g/cm^3. PP monofilament fibers were used. The fiber length is 12 mm and the diameter is 0.032 mm, the aspect ratio (l/d) of the fibers is 375. The proportions and compressive strength of the mix are detailed in Table 1.

Table 1. RPC Mix. Proportions.

Cement (kg/m^3)	Micro silica (kg/m^3)	W/binder	Sand (kg/m^3)	Superplasticizer (kg/m^3)	PP fiber (kg/m^3)	Cube compressive strength, f_{cu} (MPa)	Cylinder compressive strength, $f_{c'}$ (MPa)
900	100	0.2	1350	20	3.2	118	94.4

2.3. RPC Column Specimens

In order to conduct this research, nine RPC columns were prepared according to standard concrete mechanics principles of strain compatibility and equilibrium of internal forces for the column. Fig. 3 shows the column interaction diagram. Table 1 displays the results of compressive strength testing used to determine the mix. of the RPC columns made.

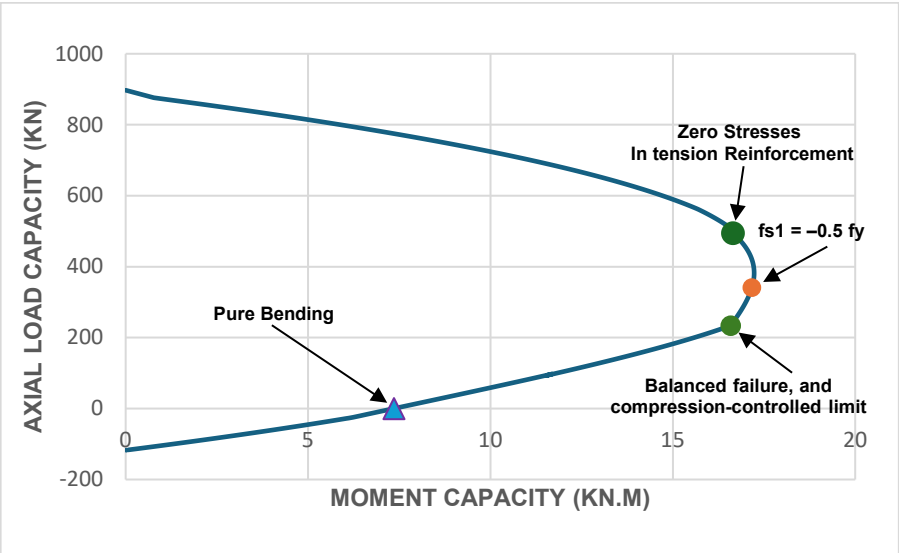

Figure 3. Column nominal strength interaction diagram.

The specimen is 1.6 m in height with 15 × 15 cm cross-sectional dimensions at the mid-height, at the brackets, the cross-section dimensions are 25 × 15 cm; the purpose of the brackets is to apply load at different eccentricities, and it was designed according to ACI318-19 [26]. Fig. 4 illustrates the column specimen drawings with reinforcement details and the arrangement of the thermocouple (K-type) embedded in the specimen. The capacities of the columns ($f_{c'}$ = 80 MPa) in relation to eccentricities are displayed in Table 2.

Table 2. Column capacities and test loads.

	Specimen designation	Temperature	Eccentricity (mm)	Ultimate axial load capacity (kN)	Ultimate moment (kN.m)	Test load (kN)	Test moment (kN.m)
1	RPC450-50		50	606	30	360	18
2	RPC450-100	450	100	181	18	110	11
3	RPC450-150		150	91	14	60	9
4	RPC600-50		50	606	30	360	18
5	RPC600-100	600	100	181	18	110	11
6	RPC600-150		150	91	14	60	9
7	RPC750-50		50	606	30	360	18
8	RPC750-100	750	100	181	18	110	11
9	RPC750-150		150	91	14	60	9

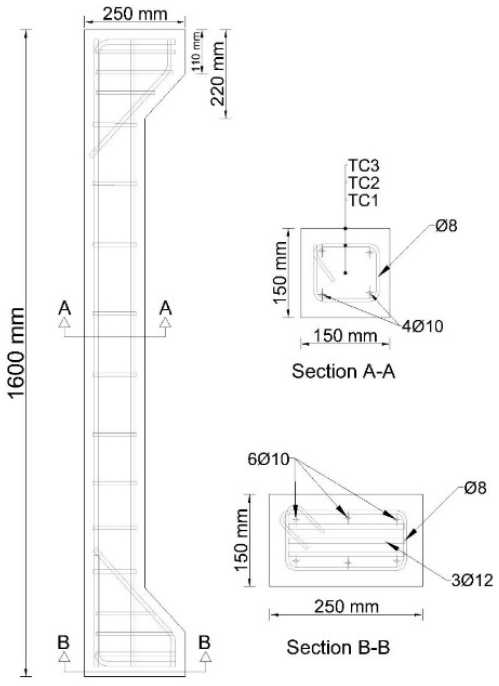

Figure 4. Dimensions and reinforcement details of RPC columns.

2.4. Experimental Procedure

This research investigated the lateral deformation performance of RPC following high-temperature exposure on nine RPC column specimens. The combination mix components of specimens are listed in Table 1. After casting, the specimens were wrapped with a plastic film for initial curing to prevent moisture evaporation and then stored at 25 °C for up to 20 hours [27]. The specimens were then demolded and immersed in water for final curing at 25 °C for 14 days. To gain an advantage in producing RPC with exceptional mechanical properties (compressive strength about 100 MPa) using the conventional curing method without any additional provisions and also to simulate the practical site conditions, this study did not adopt the principle of heat treatment curing of RPC, which is one of the basics for developing RPC [28, 29].

In this work, three temperatures and eccentricities were employed to test the mechanical behavior of RPC specimens: 450 °C, 600 °C, and 750 °C, as shown in Table 2. Each set had three specimens that were initially compressed uniaxially. The axial load applied on the column was approximately 60 % of the ultimate load according to ASTM E119 (Section 7.4.2.2) [30]. To monitor the interior temperature of the specimen, a (K-type) thermocouple was put in each specimen during casting, one in the center (TC1) and the other linked to the reinforcement (TC2). After water curing, RPC has an extraordinarily high density and can store a considerable quantity of water to avoid specimen spalling during heating (i.e., high pore pressure generated by water vaporization), the specimens were dried in the sun for at least 50 days before being exposed to fire to reduce water content. A thermocouple (Type K) was used to monitor the temperature of the furnace (TC4) and ensure that it achieved the desired temperature another one was attached to the specimen cover (TC3), and lateral displacement was recorded every 5 minutes for 2 hours for all specimens.

3. Results and Discussions

3.1. RPC Column Pre-Fire Behavior

The mechanical behavior of the RPC columns before fire exposure is presented in Figs. 5 and 6, respectively.

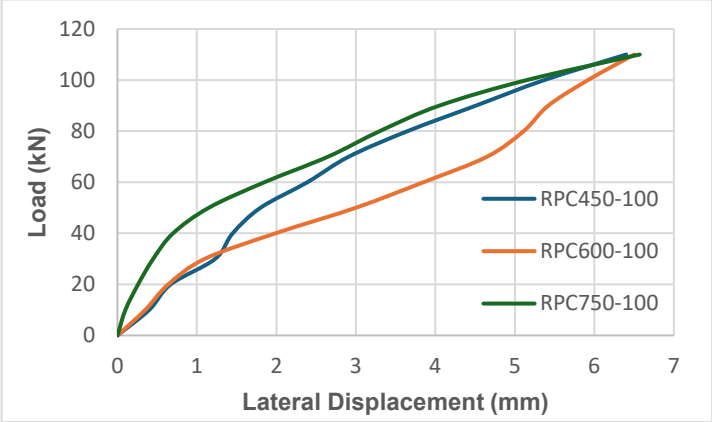

(a) Lateral displacement of 50 mm eccentricity set.

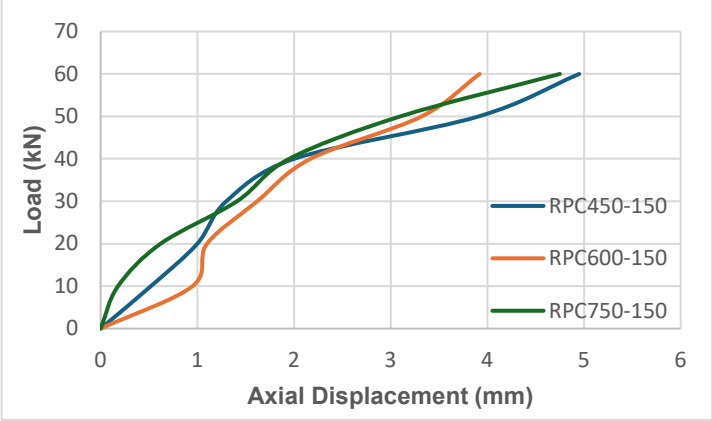

(b) Lateral displacement of 100 mm eccentricity set.

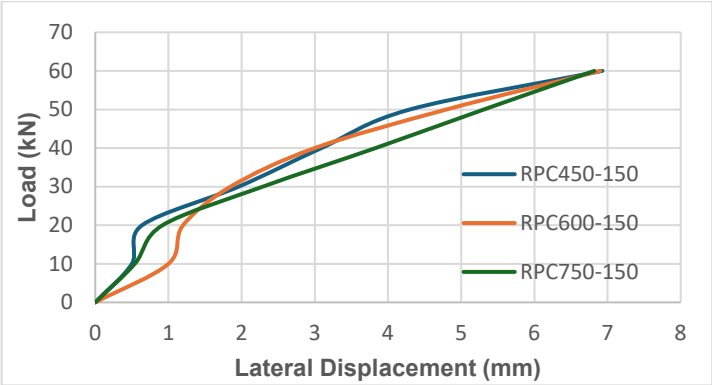

(c) Lateral displacement of 150 mm eccentricity set.

Figure 5. Lateral mid-height displacement.

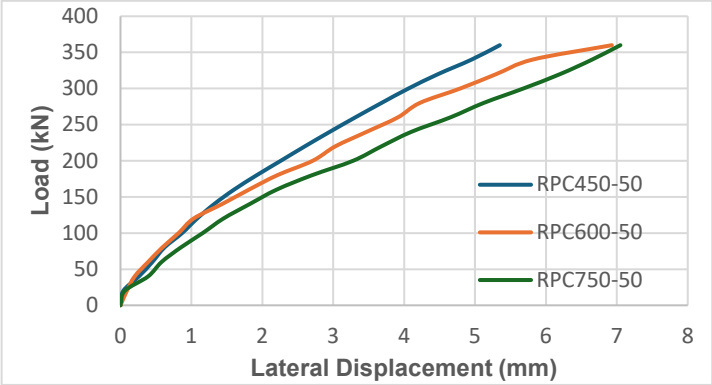

(a) Axial displacement of 50 mm eccentricity set.

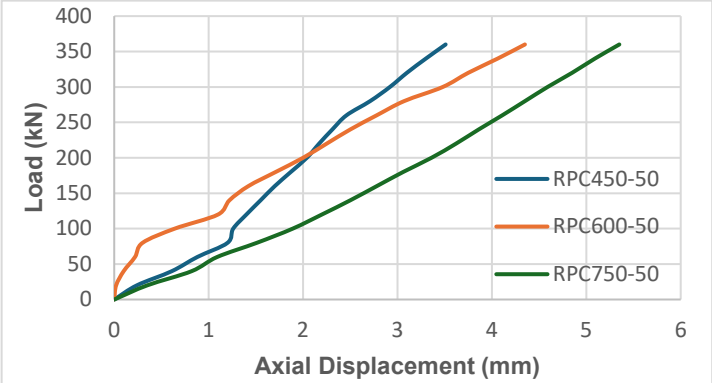

(b) Axial displacement of 100 mm eccentricity set.

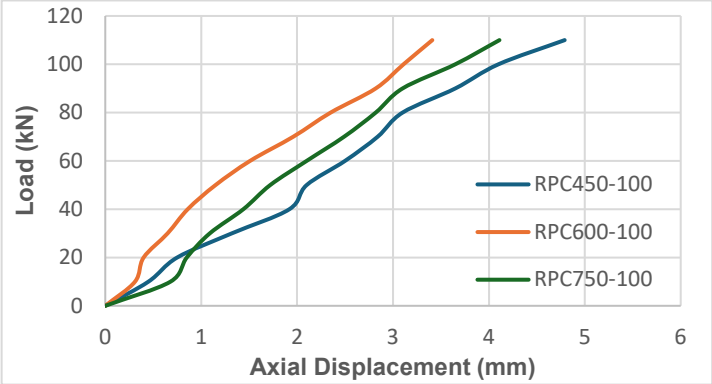

(c) Axial displacement of 150 mm eccentricity set.

Figure 6. Measured axial deformation for all sets.

As depicted in the figures, nearly all the lateral deflection (lateral buckling) of the columns is consistent regardless of eccentricity, due to the fact that all the columns were subjected to approximately

60 % of their ultimate load. Different eccentricities can have the same mid-height deflection due to the material's linear-elastic behavior and the fact that the load-carrying capacity of a column is affected by the accompanying moment as the moment increases, the applied load decreases as it is obvious in Table 2. This will give the same buckling behavior of the columns regardless of the eccentricity of the load. Fig. 6 shows that the axial displacement of the columns is approximately close to each other before the fire takes place, all columns with the same eccentricity exhibit similar structural behavior. Also decreasing axial load with increasing the applied moment can cause similar behavior of all columns and this matches with the behavior of the lateral buckling that was previously discussed. The bending moment creates tensile stress on the fiber opposite to the applied load face of the column and compressive stress on the face near the applied load, which leads to the formation of cracks on the tension face. The severity of the cracking is dependent on several factors, including the column's slenderness ratio, the magnitude of the eccentricity, and the compressive strength of the concrete. When the column is excessively slender and/or the eccentricity is large, the tensile stress on the tension face can become so high that it exceeds the tensile strength of the concrete, leading to the formation of cracks and potentially causing the column to fail.

3.2.1. Thermal profile

The thermal response for each set of specimens is presented in Fig. 7, in contrast to the first few minutes of each fire exposure, during which fire temperatures grew quickly, and the temperatures inside each column stayed constant. In addition, no plateau in temperature is seen, this plateau in temperature is a result of the latent heat spent by free capillary water in the column as it transforms from liquid to vapor also it can be since the PP fibers melt under high temperatures which creates paths for the water to escape [31]. As the bulk of this pore water evaporates, the rebar and concrete temperatures rise with the fire temperature [32]. In addition, the measures reveal that temperatures are lower inside the concrete core. This is due to the poor thermal conductivity and large thermal capacity of concrete, which impede the passage of heat energy into the interior layers of concrete [33, 34].

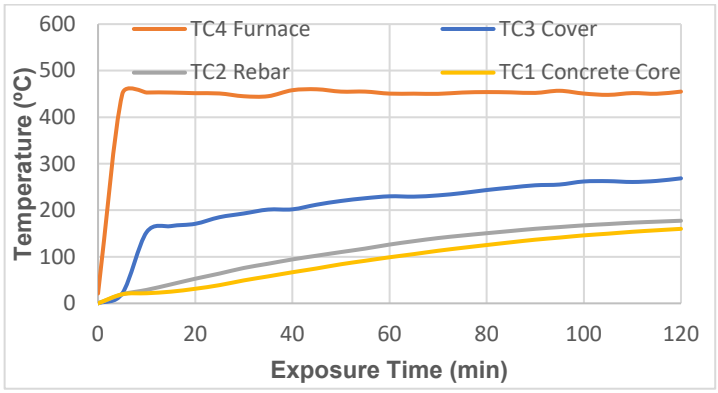

(a) Thermal profile for 450 °C fire exposure.

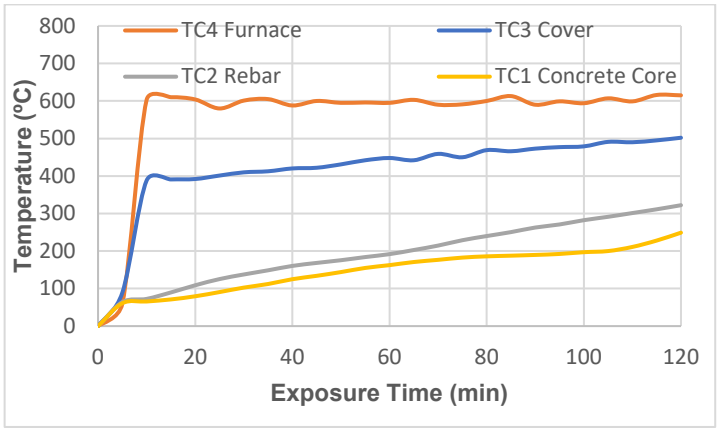

(b) Thermal profile for 600 °C fire exposure.

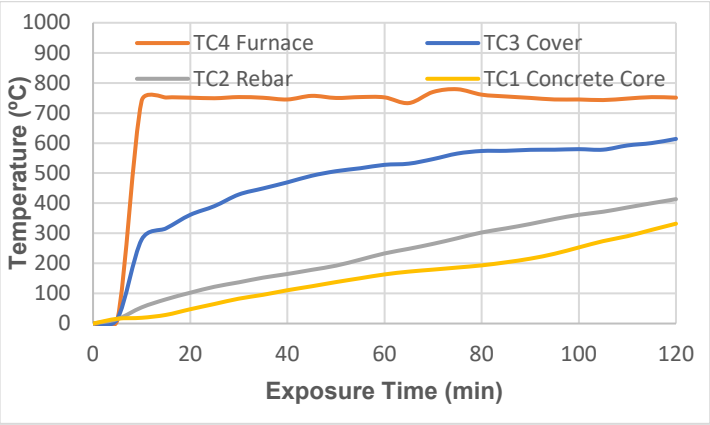

(c) Thermal profile for 750 °C fire exposure.

Figure 7. Thermal response of RPC during exposure phase.

3.2.2 Structural behavior of slender RPC column under fire

The structural behavior of RPC columns under fire is shown in Figs. 8 and 9, respectively. Lateral deformation was recorded for each set of temperature levels using a steel rod well isolated from heat using a 1200 °C ceramic blanket to prevent thermal expansion of the rod under fire and achieve accurate results. It can be noted that when comparing the same set of eccentricities with different temperatures, the deformation gets greater towards 750 °C, but when comparing different eccentricities for the same temperature, the set of e = 50 mm has higher deformation than others (Fig. 11), this is because the specimens with 50 mm eccentricity were subjected to a higher load, which makes the effect of temperature more noticeable on the specimen [35]. Also, the rate, at which the column deforms, gets lower over time.

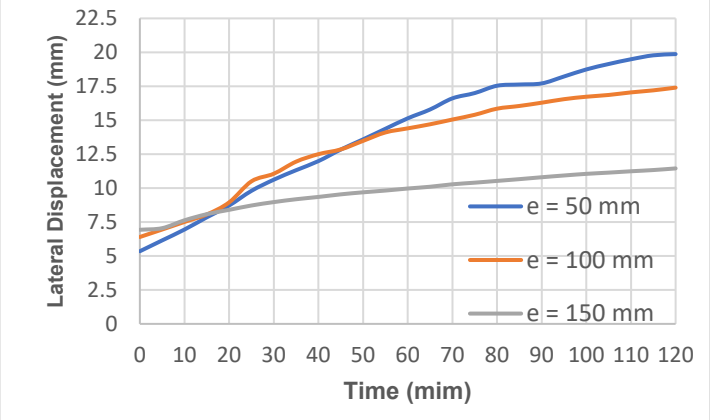

(a) Lateral displacement for 450 °C fire exposure.

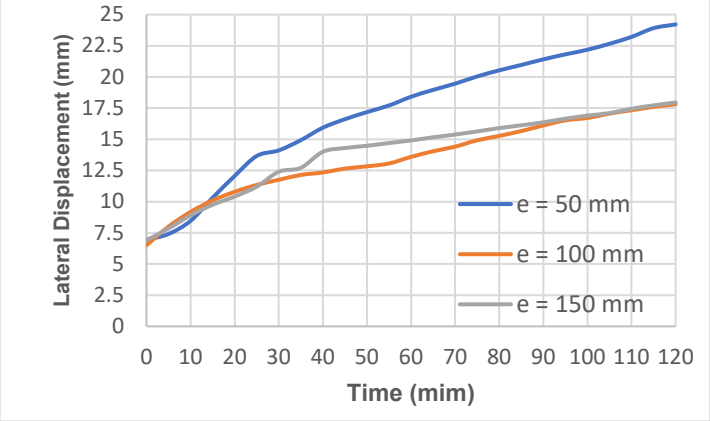

(b) Lateral displacement for 600 °C fire exposure.

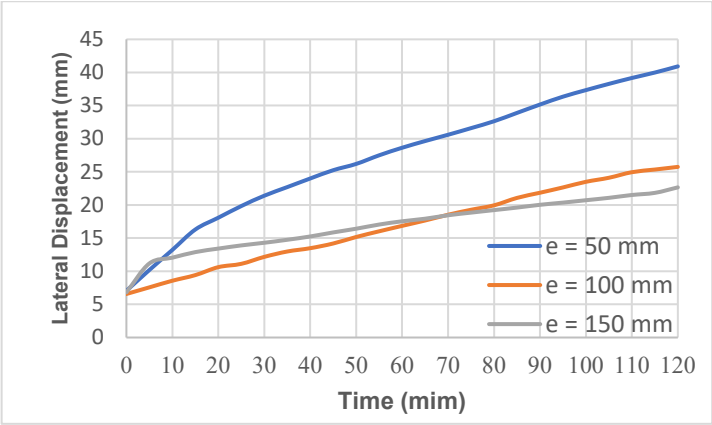

(c) Lateral displacement for 750 °C fire exposure.

Figure 8. Measured mid-height lateral displacement during fire exposure.

At the end of the test before unloading the column, the cracks that were previously formed in the tension face of the columns due to applied loads became very obvious and widened because of fire, this is due to the progressive loss in stiffness as the concrete loses its strength properties when exposed to fire, especially when the temperature reaches 200 °C and higher depending also on the amount of PP fiber in the mixture and fire duration [36, 37]. The crack patterns of the tested columns after exposure to 450°C, 600°C, and 750°C are shown in Figs 10a, 10b and 10c, respectively. In general, the cracks became more pronounced and widespread with increasing fire temperature.

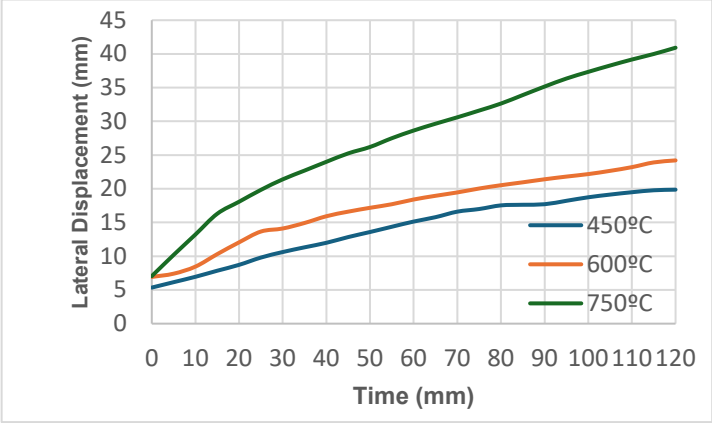

(a) Lateral displacement for 50 mm eccentricity.

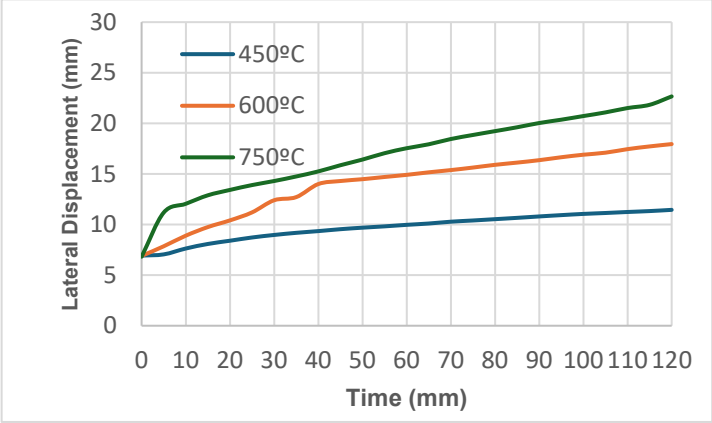

(b) Lateral displacement for 100 mm eccentricity.

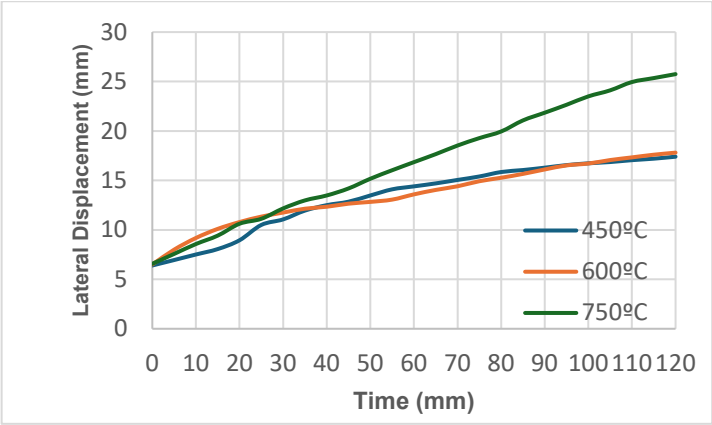

(c) Lateral displacement for 150 mm eccentricity.

Figure 9. Measured mid-height lateral displacement for different eccentricities.

(a) Crack pattern for 450 °C temp. Specimen.

(b) Crack pattern for 600 °C temp. Specimen.

(c) Crack pattern for 750 °C temp. Specimen.

Figure 10. Crack pattern for different fire level exposed specimens.

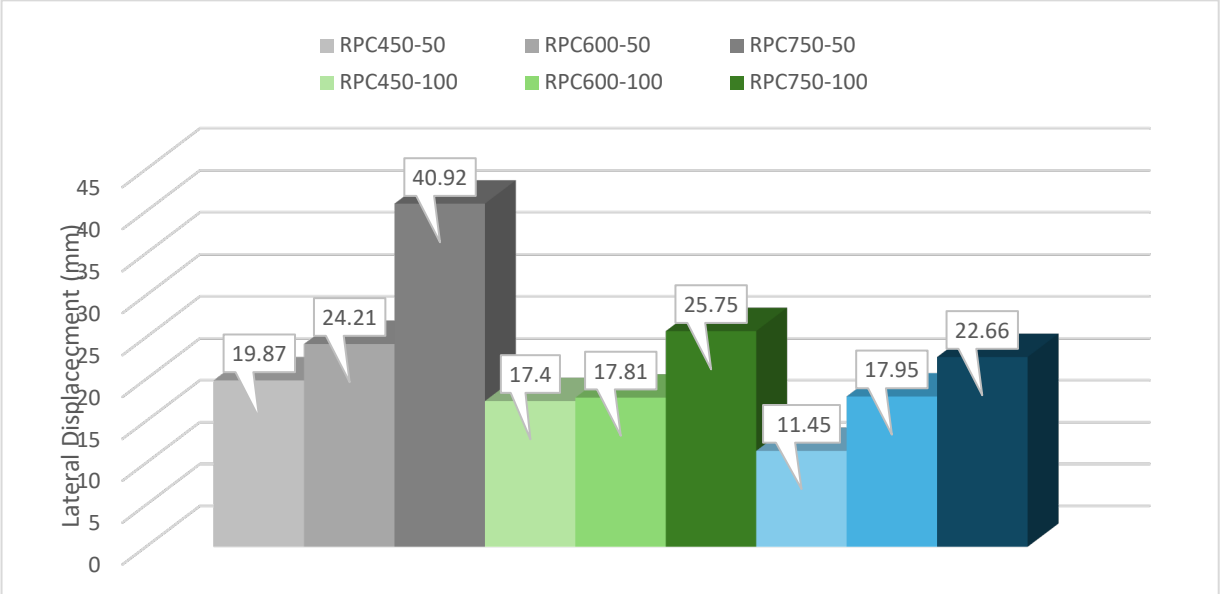

Figure 11. Max. Value of mid-height lateral displacement for RPC columns after 2 hours of fire.

4. Conclusions

In an attempt to investigate the structural behavior of RPC columns subjected to elevated temperatures, 9 specimens were made, specimens with different eccentricities of 50 mm, 100 mm, and 150 mm, each one subjected to fire flame of 450 °C, 600 °C, and 750 °C. Based on the results collected from the study, the following conclusions are summarized below:

1. The columns with the same cross-sectional area and reinforcement bars, applying 60 % of the ultimate load of each eccentricity, produce almost the same lateral deformation (±1 mm) before exposure to fire as the axial load decreases with increasing eccentricity.
2. The thermal profile (Fig. 7) shows simultaneous temperature rise in concrete core and steel reinforcement. For each exposure level of fire 450 °C, 600 °C, and 750 °C the temperature in the steel is 10 %, 18 %, and 20 % higher than the concrete core temperature at each time interval.
3. The difference in temperature between the cover of the specimens and the core of the specimens for 450 °C, 600 °C, and 750 °C is 40 %, 47 %, and 49 %, respectively, which indicates that the rate, at which the core temperature rises, is nearly identical for all levels of exposure.
4. The lateral deformation at 450 °C is higher by 14 % and 73 % when comparing 50 mm eccentricity with 100 mm and 150 mm, respectively, and all of the other groups show the same results, this is due to load intensity. It means that the effect of temperature is going to be more noticeable when the axial load is higher (Table 2).
5. When the eccentricity is constant, the temperature level will lead to more lateral deformation as it gets higher. The lateral buckling increased by 22 % and 106 % for columns subjected to 600 °C and 750 °C, respectively, compared to columns subjected to 450 °C.
6. The main conclusion is that in multistory buildings, the edge columns, which are subjected to axial load and uniaxial moment, are not considered to be more critical than internal columns, which subjected mainly to axial load.
7. The crack pattern depends on the eccentricity of loads and the temperature level around columns. More cracks with large penetrations to the concrete body are shown at higher eccentricities and higher temperatures.

References

1. Bajc, U., Kolšek, J.Č., Planinc, I., Bratina, S. Fire resistance of RC columns with regard to spalling of concrete. Fire Safety Journal. 2022. 130. Article no. 103568. DOI: 10.1016/j.firesaf.2022.103568
2. Al-Naqeeb, F., Al-Thairy, H. The behavior of reinforced concrete columns exposure to eccentric loads at high temperature. Journal of Physics: Conference Series. 2021. 1895(1). Article no. 012055. DOI: 10.1088/1742-6596/1895/1/012055
3. Santiago, A., da Silva, L.S., Real, P.V., Veljkovic, M. Numerical study of a steel sub-frame in fire. Computers & Structures. 2008. 86(15). Pp. 1619–1632. DOI: 10.1016/j.compstruc.2008.01.006
4. Raut, N., Kodur, V. Response of Reinforced Concrete Columns under Fire-Induced Biaxial Bending. ACI Structural Journal. 2011. 108(5). Pp. 610–619.
5. Abdulhaleem, K.N., Van Mohammed, R., Hamada, H.M., Humada, A.M., Majdi, A. Effect of Recycled Aggregate Concrete and Steel Fibers on the Strength of Self-Compacting Concrete. E3S Web of Conferences. 2023. 427. Article no. 02012. DOI: 10.1051/e3sconf/202342702012
6. Mohammed, V.R., Abdulhaleem, K.N., Hamada, H.M., Humada, A.M., Majdi, A. Effect of Recycled Aggregate Concrete and Steel Fibers on the Fresh Properties of Self-Compacting Concrete. E3S Web of Conferences. 2023. 427. Article no. 02013. DOI: 10.1051/e3sconf/202342702013
7. Fletcher, I., Welch, S., Torero, J., Carvel, R., Usmani, A. Behaviour of concrete structures in fire. Thermal Science. 2007. 11(2). 37–52. DOI: 10.2298/TSCI0702037F
8. Klak, F.S., Jomaa'h, M., Ahmad, S. Behavior of Reinforced Concrete Members Exposed to Fire: Review Article. Tikrit Journal of Engineering Sciences. 2022. 29(4). Pp. 56–68. DOI: 10.25130/tjes.29.4.7
9. Al-Zuhairi, A.H., Al-Ahmed, A.H.A., Hanoon, A.N., Abdulhameed, A.A. Structural behavior of reinforced hybrid concrete columns under biaxial loading. Latin American Journal of Solids and Structures. 2021. 18(6). Article no. e390. DOI: 10.1590/1679-78256640
10. Richard, P., Cheyrezy, M. Composition of reactive powder concretes. Cement and Concrete Research. 1995. 25(7). Pp. 1501–1511. DOI: 10.1016/0008-8846(95)00144-2
11. Richard, P., Cheyrezy, M.H. Reactive Powder Concretes with High Ductility and 200-800 MPa Compressive Strength. Concrete Technology: Past, Present, and Future, SP-144. American Concrete Institute. Farmington Hills, MI, 1994. Pp. 507–518.
12. Shi, C., Wang, D., Wu, L., Wu, Z. The hydration and microstructure of ultra high-strength concrete with cement–silica fume–slag binder. Cement and Concrete Composites. 2015. 61. Pp. 44–52. DOI: 10.1016/j.cemconcomp.2015.04.013
13. Sivakrishna, A., Adesina, A., Awoyera, P., Rajesh Kumar, K. Green concrete: A review of recent developments. Materials Today: Proceedings. 2020. 27(1). Pp. 54–58. DOI: 10.1016/j.matpr.2019.08.202
14. Yazıcı, H., Yardımcı, M.Y., Yiğiter, H., Aydın, S., Türkel, S. Mechanical properties of reactive powder concrete containing high volumes of ground granulated blast furnace slag. Cement and Concrete Composites. 2010. 32(8). Pp. 639–648. DOI: 10.1016/j.cemconcomp.2010.07.005

15. Savadkoohi, M.S., Reisi, M. Environmental protection based sustainable development by utilization of granite waste in Reactive Powder Concrete. Journal of Cleaner Production. 2020. 266. Article no. 121973. DOI: 10.1016/j.jclepro.2020.121973
16. Sanjuán, M.Á., Andrade, C. Reactive Powder Concrete: Durability and Applications. Applied Sciences. 2021. 11(12). Article no. 5629. DOI: 10.3390/app11125629
17. Wattanapornprom, R., Valerio, D., Pansuk, W., Nguyen, T., Pheinsusom, P. Fire Resistance Performance of Reactive Powder Concrete Columns. Engineering Journal. 2018. 22(4). Pp. 67–82. DOI: 10.4186/ej.2018.22.4.67
18. Chadli, M., Tebbal, N., Mellas, M. Impact of elevated temperatures on the behavior and microstructure of reactive powder concrete. Construction and Building Materials. 2021. 300. Article no. 124031. DOI: 10.1016/j.conbuildmat.2021.124031
19. Abdulraheem, M.S., Kadhum, M.M. Experimental investigation of fire effects on ductility and stiffness of reinforced reactive powder concrete columns under axial compression. Journal of Building Engineering. 2018. 20. Pp. 750–761. DOI: 10.1016/j.jobe.2018.07.028
20. Jomaa'h, M.M., Salahaldin, A.I., Saber, Q.A., Raheem, A.M. Large Scale Laboratory Setup for Testing Structural Performance of Slender High-Strength Concrete Columns Subjected to Axial Load and Fire: A Preliminary Study. Geotechnical Engineering and Sustainable Construction. Springer. Singapore, 2022. Pp. 611–626. DOI: 10.1007/978-981-16-6277-5_49
21. Kadhum, M. Prediction of mechanical properties of reactive powder concrete by using artificial neural network and regression technique after the exposure to fire flame. Jordan Journal of Civil Engineering. 2015. 9(3). Pp. 381–399. DOI: 10.14525/jjce.9.3.3079
22. Izzat, A.F. Effect of Fire Flame (High Temperature) on the Behaviour of Axially loaded Reinforced SCC Short Columns. Journal of Engineering. 2012. 18(8). Pp. 889–904.
23. Izzat, A.F. Retrofitting of Reinforced Concrete Damaged Short Column Exposed to High Temperature. Journal of Engineering. 2015. 21(3). Pp. 34–53. DOI: 10.31026/j.eng.2015.03.03
24. Iraqi Standard Specification No.5, Portland Cement. Baghdad: Central Agency for Standardization and Quality Control. Baghdad, 1984. 8 p.
25. ASTM C33/C33M-16: Standard Specifications for Concrete Aggregates. West Conshohocken, PA: American Society for Testing and Materials; 2016. 11 p.
26. Building Code Requirements for Structural Concrete (ACI 318-19): An ACI Standard; Commentary on Building Code Requirements for Structural Concrete (ACI 318R-19). American Concrete Institute, 2019. 12 p.
27. ASTM C192/C192M-16: Standard Practice for Making and Curing Concrete Test Specimens in the Laboratory. West Conshohocken, PA: American Society for Testing and Materials, 2016. 8 p.
28. Abdulrahman, M., Al-Attar, A., Ahmad, M. Effect of different curing conditions on the mechanical properties of reactive powder concrete. MATEC Web of Conferences. 2018. 162. Article no. 02014. DOI: 10.1051/matecconf/201816202014
29. Shi, C., Wu, Z., Xiao, J., Wang, D., Huang, Z., Fang, Z. A review on ultra high performance concrete: Part I. Raw materials and mixture design. Construction and Building Materials. 2015. 101(1). Pp. 741–751. DOI: 10.1016/j.conbuildmat.2015.10.088
30. ASTM E119-16: standard methods of fire test of building construction and materials. West Conshohocken, PA: American Society for Testing and Materials. 22 p.
31. Said, M., Abd El-Azim, A.A., Ali, M.M., El-Ghazaly, H., Shaaban, I. Effect of elevated temperature on axially and eccentrically loaded columns containing Polyvinyl Alcohol (PVA) fibers. Engineering Structures. 2020. 204. Article no. 110065. DOI: 10.1016/j.engstruct.2019.110065
32. Kodur, V., Hibner, D., Agrawal, A. Residual response of reinforced concrete columns exposed to design fires. Procedia Engineering. 2017. 210. Pp. 574–581. DOI: 10.1016/j.proeng.2017.11.116
33. Liu, H.B., Tian, K.P., Liu, J.H., Ju, Y. Experiment on Thermophysical Properties of Reactive Powder Concrete. Advanced Materials Research. 2012. 374–377. Pp. 1519–1522. DOI: 10.4028/www.scientific.net/AMR.374-377.1519
34. Li, H., Hao, X., Qiao, Q., Zhang, B., Li, H. Thermal Properties of Hybrid Fiber-Reinforced Reactive Powder Concrete at High Temperature. Journal of Materials in Civil Engineering. 2020. 32(3). Article no. 04020022.
35. Ali, F., Nadjai, A., Choi, S. Numerical and experimental investigation of the behavior of high strength concrete columns in fire. Engineering Structures. 2010. 32(5). Pp. 1236–1243. DOI: 10.1016/j.engstruct.2009.12.049
36. Zheng, W., Luo, B., Wang, Y. Microstructure and mechanical properties of RPC containing PP fibres at elevated temperatures. Magazine of Concrete Research. 2014. 66(8). Pp. 397–408. DOI: 10.1680/macr.13.00232
37. Mohamed Bikhiet, M., El-Shafey, N.F., El-Hashimy, H.M. Behavior of reinforced concrete short columns exposed to fire. Alexandria Engineering Journal. 2014. 53(3). Pp. 643–653. DOI: 10.1016/j.aej.2014.03.011

Information about authors:

Wael Almakinachi,
ORCID: https://orcid.org/0000-0002-5798-3138
E-mail: waelrami@uokirkuk.edu.iq

Ali Ihsan Salahaldin, *PhD*
ORCID: https://orcid.org/0000-0002-4198-7505
E-mail: ali.ihsan@uokirkuk.edu.iq

Received 15.02.2023. Approved after reviewing 08.10.2025. Accepted 08.10.2025.

Magazine of Civil Engineering

ISSN 2712-8172

journal homepage: http://engstroy.spbstu.ru/

Research article

UDC 532.559.3

DOI: 10.34910/MCE.140.7

Diverging flow in Y-junctions: laminar, transitional and turbulent

V.V. Lemanov ✉ , ***V.A. Fedorenko***, ***K.A. Sharov***

Kutateladze Institute of Thermal Physics, Novosibirsk, Russian Federation

✉ *lemanov@itp.nsc.ru*

Keywords: Y-junctions, diverging flow, hydraulic resistance, laminar-turbulent transition, critical Reynolds number, velocity fluctuation.

Abstract. This investigation is aimed at determining flow regimes in Y-junctions with flow division. Air velocity and velocity pulsations are measured using a hot-wire anemometer in a wide range of Reynolds numbers Re = 400–6000. A junction with diameter *d* = 6 mm is chosen as the object of study for the inlet and two outlet channels: a symmetrical arrangement of the outlet channels with an angle of 50 º between them. A long tube with diameter *d* = 6 mm and length *l*/*d* = 333 is connected to the junction inlet. Two techniques of the flow regime diagnostics have been developed. For the inlet channel of the junction, the critical Reynolds number is Re = 2000 (puff-type vortex structures appear for the first time). For two outlet channels, a significant increase in velocity pulsations occurs at lower Reynolds numbers Re = 1640–1660. By analogy with diagnostics of the flow movement in a round tube, the following classification of flow regimes in a junction is proposed: laminar flow at Re < 1640–1660, transitional flow at Re = 1660–2800, and turbulent flow at Re > 3000. The obtained data can be used to clarify the range of data for laminar, transitional, and turbulent flow regimes in round Y-junctions with flow division.

Funding: The work was carried out within the framework of the state assignment of the IT SB RAS (project No. 126021217059-6).

Citation: Lemanov, V.V., Fedorenko, V.A., Sharov, K.A. Diverging flow in Y-junctions: laminar, transitional and turbulent. Magazine of Civil Engineering. 2025. 18(8). Article no. 14007. DOI: 10.34910/MCE.140.7

1. Introduction

When liquids and gases move along tubes and channels, various elements of supply line systems (confusers, diffusers, turning channels, junctions, etc.) are widely used. It is known that hydraulic losses in these elements depend on three flow regimes: laminar, transitional and turbulent [1, 2]. However, determining the boundaries of the laminar-turbulent transition region in complex supply lines elements remains a complex problem, in particular, this applies to junctions. A junction is a part of a supply line that connects one supply line with two channels. Such an element is widely used both in ventilation air supply systems and in hydraulic mains [1, 2]. Thus, the object of research of this work is the diagnostics of flow regimes in a Y-junction.

It should be noted that junctions have a wide range of applications in industry, for example, in two-phase flow devices [3, 4], in micro-reactors of chemical technologies [5]. Junction systems are also found in medicine in the form of the human circulatory [6] and respiratory system [7].

One of the important questions in designing supply lines with junctions is determining local hydraulic resistance [2, 8, 9]. A review of the literature showed that in practice, mainly large Reynolds numbers are encountered; therefore, total pressure losses are most well studied for the turbulent flow regime [1, 2, 8–11]. Since large Reynolds numbers are most common in practice, the total pressure losses have been

studied best for the turbulent flow regime [1, 2, 8–11]. Thus, the well-known book [1] mainly provides data for Re > 10000. Laminar regimes usually correspond to low Reynolds numbers (Re < 2000) [10, 12] and are effectively implemented by numerical modeling using modern commercial codes [12–15]. For the case of turbulent flow at large Reynolds numbers (Re > 4000), both empirical correlations based on experimental data and numerical methods for various turbulence models are used [15–18]. At the same time, laminar-turbulent transition regimes in Junctions have been studied insufficiently [1, 12, 19].

The relevance of this problem is related to the unclear of determining the boundaries of the laminar-turbulent transition in complex flows. This state of research in turn depends on the achievements of the modern theory of hydrodynamic stability. This is due to the problem of determining the boundaries of the laminar-turbulent transition in complex flows. There are numerous factors that affect the flow pattern. The curvature of the streamlines can lead to the formation of Dina vortices: due to a change of geometry in the dividing edge area, separated and secondary flows arise, local non-stationarity, spiral and vortex flows, etc. are possible [9, 15, 16]. Recently, new data on the laminar-turbulent transition in pipes and channels have been obtained [20–24]. In particular, a new scenario of transition in pipes through the intermittency mechanism associated with the formation of large-scale structures (puff) has been discovered [20–22]. In this regard, the main idea of this study was to apply the latest achievements to clarify the boundaries of the laminar-turbulent transition in junctions. Thus, the purpose of the work is to diagnose flow regimes in Y-junctions. In this case, two problems were solved. First, to determine the criterion by which three flow regimes can be distinguished (laminar, transitional and turbulent). Second, to diagnose the flow regime both in the inlet channel and in the two outlet channels of the junction.

In this paper, three flow regimes in a round Y-junction with a symmetrical arrangement of outlet channels and an angle of 50 º between them in the range of Reynolds numbers Re = 400–6000 is experimentally studied. The main attention is paid to measuring the air flow velocity and its pulsations using a hot-wire anemometer, both at the inlet and outlet of the junction. Two criterion and accordantly two original methods for determining the region of laminar-turbulent transition during air movement in a junction with flow diverging are considered. Such diagnostics allow us to consider the flow regimes in the junction inlet and outlet channels.

2. Methods

The scheme of setup for experimental study of air flow regimes in a round Y-junction with symmetrical arrangement of outlet channels consists of the pneumatic and electrical parts (Fig. 1).

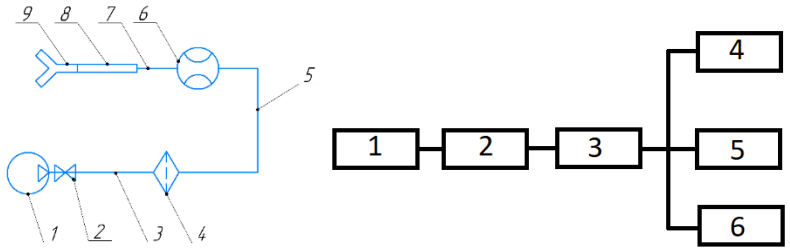

a) b)

Figure 1. Experimental setup: a) Pneumatic diagram: 1 – compressor; 2 – valve; 3 – supply line; 4 – filter system; 5 – supply line; 6 – flow regulator; 7 – supply line; 8 – tube; 9 – Y-junction; b) electrical circuit: 1 – probe; 2 – bridge; 3 – linearizer; 4 – average-reading voltmeter; 5 – RMS voltmeter; 6 –oscilloscope.

The operating principle of the pneumatic part of setup is as follows. Air from the atmosphere is compressed by the SB4/S-200.LB40 compressor and enters the 200-liter receiver (1). Valve (2) supplies air from the compressor under a pressure of 3.5 bar via supply line (3) to a system of three filters (4) (AME 350C–F04, AME 350C–F04, and AME 350C–F04–T) to remove oil and moisture. Then, air via supply line (5) enters the Bronkhorst Mass View flow regulator (6). As a result, air via supply line (7) enters a straight aluminum round tube (8) (length l = 2 m, internal diameter d = 6 mm, l/d = 333) and then flows out of the Y-junction (9). Connecting lines (3, 5, 7) are made of polyurethane plastic round tube with internal diameter d = 6 mm and length of 2, 15, and 10 m, respectively. The Y-junction (9) is printed on a 3D printer with internal diameters at the inlet and outlet of 6 mm, inlet channel length of 30 mm and two symmetrically located outlet channels 50 mm long (N1, N2); the flow separation angle is 50 º. All measurements are carried out with the compressor off; the receiver used as the source of compressed air. The thermodynamic parameters of air in the experiments correspond to atmospheric pressure and room temperature.

The electrical part of the setup is designed to record the air flow velocity. For this purpose, a constant temperature hot-wire anemometer (CTA) from Disa Elektronik was used; it consisted of: a miniature

DISA55P11 probe (1), a 55M01 bridge (2), a DISA55D10 linearizer (3), and DISA55D31 (4) and DISA55D35 (5) average-reading and root-mean-square voltmeters. The CTA operating principle is based on the dependence of the probe wire heat transfer on the gas flow velocity. The main part of the hot-wire anemometer is a measuring bridge (1), where a sensitive element in the form of a tungsten wire attached to thin conductive rods (2) is included in one arm. Then, after linearization (3), the bridge voltage is recorded by average-reading "*Ea*" (4) and root-mean-square "*e*" (5) voltmeters. The hot-wire anemometer sensor was calibrated on this setup (with the disconnected junction) using the tested flow regimes at the outlet of the tube (8). The calculation was performed using the linear formula: $Ua = a \cdot Ea$, $u = a \cdot e$, where *Ea* and *e* are the average-reading and root-mean-square values of the hot-wire anemometer bridge voltage, *a* is the calibration coefficient. Thus, the average velocity *Ua* and root-mean-square values of velocity pulsations *u* and air flow turbulence degree $Tu = (u/Ua) * 100$ % were measured using the sensor calibration and the readings of two voltmeters. The RIGOL DS1054Z digital oscilloscope (6) was used to observe the hot wire anemometer signal in real time [$E = f(t)$]. Then, using the Ultra Scope program, the data from the oscilloscope were transferred to the computer and processed in the Excel program.

Graphical dependences of the flow velocity on time $U = f(t)$, as well as dependences on the Re number were plotted for the average velocity (*Ua*) and the root-mean-square pulsations of velocity (*u*). Here, $Re = 4*Q/\pi*d*v$, where *Q* is the volumetric air flow rate, *d* is the internal diameter, and *v* is the kinematic viscosity of air.

To study the flow in a junction, two measurement techniques were modified. The first technique is based on the registration of large-scale turbulent structures, which are called "puff" in the literature [20–22]. They are formed during the laminar-turbulent transition in long round tubes [20–24]. The change in velocity over time (*t* = 1–1.5 s) in such a structure is shown in Fig. 2a. The measurements were performed at the outlet of the tube (8) on the axis for Re = 2109 without a junction. A puff has characteristic features that distinguish it from other types of disturbances: a smooth leading edge and a steep trailing edge. A significant decrease in the instantaneous velocity by 30–40% is also observed, and the puff length can reach 20–40 *d*. In Fig. 2a, a laminar section of the flow is observed at time intervals *t* = 0–1 s and *t* = 1.5–2 s. With increasing Reynolds number Re > 2109, the number of such structures increases. When turning to turbulence through the intermittency scenario, the flow becomes completely chaotic and there are no laminar regions [20–22]. These characteristic features of the puff were observed in our experiments [23–24], indicating a laminar-turbulent transition in the tube (8). The second technique is based on recording velocity pulsations with increasing Reynolds number [23, 25]. This method is used for stochastic behavior of velocity pulsations, i.e., when there are no characteristic vortex structures in the flow. An example of such velocity behavior is shown in Fig. 2b. The measurements were performed at the outlet of the junction (9) on the axis for Re = 1664. As can be seen, a chaotic change in the instantaneous velocity value over time is observed and there are no signal features that differ from a random process. In this case, the main flow characteristic is the root-mean-square pulsations of velocity *u* and the degree of flow turbulence *Tu*. The growth of these parameters with increasing Reynolds number indicates flow turbulence intensification, and a decrease in these parameters indicates turbulence attenuation.

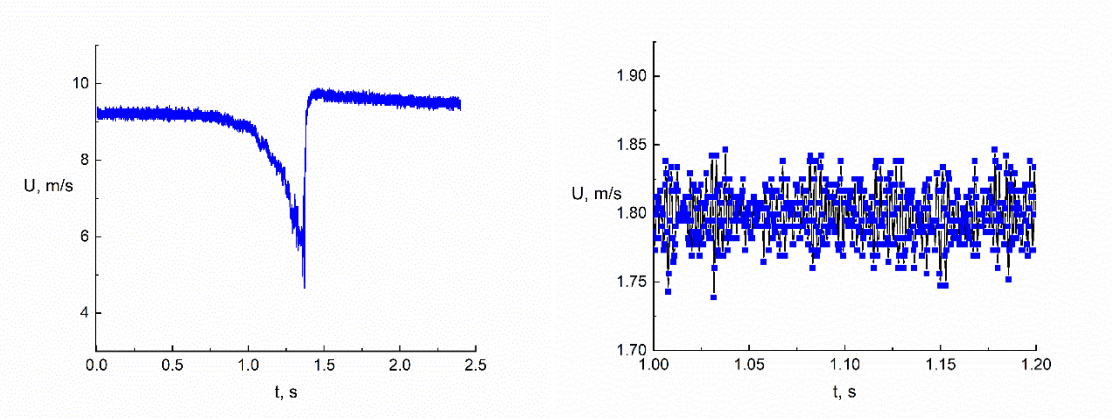

Figure 2. Variation of instantaneous velocity over time:
a) round tube outlet, Re = 2109; b) Y-junction outlet, Re = 1664.

3. Results and Discussion

The work is aimed at determining the flow regimes in a Y-junction with flow division. Two methods were used for analyzing the data obtained. The velocity and velocity pulsations were measured both at the inlet and two outlets (N1, N2) of the Y-junction in the range of Reynolds numbers Re = 400–6000. The

ranges of Reynolds numbers characteristic of laminar, transitional and turbulent flow regimes in such a junction were obtained.

The dependence of the average velocity change on the Reynolds number for the tube outlet and junction outlets N1 and N2 is presented in Fig. 3. At that, the Re number in all cases is determined by the air flow rate and the diameter of the inlet tube *d*. The flow velocity was measured on the tube axis and on the axis of the junction outlets. The data for the tube were obtained without a junction. Since the inlet part of the junction is 30 mm, and the length of the supply tube is 2 m, we believe that the data at the tube outlet correspond well to the flow parameters near the channel separation zone. In this case, the first method for determining the laminar-turbulent transition in the tube by diagnosing large-scale structures was applied; according to this method, the critical Reynolds number was Re = 2000. According to Fig. 3, three flow regimes can be distinguished for a round tube: a laminar regime at Re < 2000 (no puffs), a transitional regime (with puffs) at Re = 2000–2800; and a turbulent regime (no sections of laminar regime) at Re > 3000. For a round tube, a decrease in the velocity on the channel axis in the region of Re = = 2492–2800 is associated with a change in the velocity profile from the parabolic one, characteristic of the laminar flow, to the power-law profile, responsible for the turbulent flow. These data correlate well with the works of other authors [20, 21]. For the case of junctions (outlets N1 and N2), an almost monotonic increase in the average velocity vs. the Reynolds number is observed, without any peculiarities in the region of Re = 2000–2800, when a laminar-turbulent transition is observed in the inlet tube.

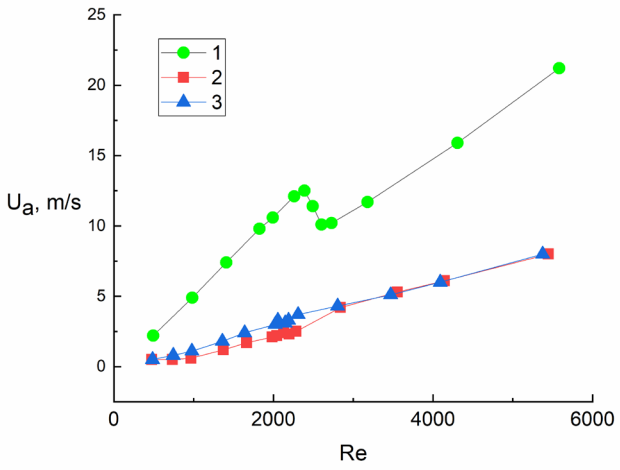

Figure 3. Velocity change in the junction:
1 – round tube outlet; 2 – outlet of junction No.1; 3 – outlet of Y-junction No.2.

In addition to the data on the average velocity, statistical data in the form of a dependence of the root-mean-square pulsations of velocity *u* on the Reynolds number Re were obtained in this work (Fig. 4). If the measurements are carried out at the tube outlet, the regime of laminar-turbulent transition is also well diagnosed using the second technique by a significant increase and decrease in velocity pulsations in a narrow range Re = 2000–2800, which corresponds to the known data for the transition in a tube [20, 23]. For Re = 2800–6000, an insignificant increase in velocity pulsations in the turbulent flow regime is observed.

For two junction outlets N1 and N2, the pulsations are approximately the same in the entire range of Re = 400–6000. A significant increase in *u* begins approximately at Re = 1640–1660, which is lower than the critical numbers for the tube outlet Re = 2000. For Re = 1640–2000, the flow regime on the oscilloscope looks like stochastic. An example of such a flow is shown in Fig. 2b. For the regime with puffs (Re = = 2000–2800), the behavior of the velocity pulsations at the junction outlet correlates with a change in *u* for the inlet tube. At Re > 2800, a slight increase in *u* is observed both for the inlet tube and for the two junction outlets. At that, the values of velocity pulsations for the junction are higher than that for the inlet tube.

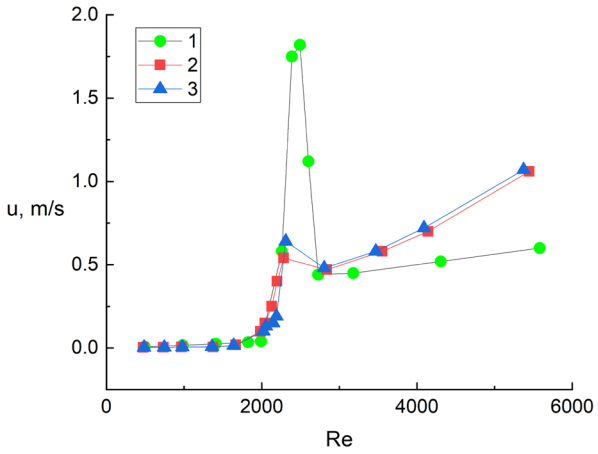

Figure 4. Velocity pulsations in the junction:
1 – round tube outlet; 2 – outlet of Y-junction No.1; 3 – outlet of Y-junction No.2.

By combining the data obtained in Figs. 3, 4, we can plot a diagram of the dependence of turbulence degree *Tu* on Reynolds number Re, which is shown in Fig. 5. Note that the value of *u* is normalized here to the value of the local velocity at the measurement point. The behavior of the turbulence degree for the tube corresponds to the data in Figs. 3 and 4, i.e., there is an extremum in the transition region. The *Tu* parameters for the junction outlets N1 and N2 are qualitatively the same in the entire range of Re numbers. This figure shows clearly that the growth of *Tu* for the junction begins with the Reynolds numbers significantly lower than the critical numbers for the tube outlet. The maximum values of velocity pulsations for the tube are *Tu* = 16 %; for the junction, *Tu* = 12–22 %, and they are located in the range Re = = 2300–2400. Thus, extreme turbulence corresponds approximately to the maximum pulsations in the inlet round channel. At Re > 3000, a slight decrease in *Tu* is observed for the inlet tube. It should be also noted that at Re > 3000, the turbulence level for the junction outlets N1 and N2 is approximately twice as large as *Tu* for the round tube outlet. By analogy with the diagnostics of flow movement in a round tube, the following classification of flow regimes in the junction is proposed. Laminar regime occurs at Re < 1640–1660, transitional regime occurs at Re = 1660–2800, and the turbulent one takes place at Re > 3000.

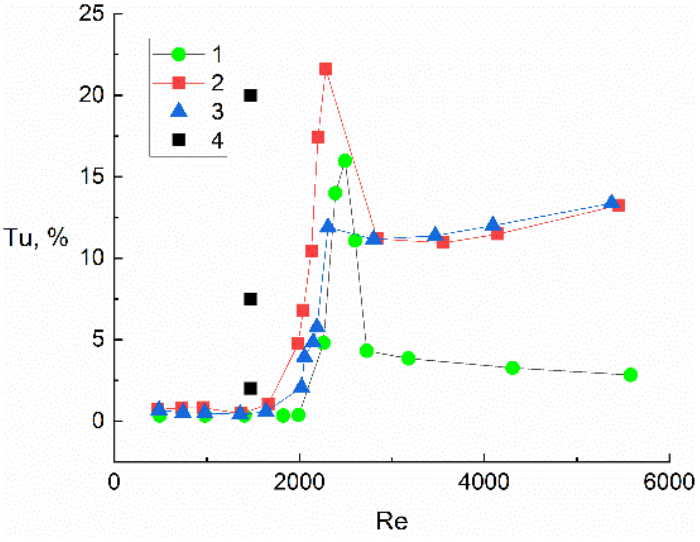

Figure 5. Degree of turbulence in the junction:
1 – round tube outlet; 2 – outlet of Y-junction No. 1; 3 – outlet of Y-junction No. 2, 4 – [26].

For comparison, data [26] are provided for a round Y-junction with an angle of 50 ° and a straight-through channel at Re = 1475. In this case, separated flow is observed. As a result, the turbulence level increases from *Tu* = 2 % in the inlet channel to higher values in the outlet channels. Moreover, due to the asymmetry of the tee geometry, on the axis in the straight outlet channel *Tu* = 20 %, and in the inclined channel – *Tu* = 7.5 %.

4. Discussion

The study is aimed at determining the boundaries for three flow regimes in a junction. The experiments were carried out using a constant-temperature hot-wire anemometer in an air flow. The values of instantaneous velocity, average velocity, and root-mean-square velocity pulsation were measured in a round Y-junction in a wide range of Reynolds numbers Re = 400–6000. A junction with diameter d = 6 mm for the inlet and outlet channels was chosen as the object of study for a symmetrical arrangement of the outlet channels with an angle of 50 º between them. For the first time, two methods for diagnosing flow regimes during air movement in a junction were proposed. The first diagnostics is based on recording large-scale turbulent structures of the puff type [20–24], which are formed during the laminar-turbulent transition in long round tubes. It is used to determine the flow regime in the junction inlet channel, when intermitting single long vortex structures of the puff type appear along with the laminar flow. The second method is based on recording velocity pulsations with an increase in the Reynolds number [24, 25]. This method is used for chaotic behavior of velocity pulsations, i.e., when there are no organized vortex structures in the flow. The second diagnostics is used both for the inlet channel and for two outlet channels of the junction. The conditions at the junction inlet are of significant importance for determining the flow regime [9]. In this study, a long round tube (d = 6 mm, l/d = 333) was placed at the junction inlet; at the exit of this tube, a velocity profile corresponding to certain flow regimes was formed: parabolic profile for the laminar flow, the transitional profile in the region of intermediate Re numbers, and the power-law profile for the turbulent flow regime. The use of other geometries of the inlet section before the junction is a special problem and it requires additional study.

The flows in the inlet and outlet channels of Y-junctions must be considered separately. For the inlet channel, the critical Reynolds number is Re = 2000 (single puff-type structures appear for the first time). The transition to turbulence occurs at Re = 2800, when puff-type structures follow continuously and laminar sections are absent. These data are in good agreement with known works for the transition in a pipe [20, 23]. At the same time, for the two outlet channels, a significant increase in pulsations occurs at lower Reynolds numbers Re = 1640–1660. In this case, the behavior of the instantaneous velocity value is of a random character and puff-type structures are not observed. New data indicate that the laminar-turbulent regime in junctions can occur at Reynolds numbers significantly lower than Re = 2000. Such low critical Reynolds numbers for symmetrical Y-junctions have not been published in the literature before. Local turbulization is known in the literature at Reynolds numbers Re = 1460–1475 for fluid flow in an asymmetric Y-tee [26,27]. For pressure Y-junctions, for example, in [1], the values Re = 2000–3000 obtained in experiments are given, in the calculations [13, 19], the value Re = 2200–2300 was obtained. This difference may be due to the fact that the laminar-turbulent transition mode in experiments is determined by measurements of the average value of the pressure drop. At the same time, measurements of velocity pulsations have a significantly higher sensitivity [20]. From the point of view of numerical modeling, accurate calculations by the DNS (Direct Numerical Simulation) method in junctions have not yet been carried out.

Apparently, the reason for a decrease in the critical Reynolds number in the Y-junction is the complex three-dimensional flow in the separation region. It is known that in Y-junctions, separation and secondary flows, non-stationarity spiral and vortex structures can occur [9, 15, 16]. These processes can play the role a trigger for an earlier laminar-turbulent transition, but further study is required to determine the real causes of this phenomenon. In the region of high Reynolds numbers (Re > 3000), the turbulence level for the junction outlets is approximately twice as high as the turbulence level at the outlet of a round tube. This suggests that in a Y-junction, the generation of turbulent energy exceeds the pulsation energy generated by the formation of puff structures in round tubes.

5. Conclusions

Recently, new data have been obtained on the laminar-turbulent transition in pipes and channels [21, 22]. In this regard, the main objective of this study was to apply the latest achievements in the field of transition to clarify the boundaries of the three flow regimes in junctions. Based on the conducted research, the following conclusions can be drawn.

1. A new experimental method has been developed for determining the flow regimes (laminar, transitional and turbulent) in a junction based on two criteria: the presence of puff-type vortex structures and the degree of flow turbulence.
2. For the inlet part of the junction, the main criterion is the presence of puff-type vortex structures and the degree of flow turbulence.
3. For the two outlet parts of the junction, the main criterion is the degree of flow turbulence.

4. For the conditions of our experiment, the following values were obtained for the outlet part of the round Y-junction: laminar mode – Re < 1640–1660, transitional – Re = 1660–2800, turbulent – Re > 3000.

The program of further research includes the study of flow regimes and local hydraulic losses with variations in the main parameters of round junctions (flow separation angle, ratio of inlet and outlet diameters, effect of the dividing edge, and geometry of inlet part before the junctions). The obtained data can be recommended for specifying the range of laminar, transitional and turbulent flow regimes in round Y-junctions with flow separation.

References

1. Idelchik, I.E. Handbook of Hydraulic Resistance. 4th edn. Begell House. Danbury, 2007. 878 p. DOI: 10.1615/978-1-56700-251-5.0
2. Rennels, D.C. Pipe Flow: A Practical and Comprehensive Guide. 2nd edn. Wiley. Hoboken, 2022. 387 p. DOI: 10.1002/9781119756460
3. Morris, J.F. Toward a fluid mechanics of suspensions. Physical Review Fluids. 2020. 5. Article no. 110519. DOI: 10.1103/PhysRevFluids.5.110519
4. Lu, P., Zhao, L., Zheng, N., Liu, S., Li, X., Zhou, X., Yan, J. Progress and prospect of flow phenomena and simulation on two-phase separation in branching T-junctions: A review. Renewable and Sustainable Energy Reviews. 2022. 167. Article no. 112742. DOI: 10.1016/j.rser.2022.112742
5. Dong, Z., Wen, Z., Zhao, F., Kuhn, S., Noël, T. Scale-up of micro-and milli-reactors: An overview of strategies, design principles and applications. Chemical Engineering Science: X. 2021. 10. Article no. 100097. DOI: 10.1016/j.cesx.2021.100097
6. Carpenter, H.J., Gholipour, A., Ghayesh, M.H., Zander, A.C., Psaltis, P.J. A review on the biomechanics of coronary arteries. International Journal of Engineering Science. 2020. 147. Article no. 103201. DOI: 10.1016/j.ijengsci.2019.103201
7. Faizal, W.M., Ghazali, N.N.N., Khor, C.Y., Badruddin, I.A., Zainon, M.Z., Yazid, A.A., Ibrahim, N.B. Computational fluid dynamics modelling of human upper airway: A review. Computer Methods and Programs in Biomedicine. 2020. 196. Article no. 105627. DOI: 10.1016/j.cmpb.2020.105627
8. Gorunovich, S.B. Poteri davleniya v truboprovodakh. Troyniki [Pressure losses in pipelines. Tees]. Novosti Teplosnabzheniya [Heating News]. 2010. 4. Pp. 15–21.
9. Bassett, M.D., Winterbone, D.E., Pearson, R.J. Calculation of steady flow pressure loss coefficients for pipe junctions. Proceedings of the Institution of Mechanical Engineers, Part C: J. Mechanical Engineering Science. 2001. 215(8). Pp. 861–881. DOI: 10.1177/095440620121500801
10. Kiser, C.C., Handy, T.A., Lemley, E.C., Papavassiliou, D.V., Neeman, H.J. Reynolds Number Dependence for Laminar Flow Loss Coefficients in Tee and Wye Junctions. American Society of Mechanical Engineers. Fluids Engineering Division (Publication) FEDSM. 1. Pp. 341-347. DOI: 10.1115/FEDSM-ICNMM2010-31026
11. Kalenik, M., Chalecki, M., Wichowski, P. Real Values of Local Resistance Coefficients during Water Flow through Welded Polypropylene T-Junctions. Water. 2020. 12(3). Article no. 895. DOI: 10.3390/w12030895
12. Ring, B.P., Lin, Y., Henderson, A.W., Hossan, M., Lemley, E.C. Reynolds number dependence of laminar loss coefficients for a rectangular-cross section square-cornered tee junction. Proceedings of the ASME. 2014. Article no. FEDSM2014-21660. DOI: 10.1115/FEDSM2014-21660
13. Nigmatullina, G.F., Azizov, B.R., Varsegova, E.V., Osipova, L.E. Determination of Coefficients of Local Resistances of Press fittings in Laminar and Transient Modes of Fluid Flow. Stroitelnye Konstruktsii, Zdaniya i Sooruzheniya [Building Structures, Buildings and Facilities]. 2023. 2(3). Pp. 18–26.
14. Hayes, R.E., Nandakumar, K., Nasr-El-Din, H. Steady laminar flow in a 90 degree planar branch. Computers & Fluids. 1989. 17(4). Pp. 537–553. DOI: 10.1016/0045-7930(89)90027-3
15. Mynard, J.P., Valen-Sendstad, K. A unified method for estimating pressure losses at vascular junctions. International Journal for Numerical Methods in Biomedical Engineering. 2015. 31(7). Article no. e02717. DOI: 10.1002/cnm.2717
16. Hager, W.H. An Approximate Treatment of Flow in Branches and Bends. Proceedings of the Institution of Mechanical Engineers, Part C: J. Mechanical Engineering Science. 1984. 198(1). Pp. 63–69. DOI: 10.1243/PIME_PROC_1984_198_088_02
17. Paliivets, M.S. On the issue of determining hydraulic resistances of tees of metal-polymer pipelines. Prirodoobustrojstvo. 2023. 4. Pp. 79–85. DOI: 10.26897/1997-6011-2023-4-79-85
18. Ziganshin, A.M., Safiullina, G.R., Eremina, S.V., Gaifullin, A.A. Validation of a Numerical Model of a Flow in an Exhaust AND Supply Symmetrical Ventilation Tees. News KSUAE. 2021. 1. Pp. 58–70. DOI: 10.52409/20731523_2021_1_58
19. Kalyakin, A.M., Chesnokova, E.V. New relationship for determining the coefficient of hydraulic resistance in the transition zone of resistance (from laminar to turbulent flow). Magazine of Civil Engineering. 2012. 2. Pp. 51–55. DOI: 10.5862/MCE.28.8
20. Wygnanski, I.J., Champagne, F.H. On transition in a pipe. Part 1. The origin of puffs and slugs and the flow in a turbulent slug. Journal of Fluid Mechanics. 1973. 59(2). Pp. 281–335. DOI: 10.1017/S0022112073001576
21. Mullin, T. Experimental Studies of Transition to Turbulence in a Pipe. Annual Review of Fluid Mechanics. 2011. 43. Pp. 1–24. DOI: 10.1146/annurev-fluid-122109-160652
22. Avila, K., Moxey, D., De Lozar, A., Avila, M., Barkley, D., Hof, B. The Onset of Turbulence in Pipe Flow. Science. 2011. 333(6039). Pp. 192–196. DOI: 10.1126/science.1203223
23. Lemanov, V.V., Lukashov, V.V., Sharov, K.A. Transition to Turbulence through Intermittence in Inert and Reacting Jets. Fluid Dynamics. 2020. 55(6). Pp. 768–777. DOI: 10.1134/S0015462820060087
24. Lemanov, V., Lukashov, V., Sharov, K. Turbulent Superstructures in Inert Jets and Diffusion Jet Flames. Fluids. 2021. 6(12). Article no. 459. DOI: 10.3390/fluids6120459
25. Bradshaw, P. The effect of initial conditions on the development of a free shear layer. Journal of Fluid Mechanics. 1966. 26(2). Pp. 225–236. DOI: 10.1017/S0022112066001204

26. Gataulin, Y.A., Smirnov, E.M., Molochnikov, V.M., Mikheev, A.N. The structure of a 3D flow with local turbulence in the branching juncture of a circular-section channel. St. Petersburg State Polytechnical University Journal. Physics and Mathematics. 2022. 15(4). Pp. 81–94. DOI: 10.18721/JPM.15406
27. Molochnikov, V.M., Nikiforov, I.V., Pashkova, N.D. Structure of Swirling Flow in the Channel Branching Area at Moderate Reynolds Numbers. Fluid Dynamics. 2024. 59(5). Pp. 1038–1055. DOI: 10.1134/S0015462824602663

Information about the authors:

***Vadim Lemanov**, PhD in Technical Sciences*
ORCID: https://orcid.org/0000-0001-5049-8888
E-mail: lemanov@itp.nsc.ru

***Viktor Fedorenko**, PhD in Technical Sciences*
E-mail: vitya.fedorenko.335@mail.ru

***Konstantin Sharov**, PhD in Technical Sciences*
E-mail: sharov@itp.nsc.ru

Received 09.04.2025. Approved after reviewing 29.10.2025. Accepted 30.11.2025.

Magazine of Civil Engineering

ISSN 2712-8172

journal homepage: http://engstroy.spbstu.ru/

Research article

UDC 532.517

DOI: 10.34910/MCE.140.8

Reliability studies of the frame of the C1 shipping opening

D. Sharapov ✉ , ***G.L. Kozinets***, ***P.V. Kozinets***

Peter the Great St. Petersburg Polytechnic University

✉ *sharapov.dm@gmail.com*

Keywords: Caisson gate frame, shipping opening C1, Neva Bay, dry dock, calculated stresses, calculated deflections

Abstract. This article presents a comprehensive computational study of the metal frame of the caisson gate of the C1 shipping opening, part of the St. Petersburg flood protection system. The relevance of this study stems from the need to ensure the strength, stability, and safe operation of this unique 120-meter-long structure, which supports the segmental caisson gate during its movement from the dry dock to the structure's span. The frame is distinguished by its cantilever structure of variable thickness and reinforced with stiffeners. The aim of the study was to develop an adequate spatial computational model of the frame and caisson gate and analyze their stress-strain state for a stationary position in a dry dock. The study was conducted using the finite element method, taking into account constant static loads, including the structures' own weight and hydrostatic pressure. The paper presents the developed spatial finite element model and describes the adopted boundary conditions and loads. Permissible stresses and deflections are determined. The calculations yielded stress and displacement fields. It was determined that the maximum equivalent stresses in the frame do not exceed permissible values. The maximum frame deflection is also within acceptable limits. An analysis of the dynamic characteristics of the structure was conducted. The natural frequencies of vibration were determined for the caisson gate. A stability analysis was performed, showing that the safety factor for the first positive buckling mode exceeds the minimum required. Based on the obtained results, a conclusion was reached that the calculated stresses and deformations comply with regulatory requirements and provide the necessary safety and stability margins. To monitor the condition of the structure during operation, it is recommended to install vibration sensors at critical points, as well as conduct further research.

Funding: The study was supported by a grant from the Russian Science Foundation No. 23-19-20062 and the St. Petersburg Science Foundation, agreement No. 23-19-20062

Citation: Sharapov, D., Kozinets, G.L., Kozinets, P.V. Reliability studies of the frame of the C1 shipping opening. Magazine of Civil Engineering. 2025. 18(8). Article no. 14008. DOI: 10.34910/MCE.140.8

1. Introduction

The object of this study is the metal frame of the caisson gate of the C1 Shipping opening, which is part of the St. Petersburg Protective Structures Complex. The purpose of the metal frame is to support the caisson gate during its movement from the dry dock to the fairway. A distinctive feature of the metal frame design is that it is welded from steel sheets of varying thicknesses and reinforced with stiffeners. A through-passage is possible within the frame. Two caisson gates with two metal frames, each 120 m long, are symmetrically located at the C1 shipping opening. The opening allows the passage of large vessels.

The study is relevant due to the need to calculate the stresses and strains of the frame for several design positions. The strength of the frame affects the safety of the caisson gate and determines its operability. When designing the frame, deformations due to temperature loads were not taken into account.

The structure under consideration is located in the Neva Bay, which has been the subject of numerous studies. A number of papers examine the historical retrospective [1–4]. A valuable source of information is provided by papers containing data on quantitative changes in the volume of the Neva Bay, taking into account the volume of sediment [5–7]. Previously, the authors conducted work analyzing changes in loads caused by changes in the Neva Bay [8–9]. The following papers are devoted to modeling processes in the Neva Bay [10–13].

A key feature of the metal frame calculation is its length of 120 m and its cantilever nature. There are several studies of metal cantilever frames over 100 m in length in the scientific literature.

[14] examines the fundamental principles of finite element method (FEM) applicable to the calculation of any large frame. For caisson frame analogs (e.g., gantry crane frames, large-span load-bearing frames in workshops, and support structures for lock gates), key tasks include identifying stress concentration zones at the joints of the elements, assessing overall and local stability, and analyzing deformations (deflections) under their own weight and operational loads.

For frames over 100 m in length, accounting for geometric nonlinearity becomes critical. [15, 16] emphasize the need for nonlinear analysis. This allows for an accurate assessment of the frame's behavior under extreme loads, which is directly related to safety. Changizi and Jalalpour [17] applied topology optimization to steel frames to minimize material consumption while maintaining strength and stiffness constraints.

In Russia, the key document is [18]. This set of rules establishes the general principles of strength, stability and fatigue calculations, methods for determining the design resistance of steel and welded joints. For the caisson gate frame, the sections devoted to the calculation of elements under complex stress states and composite sections will be critical. Since the frame is part of a hydraulic structure, it is possible to use industry standards, such as [19, 20]. Since the specified document does not take into account all loads during freezing, it is possible to apply the methods proposed in [21, 22]. For comparative analysis, international standards can be used, for example, Eurocode 3 (EN 1993): Design of steel structures [23] and the American standards AISC 360 (Specification for Structural Steel Buildings) [24].

Since large caisson gate frames are unique structures, it is necessary to consider non-direct analogs, such as harbor crane frames [25]. [26] is devoted to the calculation of overhead and gantry crane frames, as is the regulatory document PB 10-382-00 "Rules for the Design and Safe Operation of Overhead Cranes." These structures also experience significant dynamic and moving loads, and their safety is an absolute priority.

Among the studies in the field of hydraulic gates, [27] is devoted to the study and optimization of hydraulic gates – key elements of hydraulic structures. In the first stage, the work examined existing hydraulic gate designs, focusing on the analysis of their loads and structure. A detailed structural analysis was then conducted using ANSYS software. The goal was to find the optimal gate design by varying the position, size, and arrangement of the beams.

The study aimed to determine the stresses and strains in the gate frame and the forces in the ball joint.

The main objectives of the study are:

1. Develop a computational model of the support frame and collect loads for three caisson gate positions.
2. Calculate forces, stresses, and deformations.
3. Determine the locations for installing support structures, strain gauges, and vibration sensors.
4. Calculate the safety factor of the caisson gate support frame.
5. Conclusions on the safety factor and stability assessment and recommendations for the operation of the structures.

2. Methods

The study analyzed the metal frame of the caisson gate of the C1 navigation opening, which is part of the St. Petersburg Protective Structures Complex. The caisson gate support frame is designed to connect the segmental caisson gate to the ball bearing installed on the shore abutment of the C1 navigation structure and transfer the loads acting on the caisson gate to it. The working documentation (project 07-120KM) was developed by the "Lenproektstalkonstruktsiya" State Design Institute. Main parameters of floating gate are presented in the Table 1.

Table 1. Parameters of the floating gate.

Main beams, pcs.	2
Spacer beams, pcs.	3
Length of main beam, m	115.544
Total width, m	58.7
Main beam height, min/max, m	3.08/7.638
Angle between main beams, degrees	26.1622
Weight of support frame, t	1800
Shutter leaf	
Height/width/length	22/8.3/119.6
Weight, t/displacement, m^3	2938/3914
Movement radius, m	130
Diving depth, m	16
Ball joint	
Height/width, m	4/4
Hinge head diameter, m	1.5
Weight, t	85
Camber gate drive	
Max force, t	350
Length of track, m	171

The triangular support frame consists of two main box-section beams of variable height and variable stiffness. The longitudinal axes of the main beams are positioned at an angle of $\alpha \approx 13^\circ$ relative to the longitudinal axis of symmetry of the gate leaf and are centered on the ball joint. The connection of the main beams to the caisson gate, the ball joint adapter, and the three spacer beams is rigid and welded. The spacer beams have a box-section. The metal structure material is steel 10 HSND-12 (Russian State Standard GOST 19282-73, Table 2).

Table 2. Physical and mechanical properties of steel.

Characteristic	**Value**
Material	Steel 10 HSND-12 (Russian State Standard GOST 19282-73)
Density p_s, t/mm^3	7.9×10^{-9}
Yield strength R_y, MPa	390
Poisson coefficient, v	0.30
Modulus of elasticity E_s, MPa	2.1×10^5

The initial data for constructing the calculation model were working drawings of the frame's metal structure. Figs. 1 and 2 show cross-sections and a plan of the support frame.

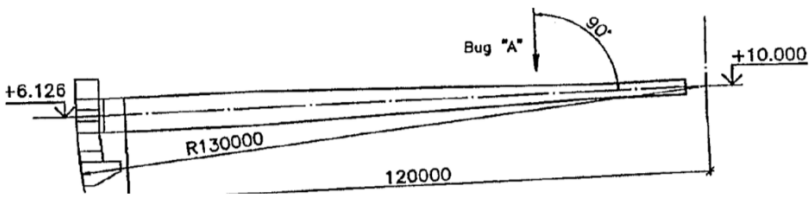

Figure 1. Section along the frame (longitudinal).

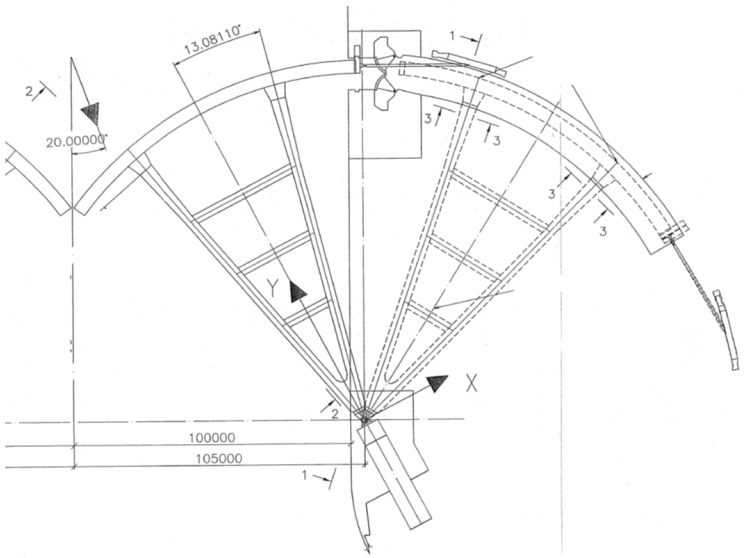

Figure 2. Frame plan.

The design model utilizes:

- 3-node flat elements for the frame's metal structure. Element thicknesses range from 12 to 40 mm, according to the design data;
- 3-node T-beam elements for horizontal longitudinal stiffeners welded inside the frame.

The spatial model of the structure is shown in Fig. 3.

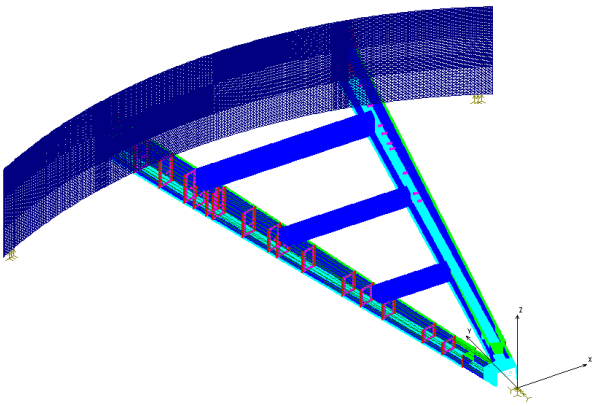

Figure 3. Spatial finite element model of the frame and caisson structure.

The origin is located at the hinge center. The X-axis is transverse to the frame, the Y-axis is longitudinal, and the Z-axis is vertical. Movement along all axes of the hinge assembly is prohibited, and rotation along the Y-axis (torsion) is prohibited. Rotation about the Z-axis (in the vertical direction) and about the X-axis (in the direction of travel) is permitted. Loads and actions are presented in the Table 3.

Table 3. Loads and actions.

Loads and actions		Calculated load values
Constant	Self-weight of structures	Calculated based on the elemental density for steel
Temporary	Hydrostatic load on the caisson gate when the dock chamber is filled to a depth of 6 meters from the top of the keel block, MPa	0.06
	Force from the tractor's work, initial moment of movement, tons	35

Currently, spatial frame modeling is performed in a spatial setting based on structural mechanics equations. Calculation standards for unique structures are based on the rules of structural mechanics. It should be noted that combined modeling of the frame and caisson gate allows for accurate frame stresses

and deflections. When solving the spatial modeling problem, after geometric modeling of the frame, the calculation model is discretized, and the physical properties of the steel elements, boundary conditions, and loads are specified. The mathematical model is constructed based on the available frame design material and the loads acting on the frame. Modeling and calculations were performed using the FEM in the SolidWorks software package. Stress and strain testing of the spatial metal frame was performed taking into account constant static loads for the first and second groups of limit states. The welded frame material is 10 HSND-12 steel (Russian State Standard GOST 19282-73), which is used for welded metal structure elements and various components requiring increased strength and corrosion resistance during operation at temperatures ranging from –70 to +450 °C.

The permissible stresses during normal operation are determined by the formula:

$$[\sigma] = \frac{R_n c \gamma_c}{\gamma_m \gamma_n}, \quad (1)$$

where R_n – standard resistance of steel; $R_n = \min\left\{R_y, R_u/1,3\right\}$; where R_y – yield strength; R_u – temporary resistance; c – the conversion factor from the basic to the derived design resistances, c = 1, coefficient for shift c = 0.58; γ_c – operating conditions coefficient, γ_c = 1; γ_m – material safety factor; γ_n – reliability coefficient.

For steel 10 KhSND-12 GOST 19282-73 (Russian State Standard) with a thickness of 12–40 mm:

R_y = 390 MPa, R_u = 530 MPa.

Thus, R_n = min {390, 530/1.3} = 390 MPa.

The material safety factor for steel 10 HSND-12 GOST 19282-73 (Russian State Standard) is γ_m = 1.05.

The safety factor for the intended purpose is taken:

for total stresses under the main combination of loads (concentrated load plus dead weight): γ_n = 1.4;

for local stresses: γ_n = 1.0.

Thus, the permissible stresses during normal operation are:

total

$$[\sigma]_{total} = \frac{390 \cdot 1 \cdot 1}{1.05 \cdot 1.4} = 265 \text{ MPa}; \quad (2)$$

local

$$[\sigma]_{local} = \frac{390 \cdot 1 \cdot 1}{1.05 \cdot 1 \cdot 1} = 337 \text{ MPa}. \quad (3)$$

The permissible deflection of the console under normal operating conditions is determined by the formula: [f] = L/400 = 120000/400 = 300 (mm), where L =120000 mm – frame length.

Computational studies were conducted within the framework of a spatial formulation of the elasticity theory problem. The calculations were performed using the FEM. Model analysis included verification of the computational model, specifically, comparing the results of stress and strain calculations with data from in-situ frame observations and adjusting the model – all of which constitute the essence of the spatial frame modeling method. An accurate mathematical model completely replaces the frame and caisson gate during the study. The essence of the modeling method is based on the principle of analogy (verification), or the ability to study a metal frame through the analysis of a similar model.

3. Results and Discussion

The frame calculation results are presented for the case of the caisson gate being located in a dry dock and on keel blocks. The self-weight of the structures is taken into account. When the caisson gate is supported on the keel blocks, the support hinge does not move, and rotation is permitted. Figs. 4–13

present the calculation results for stresses, deformations, vibration modes, and the buckling mode of the frame.

Figs. 4–6 show the stresses in the frame from constant static loads, which amount to 200 MPa. The maximum local stresses do not exceed the local permissible stress of 337 MPa. The overall stresses of 125 MPa do not exceed the overall permissible values of 265 MPa.

The resulting reaction at the support hinge is 499.1 kN.

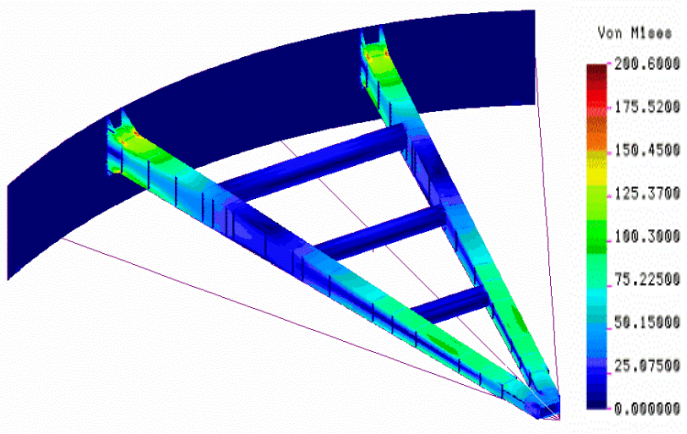

Figure 4. Equivalent stresses (25–200 MPa).

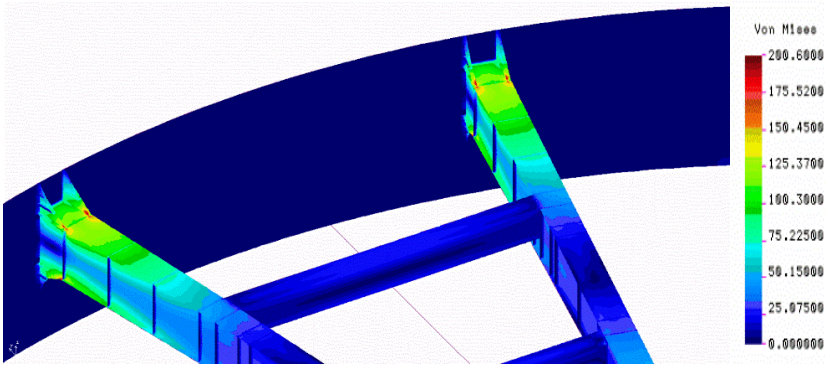

Figure 5. Maximum equivalent stresses (200 MPa).

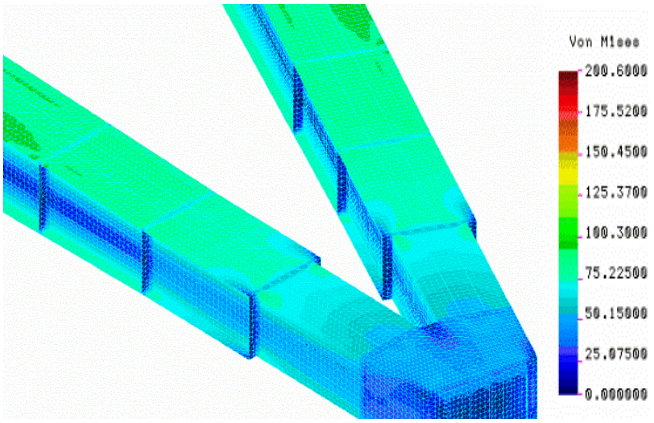

Figure 6. Equivalent stresses (125 MPa).

Figs. 7 and 8 show frame deformations from constant static loads ranging from 0 to 207 mm. The maximum deflection is 207 mm at a distance of 45–49 m from the support hinge.

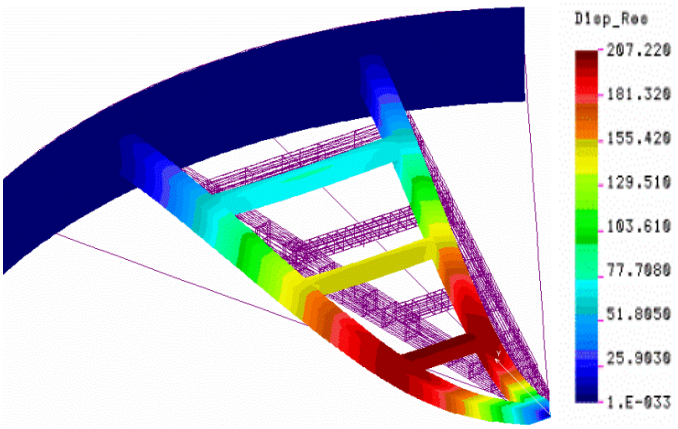

Figure 7. Deformations (0–207 mm), general view.

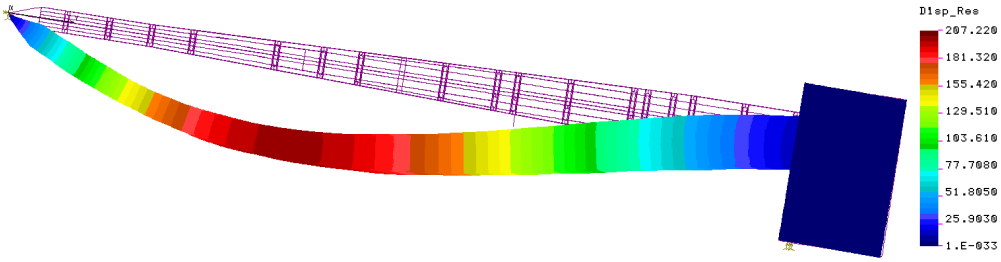

Figure 8. Deformations (0–207 mm), side view.

The maximum deflection is 207 mm at a distance of 45–49 m from the support hinge. The forces at the support hinge are 499.1 kN.

Figs. 9–13 show the natural frequencies of the frame and caisson gate, which are: for the caisson gate, low-frequency vibrations with a frequency of F_{1bat} = 0.00086 Hz, for the frame – the first natural frequency – F_{1frame} = 1.19 Hz.

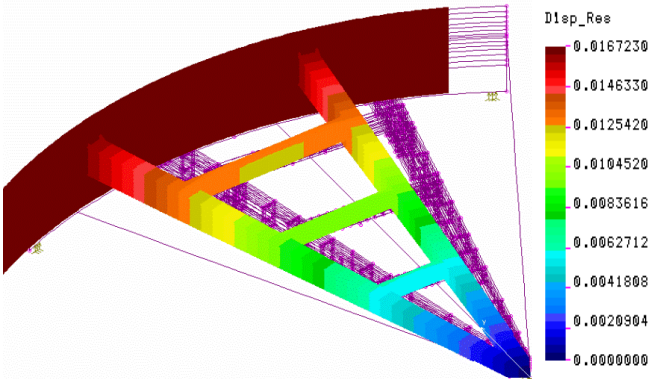

Figure 9. The first form of oscillations is low-frequency oscillations of the caisson shield with a frequency of 0.00086 Hz.

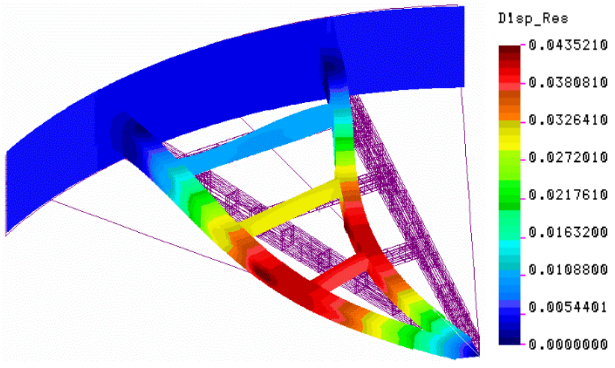

Figure 10. The second form of vibration is low-frequency vibration of the frame with a frequency of 1.19 Hz.

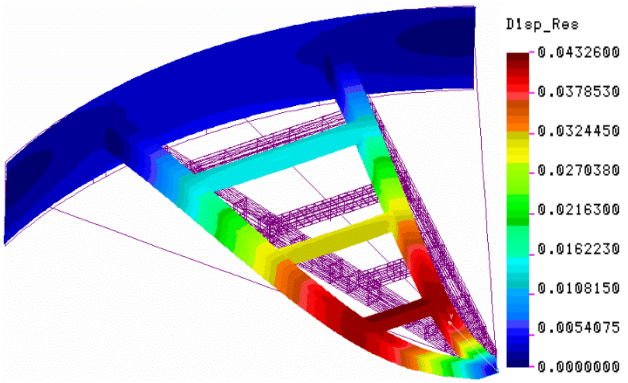

Figure 11. The third form of oscillation is low-frequency frame oscillation with a frequency of 1.45 Hz.

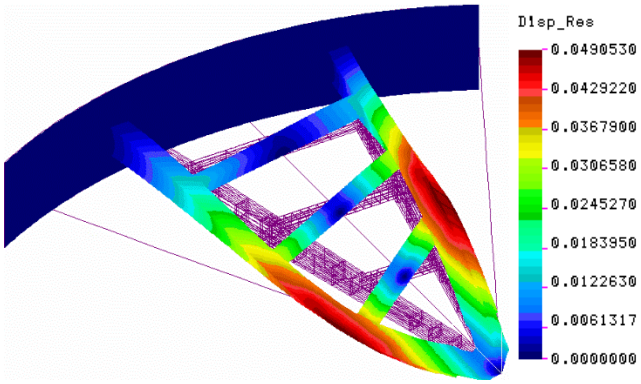

Figure 12. The fourth form of oscillation is low-frequency frame oscillation with a frequency of 2.16 Hz.

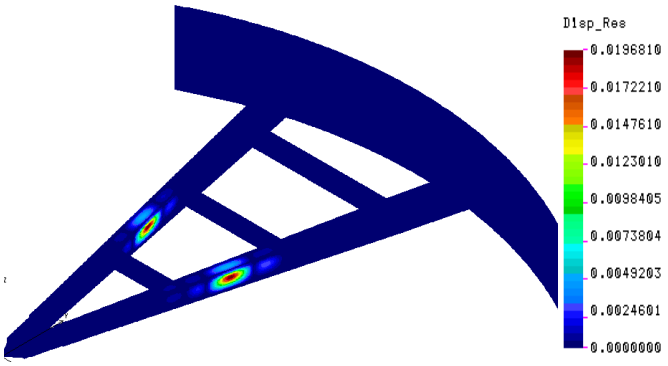

Figure 13. The ninth (first positive) form of loss of stability with a stability factor of k = 2.94.

Table 4 shows the results of stability calculations for certain forms of stability loss.

Table 4. Results of stability calculations.

Loss of stability form	Safety factor
1	–3.05398
2	–2.93869
3	–2.69893
4	–2.69631
5	–2.46168
6	–2.36357
7	–0.01226
8	–0.012261
9	2.94149
10	3.19072

The obtained results have no direct analogues. The closest studies on the issue under consideration were conducted in [28–30]. [29] Considers the results of experimental and numerical studies of the frame of the building framework with a span of 12 m with elements of a composite double-box section made of cold-formed galvanized sections. Nodal connections of thin-walled sections and multi-row bolted friction connections are investigated. In [31], an integrated approach to the creation of digital twins for offshore wind turbines is presented, which correlates with the methodology for calculating the caisson gate frame using a finite element model. The obtained values of stresses (200 MPa) and deformations (207 mm) are consistent with those considered in the article. [32] Describes in detail the design loads for hydraulic gates, including hydrostatic and operational loads. The obtained values of the safety factor correspond to modern design standards outlined in the paper. [33] Emphasizes the importance of vibration monitoring, confirming the need to install vibration sensors at critical points of the frame. [34] Demonstrates the application of modern risk analysis methods to offshore structures. The proposed measures for monitoring and model calibration in the study are consistent with the principles of predictive maintenance. The need for model calibration using in-kind measurement data, stated in the conclusions, is supported by the principles of digital twin construction in [31], which places particular emphasis on model verification using experimental data.

The obtained results demonstrate compliance with modern scientific and technical requirements for the design and analysis of unique hydraulic structures, and the proposed directions for further research are relevant in the context of the development of digital modeling and monitoring technologies.

4. Conclusions

Calculation results for the caisson gate frame for a stationary position in a dry dock have been obtained. Stresses and strains in the frame structure do not exceed permissible values and meet regulatory strength requirements.

The safety factor for overall stresses for the designed steel grade Steel 10 HSND-12 (Russian State Standard GOST 19282-73) is $K = 2$ for the frame position in a dry dock.

The safety factor for deflections is 90 mm.

The safety factor for frame buckling is $K = 2.94$.

The frame's natural frequencies are low, due to the considerable length of the frame – 120 m – and the significant dimensions of the caisson gate shield.

To monitor frame vibrations, vibration sensors should be installed at the hinge base and at the ends of the frame branches. Supporting structures should be provided at the ends of the frame and at the hinge base.

Further research requires:

1. Inspect the frame to confirm the rigidity of all elements.
2. Calibrate the model for existing deformations (winter-summer).
3. Compare the calculation results with sensor readings.
4. Perform dynamic calculations of the frame under loads from surge waves and wind.

References

1. Dolukhanov, P.M., Subetto, D.A., Arslanov, K.A., Davydova, N.N., Zaitseva, G.I., Djinoridze, E.N., Kuznetsov, D.D., Ludikova, A.V., Sapelko, T.V., Savelieva, L.A. The Baltic Sea and Ladoga Lake transgressions and early human migrations in North-western Russia. Quaternary International. 2009. 203(1–2). Pp. 33–51. DOI: 10.1016/j.quaint.2008.04.021
2. Andrén, T., Björck, S., Andrén, E., Conley, D., Zillén, L., Anjar, J. The Development of the Baltic Sea Basin During the Last 130 ka. The Baltic Sea Basin. Central and Eastern European Development Studies (CEEDES). Springer. Berlin, Heidelberg, 2011. Pp. 75–97. DOI: 10.1007/978-3-642-17220-5_4
3. Ryabchuk, D., Zhamoida, V., Orlova, M., Sergeev, A., Bublichenko, J., Bublichenko, A., Sukhacheva, L. Neva Bay: A Technogenic Lagoon of the Eastern Gulf of Finland (Baltic Sea). The Diversity of Russian Estuaries and Lagoons Exposed to Human Influence. Estuaries of the World. Springer. Cham, 2017. Pp. 191–221. DOI: 10.1007/978-3-319-43392-9_7
4. Prishchepenko, D.V., Ryabchuk, D.V., Zhamoida, V.A., Sergeev, A.Y., Leontev, F.A., Grigoriev, A.G., Neevin, I.A., Budanov, L.M., Kovaleva, O.A. Main trends and results of 300-years anthropogenic impact on the geological environment and ecosystem of the Eastern Gulf of Finland. Continental Shelf Research. 2023. 265. Article no. 105058. DOI: 10.1016/j.csr.2023.105058
5. Martyanov, S., Ryabchenko, V. Bottom sediment resuspension in the easternmost Gulf of Finland in the Baltic Sea: A case study based on three–dimensional modeling. Continental Shelf Research. 2016. 117. Pp. 126–137. DOI: 10.1016/j.csr.2016.02.011
6. Ludikova, A.V., Subetto, D.A., Kuznetsov, D.D., Orlov, A.V., Shatalova, A.E. New Diatom and Sedimentary Data Confirm the Existence of the Northern Paleo-Outlet from Lake Ladoga to the Baltic Sea. Quaternary. 2024. 7(3). Article no. 31. DOI: 10.3390/quat7030031

7. Chusov, A., Shilin, M., Gogoberidze, G., Bobylev, N., Ershova, A., Lednova, J. (2020). Long-term monitoring of the dredged material deposit sites in the Eastern Gulf of Finland. E3S Web of Conferences. 164. Article no. 01010. DOI: 10.1051/e3sconf/202016401010
8. Kozinetc, G.L., Badenko, V.L., Sharapov, D.A., Shonina, E.V. Method of integrated consideration of factors for calculation of anchor system of pontoons. Magazine of Civil Engineering. 2024. 17(7). Article no. 13108. DOI: 10.34910/MCE.131.8
9. Kozinetc, G.L., Badenko, V.L., Sharapov, D.A., Shonina, E.V. Loads on hydraulic engineering and berthing structures of the coastal zone of the Neva Bay. Magazine of Civil Engineering. 2024. 17(8). Article no. 13206. DOI: 10.34910/MCE.132.6
10. Popov, S.K., Lobov, A.L. Hydrodynamic modeling of floods in Saint Petersburg considering the operating dam. Russian Meteorology and Hydrology. 2017. 42. Pp. 267–274. DOI: 10.3103/S1068373917040070
11. Sokolov, A., Chubarenko, B. Case-Study Modelling Analysis of Hydrodynamics in the Nearshore of the Baltic Sea Forced by Extreme Along-shore Wind in the Case of a Cross-shore Obstacle. Archives of Hydro-Engineering and Environmental Mechanics. 2018. 65(3). Pp. 163–176. DOI: 10.1515/heem-2018-0011
12. Ryabchenko, V., Dvornikov, A., Haapala, J., Myrberg, K. Modelling ice conditions in the easternmost Gulf of Finland in the Baltic Sea. Continental Shelf Research. 2010. 30(13). Pp. 1458–1471. DOI: 10.1016/j.csr.2010.05.006
13. Andreev, P.N., Dvornikov, A.Y., Ryabchenko, V.A., Tsepelev, V.Y., Smirnov, K.G. Simulation of storm surges in the Neva Bay on the basis of a three-dimensional model of circulation in the conditions of maneuvering by gates of the flood protection barrier. Fundamental and Applied Hydrophysics. 2013. 6 (4). Pp. 23–31.
14. Bazhenov, V.A., Dashchenko, A.F., Orobey, V.F., Suryaninov, N.G. Chislennyye metody v mekhanike [Numerical Methods in Mechanics]. Odessa: Standart, 2005. 564 p.
15. Zenkevich, O., Morgan, K. Finite Elements and Approximation. Moscow: Mir, 1986. 320 p.
16. Zenkevich, O. Finite Element Method in Engineering. Moscow: Mir, 1975. 541 p.
17. Changizi, N., Jalalpour, M. Topology optimization of steel frame structures with constraints on overall and individual member instabilities, Finite Elements in Analysis and Design. 141. 2018. Pp. 119–134. DOI: 10.1016/j.finel.2017.11.003
18. Normative document in Russia: SP 16.13330.2017. Steel Structures (updated version of SNiP II-23-81*).
19. Normative document in Russia: SP 101.13330.2012. Retaining Walls, Shipping Locks, Fish Passages, and Fish Protection Structures.
20. Normative document in Russia: SP 38.13330.2018. Loads and Impacts on Hydraulic Structures (Wave, Ice, and Ship).
21. Sharapov, D. Ice adhesion to hydrotechnical structures. E3S Web of Conferences. 2023. 431. Article no. 03006. DOI: 10.1051/e3sconf/202343103006
22. Sharapov, D. Evolution of ice load prediction tools for hydrotechnical construction. E3S Web of Conferences. 2023. 402. Article no. 05023. DOI: 10.1051/e3sconf/202340205023
23. EN 1993-1-1 (2005) (English): Eurocode 3: Design of steel structures – Part 1-1: General rules and rules for buildings [Authority: The European Union Per Regulation 305/2011, Directive 98/34/EC, Directive 2004/18/EC].
24. AISC-360 2016. Specification for Structural Steel Buildings Supersedes the Specification for Structural Steel Buildings.
25. Caglayan, B., Ozakgul, K., Tezer, O., Uzgider, E. Fatigue life prediction of existing crane runway girders. Journal of Constructional Steel Research. 2010. 66(10). Pp. 1164–1173. DOI: 10.1016/j.jcsr.2010.04.009
26. Grigoriev, V.P. Ensuring the Stability of Self-Propelled Boom Cranes When Working on Soft Soils: Candidate of Technical Sciences Dissertation. Moscow, 2020.
27. Biplov A., Ashrut A., Niraj J., Kausal K.C. Analysis-and-optimization-of-hydraulic-gate. Kathmandu University, 2021. 22 p.
28. Ivanov, A.B., Petrov, S.M. Eksperimentalnyye issledovaniya napryazheniy v elementakh batoporta [Experimental studies of stresses in the elements of the caisson gate]. Vestnik MGSU. 2019. 14(12). Pp. 1385–1396.
29. Tarasov, A., Tarasov, I., Petukhova, I. Frame Construction with Bearing Elements of a New Type of Galvanized Steel. International Research Journal. 2015. 11(42). Pp. 131–134. DOI: 10.18454/IRJ.2015.42.110
30. Semko, V.A., Prokhorenko, D.A. Analiz konstruktivnykh mer dlya povysheniya nadezhnosti pokrytiy iz legkikh stalnykh tonkostennykh profiley [Analysis of design measures to improve the reliability of coatings made of light steel thin-walled sections]. 2011. 5. Pp. 18–23.
31. Liu Yi, Zhang Jian-Min, Min Yan-Tao, Yu Yantao, Lin Chao, Hu Zhen-Zhong. A digital twin-based framework for simulation and monitoring analysis of floating wind turbine structures. Ocean Engineering. 283. 2023. Article no. 115009. DOI: 10.1016/j.oceaneng.2023.115009
32. Ryszard, D., Tim, P. Chapter 3 – Structural Types of Hydraulic Gates. Lock Gates and Other Closures in Hydraulic Projects. 2019. Pp. 35–282. DOI: 10.1016/B978-0-12-809264-4.00003-3
33. De la Peña, Z.I., Freire, S.M.J., López, B.B. Industry 4.0 in the port and maritime industry: A literature review. Journal of Industrial Information Integration. 2020. 20. Article no. 100173. DOI: 10.1016/j.jii.2020.100173
34. Sokukcu, M., Sakar, C. Risk analysis of collision accidents during underway STS berthing maneuver through integrating fault tree analysis (FTA) into Bayesian network (BN). Applied Ocean Research. 2022. 126. Article no. 103290. DOI: 10.1016/j.apor.2022.103290

Information about the authors:

***Dmitry Sharapov**, PhD in Technical Sciences*
ORCID: https://orcid.org/0000-0001-8650-2375
E-mail: sharapov.dm@gmail.com

***Galina Kozinets**, Doctor of Technical Sciences*
E-mail: kozinets_gl@spbstu.ru

Pavel Kozinets,
E-mail: kozinets_pv@spbstu.ru

Received 14.07.2025. Approved after reviewing 29.11.2025. Accepted 02.12.2025.

Magazine of Civil Engineering

ISSN 2712-8172

journal homepage: http://engstroy.spbstu.ru/

Research article

UDC 624.139

DOI: 10.34910/MCE.140.9

Determining the temperature of soil under a building with a ventilated basement

M.I. Nizovtsev ✉ , ***A.N. Sterlyagov***

Kutateladze Institute of Thermophysics, Novosibirsk, Russian Federation

✉ *nizovtsev@itp.nsc.ru*

Keywords: permafrost, soil freezing and thawing, soil moisture, radiation balance, building with ventilated basement, calculation model.

Abstract. This work is aimed at computational comparative studies of natural changes in soil temperature and under a building with a ventilated basement in Norilsk. In contrast to conventional projects, it was planned to locate a small part of the building directly on the ground, which could lead to additional thawing of the soil. Laboratory data on soil samples in the thawed and frozen state, taken from boreholes at the construction site, and the results of soil temperature measurements at a depth of about 14 m were used to perform calculations. When forming the boundary conditions of the calculation model on the outer surface of the soil, the radiation balance for the conditions of Norilsk was considered. It was found that the radiation balance from May to August is positive and leads to soil heating, and in the rest, most part of the year, it is negative and causes soil cooling. New results obtained demonstrate that a decrease in the moisture content of the surface soil layers reduces the influence of phase transitions on the thermal-inertial properties of the soil, which leads to an increase in the thickness of the active soil layer (where annual temperature fluctuations are observed), an increase in the depth of thawing in the summer-autumn period, and a decrease in the soil temperature under the active layer. The temperature distributions over the depth of soil under different sections of the building with a ventilated basement and in the immediate vicinity of the building in a long-term operation cycle after completion of its construction were calculated. According to calculation results, the maximum depth of soil thaw under a building with a ventilated basement decreased by 12 % compared to natural conditions, reaching 1.1 m. It is shown that for multi-story buildings with ventilated basements, individual structural elements with insulation can be located directly on the ground surface, and additional thawing of the soil will not occur under them. However, for this case, the absence of additional thawing of soil should be confirmed by a heat engineering calculation taking into account the ratio of surface areas of the ventilated basement and the structural elements located on the ground, as well as the features of their insulation.

Funding: The work was carried out within the framework of the state assignment of the IT SB RAS (project No. 126021217057-2).

Citation: Nizovtsev, M.I., Sterlyagov, A.N. Determining the temperature of soil under a building with a ventilated basement. Magazine of Civil Engineering. 2025. 18(8). Article no. 14009. DOI: 10.34910/MCE.140.9

1. Introduction

The object of study of this work is the distribution of temperature in permafrost soils in the annual cycle during the construction of buildings with a ventilated basement in Norilsk.

According to expert findings, the actual area of permafrost is 15 % of the land area in the Northern Hemisphere and 0.5–0.6 % in the Southern Hemisphere [1]. In Russia, about 60–65 % of the land surface,

which is 11 mln km^2, is presented by permafrost zones, and permafrost is continuously distributed over 85 % of the Arctic zone [2].

The Russian Arctic is one of the most urbanized regions of Russia with the urban population accounting for about 88 % [3]. There are six cities in the Russian Arctic with a population of over 100,000 people: Murmansk, Arkhangelsk, Severodvinsk, Novy Urengoy, Noyabrsk, and Norilsk. In these cities, a large number of multi-story buildings have been built and are in operation. Cities in the Arctic are heat islands in regions with a cold continental climate, where the average annual surface temperature of the earth is approximately 6 °C higher than the surface temperature of the soil under natural conditions.

The general trend of climate warming is also manifested by an increase in permafrost temperature in different regions of the world [4]. The temperature regime of permafrost is usually characterized by the average value of annual temperature measured at a depth of zero annual soil temperature amplitudes, which is usually 10–15 m in the northern regions of Western Siberia. The observed warming for permafrost soil in the Arctic region is 2.8 °C, which corresponds to the average annual temperature increase of 0.056 °C/year. In the European north of Russia, the increase in permafrost temperature is slower and is 0.04 °C/year [5]. Thus, Arctic permafrost is warming faster, which is associated with a more significant increase in the air temperature in the Arctic region [6].

Some studies have modeled the average annual change in shallow permafrost temperature associated with warming. Thus, modeling performed for the western part of the Yamal Peninsula showed that the average annual change in soil temperature could reach a depth of 50 m in the next 50 years, while permafrost could become 1.3 °C and 2.3 °C warmer at depths of 20 m and 7–10 m, respectively [7]. The current trend of climate warming will obviously continue, which is confirmed by modeling of the general circulation in the atmosphere [8].

If the warming trend does not change to cooling by the end of the 21st century, most of the underground permafrost will melt, leading to irreversible changes in the landscape and destruction of the built environment [9]. The damage from permafrost thawing in Russia by 2050 is estimated to be around 105 billion dollars [10].

Almost 4,000,000 people, about 70 % of the existing infrastructure, and 45 % of hydrocarbons in the Russian Arctic are located in areas with a high potential for melting of near-surface permafrost and associated risks of soil instability by 2050 [11].

Design and construction of structures in permafrost regions requires consideration of global warming trends and the associated increase in permafrost temperature. Permafrost warming can change its properties due to an increase in the content of unfrozen pore water, which can be unevenly distributed in heterogeneous permafrost. Unfrozen water can exist in soils over a wide range of negative temperatures. The liquid component of pore moisture has been the subject of research for about 100 years, but many aspects of the problem remain poorly understood, including control of the phase composition of moisture in permafrost [12] and the influence of surface soil moisture on the depth of soil thawing during the summer-autumn period.

Although the temperature of permafrost in the Northern Hemisphere reaches –12 ÷ –10 °C, some part of the pore moisture remains unfrozen [13].

Prolonged warming in the Arctic is accompanied by a gradual increase in the temperature of the near-surface permafrost and an associated increase in the content of unfrozen water at the depths reached by heat waves. These processes cannot be classified as melting, since the soil does not become completely thawed and remains at negative temperatures, although it contains a large amount of unfrozen water. Thus, permafrost degradation actually occurs [12].

The amount of unfrozen pore water depends on the soil salinity and peat content; it is much greater in saline and peat-rich soils than in non-saline rocks with a lack of organic matter [14]. These soil features must be taken into account when operating existing engineering structures and when preparing new projects.

Permafrost retains a huge cold resource and is unlikely to melt to a catastrophic degree in the coming decades. However, constant warming of the near-surface permafrost can change the phase composition of the pore moisture due to an increase in unfrozen water, and this will cause transition of the solid permafrost into a more plastic state. The content of unfrozen water can increase even more as a result of thermal impact during the construction of buildings and structures, drilling operations, laying pipelines, etc. [15].

The widespread occurrence of permafrost in the Arctic region and the extremely harsh climate create great difficulties during construction [16]. There are a number of proven technologies for constructing facilities in Arctic conditions, and the technology of using a ventilated basement in buildings is one of the most common among them. This technology ensures heat removal from the building and prevents its

penetration into the soil [17]. Measurements of soil temperature distribution under a building with a ventilated basement in the city of Yakutsk showed that soil cooling was especially significant in the first two to three years after the completion of construction: by 3–4 °C and 0.3 °C at the depths of 6 m and 18 m, respectively. During the construction of buildings with ventilated basements, a decrease in soil temperature under them was 3–6 °C in Norilsk, 1–3 °C in Yakutsk [18], and 0.5–1.5 °C in Igarka [19]. In addition, the technologies of injection soil stabilization and improvement of soil properties by jet grouting are also used [20]. Therefore, there are limited data in the literature on the reduction of soil temperature under buildings with ventilated basement, but there are no results of such measurements over a long period of time with a detailed description of the composition and properties of the soils.

One of the methods for creating industrial infrastructure on permafrost soils is the method of pile foundation, which is erected in winter with preliminary soil strengthening [21]. The developers of this method calculate possible warming scenarios that may result in a decrease in the bearing capacity of piles, using the software package “Frost 3D”. In the case of a risk of a significant reduction in the bearing capacity, it is suggested to use thermosiphons for additional soil freezing.

Construction of infrastructure in permafrost regions can cause changes in the properties of permafrost. Laying highways and constructing embankments over permafrost inevitably lead to the changes in local microclimate conditions and affect the surrounding vegetation, snow cover, and soil water balance [22].

To analyze the state of permafrost, it is proposed to use a method based on the application of freezing and thawing indices applying the results of the field measurements in soils at construction sites [23]. Such an analysis of the numerical values of the indices allows an estimate of the final impact of the entire spectrum of anthropogenic and natural factors on the state of permafrost. The development of numerical methods for predicting the strength of permafrost [24] and the processes of formation of frost cracks, taking into account changes in temperature fields and the physical and mechanical properties of permafrost is an important issue [25].

The results of comparative calculations of the depth of soil freezing performed with application of engineering calculation methods, as well as numerical methods, using the software packages “Frost 3D” and “Borey 3D”, widely applied in Russia for permafrost soils, are presented in [26]. Based on this work, it was concluded that for further improvement of calculation methods, an increase in their accuracy and further development, it is necessary to use them together with the field measurements.

In particular, this research was aimed at computational studies of changes in soil temperature under a building with a ventilated basement, whose construction is planned on permafrost soils in Norilsk. In contrast to conventional projects, this project plans to locate a small part of the building directly on the ground. Data of laboratory studies of soil samples in the thawed and frozen state, taken from boreholes at the construction site, as well as the results of measuring soil temperatures at a depth of about 14 m, were used in calculations. Another objective set in this work was to consider the effect of soil moisture and associated phase transitions of pore moisture during freezing and thawing of the soil on the temperature distribution in permafrost soils in a long-term observation cycle.

When constructing various industrial and residential facilities on permafrost soils, the problems associated with specific design solutions arise. So, this calculation study was started by the project for the construction of a multi-story residential building in Norilsk. The multi-story residential building, like many facilities in Norilsk, is supposed to be built with a ventilated basement to prevent thawing of the permafrost soil underneath it (Fig. 1), but the small elevator area compared to the total area of the building (Fig. 2) is located on reinforced concrete blocks installed directly on the ground. The floor of the elevator is insulated with a 200 mm thick layer of extruded polystyrene foam. Thus, the question about possible thawing of soil under the elevator arose.

Figure 1. Ventilated underground space of a residential building on permafrost soil.

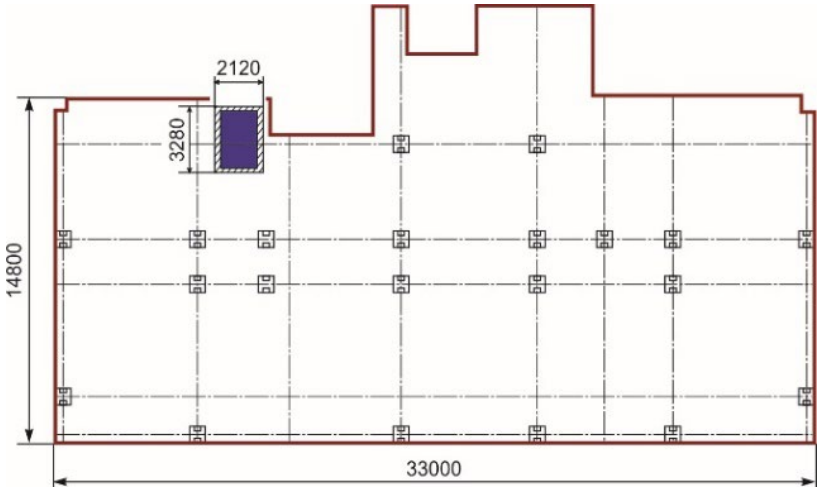

Figure 2. Floor framing plan of the 1st floor.

It was decided to expand the question posed and consider the following set of tasks when performing computational studies:

- to determine the natural temperature changes in the annual cycle over the soil depth and a temperature change under a ventilated basement in the conditions of Norilsk;
- to determine the greatest depth of soil thawing under these conditions;
- to find out the effect of phase transformations of moisture in the soil during cyclic processes of freezing and thawing on the temperature distribution in permafrost soil;
- to determine the dynamics of changes in the distribution of soil temperature in different zones under a residential building with a ventilated underground and under an elevator located on reinforced concrete blocks installed directly on the ground.

2. Methods

The calculations were carried out using the software packages “Frost 3D” and “Borey 3D”, designed to perform non-stationary numerical thermal calculations in multilayer soils taking into account the processes of their freezing and thawing. The processes of heat distribution in the soil with phase transformations can be described by a differential equation written in the enthalpy form [27]:

$$\frac{\partial H}{\partial \tau} = div\left(\lambda \times gradT\right) + f, \tag{1}$$

where $H\left(\tau, T\right)$ is the enthalpy of unit volume of soil, τ is time, T is the soil temperature, $\lambda\left(T\right)$ is the coefficient of soil thermal conductivity, and $f\left(\tau\right)$ is the power of internal heat sources.

Taking into account the phase transitions in the soil:

$$H\left(T_1\right)=\int_0^{T_1}\left[C\left(T\right)+Q\times\delta\left(T-T_{of}\right)dT\right], \tag{2}$$

where $C\left(T\right)$ is the volumetric heat capacity of soil, Q is the heat of phase transition, T_{of} is the temperature at onset of freezing, $\delta\left(T-T_{of}\right)$ is the delta-function.

$$C_{eff}=C_f+\rho_{df}L\frac{\partial W_w}{\partial T}, \tag{3}$$

where C_f is the heat capacity of soil in frozen state, W_w is humidity due to unfrozen water, ρ_{df} is the density of dry soil, and L is the specific heat of ice melting.

The coefficient of soil thermal conductivity depends on temperature in the following manner:

$$\lambda\left(T\right)=\begin{matrix}\lambda_{th},\ T>T_{of}\\ \lambda_{eff},\ T<T_{of}\end{matrix}, \tag{4}$$

where λ_{th} is the coefficient of thermal conductivity of thawed soil and λ_{eff} is the coefficient of effective thermal conductivity of frozen soil.

$$\lambda_{eff}=\lambda_f-\frac{\lambda_f-\lambda_{th}}{W_{tot}-W_{w\lambda}}\left(W_w-W_{w\lambda}\right), \tag{5}$$

where λ_f is the coefficient of thermal conductivity of frozen soil, W_{tot} is the total soil humidity, and $W_{w\lambda}$ is the humidity due to unfrozen water at determination temperature λ_f.

A change in the moisture content during soil freezing was taken into account in calculations depending on the soil type and its temperature, according to [28]. A decrease in the content of unfrozen moisture in the soil during its freezing depends on the type of soil. According to the degree of an increase in the proportion of unfrozen moisture in soils during freezing, the following sequence is observed: filled soil, sandy clay, clay loam, and clay (Fig. 3a). Peat should be singled out separately: usually it has higher moisture content and larger amount of unfrozen moisture at negative temperatures (Fig. 3b).

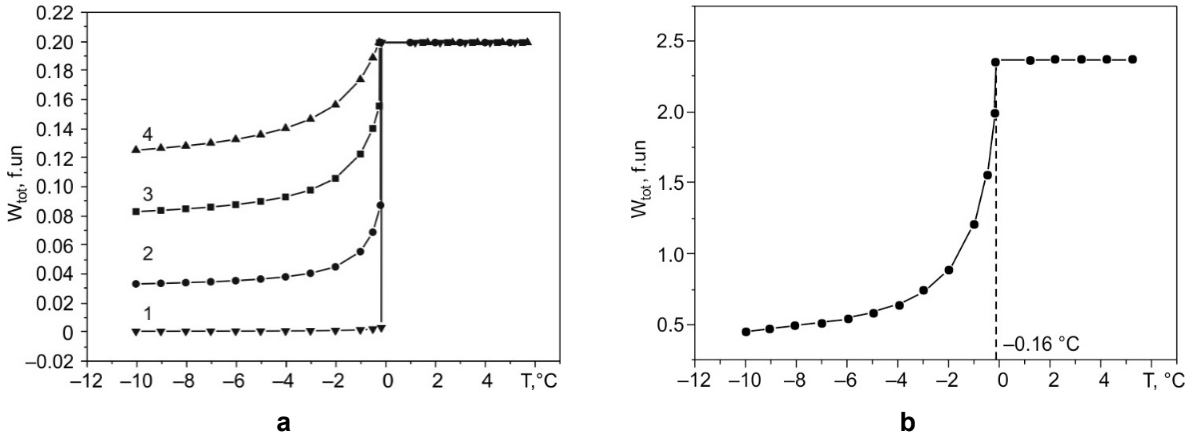

Figure 3. A change in total soil moisture during freezing:
a) 1 – filled soil, 2 – sandy clay, 3 – clay loam, 4 – clay; b) peat.

The dependence of the amount of unfrozen water on soil temperature depends on the soil type and its temperature at onset of freezing T_{of}. For soil temperatures $T>T_{of}$, a constant value of the amount of unfrozen water W_{tot} was adopted. This value, like the freezing onset temperature T_{of}, was determined based on laboratory measurements for each soil type. For soil temperatures $T\le T_{of}$, the dependence of the amount of unfrozen water on temperature was determined in the software package as a calculation curve based on SP 25.13330.2025 and approximated as a function:

$$W_w(T) = A + B/(C - T), \tag{6}$$

where A, B and C are the approximation parameters, T is the soil temperature, °C.

Thus, over the entire temperature range, the dependence of the amount of unfrozen water on the soil temperature was described by the expression:

$$W_w(T) = \begin{matrix} W_{tot}, & T \geq T_{of} \\ A + B/(C - T), & T \leq T_{of} \end{matrix}. \tag{7}$$

Solar radiation is one of the main factors influencing the soil temperature. Let us consider the radiation balance of the soil surface R:

$$R = (W_{dir} + W_{dif})(1 - A) - l_{eff}, \tag{8}$$

where W_{dir} and W_{dif} are the powers of direct and diffuse solar radiation reaching the soil surface, A is the surface albedo, and l_{eff} is the effective power of long-wave surface radiation [29]:

$$l_{eff} = l_{eff.0}\left(1 - c \times n^2\right) + 4\varepsilon\sigma T^3 (T_{sur} - T); \tag{9}$$

$$l_{eff.0} = \varepsilon\sigma T^4 \left(0.39 - 0.058\sqrt{(e/133.32) \times 6.973 \cdot 10^{-6}}\right) \text{ is the dependence of M.E. Berlyand,} \tag{10}$$

where $l_{eff.0}$ is the effective power of long-wave radiation of the surface without taking into account clouds, W/m²; ε is the surface emissivity coefficient; σ is the Stefan-Boltzmann constant; e is the partial pressure of water vapor, Pa; n is the cloud cover; and c = 0.80 at 69 latitude.

Let us determine the radiation balance of the Earth surface during the year in Norilsk using long-term observation data [30]. The data on distribution of the average power of total solar radiation falling on the surface (1), the surface albedo (2), and the average power of solar radiation absorbed by the surface taking into account its reflective properties (3) are shown in Fig. 4. According to the observations, the average monthly power of solar radiation in the summer in the conditions of Norilsk did not exceed 220 W/m², and the power absorbed by the soil taking into account the surface albedo was less than 180 W/m².

The annual distribution of the effective long-wave radiation power of the surface under clear skies $I_{eff.0}$ taking into account the cloud cover according to data of [31] is shown in Fig. 5. In summer, the effect of the cloud cover has a smaller screening effect on long-wave cooling of the surface than in other periods of the year, and the effective long-wave radiation power of the surface exceeds 60 W/m².

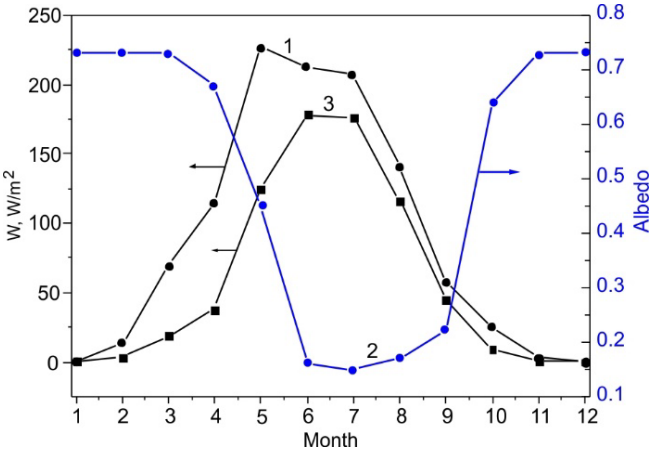

Figure 4. Average power of total solar radiation: 1 – falling on the surface, 3 – absorbed by the surface. 2 – albedo of the surface.

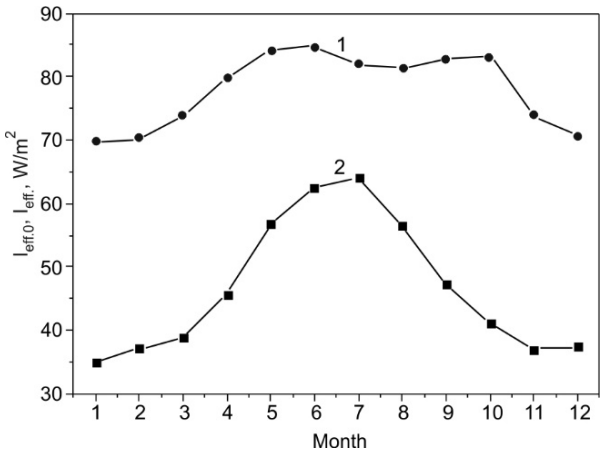

Figure 5. Average power of effective long-wave radiation of the surface: 1 – $I_{eff.0}$, 2 – I_{eff}.

Let us determine the heat flux on the outer surface:

$$Q_{sur} = R + Q_{con} - Q_{eva}, \tag{11}$$

where Q_{con} is the convective heat flux over the surface, Q_{eva} is the heat flux from the soil surface associated with moisture evaporation, which can be approximately determined, $Q_{eva} = mL$, where m is the mass of precipitation per 1 m^2 in the form of rain, and L = 2.5×10^6 J/kg is the heat of water evaporation.

The distribution of the average radiation balance during the year, as well as the radiation balance together with heat removal from the soil surface during moisture evaporation are shown in Fig. 6. According to the results presented, from May to August, the radiation balance is positive and leads to soil heating, and during the rest of the year, it is negative and causes soil cooling.

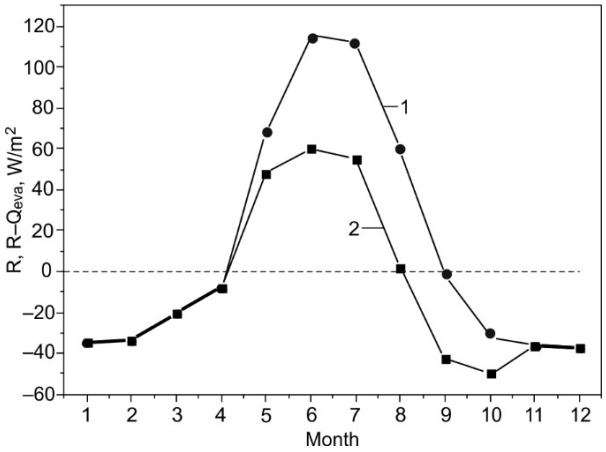

Figure 6. Average values over the year: 1 – *R*, 2 – *R* – Q_{eva}.

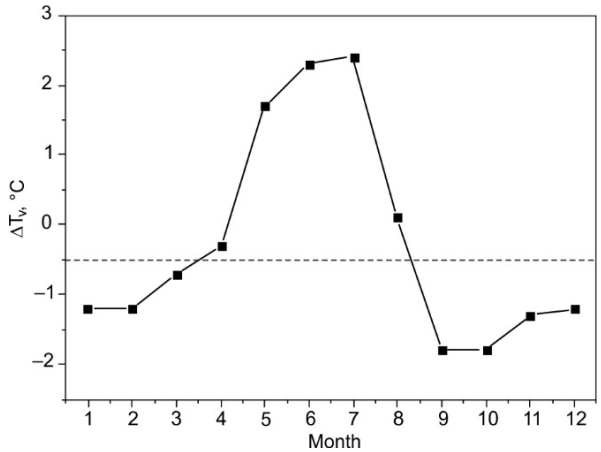

Figure 7. Calculated correction to the average monthly air temperature.

During calculations, the following heat flux was specified on the outer surface of the soil:

$$Q_{s.sur} = k\left(T^* - T_{s.sur}\right), \tag{12}$$

where k is the heat transfer coefficient taking into account a snow layer on the soil surface.

$$k = 1/\left(1/\alpha_{con} + d_s/\lambda_s\right), \tag{13}$$

where α_{con} is the convective heat transfer coefficient taking into account the wind speed, d_s is the snow layer thickness [32], and λ_s is the thermal conductivity coefficient of snow, T^* is the effective air temperature taking into account the radiation balance and moisture evaporation from the soil surface:

$$T^* = T_v + \Delta T_v = T_v + \left(R - Q_{eva}\right)/\alpha_{con}\,. \tag{14}$$

The resulting calculated correction to the average monthly air temperature ΔT_v for the climatic conditions of Norilsk is shown in Fig. 7. In the summer months, when calculating soils, this correction increases the average monthly air temperature by up to 3 °C, and in the winter months, on the contrary, it decreases it by 1–2 °C.

In calculations, a soil body with a thickness of 50 m was considered, and adiabatic conditions $\left(Q = 0\right)$ were assumed on its lower surface, which is well confirmed by the results of the field measurements.

To calculate the temperature change over the soil depth under different boundary conditions, the data on the soil composition and the thickness of soil layers were taken from the technical report on the results of engineering and geological surveys at the construction site of a multi-story residential building in Norilsk. A total of 10 boreholes were drilled at the construction site and soil samples were taken. The data from one of the boreholes with a description of soils, the depth and thickness of layers, and the distribution of soil temperature over the depth at the beginning of June 2023 are presented as an example in Fig. 8.

Absolute mark 48.7 m
Depth 14.20 m
Drilling date 19.04.2023

EGE No.	Abs. mark	Depth of occurrence	Thickness	Soil description
1	47.60	1.10	1.10	Filled soil
2	46.70	2.00	0.90	Peat, moderately decomposed
3	43.80	4.90	2.90	Clay loam of layered cryogenic structure, frozen, non-saline
4	38.60	10.10	5.20	Clay of layered cryogenic structure, frozen, non-saline, with inclusion of crushed stone
5	38.20	10.50	0.40	Clay loam of layered cryogenic structure, frozen, with inclusion of crushed stone, non-saline
6	36.50	12.20	1.70	Soil with crushed stones of layered cryogenic structure, frozen, non-saline with sandy loam filler
7	34.50	14.20	2.00	Dolerite (basalt), slightly cracked, slightly weathered, medium strength

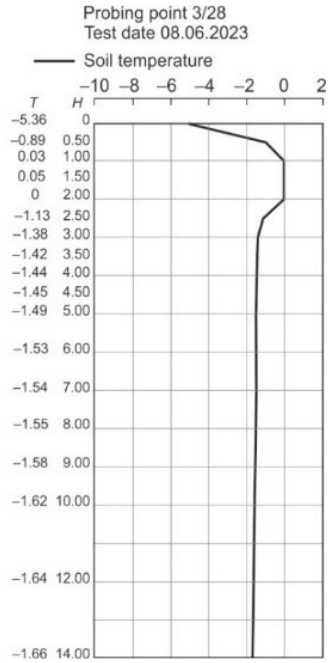

Figure 8. Data for one of the boreholes.

Based on the survey results, seven types of soils were identified. The soil temperature at a depth of 14 m remained almost unchanged and was approximately –1.7 °C. The list of all soil types according to their location from the surface with indication of their thickness based on the results of averaging information from 10 boreholes is presented in Table 1.

Table 1. Types and average thickness of soil layers.

Soil No.	Description of soils	Layer thickness, m
1	Filled soil	1.49
2	Peat, moderately decomposed	0.84
3	Clay loam of layered cryogenic structure, frozen, non-saline	2.9
4	Clay of layered cryogenic structure, frozen, non-saline, with inclusion of crushed stone	5.88
5	Clay loam of layered cryogenic structure, frozen, with inclusion of crushed stone, non-saline	0.91
6	Soil with crushed stones of layered cryogenic structure, frozen, non-saline with sandy loam filler	1.3
7	Dolerite (basalt), slightly cracked, slightly weathered, medium strength	below 13.32 m

Based on the results obtained in the specialized soil testing laboratory, the soil properties in the thawed and frozen state are summarized in Table 2, where $\rho_{d.s.}$ is the density of dry soil, λ_f and λ_{th} are the thermal conductivity coefficient of frozen and thawed soil, c_f and c_{th} are the volumetric heat capacity of frozen and thawed soil, W is the soil moisture content, T_{of} is the temperature at onset of freezing.

Table 2. Soil properties.

Soil No.	$\rho_{d.s}$, kg/m^3	λ_f, W/m^{2}K	λ_{th}, W/m^{2}K	c_f, ×10^{-6} J/kgK	c_{th}, ×10^{-6} J/kgK	W, %	$T_{of,}$ °C
1	1800	1.88	1.76	2.32	3	17	0
2	290	1.07	0.62	2.15	3.44	243	–0.2
3	1450	1.63	1.47	2.23	3.07	21.6	–0.2
4	1250	1.8	1.57	2.12	3.10	38.4	–0.25
5	1550	1.66	1.50	2.29	3.12	26	–0.2
6	1810	1.90	1.79	2.34	3.02	17.2	0

The data on the types of soil layers, their average thickness and properties in the thawed and frozen state are used in further calculations to determine the temperature distribution over the depth of the soil under different boundary conditions on its surface.

3. Results and Discussion

At the initial stage, a change in the soil temperature under natural conditions in the annual cycle was calculated for the city of Norilsk. The boundary conditions on the outer surface of the soil were determined taking into account all the factors specified earlier for the climatic conditions of the city of Norilsk, given in Table 3.

Table 3. Climatic Parameters.

Month of the year	Air temperature, °C	Wind speed, m/s	Thickness of snow, ×10^3, m	Rainfall, ×10^3, m	Average total solar radiation power, W/m^2	Surface albedo	Cloudiness
1	–27.6	6	278	0	0.7	0.73	0.78
2	–27.1	5.4	350	0	12.8	0.73	0.76
3	–22.1	6	406	0	69.1	0.73	0.77
4	–13.8	6.1	455	0	115	0.67	0.73
5	–5.3	5.8	365	21.6	227	0.45	0.64
6	6	5	0	57.8	212.2	0.16	0.58
7	14	4.2	0	61.3	207	0.15	0.54
8	10.4	4.1	0	60.4	140.4	0.17	0.63
9	3.6	4.5	0	43	57.5	0.22	0.73
10	–8.7	5.7	101	18.6	24.7	0.64	0.79
11	–22.2	5.5	244	0	3	0.73	0.79
12	–25.7	6.1	286	0	0	0.73	0.77

Calculations were carried out for a soil body 50 m thick. The types of soil layers and their thickness corresponded to Table 1, and the properties of soils in the thawed and frozen state corresponded to Table 2. The initial temperature distribution in the soil was assumed to be constant at –2 °C. The calculation began in mid-October and was performed for a period of 10 years; then, the temperature distribution across the soil thickness was compared with the initial value, and the next iteration of calculation was performed. The calculation was completed, and the regime of the soil temperature change was considered steady-state at a maximum difference in temperature between the initial and final values of < 0.01 °C. On average, the calculation with reaching the steady-state regime covered a time period of about 250 years. The flowchart of the calculation program is shown in Fig. 9.

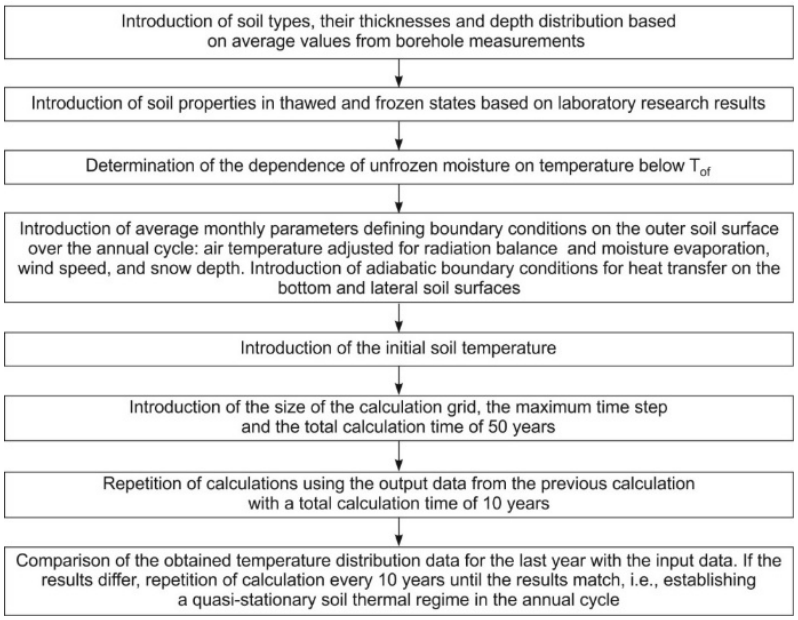

Figure 9. The flowchart of the calculation program.

When reaching a steady-state regime of soil temperature change during the year, soil temperature profiles were determined for the middle of each month. The temperature distributions over the soil depth in February and July, obtained by calculations with average data of long-term measurements for these months in Norilsk, are compared in Fig. 10 [32]. To validate the calculation model quantitatively, the root mean square error (RMSE) between the calculated and average experimental temperatures in Fig. 10 was determined according to the relationship:

$$RMSE = \sqrt{\frac{1}{n}\sum_{i=1}^{n}\left(\frac{T_{calc} - T_{\exp}}{T_{\exp}}\right)^2}, \quad (15)$$

where $T_{\exp}$ is the measured temperature, T_{calc} is the calculated temperature, n is the number of experimental points.

The RMSE between the calculated temperatures and the long-term average experimental temperatures was 0.67 °C for February (Fig. 10a) and 1.68 °C for July (Fig. 10b).

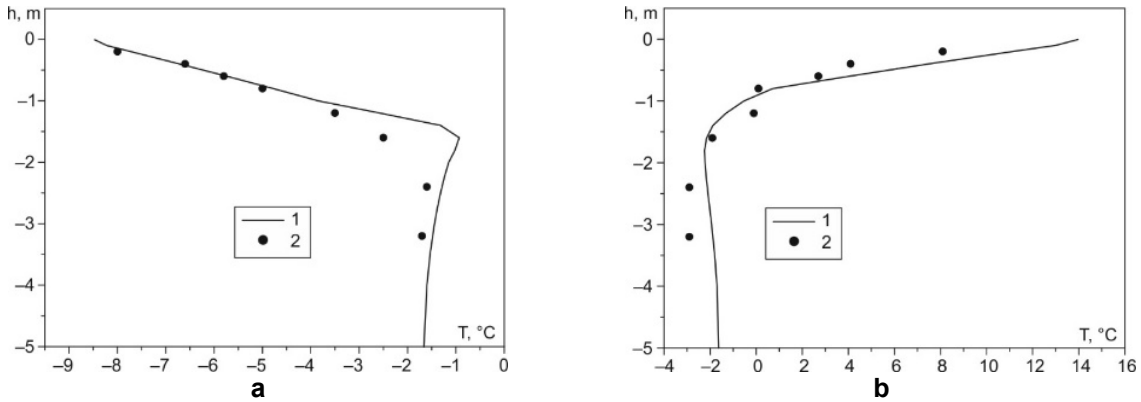

Figure 10. Comparison of temperature distribution under natural conditions: a) February, b) July; 1 – calculation, 2 – measurement data [32].

The results of calculations of changes in distribution of soil temperature over the depth in different months of the year are shown in Fig. 11a.

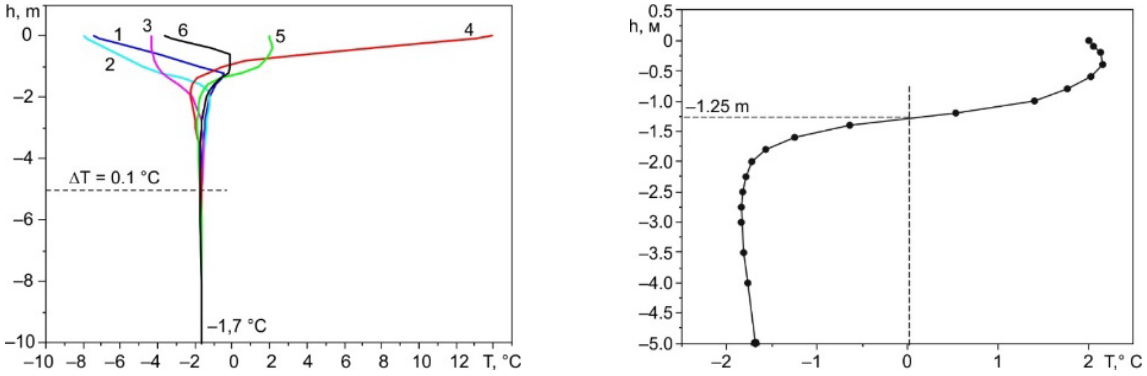

a b

Figure 11. Distribution of soil temperature under natural conditions: a) by month: 1 – January, 2 – March, 3 – May, 4 – July, 5 – September, 6 – November; b) September in detail.

It is possible to distinguish the active soil layer, where the temperature changed during the year. If we conditionally take the soil layer, where the temperature change during the year is ΔT > 0.1 °C, as the active layer; then, according to calculations performed, the boundary of the active layer under natural conditions was at a depth of about 5 m. Below this depth, the soil temperature did not change during the year and it was –1.7 °C, which is in good agreement with the results of actual measurements in boreholes at the construction site of a multi-story residential building (see Fig. 8).

The greatest depth of soil thawing (depth with soil temperature above 0 °C) under natural conditions, according to calculations, was observed in September, and it amounted to 1.25 m (Fig. 11b).

The calculation complexes applied take into account the thermal effects associated with freezing and thawing of moisture contained in the soil, so it is of particular interest to clarify the influence of phase transitions on the temperature distribution in permafrost soils. For this purpose, temperature changes over the soil depth under natural conditions were calculated without taking into account phase transitions during freezing and thawing of moisture, which in practice corresponds to dry soils.

The results of calculations without taking into account phase transitions are presented in Fig. 12.

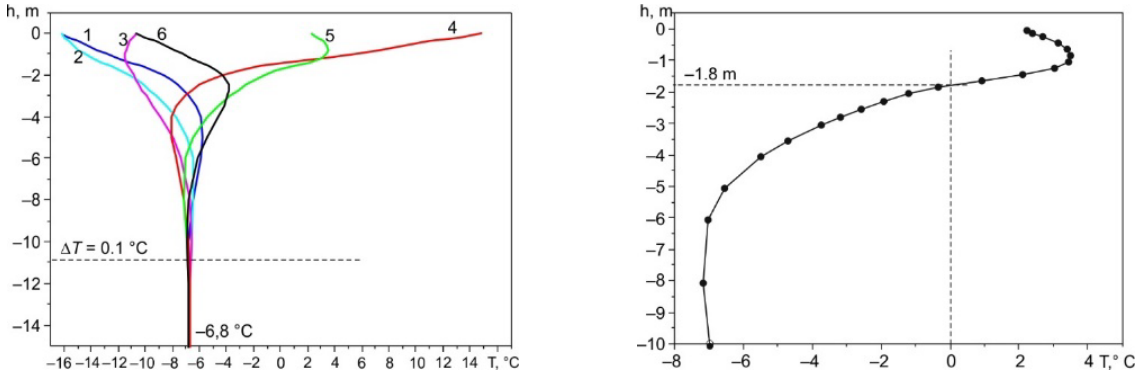

a b

Figure 12. Distribution of temperature in the soil under natural conditions without phase transitions: a) by months: 1 – January, 2 – March, 3 – May, 4 – July, 5 – September, 6 – November; b) September in detail.

Under these calculation conditions, the depth of the active layer increased compared to Fig. 11a by more than twice up to 11 m, and the constant soil temperature at this depth of –6.8 °C decreased significantly. The greatest depth of soil thawing, as in the previous calculation, was observed in September, but it increased by 0.5 m and amounted to –1.8 m (Fig. 12b).

Thus, the calculations showed that the moisture contained in the soil due to phase transitions during freezing and thawing of the soil has a screening effect, reducing the thickness of the active layer with soil temperature changes and the depth of soil thawing in the summer-autumn period, and prevents a general decrease in temperature in the deep soil layers.

When constructing buildings on permafrost soils, the construction technology with the use of a ventilated basement seems to be very good in order to prevent soil thawing and maintain its bearing

capacity (Fig. 1). The change in distribution of soil temperature, when the upper boundary of soil is under the conditions of a ventilated basement of unlimited size, was calculated taking into account the climatic features of Norilsk. The initial temperature distribution in the soil was assumed to be constant at –2 °C.

Unlike the previously considered case, when the soil was under natural conditions, the boundary condition on the outer surface of the soil was changed during the calculations: the absence of snow cover during the cold period of the year and changes in the radiation balance due to the shielding of direct solar radiation and effective long-wave radiation of the soil surface by the building were taken into account.

The results of calculating the change in the distribution of soil temperature in the annual cycle under the conditions of a ventilated basement are presented in Fig. 13.

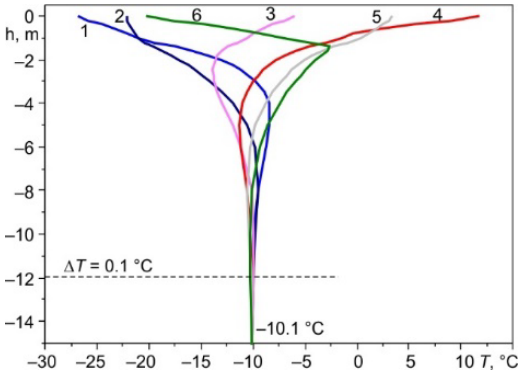

Fig. 13. Temperature distribution in the soil during the year under conditions of a ventilated basement: 1 – January, 2 – February, 3 – March, 4 – April, 5 – May, 6 – June, 7 – July, 8 – August, 9 – September, 10 – October, 11 – November, 12 – December.

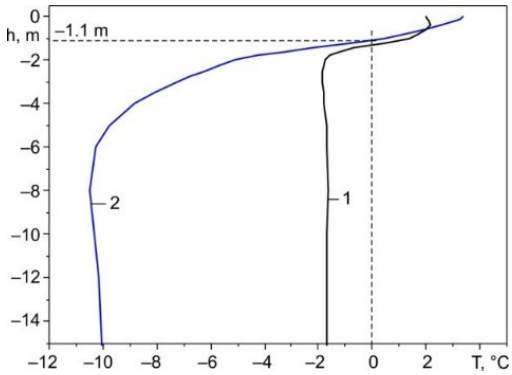

Figure 14. Comparison of the results of temperature distribution calculations in the soil in September: 1 – under natural conditions, 2 – under conditions of a ventilated basement.

When analyzing the results, attention should be paid to two features of a change in the soil temperature distribution during the annual cycle. The first feature is a significant decrease in the soil temperature below the active layer to –10.1 °C compared to the temperature of –1.7 °C, obtained earlier for the soil under natural conditions (see Fig. 11a). The second feature is associated with an increase in the thickness of the active layer of the soil to 12 m compared to the thickness of the active layer of 5 m for the soil under natural conditions. However, despite an increase in the active layer thickness under conditions of a ventilated basement, taking into account the general cooling of the soil, the maximum depth of soil thawing in September even decreased compared to the depth of soil thawing under natural conditions and amounted to –1.1 m (Fig. 14).

Thus, the absence of snow cover and direct solar radiation were the main factors that led to a decrease in the soil temperature under conditions of the ventilated basement of the building compared to the soil temperature under natural conditions and a decrease in the maximum depth of soil thawing in September. Therefore, when choosing the design of a ventilated basement, it is necessary to ensure that the soil surface in the ventilated basement is protected from solar radiation in the summer and is not covered with snow in the winter. Ventilated basement technology for the construction of multi-story buildings on permafrost soils has proven itself in practice and is becoming especially relevant in view of the observed global warming in northern regions.

Let us consider the soil temperature under a residential building with a ventilated basement and an elevator located on reinforced concrete blocks installed directly on the ground. The plan of the 1st floor with the overall dimensions of the ventilated basement and the elevator is shown in Fig. 2. To calculate the soil temperature, a 50 m thick design section was selected. In the central area of its surface, there is a zone

with boundary conditions characteristic of a ventilated basement and a small section of the elevator (Fig. 15).

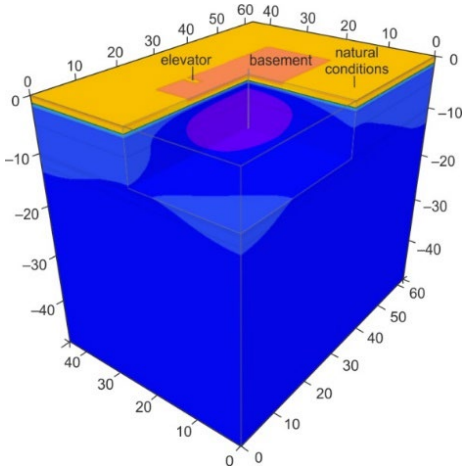

Figure 15. Design section.

In the calculations, it was assumed that the air temperature in the elevator during the heating season was 5 °C, and without heating, the air temperature there was equal to the air temperature outside. The surface area around the building in the figure, highlighted in yellow, corresponded to the soil surface under natural conditions; the length of this section from each side of the building was 15 m. Thus, on the outer surface of the soil, 3 sections with different boundary conditions were identified, while the distribution of soil temperature over the depth was determined at the center of each of these sections. The distribution of the initial soil temperature over the depth in calculations was taken as the temperature distribution obtained under natural conditions.

The distribution of soil temperature in September under a ventilated basement, under an elevator and in a section of soil directly next to the building under natural conditions after 1 year, 5 years, 30 years, and 250 years (the time required to reach a steady state in the annual cycle) from the start of the calculation is presented in Fig. 16.

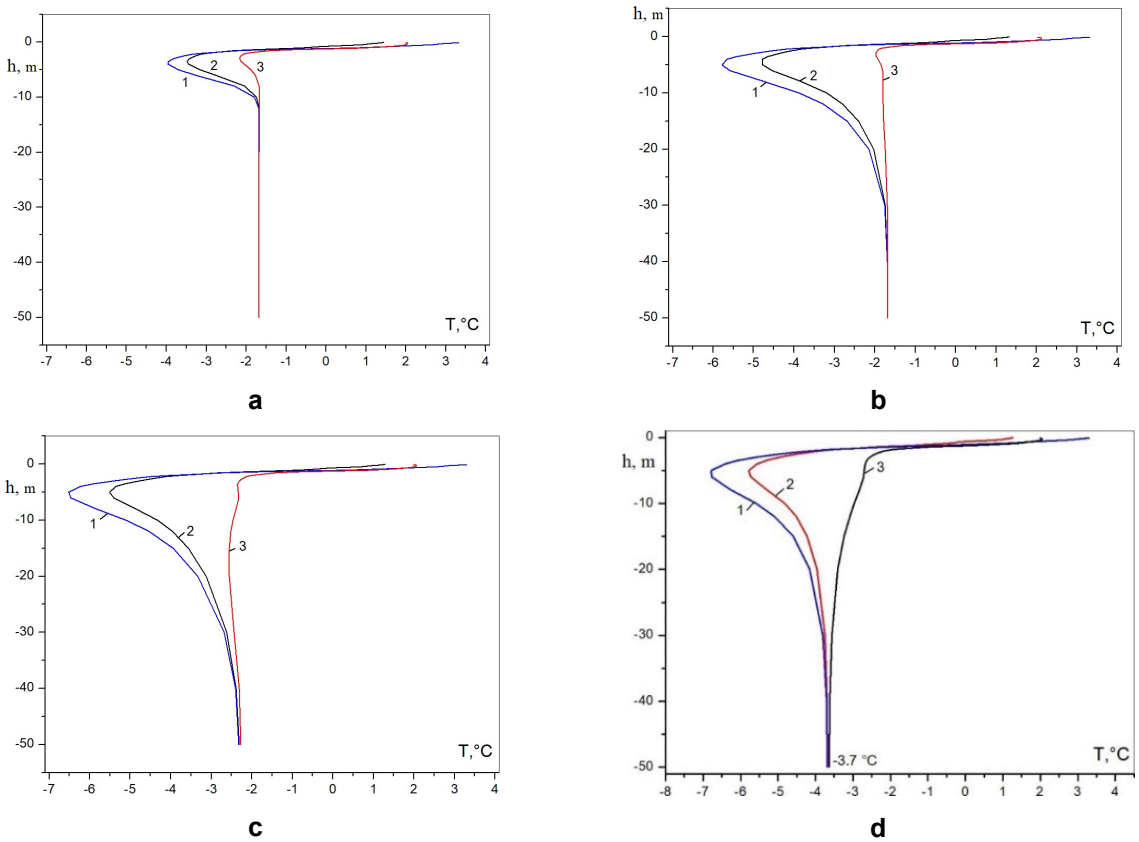

Figure 16. Temperature change in the soil depth after: a) 1 year, b) 5 years, c) 30 years, d) 250 years; 1 – under a ventilated basement, 2 – under an elevator, 3 – near a building.

According to the calculations, after 5 years, the lowest soil temperature was obtained under the ventilated basement, slightly higher temperature was obtained under the elevator, and the highest temperature was obtained near the building. The soil temperatures under all the considered areas converged gradually with increasing soil depth and reached a constant value. The soil temperature at a depth of 50 m after 5 years did not change and was equal to –1.7 °C, which corresponded to the temperature below the active layer for soil under natural conditions (Fig. 16a). After 30 years, a noticeable decrease in temperature was observed throughout the entire depth of the calculated area (Fig. 16c), and after 250 years, the temperature stabilized at a depth of 50 m with a soil temperature of –3.7 °C (Fig. 16d).

To determine the maximum depth of soil thawing, let us consider the temperature distribution in the surface layers of the soil in September with an established annual cycle of soil temperature change (Fig. 17).

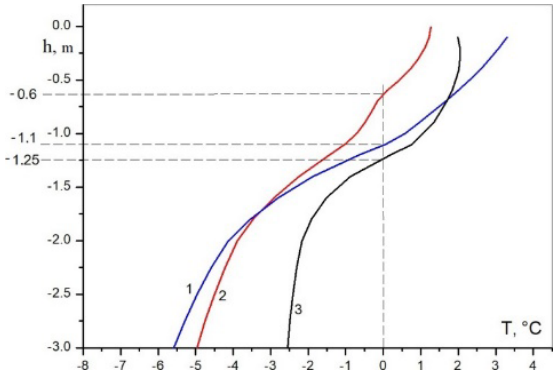

Fig. 17. Determination of the maximum depth of soil thawing: 1 – under a ventilated basement, 2 – under an elevator, 3 – near a building.

The calculation results show that the depth of soil thawing near the building was –1.25 m, under the ventilated basement, it was –1.1 m, and the smallest depth of soil thawing was obtained under the elevator: it was –0.6 m, which is associated, on the one hand, with good insulation of the elevator floor, and, on the other hand, with inertial thermal processes occurring in the soil.

Thus, the calculations performed showed that in multi-story buildings with ventilated basements, constructed in regions with permafrost soils, individual structural elements can be located directly on the ground surface. This will not cause additional soil thawing underneath them; however, in each specific case this should be confirmed by special calculations. When calculating, it is necessary to consider the thermal conditions in the rooms above the structural elements located on the ground, the ratio of the areas of the ventilated basement to the foundation of the structure, and additional insulation from the ground surface. It should be noted that the optimal location for such structures is the central zone of the ventilated basement.

4. Conclusions

The performed calculations of changes in soil temperature during the annual cycle in the climatic conditions of Norilsk using data on the types and thicknesses of soil layers obtained from boreholes, as well as on the basis of the characteristics of soil samples in thawed and frozen states, allowed us to draw the following conclusions:

1. The radiation balance for Norilsk conditions from May to August is positive and leads to soil heating, and for the rest of the year, it is negative and leads to its cooling. The radiation balance and evaporation of moisture from the soil surface, when calculating its temperature, can be taken into account through a correction to the average monthly air temperature. In the summer months, this correction increases the average monthly air temperature to 3 °C, and in the winter months, on the contrary, it decreases the air temperature by 1–2 °C.
2. In the natural climatic conditions of Norilsk, the greatest thawing of the soil is observed in September, and the maximum depth of soil thawing is –1.25 m.
3. A decrease in the moisture content of the surface layers of soil is shown by a decrease in the influence of phase transitions on the thermal-inertial properties of the soil, which leads to an increase in the thickness of the active soil layer, where annual temperature fluctuations occur, to an increase in the depth of soil thawing in the summer-autumn period, and to a decrease in soil temperature below the active layer.
4. The absence of snow cover and direct solar radiation are factors that lead to a significant decrease in the temperature of soil under the ventilated basement of a multi-story residential building compared to natural conditions and a decrease in the maximum thawing depth in September to

–1.1 m. When selecting a ventilated basement design, it is important to ensure that the soil surface within the ventilated basement is protected from solar radiation in the summer and is not covered by snow in the winter.

5. For multi-story buildings with ventilated basements, individual structural elements, when insulating them, can be placed directly on the ground surface, without additional thawing of the soil underneath them. However, in this case, the absence of additional soil thawing must be confirmed by a thermal engineering calculation taking into account the thermal conditions in the rooms above the structural elements, the area ratio of the ventilated basement to the structure foundation, and their additional insulation from the ground surface. It should be noted that the optimal location for such structures is the central zone of the ventilated basement.

References

1. Obu, J. How Much of the Earth's Surface is Underlain by Permafrost? Journal of Geophysical Research: Earth Surface. 2021. 126(5). Article no. e2021JF006123. DOI: 10.1029/2021JF006123
2. Nevechnaya merzlota [Not permafrost]. [Online]. URL: https://porarctic.ru/ru/projects/geokrio (date of application: 17.06.25).
3. Anisimov, O., Badina, S., Beloluckaya, M., et al. Izmenenie klimata v Rossijskoj Arktike: riski i novye vozmozhnosti [Climate Change in the Russian Arctic: Risks and New Opportunities]. Skolkovo: Moscow School of Management, 2022. 105 p.
4. Biskaborn, B.K., Smith, S.L., Noetzli, J., Matthes, H., Vieira, G., Streletskiy, D., et al. Permafrost is warming at a global scale. Nature communications. 2019. 10(1). Article no. 264. DOI: 10.1038/s41467-018-08240-4
5. Malkova, G., Drozdov, D., Vasiliev, A., Gravis, A., Kraev, G., Korostelev, Y., et al. Spatial and Temporal Variability of Permafrost in the Western Part of the Russian Arctic. Energies. 2022. 15(7). Article no. 2311. DOI: 10.3390/en15072311
6. Masson-Delmotte, V., Zhai, P., et al. IPCC Special Report: Global Warming of 1.5 °C. Summary for Policymakers. World Meteorological Organization. Geneva, 2018. 32 p.
7. Osipov, V., Aksyutin, O., Sergeev, D., Tipenko, G., Ishkov, A. Using the Data of Geocryological Monitoring and Geocryological Forecast for Risk Assessment and Adaptation to Climate Change. Energies. 2022. 15(3). Article no. 879. DOI: 10.3390/en15030879
8. Jorgenson, M.T., Racine, C.H., Walters, J.C., Osterkamp, T.E. Permafrost Degradation and Ecological Changes Associated with a Warming Climate in Central Alaska. Climatic Change. 2001. 48(4). Pp. 551–579. DOI: 10.1023/A:1005667424292
9. McKenzie, J.M., Kurylyk, B.L., Walvoord, M.A., Bense, V.F., Fortier, D., Spence, C., Grenier, C. Invited perspective: What lies beneath a changing Arctic? The Cryosphere. 2021. 15(1). Pp. 479–484. DOI: 10.5194/tc-15-479-2021
10. Streletskiy, D.A., Suter, L.J., Shiklomanov, N.I., Porfiriev, B.N., Eliseev, D. O. Assessment of climate change impacts on buildings, structures and infrastructure in the Russian regions on permafrost. Environmental Research Letters. 2019. 14(2). Article no. 025003. DOI: 10.1088/1748-9326/aaf5e6
11. Hjort, J., Karjalainen, O., Aalto, J., Westermann, S., Romanovsky, V. E., Nelson, F.E., Etzelmüller, D., Luoto, M. Degrading permafrost puts Arctic infrastructure at risk by mid-century. Nature communications, 2018. 9(1). Article no. 5147. DOI: 10.1038/s41467-018-07557-4
12. Chuvilin, E., Sokolova, N., Bukhanov, B. Changes in Unfrozen Water Contents in Warming Permafrost Soils. Geosciences. 2022. 12(6). Article no. 253. DOI: 10.3390/geosciences12060253
13. Romanovsky, V.E., Drozdov, D.S., Oberman, N.G., Malkova, G.V., Kholodov, A.L., Marchenko, S.S., et al. Thermal state of permafrost in Russia. Permafrost and Periglacial Processes. 2010. 21(2). Pp. 136–155. DOI: 10.1002/ppp.683
14. Wang, L., Liu, J., Yu, X., Wang, T., Feng, R. A Simplified Model for the Phase Composition Curve of Saline Soils Considering the Second Phase Transition. Water Resources Research. 2021. 57(1). Article no. e2020WR028556. DOI: 10.1029/2020WR028556
15. Wang, D., Tighe, S.L., Yin, S. Preliminary Analysis of Permafrost Degradation in Ingraham Trail, Northwest Territories. Lecture Notes in Civil Engineering. 240: Proceedings of the Canadian Society of Civil Engineering Annual Conference 2021. CSCE 2021. Springer. Singapore, 2021. Pp. 109–121. DOI: 10.1007/978-981-19-0507-0_11
16. Vasiltsov, V.S., Vasiltsova, V.M. Strategic Planning of Arctic Shelf Development Using Fractal Theory Tools. Journal of Mining Institute. 2018. 234. Pp. 663–672. DOI: 10.31897/PMI.2018.6.663
17. Ershov, E.D. Geokriologiya SSSR. Evropejskaya territoriya SSSR [Geocryology of the USSR. European Territory of the USSR]. Moscow: Nedra, 1988. 358 p.
18. Ershov, E.D. Geokriologiya SSSR. Zapadnaya Sibir' [Geocryology of the USSR. Western Siberia]. Moscow: Nedra, 1989. 454 p.
19. Khrustalev, L.N., Parmuzin, S.Y., Emelyanova, L.V. Nadezhnost' severnoj infrastruktury v usloviyah menyayushchegosya klimata [Stability of northern infrastructure under changing climate]. Moscow: University Book Press, 2011. 342 p.
20. Mangushev, R.A., Karlov, V.D., Sakharov, I.I., Osokin, A.I. Osnovaniya i fundamenty [Foundations and Foundations: Textbook for Bachelors of Construction and Specialists in the Field of Construction of Unique Buildings and Structures]. ASV Publishing House, 2019. 468 p.
21. Buslaev, G., Tsvetkov, P., Lavrik, A., Kunshin, A., Loseva, E., Sidorov, D. Ensuring the Sustainability of Arctic Industrial Facilities under Conditions of Global Climate Change. 2021. 10(12). Article no. 128. DOI: 10.3390/ resources10120128
22. Peng, H., Ma, W., Mu, Y. H., Jin, L. Impact of permafrost degradation on embankment deformation of Qinghai-Tibet Highway in permafrost regions. Journal of Central South University. 2015. 22(3). Pp. 1079–1086. DOI: 10.1007/s11771-015-2619-2
23. Vasilev, G.G., Dzhalyabov, A.A., Leonovich, I.A. Analysis of the Causes of Engineering Structures Deformations at Gas Industry Facilities in the Permafrost Zone. Journal of Mining Institute. 2021. 249. Pp. 377–385. DOI: 10.31897/PMI.2021.3
24. Kotov, P., Stanilovskaya, J. Long-term strength of frozen saline soils. Magazine of Civil Engineering. 2022. 5(13). Article no. 11307. DOI: 10.34910/MCE.113.7
25. Stetjukha, V.A. Frost cracks formation in permafrost regions. Magazine of Civil Engineering. 2021. 4(104). Article no. 10405. DOI: 10.34910/MCE.104.5
26. Alekseev, A.G. Calculation of seasonal soil freezing depth by engineering and numerical methods. Bulletin of Science and Research Center of Construction. 2024. 42(3). Pp. 56–82. DOI: 10.37538/2224-9494-2024-3(42)-56-82

27. Borej 3D. Rukovodstvo pol'zovatelya [Boreas 3D. User's Guide]. Version 2024.3. 129 p.
28. Russian State Standard SP-25.13330.2020. Osnovaniyania I fundamenty na vechnomerzlykh gruntah [Soil bases and foundations on permafrost soils]. Moscow: Ministry of Construction of Russia, 2020. 110 p.
29. Budyko, M.I. Teplovoj balans zemnoj poverhnosti [The thermal balance of the Earth's surface]. Leningrad: Hydrometeorological Publishing House, 1956. 255 p.
30. Nauchno-prikladnoj spravochnik po klimatu SSSR. Mnogoletnie dannye [Scientific and applied handbook on the climate of the USSR. Long-term data]. Series 3. Parts. 1–6. Iss. 21: Krasnoyarskij kraj. Tuvinskaya ASSR [Krasnoyarsk Krai. Tuvan ASSR]. Book 1. Leningrad: Gidrometeoizdat, 1990. 623 p.
31. Pogoda v Noril'ske [Weather in Norilsk]. [Online]. URL: https://norilsk.ginfo.ru/pogoda (reference date: 17.06.2025).
32. Fedotov, A.A., Kaniber, V.V., Hrapov, P.V. Analysis and Forecasting of Changes in the Soil Temperature Distribution in the Area of the City of Norilsk. International Journal of Open Information Technologies. 2020. 8(10). Pp. 51–65.

Information about the authors:

***Mikhail Nizovtsev**, Doctor of Technical Sciences*
ORCID: https://orcid.org/0000-0003-2372-6544
E-mail: nizovtsev@itp.nsc.ru

***Aleksey Sterlyagov**, PhD in Technical Sciences*
ORCID: https://orcid.org/0000-0001-8443-6474
E-mail: 30j@mail.ru

Received 03.07.2025. Approved after reviewing 30.11.2025. Accepted 02.12.2025.

Magazine of Civil Engineering

ISSN 2712-8172

journal homepage: http://engstroy.spbstu.ru/

Research article

UDC 69

DOI: 10.34910/MCE.140.10

The durability of white cement by using additives

M.A. Abdulrehman[1] ✉ , ***H.A. Goaiz***[2], ***A.A. Salman***[1], ***M.Q. Motair***[3]

[1] *Materials Engineering Department, Faculty of Engineering, Mustansiriyah University, Baghdad, Iraq*

[2] *Civil Engineering Department, Faculty of Engineering, Wasit University, Wasit, Iraq*

[3] *National Center for construction laboratories, Baghdad, Iraq*

✉ *aljaraah_muhammad@yahoo.com*

Keywords: Durability, dry shrinkage, white cement, steel fiber, PVP

Abstract. White cement mortar suffers from the appearance of cracks when it is used in the facades of buildings, and these cracks affect its durability and shelf life. Therefore, three additives were suggested to be used with white cement mortar to reduce shrinkage, taking into consideration that they do not negatively affect other cement properties. A type of water-soluble polymer, Polyvinylpyrrolidone (PVP), as well as two types of steel fibers (hooked fibers and straight fibers) and they were all used in proportions 0 %, 1 %, 2 %, and 3 % of the weight of cement. A set of physical and mechanical tests were carried out in addition to dry shrinkage test such as setting time, compressive strength, flexural strength, and water absorption. It was found through these tests that all the additives reduced the dry shrinkage and the best results were obtained when using steel fibers with hooked ends by 3 % where the dry shrinkage was decreased by 75 %. The same type of fiber gave the highest flexural strength, with an increase of 16 % by using the same ratio. As for the use of 1 % straight steel fibers, it achieved the highest value in the compressive strength test, with an increase of 5 %. As for PVP, it reduced the water absorption by 6 % when it was used by 3 %.

Citation: Abdulrehman, M.A., Goaiz, H.A., Salman, A.A., Motair, M.Q. The durability of white cement by using additives. Magazine of Civil Engineering. 2025. 18(8). Article no. 14010. DOI: 10.34910/MCE.140.10

1. Introduction

Although its manufacturing cost is higher than ordinary Portland cement (OPC), however, white Portland cement (WPC) is widely used for aesthetic and decorative purposes, whether it is used as white cement alone or colored materials (pigments) are added. The energy saving factor is one of the most important factors encouraging the use of WPC in surface finishes because it is reflective of the sun's rays, as it provides light as well as reduces the heat entering the buildings. WPC has similar properties to ordinary cement, except for the color and the proportion of some compounds such as manganese and iron [1]. The uses of WPC in the construction of buildings are limited, and the main reason for that is because suffers from shrinkage at an early age and thus the causes formation of cracks [2]. Several studies have been published on WPC and the additives used for the purpose of improving some of its properties, including Carbone et al., who discussed the effect of a styrene-acrylic emulsion and ethylene-vinyl acetate on the properties of WPC mortar [3]. Cherop et al. added non-ionic cellulose ethers to WPC and studied their effect on it [4]. Shahi et al. assessed the impact of incorporating TiO_2 nanoparticles into white cement on the strength of their push-out bonds [5]. Dantas et al. investigated the impact of TiO_2 on the setting time of white cement [6]. Alshoaibi et al. enhanced the self-cleaning capacity of white cement by incorporating nanopowders, including silver, zinc oxide, and titanium oxide [7]. Chen et al. enhanced the creep and viscosity properties of cement by incorporating polypropylene and polyvinyl alcohol into 3D-printed

structures [8]. Abdelzaher et al. recycled plastic waste and utilized it as an infill in white cement applications, thereby resolving the issue of plastic waste without impairing the properties of white cement [9].

As for the cement mortar without additives, it is prone to crack formation, and thus deformations occur due to shrinkage or other reasons related to the change in size where the addition of fibers can help reduce or control cracks [10, 11].

As mentioned earlier, the most prominent uses of WPC mortar are in surface finishes, especially considering that these finishes can have wide areas and dimensions and there are no breaks between them. Therefore, cracks are among the most important problems affecting the durability of WPC mortar.

Hence the aim of this study is to improve the durability of WPC mortar and controlling cracks by reducing shrinkage, which is the main cause of cracks when using white cement in large dimensions. through using three additives (Polyvinylpyrrolidone (PVP), hooked steel fibers, and straight steel fibers) and then studying the effect of the additives on the other properties of mortar in order to ensure that the additives have no negative effects and it is worth noting that the effect of any of the additives used in this research on the durability of white cement have been not studied previously.

2. Materials and Experimental work

2.1. Materials

2.1.1. White Portland cement

The physical test and chemical analysis of the white cement used in this research were carried out, and it was found to be in conformity with the conditions of Iraqi Standard No. 5 of 2021 [12]. It is worth noting that the white cement used in this research was manufactured by the Iranian Urmia Company.

2.1.2. Fine aggregate

When making cement mortar, standard sand must be used, standard sand was obtained after sieving and purification stages for sand found in Al-Akhaidar area – Karbala (Iraq), so standard sand compatible with ASTM-C778 [13] requirements was used. The gradation of standard aggregates is shown in Table 1.

Table 1. Sieve analysis of standard aggregate

Sieve size	Passing %
1.18 mm	100
0.600 mm	98.6
0.425 mm	74.1
0.300 mm	24.3
0.150 mm	0.12

2.1.3. Polyvinylpyrrolidone

PVP is a water-soluble polymer derived from N-vinylpyrrolidone as the monomer and was provided by the CDH Company (India) in powder form, as shown in Fig. 1, and it is characterized by solubility in water. The PVP characteristics obtained from the manufacturer are shown in Table 2.

Figure 1. PVP polymer.

Table 2. Properties of PVP.

Properties	Value
Melting point	150 °C
Color	White
pH	4–7
Chemical formula	$(C_6H_9NO)n$

2.1.4. Steel fibers

Two types of steel fibers were used in this research, and both types were supplied by the Turkish Atlas Company, one type was hooked ends and the other type was straight, and their properties are shown in Table 3 and their image is included in Fig. 2.

Table 3. Characterizes of steel fibers.

Properties	Straight steel fiber	Hooked steel fiber
Shape	Straight	Hooked End
Aspect ratio (l/d)	75	50
Tensile strength	2850 MPa	1100 MPa
Diameter	0.2 mm	0.7 mm
Length	15 mm	35 mm
Appearance	Gold	Grey
Density	7840 kg/m^3	7800 kg/m^3

Figure 2. Types of steel fiber: (A) straight and (B) with hooked ends.

2.1.4. Water

For the purpose of completing the hydration reaction with cement, distilled water was used to give ideal reaction conditions away from the effects of impurities.

2.2. Mixture Coding

The code for each mixture is shown in Table 4.

Table 4. Code of each mixture

Mix.	Type of admixture	Weight ratio of cement
RM	–	–
PM1	PVP	1 %
PM2	PVP	2 %
PM3	PVP	3 %
HM1	Hooked steel fiber	1 %
HM2	Hooked steel fiber	2 %
HM3	Hooked steel fiber	3 %
SM1	Straight steel fiber	1 %
SM2	Straight steel fiber	2 %
SM3	Straight steel fiber	3 %

2.3. Curing

Curing conditions differ from one test to another. For example, the fresh state tests were done directly and did not need any curing. As for the hardened state tests, they were also variable. For example, the dry

shrinkage test required the sample to be placed in water for two days (after being placed in the mold for 24 hours) and then placed in an open air area at a temperature room for 25 days. As for the other tests, which are compressive strength, flexural strength, and water absorption, they have similar curing conditions, as they were immersed in water for a period of 27 days (after being placed in the mold for 24 hours).

2.4. Tests

2.4.1. Setting time

A standard Vicat apparatus (its image is in Fig. 3) was used to determine the amount of water needed to determine the consistency required to perform a setting time test, which was carried out in accordance with ASTM-C191 [14] when mixing cement with the additives used in this study. This test was performed by preparing the cement paste (without or with additives) and mixed with water determined by the consistency test then the dough was placed into the mold, the initial setting time was done by using the needle placed at the point where it contacts the surface of the test mass and allowing it to penetrate the test specimen due to its weight. This process was repeated to the point where the needle penetrates the cement paste to 5 ± 0.50 mm from the bottom of the mold. The initial setting time is calculated from the moment that the water is added to the cement until the time the needle penetrates to a distance of 5 ± ± 0.50 mm from the bottom. While the final setting time was determined using a needle that has a 5 mm diameter circle at its tip. If the needle reaches the surface of the die, it will leave a mark without penetration.

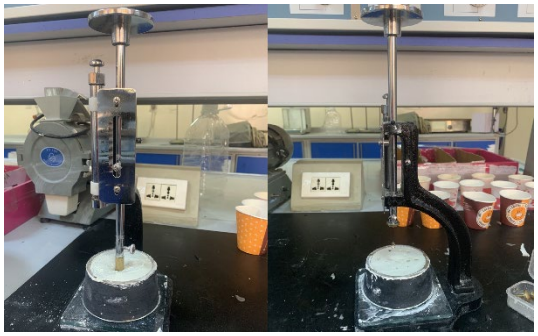

Figure 3. Vicat apparatus.

2.4.2. Dry shrinkage test

This test was performed in accordance with ASTM-C596 [15] where a cement to sand ratio 1 : 2 was used. Before placing the mortar into the molds for shrinkage test, a test shall be performed for each mortar to determine the amount of water that each sample needs in order to obtain a flow of 110 % (as shown in Fig. 4). The test molds had dimensions of 25 × 25 × 285 mm. The test was carried out by measuring the difference in the length of the prisms of the mortar before drying (after 3 days of pouring) and after drying (after 28 days of pouring). This test shows the possibility of cracking in the mortar because shrinkage is one of the main causes of cracks. The dry shrinkage test inspection machine is shown in Fig. 5.

Figure 4. Flow table test.

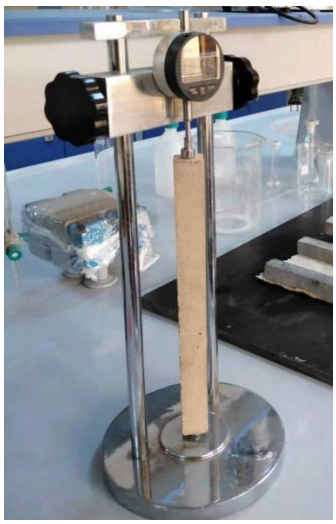

Figure 5. Dry shrinkage test.

2.4.3. Compressive strength test

The compressive strength test was determined according to ASTM-C150 [16] using cubes measuring 50 × 50 × 50 mm and averaging the compressive strength of three samples for each mix. The specimens were tested at loading rate of 1200 N/sec. The mixing ratio of cement : sand: water was 1 : 2.75 : 0.485, respectively, based on the requirements of the ASTM-C150 [11]. The cubes were tested 28 days after pouring the samples by a hydraulic machine with a capacity of 250 kN. Fig. 6 shows a sample during the test.

Figure 6. Compressive strength test.

2.4.4. Flexural strength

This test was performed with a 40 × 40 × 160 mm prism prepared in accordance with ASTM-C348 [17]. The mixing ratio of cement : sand : water was 1 : 2.75 : 0.485, respectively. Flexural strength was calculated by means of a three-point loading test for samples of all mortar mixtures with an age of 28 days, and the results were calculated for an average of 3 samples. A testing machine with a capacity of 250 kN was used to test the samples. Fig. 7 shows a sample during the test.

Figure 7. Flexural strength test.

2.4.5. Water absorption

Tests were carried out for samples with an age of 28 days using two cubic samples for each mix of mortar, and a water absorption test was performed depending on BS 1881-122 [18].

3. Results and Discussion

3.1. Setting Time

The results of the setting time test were listed in Table 5 and Fig. 8. It can be understood from Table 5 that increasing the use of the percentage of PVP as a weight ratio from the weight of cement leads to an increase in the initial and final setting times where when adding 3 % of PVP, the initial setting time was increased by 80 % and the final setting time was increased by 64 %. This is due to the emergence of a polymeric film that is formed by PVP in the mortar and encapsulates the cement particles and hinders the cement particles from interacting with water, thus slowing the hydration of the cement [19]. It was also found that the steel fibers had no significant effect on the setting time, as it increased by a few minutes when the content of steel fibers increased in the cement because the surface of the steel fibers was smooth and free from roughness, so no agglomeration was observed during mixing [20].

Table 5. Initial and final setting time

Mixtures	Setting time	
	Initial (min.)	Final (min.)
RM	100	165
PM1	120	220
PM2	155	245
PM3	180	270
HM1	105	175
HM2	110	190
HM3	120	200
SM1	110	185
SM2	125	205
SM3	150	235

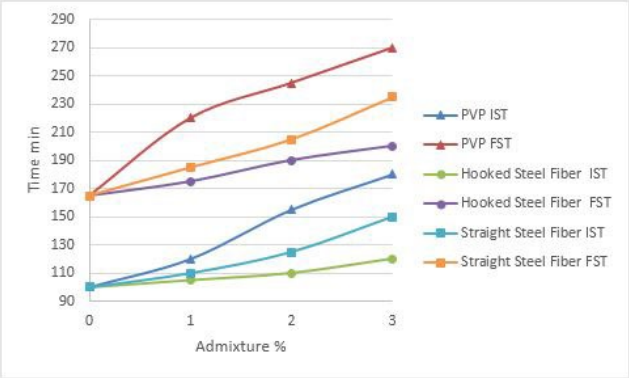

Figure 8. Setting time results.

3.2. Dry Shrinkage

The results of the dry shrinkage test were listed in Table 6 and Fig. 9. In Table 6, it was observed that the shrinkage decreases with increasing the content of PVP in the cement, as the shrinkage values were decreased by 50 % when adding 3 % because PVP is considered effective in reducing dry shrinkage in mortar due to its high ability to reduce the surface tension of the medium [21]. It can also be observed that as the amount of fiber increases as a percentage of the weight of cement, the shrinkage values decrease due to the fact that steel fibers hinder crack growth, this is because steel fibers have high ductility with a strong crack control effect as the dry shrinkage leads to a reduction in starting the crack [22]. It can also be noted that the fibers with hooked ends have a higher capacity than the straight fibers because of their role in creating stronger interlocked particles, as the hooked fibers caused a shrinkage reduction of 75 %, while the straight fibers reduced shrinkage by 63 %. Since the fiber is a non-pozzolan material, when added, it reduces the heat given off by the cement because the cement content is reduced in the slurry, and the reaction is slowed slightly because it provides insulation between the particles.

Table 6. Results of dry shrinkage test.

Mixtures	Dry shrinkage (%)
RM	0.008
PM1	0.007
PM2	0.005
PM3	0.004
HM1	0.005
HM2	0.003
HM3	0.002
SM1	0.006
SM2	0.004
SM3	0.003

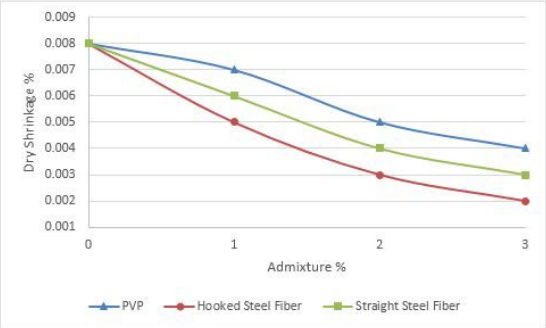

Figure 9. Dry shrinkage results.

3.3. Compressive Strength

The results of compressive strength test were listed in Table 7 and Fig. 10. From Table 7, it was noted that adding PVP in cement, it causes a slight increase in compressive strength and then decreases because the addition of PVP has a positive effect, in addition to being a water-soluble binder, it also reduces the gaps (pores) in the cement mortar [23]. As for the negative effects of compressive strength, if the PVP content is too high, the polymer film that surrounds the cement particles will prevent both the reaction and hydration processes between the cement particles and water, which leads to a decrease in the values of the compressive strength [14]. It was also observed that steel fibers increase the compressive strength, as the compressive strength was increased by 5 % when adding straight steel fibers by 1 %, and it is known that steel fibers work to withstand stresses and increase ductility [24], but increasing the percentage of steel fibers leads to a decrease in the amount of binder and thus reduce compressive strength. It was also noted that the straight fibers caused a higher increase than the hooked fibers due to having a higher aspect ratio.

Table 7. Result of compressive strength test.

Mixtures	Compressive strength (MPa)
RM	26.3
PM1	26.5
PM2	26.8
PM3	26.4
HM1	26.7
HM2	26.5
HM3	26.3
SM1	27.5
SM2	27.4
SM3	26.9

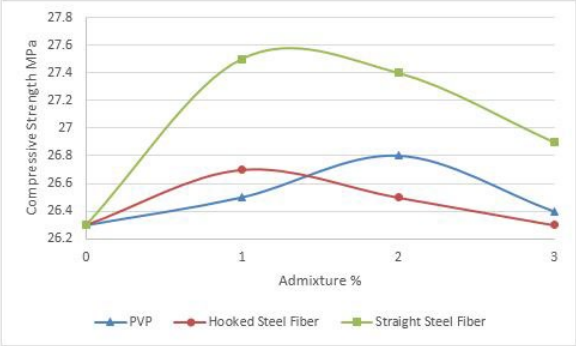

Figure 10. Compressive strength results.

3.4. Flexural Strength

The results of flexural strength test were listed in Table 8 and Fig. 11. It has been observed from Table 8 that by adding PVP as a percentage in cement, the flexural strength increases slightly, as it increases by 3 % when added by 1 %, then it decreases with increasing the addition. Where the decrease in flexural strength is attributed to the slowdown in the hydration rate of cement and this effect was mentioned previously, and the reason for the slight increase is due to the fact that PVP has a strong tensile strength compared to cement [14]. One of the important things in the following table is the increase obtained by using steel fibers with hooked ends where the flexural strength increased by 14 % when using 3 % of fibers. It is also known that steel fibers hinder crack growth and increase ductility and thus improve tensile properties. It is also noted that fibers with ends hooked fibers had better results than straight fibers, and this is because the fibers with hooked ends play a role similar to the anchor, which gives higher strength [25]. It was possible to obtain a higher increase in the value of flexural strength and it not caused by the decrease in the binder in the mortar.

Table 8. Results of flexural strength.

Mixtures	Flexural strength (MPa)
RM	6.3
PM1	6.5
PM2	6.3
PM3	6.3
HM1	6.8
HM2	7.1
HM3	7.2
SM1	6.4
SM2	6.7
SM3	6.9

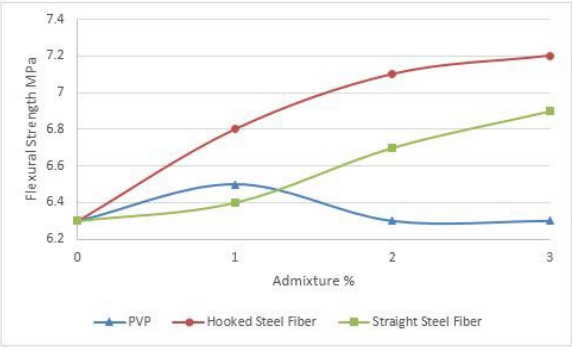

Figure 11. Flexural strength results.

3.5. Water Absorption

The results of the water absorption test were listed in Table 9 and Fig. 12. It has been observed from Table 9 that the value of absorption decreases when adding the polymer PVP, as the absorption decreases by 6 % when adding 3 % of the polymer, due to the role that the polymer plays in filling the mortar voids

and thus reducing absorption [19]. It was also noted that the use of steel fibers caused a slight increase in absorption, and it reached the largest increase by 2.6 % when using straight fibers by 3 %, which is naturally not a significant increase, and we build our interpretation of this behavior as it was said by previous researchers “This is likely due to the emergence of an interfacial transition zone at the periphery of the fibers” [20].

Table 9. Result of water absorption.

Mixtures	Water absorption (%)
RM	3.85
PM1	3.77
PM2	3.71
PM3	3.60
HM1	3.86
HM2	3.89
HM3	3.91
SM1	3.90
SM2	3.92
SM3	3.95

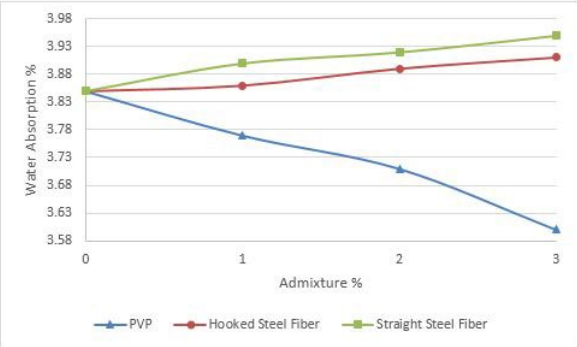

Figure 12. Water absorption results.

4. Conclusion

Based on all the tests that were conducted in this research, it was proved that all the used additives reduce shrinkage and increase the durability of the white mortar and do not have any negative effects on other properties if they are used in reasonable and acceptable proportions. Also, the following conclusion points can be drawn:

1. The initial setting time of the white cement was increased by 80 % and the final setting time was increased by 64 % for PVP fiber. In contrast, the steel fiber had no effect on the sitting time of the white cement according to the test results of this study, therefore, in cases where longer setting time is required, PVP should be used.
2. In terms of drying shrinkage reduction in white cement mixtures, the steel fibers with hooked ends showed approximately 75 % reduction, which was achieved by 3 % of hooked steel fiber content. Based on the results of this test, it is recommended to use hooked steel fibers in applications where white cement is used in large parts.
3. In general, the experimental results showed that the compressive strength of the white cement mixture was slightly improved by the addition of all types of fiber (PVP, straight steel, and hooked steel). The most important thing is that there is no negative effect when using any type of additives.
4. The flexural strength of the white cement containing 3 % of hooked steel fiber showed the highest increase by nearly 14 % compared to the flexural strength of the white cement mixture without any addition, this improvement gives it an advantage when using white cement in applications that are subject to tension.
5. Based on the test results of the water absorption for all the white cement mixtures, the using of 3 % of PVP fiber showed a 6 % water absorption reduction, which was the best results among other

addition of fiber in this study, even if the improvement is not major, it may help to keep the buildings' durability intact.

References

1. Farny, J.A. White cement concrete. 1st ed. Portland Cement Association. New York, 2001. 24 p.
2. Hamad, B.S. Comparative studies of Type I and White Portland cements. Journal of Advanced Cement-Based Materials. 1995. 2(1). Pp. 127–168.
3. Carbone, C.E., Santos, H., Romano, R.C.O., Pileggi, R.G. Efeito da adição de látex nas pastas de cimento branco no estado endurecido. Ambiente Construído. 2013. 13(3). Pp. 317–330. DOI: 10.1590/S1678-86212013000300019
4. Cherop, P.T., Kiambi, S.L., Kosgey, E.K. Effect of non-ionic cellulose ethers on properties of white portland cement. International Journal of Applied Engineering Research. 2017. 12(10). Pp. 2502–2508.
5. Shahi, S., Samiei, M., Bahari, M., Yavari, H., Rahbar Mahvarian, M. Effect of Incorporating Titanium Dioxide Nanoparticles into White Portland Cement, White Mineral Trioxide Aggregate, and Calcium Enriched Mixture Cement on the Push-out Bond Strength to Furcal Area Dentin. Journal of Dentistry. 2023. 24(4). Pp. 422–428. DOI: 10.30476/dentjods.2023.92290.1627
6. Dantas, S.R.A., Maciel, M.H., Romano, R.C.O., Pileggi, R.G., Sanchez, L.F.M. Influence of TiO_2 on the kinetic reaction of white Portland cement suspensions. Further Reduction of CO2 -Emissions and Circularity in the Cement and Concrete Industry: The 16th International Congress on the Chemistry of Cement 2023 (ICCC2023). Bangkok, 2023.
7. Alshoaibi, A., Hussain, F., Aslam, M., Zubairi, H., Aijaz., A., Majeeed, F., Khan, I. Synthesis and Use of Nano Particles for Enhancing the Self-Cleaning Effects in White-Cement. 2023. Preprint. DOI: 10.21203/rs.3.rs-2985468/v1
8. Chen, M., Xu, J., Yuan, L., Zhao, P., Li, Q., Lu, L., Wang, L. Use of creep and recovery protocol to assess the printability of fibre-reinforced 3D printed white Portland cement composites. Virtual and Physical Prototyping. 2024. 19(1). Article no. e2331201. DOI: 10.1080/17452759.2024.2331201
9. Abdelzaher, M., Farghali, A.A., Hamouda, A.S. Effective impact of nano-plastic-waste incorporated with nanotitina on the physical, mechanical and microstructural properties of white cement pastes composites for progressing towards sustainability. Scientific Reports. 2024. 14(1). Article no. 12581. DOI: 10.1038/s41598-024-62661-4
10. Deshmukh, S., Bhusari, J., Zende, A. Effect of glass fibers on ordinary Portland cement concrete. IOSR Journal of Engineering. 2012. 2(6). Pp. 1308–1312. DOI: 10.9790/3021-026113081312
11. Tirumala, S.S., Rao, P.S.R.S. Relationship between Compressive, Split Tensile, Flexural Strength of Self Compacted Concrete. i-Manager's Journal on Future Engineering and Technology. 2008. 3(1). Pp. 78–82. DOI: 10.26634/jfet.3.1.706
12. IQS.2021. Iraqi specification for Portland cement test no. 5.
13. ASTM-C778. Standard Specification for Standard Sand. ASTM International. West Conshohocken, PA, 2021. 3 p. DOI: 10.1520/C0778-21
14. ASTM-C191. Test Method for Time of Setting of Hydraulic Cement by Vicat Needle. ASTM International. West Conshohocken, PA, 2021. 8 p.
15. ASTM-C596. Drying shrinkage of mortar containing hydraulic cement. ASTM International. West Conshohocken, PA, 2021. 3 p.
16. ASTM-C109. Standard Test Method for Compressive Strength of Hydraulic Cement mortars. ASTM International. West Conshohocken, PA, 2021. 12 p.
17. ASTM-C348. Flexural Hydraulic Cement Mortars Test Equipment. ASTM International. West Conshohocken, PA, 2021. 6 p.
18. BS-1881:122. Method for Determination of Water Absorption. British Standard. London, 2011.
19. Liu, B., Yin, L., Chen, J., Li, M., Tang, D., Zhang, Y. Experimental Study on the Influence of PVA Content on the Performance of Grouting Material in Deep Stope. Geofluids. 2021. 2021(1). Article no. 6684754. DOI: 10.1155/2021/6684754
20. Małek, M., Jackowski, M., Łasica, W., & Kadela, M. Influence of Polypropylene, Glass and Steel Fiber on the Thermal Properties of Concrete. Materials. 2021. 14(8). Article no. 1888. DOI: 10.3390/ma14081888
21. Zhang, Y.C., Li, Q.N. Experimental Study and Performance Analysis of Concrete Shrinkage-Reducing Agents. Advanced Materials Research. 2011. 311-313(1). Pp. 1879–1883.
22. Jhatial, A.A., Sohu, S., Bhatti, N.-ul-K., Tahir Lakhiar, M., Oad, R. Effect of steel fibres on the compressive and flexural strength of concrete. International Journal of Advanced and Applied Sciences. 2018. 5(10). Pp. 16–21.
23. Abbas, W.A., Iqbal, N.K., Mahdi Jasim, H. Investigation of the Optimal Percentage from Polyvinyl Alcohol on Flexural Strength of Cement Mortar Composite. International Journal of Engineering & Technology. 2018. 7(4.20). Pp. 584–587. DOI: 10.14419/ijet.v7i4.20.26423
24. Vallarasu Manoharan, S., Anandan, S. Steel Fibre Reinforcing Characteristics on the Size Reduction of Fly Ash Based Concrete. Advances in Civil Engineering. 2014. 2014(1). Article no. 217473. DOI: 10.1155/2014/217473
25. Ye, Y., Liu, J., Zhang, Zh., Wang, Z., Peng, Q. Experimental Study of High-Strength Steel Fiber Lightweight Aggregate Concrete on Mechanical Properties and Toughness Index. Advances in Materials Science and Engineering. 2020. 2020. Article no. 5915034. DOI: 10.1155/2020/5915034

Information about the authors:

Mohammed Abdulrehman,
ORCID: https://orcid.org/0000-0001-8567-5880
E-mail: aljaraah_muhammad@yahoo.com

Hussam Goaiz,
E-mail: hussam@uowasit.edu.iq

Ali Salman,
E-mail: ali.eng2017@uomustansiriyah.edu.iq

Mohammed Motair,
E-mail: mqmr2020@gmail.com

Received 14.02.2023. Approved after reviewing 09.07.2025. Accepted 09.07.2025.